SAND2024-16082R

RANGERS

Modeling Report on Integrity and Performance Assessment of Engineered Barrier Systems in a Salt Repository for HLW/SNF

BGE TEC 2024

Technical Report

RANGERS

Modeling Report on Integrity and Performance Assessment of Engineered Barrier Systems in a Salt Repository for HLW/SNF

Project Coordinators
BGE TEC 2024
Eric Simo (BGE TEC)
Ed Matteo (SANDIA)

Authors
Eric Simo (BGE TEC)
Philipp Herold (BGE TEC)
Andree Lommerzheim (BGE TEC)
Andreas Keller (BGE TEC)
Edward Matteo (Sandia)
Carlos M. Lopez (Sandia)
David Fukuyama (Sandia)
Richard S. Jayne (Sandia)
Kristopher L. Kuhlman (Sandia)
Melissa M. Mills (Sandia)

Date
2024

Client
BMUB

The report was compiled as part of the project:
“Methodology for Design and Performance Assessment of Engineered Barrier Systems in a Salt Repository for HLW/SNF (RANGERS).”
Sandia National Laboratories is a multimission laboratory managed and operated by National Technology & Engineering Solutions of Sandia, LLC, a wholly owned subsidiary of Honeywell International Inc., for the U.S. Department of Energy’s National Nuclear Security Administration under contract DE-NA0003525.

RANGERS

Modeling Report on Integrity and Performance Assessment of Engineered Barrier Systems in a Salt Repository for HLW/SNF

BGE TEC 2024

Project Coordinators
Eric Simo (BGE TEC)
Ed Matteo (SANDIA)

Authors
Eric Simo (BGE TEC)
Philipp Herold (BGE TEC)
Andree Lommerzheim (BGE TEC)
Andreas Keller (BGE TEC)
Edward Matteo (Sandia)
Carlos M. Lopez (Sandia)
David Fukuyama (Sandia)
Richard S. Jayne (Sandia)
Kristopher L. Kuhlman (Sandia)
Melissa M. Mills (Sandia)

Date
2024

Client
BMUB

Total pages: 212

Authors:	Reviewer:	QS:	Release:
E. Simo	P. Herold	M. L. v. Borstel	T. Berlepsch
12	13	14	15

Contents

List of Figures

List of Tables

1. Introduction

The Engineered Barrier System (EBS) plays an important role in ensuring the long-term safety and containment of high-level waste (HLW) and spent nuclear fuel (SNF) in deep geological repositories in salt formation. As part of a multi-barrier system, the EBS works alongside the natural barrier, which is the salt formation itself and the technical barrier comprising the disposal casks. The primary function of the EBS is to maintain containment during a defined period until the backfill used in the repository made of crushed salt, develops its sealing capacity through compaction. Over the time, the backfill eventually compacts to a state of low porosity and permeability, acting as a long-term seal. However, until this process is complete, the EBS must retain its structural and functional integrity. Regulatory guidelines in Germany currently require the EBS to remain effective for up to next ice age, that is expected in 50,000 years. The significant hydro-geological and topographic changes expected during an ice age could make it impossible to accurately predict the hydro-chemical conditions within the repository system at that time.

In response to these challenges, BGE TECHNOLOGY GmbH (BGE TEC) and Sandia National Laboratories (SNL) have jointly developed a comprehensive methodology for the design and safety assessment of engineered barrier systems within the scope of the RANGERS project. This methodology is tailored for repositories in salt formations. The developed methodology provides a structured approach for designing and assessing the performance of the EBS in salt-based repositories. It begins with defining a sealing concept based on the geological characteristics of the selected site and the overall repository design. The entire repository system, comprising the geological site, repository infrastructure, and EBS, is then subjected to a Features, Events, and Processes (FEP) analysis, focusing solely on those FEPs that affect the EBS. The derived FEPs help identify the loads and stresses acting on the EBS, which serve as the foundation for conducting an integrity assessment. This analysis helps predict the EBS's evolution and performance over the regulatory time frame, feeding into integrated performance assessment simulations.

Based on this approach, a robust modeling concept has been developed, allowing for systematic numerical analyses required for both integrity and performance assessments. This concept enables precise and stringent safety assessments, ensuring the long-term containment of HLW and SNF. The present report focuses on the application of this methodology to a generic repository system in salt formations, detailing the processes and outcomes of the developed approach.

2. Modeling Concept

The modeling concept is derived from the methodology for design and performance assessment of EBS developed in RANGERS. The key objective of this methodological approach is the performance assessment of geotechnical barriers within the safety assessment of a salt repository system. The methodological approach was developed in accordance with the German specifications of the EndlSiAnfV (Final Repository Safety Requirements Ordinance). It is summarized in Figure 2.-1. According to EndlSiAnfV §5 (1), the integrity of the EBS must be examined, demonstrated, and justified for the expected evolution over the planned functional time. Based on this, a distinction is made between the integrity demonstration and the integrity evaluation. The integrity demonstration conducts the integrity assessment for the reference scenario (or expected evolution). In the integrity evaluation, alternative scenarios relevant to the EBS are addressed. This step is not explicitly required in the EndlSiAnfV but creates the basis for a better evaluation of the robustness proof and for illustrating the optimization potential of the EBS. This is particularly important since the alternative scenarios represent states of the EBS that deviate from the reference case beside representing evolutions with a lower probability of occurrence. The analysis of the repository system for such unfavorable cases lays the fundamentals for a better assessment of the robustness proof and for illustrating the optimization potential of the EBS as prescribed in EndlSiAnfV §6 (1).

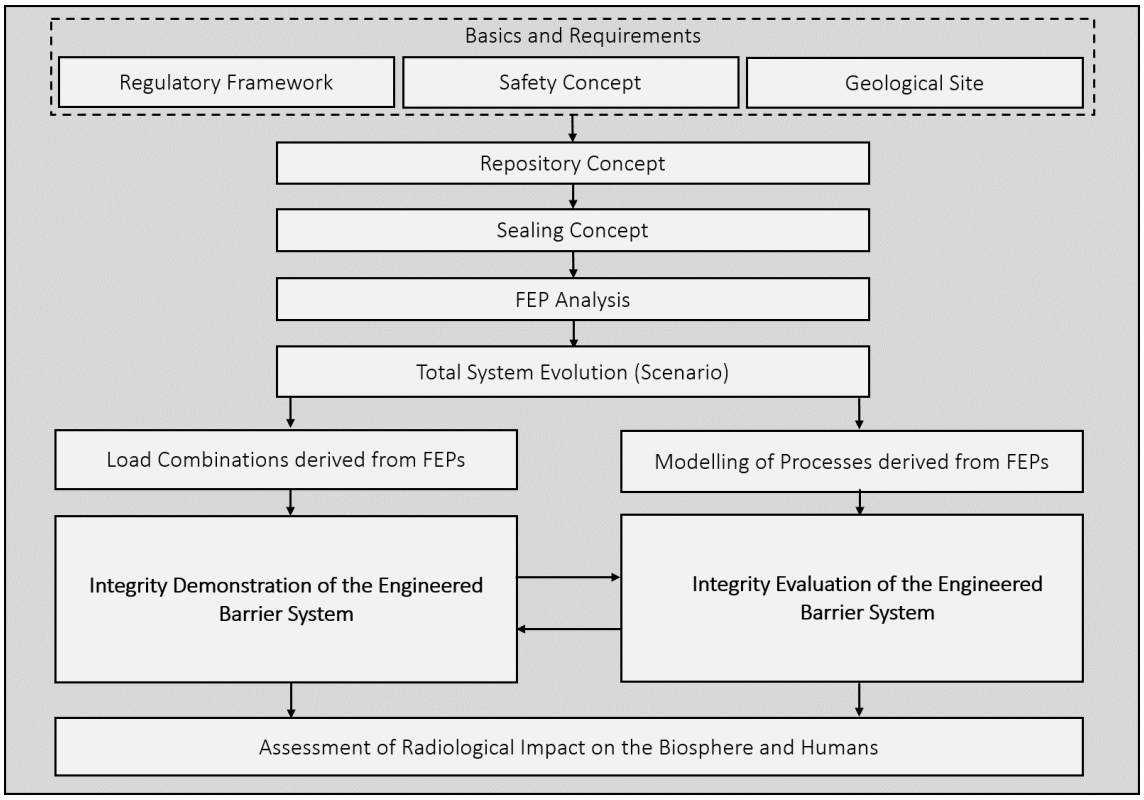

Figure 2.-1: RANGERS methodology diagram for the design, integrity and performance of engineered barrier system in salt repositories.

2.1 Integrity demonstration

The integrity demonstration primarily provides evidence of the preservation of mechanical integrity and hydraulic resistance. Partial safety proofs based on the verification concept developed by Müller-Hoeppe et al. (2012b) are used for this purpose, taking into account the concept of partial safety factors. The partial proofs must be provided for hydraulic permeability, mechanical stability, and long-term stability over the envisaged functional period. The proof of manufacturability is discussed in the SOTA (State of the Art) report of the RANGERS project (Keller et al., 2021).

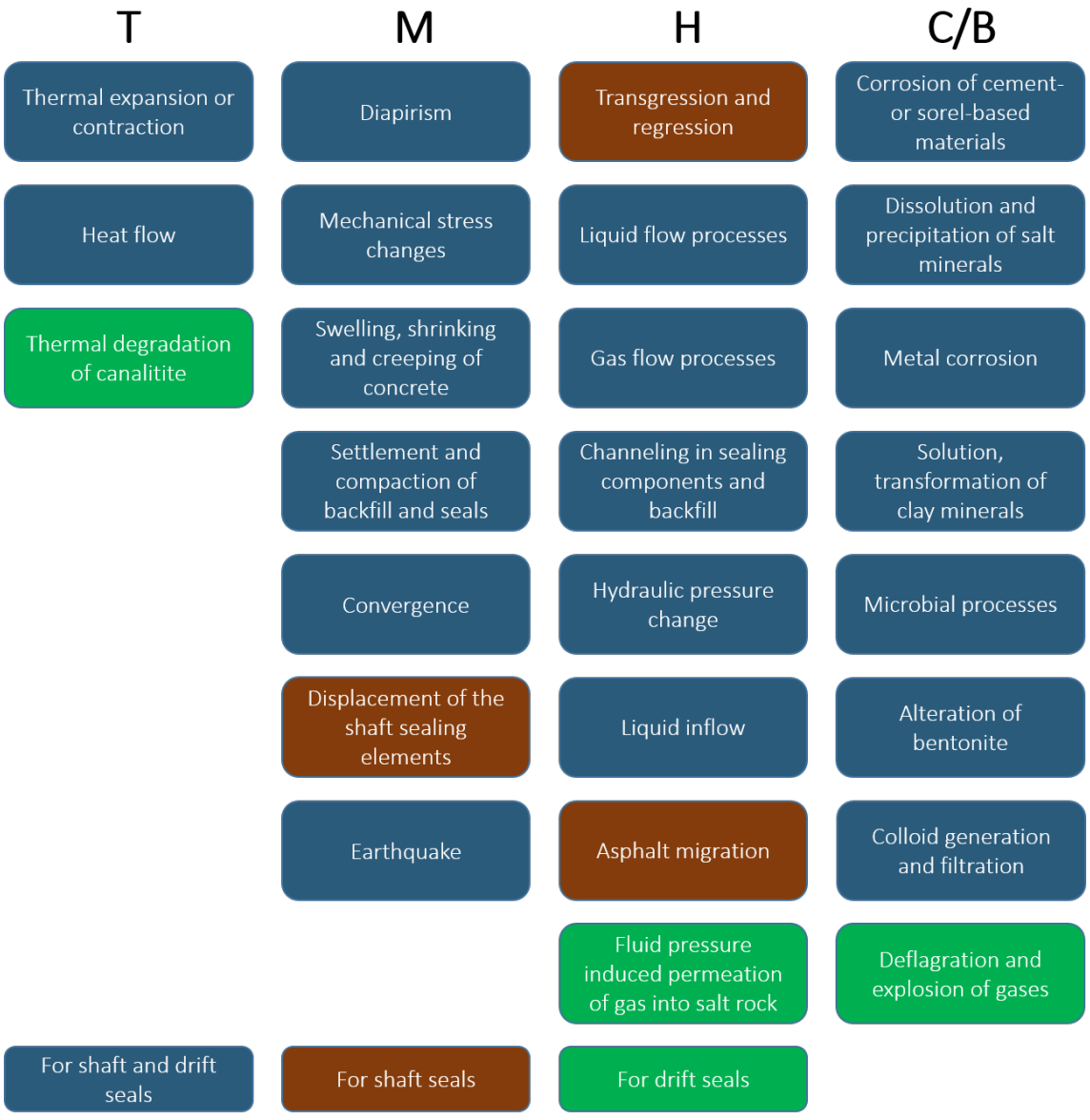

Figure 2.-2: Summary of all initial FEP impacting the EBS established in Table 7.2 and 7.3 of the methodology report (Simo et al., 2024): blue color represents FEP relevant for the shaft and drift sealing system, brown color shows FEP relevant only for shaft sealing system and green color: FEP relevant for drift sealing system.

The integrity demonstration is to be performed for the reference scenario. The reference

scenario is described by the so-called initial barriers, initial Features, Events and Processes (FEP) and FEP that are linked to radionuclide mobilization and transport. The initial barriers are the key components of the EBS. The initial FEP are processes that may directly affect the functionality of the EBS and are therefore relevant for EBS performance assessment. They were described in greater detail in the methodology report (Simo et al., 2024). Figure 2.-2 summarizes all initial FEP that are relevant for the design and performance assessment of the EBS. They are based on expert judgment and therefore not exhaustive.

In the next step, the initial FEP are further evaluated based on their relevance for the partial verification proof that needs to be fulfilled in the course of the integrity demonstration. This assessment can be carry out specifically for each component of the EBS such as the shaft or the drift sealing system. The FEP are combined to check the verification criteria according to the conceptual model presented in Figure 2.-3

		Specification of hydraulic resistance			Demonstration of structural integrity				
		Hydraulic resistance: sealing element	**Hydraulic resistance: contact zone**	**Hydraulic resistance: EDZ**	Structural stability	Crack limitation	Deformation limitation	Filtration stability	Long-term stability
		Reference Scenario / Alternative Scenarios							
Initial FEPs	Modelling case 1: Combination of FEPs		■	■					■
	Modelling case 2: Combination of FEPs				■	■			
	Modelling case 3: Combination of FEPs				■	■			
	Modelling case 4: Combination of FEPs	■					■		

Figure 2.-3: Conceptual definition of modeling cases to check the verification criteria.

For the long-term stability of the EBS, the geochemical conditions in the repository system play an important role in the potential degradation of the construction materials from which the EBS is made. Geochemical changes can be further driven by temperature or temperature may affect the properties of geomaterials and endanger their sealing properties over time. From this, one derives that FEP from the chemical and thermal process classes are relevant for the assessment of the long-term stability proof. Therefore, thermal and geochemical analyses are needed to carry out the proof. The FEP used for this analyses are highlighted in Figure 2.-4

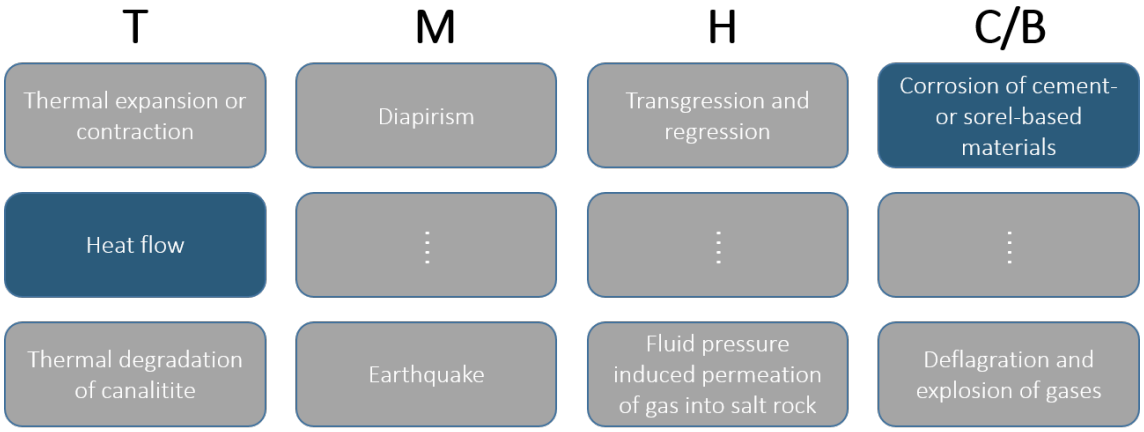

Figure 2.-4: Initial FEP of relevance for the long-term stability proof.

As for the mechanical integrity proof, a differentiation is to be made between the components of the EBS as different loads can be relevant for some components but can be neglected for other components. In general, all FEP leading to a mechanical impacts should be considered in this step. The FEP identified for the verification proof are highlighted in Figure 9.-1. Those FEP cover the thermal, mechanical, and hydraulic processes.

The chemical FEP can be excluded from the integrity proof because those FEP lead typically to a degradation of the materials. These chemical degradation processes are already considered in the long-term stability proof. For the case where the effect of the chemical FEP cannot be quantitatively predicted, as it is the case in ice age conditions, the assessment of the EBS performance resulting from the chemical damage is investigated in the integrity evaluation.

Although the processes of swelling, shrinking or creeping might be driven by chemical processes at a microscale, their impact on the barrier are mechanical and thus does not technically belong to the chemical process.

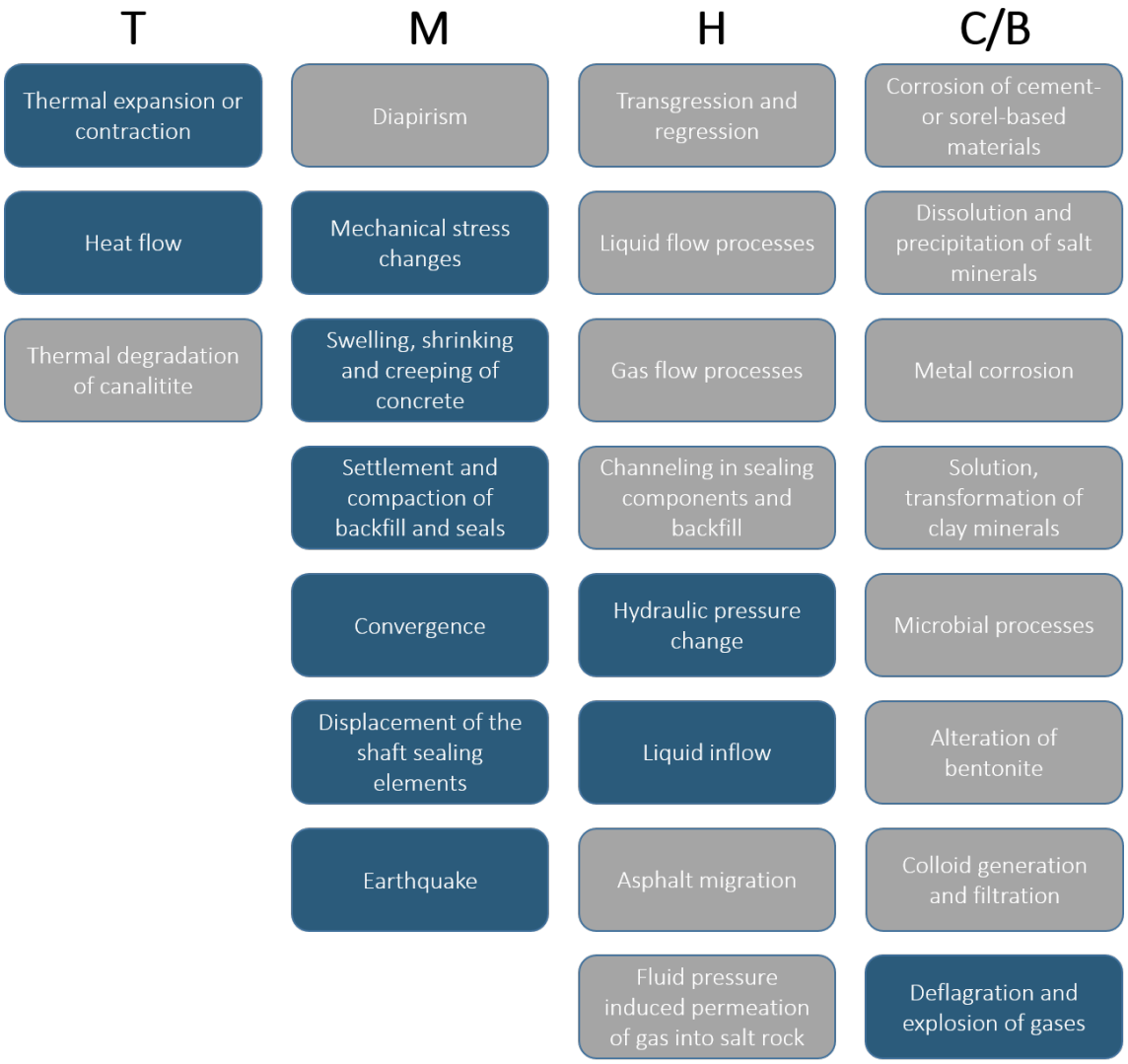

Figure 2.-5: Initial FEP of relevance for the mechanical integrity proof.

The hydraulic resistance will be analyzed by FEP of the hydraulic process class. Those FEP are important to describe the hydraulic evolution of the repository system and thus the performance of the EBS upon hydraulic flow. They are highlighted in Figure 2.-6

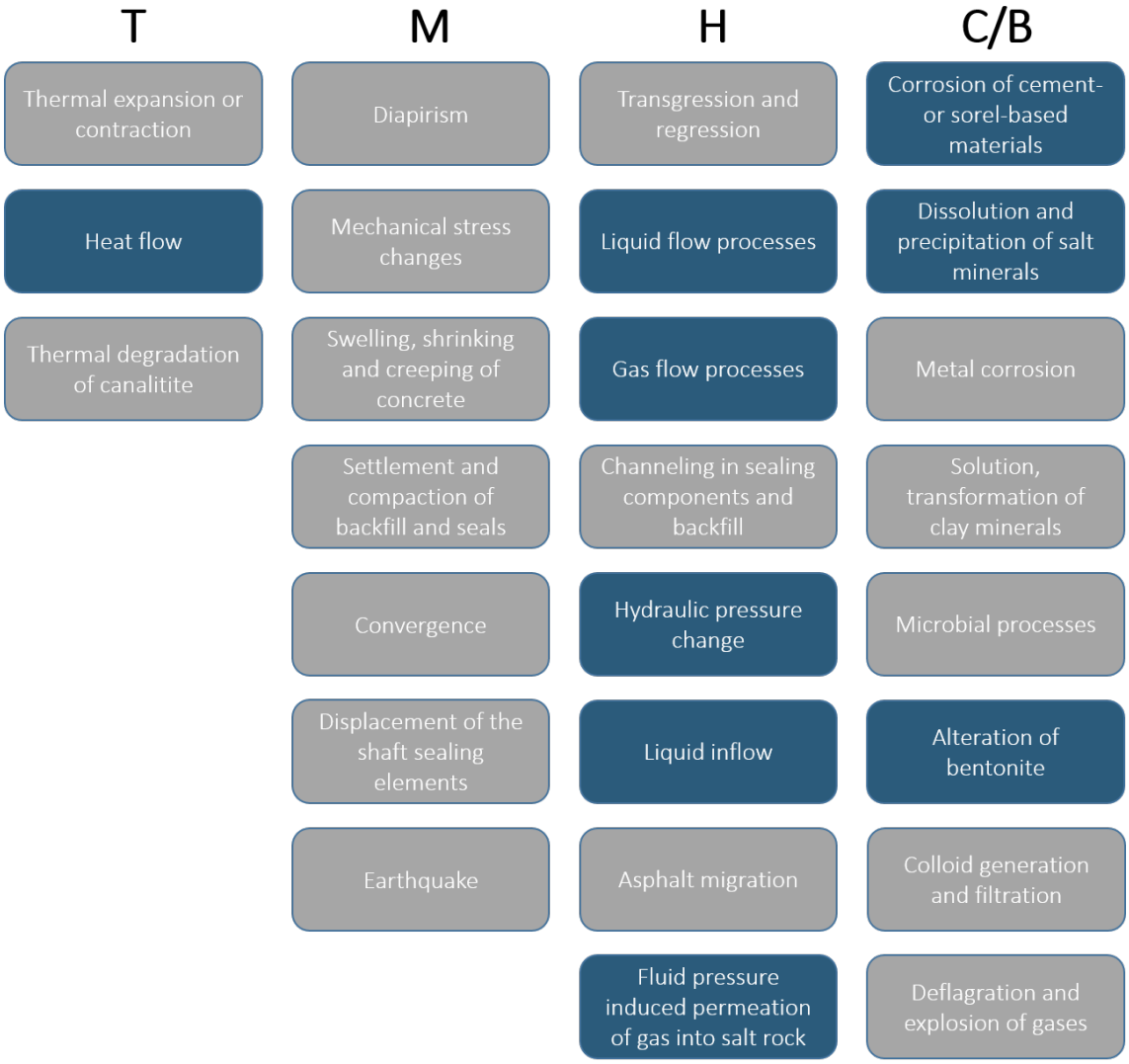

Figure 2.-6: Initial FEP of relevance for the hydraulic resistance proof.

From the initial FEP, some FEP remained unused or are not considered in the different partial verification proofs elaborated above. This is because those FEP cannot be assessed numerically or are not yet well understood to be conceptualized in numerical applications (for instance: microbial processes, alteration of bentonite or colloidal generation and filtration, asphalt migration). They could also be not relevant for the specific assessment of the EBS (e.g., thermal degradation of carnalitite or transgression and regression if the repository system is not located in coastal region). For such FEP, a verbal argumentative approach is adequate based on experimental evidence. They require further research effort for a quantitative assessment and can be added later in the numerically based assessment as soon as new scientific findings are available.

2.2 Integrity evaluation

The integrity evaluation assesses the state on the system for alternative scenarios. The alternative scenarios relevant for the EBS have been identified and characterized in the methodology report. Those scenarios consider unfavorable characteristics of initial FEP resulting in an impairment or failure of an EBS. Therefore the detrimental impact of those processes and the consequences on the repository system development will be analyzed in two alternative scenarios which are the failure of a shaft seal, and the failure of a drift seal. This means from the modeling point of view that the conceptual models used in the assessment of the integrity demonstration need to be modified by considering a shaft or a drift seal failure. For the integrity evaluation, hydraulic analyses are predominantly required. This is because the alternative scenarios assume that mechanical integrity is no longer present. The assessment of the overall system in such situations is the objective of the integrity evaluation. Mechanical modeling case can also derive from the alternative scenarios. The most prominent of them is the additional hydraulic load acting on the drift seal when a failure of the shaft seal is assumed. This has to be evaluated numerically.

2.3 Summary

In summary, starting with the repository system and the description of the near-field of the EBS, a specific FEP list for the EBS was developed in the methodology part of RANGERS. From this study, the initial FEP have been identified. The relevant alternative scenarios for the EBS have been also developed. By this procedure, a stringent derivation strategy of modeling cases from this FEP and scenarios was finally achieved. The abstraction of FEP into modeling scenarios requires the formulation of mathematical models that accurately capture the underlying mechanisms of these FEP. In the context of numerical assessments, these mathematical representations are further refined into computational models. Subsequently, these models are solved within a numerical framework that embodies either the entire repository system or a subsection of it. Adhering to the guidelines proposed in the methodology report, it is imperative to employ a comprehensive and realistic integrated model that encompasses the majority of the EBS components. This approach is crucial for accounting for the interaction between the FEP in the analysis. Fortunately, advancements in computational methods over the past decades have significantly enhanced the capabilities of numerical simulators. These programs can now simulate increasingly intricate processes and manage larger domains, thereby transforming the recommendations into feasible practices.

To illustrate the methodology and the modeling concept, Various modeling assessments were carried out in the scope of RANGERS. These modeling activities covers a great majority of FEP and aim at fulfilling all the criteria included in the verification concept. The modeling work is divided between the partners Sandia and BGE TECHNOLOGY using their expertise in a synergistic manner to deepen the feasibility of performance assessment in salt repositories. The numerical activities are summarized for the integrity demonstration and the integrity evaluation in Figure 2.-7 and Figure 2.-8

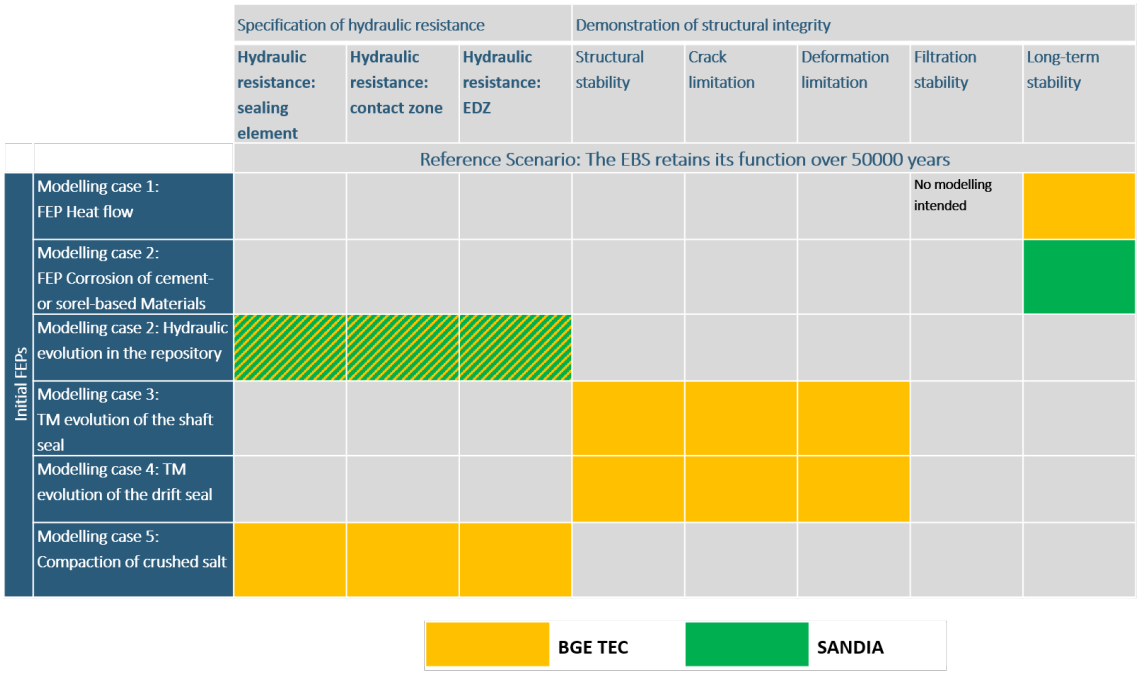

Figure 2.-7: Numerical modeling to assess the integrity demonstration.

Figure 2.-8: Numerical modeling to assess the integrity evaluation.

3. Model and Workflow Development

3.1 Developments in PFLOTRAN for performance assessment of salt repositories

Motivated by application to the RANGERS project, Sandia has undertaken a series of significant initiatives aimed at enhancing the modeling capabilities for salt repositories using PFLOTRAN – an open-source massively parallel reactive flow and transport simulator, the project homepage is given at `https://pflotran.org/`. These advancements improve the applicability of high-performance parallel flow and transport simulations, with a particular focus on incorporating Thermal, two-phase Hydrological, and Chemical (TH^2C) processes in a salt repository. Using these enhancements, we are now beginning to be equipped to simulate the majority of the FEPs linked to radionuclide mobilization and transport in a salt repository in an integrated manner, increasing reliability in our models and removing many practical simplifications previously needed to simulate these conditions. This integrated approach not only enhances the accuracy of our simulations but also provides a better understanding of the complex interactions within salt repositories, thereby contributing significantly to our ability to predict and manage their behavior over time. The different developments will be described in this section. A benchmark exercise that was carried out to verify the developments will be also described in this section. Modeling applications are shown using these new developments.

3.1.1 Salinity-dependent PFLOTRAN equations of state

The dissolution of salt (halite or sodium chloride) can significantly change the solution density, enthalpy, viscosity, and saturation pressure. In a multi-phase system, these changes become particularly important in reaching an accurate solution that includes boiling and condensation of water. Of primary importance is the solubility of salt in water. PFLOTRAN now has implemented several equations of state, including the formulation described by Sparrow (2003) to find the temperature-dependent solubility (Nole et al., 2022).

The solubility, X_{sat} in terms of mass fraction, is expressed as a function of temperature, T(℃):

$$X_{\text{sat}} = 0.2628 + 6.275 \times 10^{-6} T + 1.084 \times 10^{-6} T^2 \tag{1}$$

The mass fraction used in the Sparrow equations of state can be related to molality by:

$$X = \frac{mM_{\text{NaCl}}}{1000 + mM_{\text{NaCl}}} \tag{2}$$

where X is the mass fraction of salt, m is the molality of the solution (mol NaCl/kg H_2O) and M_{NaCl} is the molar mass of NaCl (58.443 g/mol).

The density of brine is a function of temperature, pressure, and salt concentration. Two options for density computation are available: Sparrow (2003), and Batzle and Wang (1992).

The Sparrow equation for brine density, ρ_b^{SP} (kg/m^3), is a function of salt concentration, X (mass fraction) and temperature, T (℃):

$$\rho_b^{SP} = A + BT + CT^2 + DT^3 + ET^4 \tag{3}$$

where:

$$A = (1.001 + 0.7666X - 0.0149X^2 + 0.2663X^3 + 0.8845X^4) \times 10^3$$
$$B = 0.0214 - 3.496X + 10.02X^2 - 6.563X^3 - 31.37X^4$$
$$C = (-5.263 + 39.87X - 176.22X^2 + 363.53X^3 - 7.784X^4) \times 10^{-3}$$
$$D = (15.42 - 167X + 980.7X^2 - 2573X^3 + 876.6X^4) \times 10^{-6}$$
$$E = (-0.0276 + 0.2978X - 0.2017X^2 + 6.3453X^3 - 3.914X^4) \times 10^{-6}$$

The Batzle and Wang formulation first calculates pure water density ρ_w (g/cm^3) as a function of pressure P (MPa), and temperature T (°C):

$$\rho_w = 1 + 1 \times 10^{-6}(-80T - 3.37T^2 + 0.00175T^3 + 489P - 2TP + 0.016T^2P - 1.3 \times 10^{-5}T^3P - 0.333P^2 - 0.002T^2)$$

The Batzle and Wang formulation then uses the pure water density to calculate a brine density ρ_b^{BW} (g/cm^3) as a function of pressure, temperature, and salt concentration, S (ppm / 10^6):

$$\rho_b^{BW} = \rho_w + S(0.668 + 0.44S + 1 \times 10^{-6}(300P - 2400PS + T(80 + 37S - 3300S - 13P + 47SP))) \quad (4)$$

A correction was made to the original Batzle and Wang density subroutine, which incorrectly computed the molar density of water from the mass density, ρ_b^{BW}, without removing the salt component. Molar density is now calculated as follows:

$$\rho_{w,\text{molar}} = \frac{\rho_b^{BW}(1 - S)}{M_{H_2O}} \quad (5)$$

where $\rho_{w,\text{molar}}$ is the molar density of water (kmol/m^3), ρ_b^{BW} is the Batzle and Wang brine density (kg/m^3), S is the salt mass fraction (ppm/$1 \cdot 10^6$), and M_{H_2O} is the molar mass of water (kg/kmol).

Vapor pressure lowering with increased solute concentration is an important consideration of multi-phase flow near the boiling point. Increased concentrations of salt in brine lowers the vapor pressure, increasing the boiling point of the water. PFLOTRAN now has implemented two options for vapor pressure calculation: Sparrow (2003) and Haas Jr. (1976).

The Sparrow formulation calculates vapor pressure, P_{vap}^{SP} (MPa) as a function of temperature, T (°C) and dissolved salt concentration, X (mass frac.):

$$P_{vap}^{SP} = A + BT + CT^2 + DT^3 + ET^4 \quad (6)$$

where:

$$A = (0.9083 - 0.569X + 0.1945X^2 - 3.736X^3 + 2.82X^4) \times 10^{-3}$$
$$B = (-0.0669 + 0.0582X - 0.1668X^2 + 0.6761X^3 - 2.091X^4) \times 10^{-3}$$
$$C = (-7.541 - 5.143X + 6.482X^2 - 52.62X^3 + 115.7X^4) \times 10^{-6}$$
$$D = (-0.0922 + 0.0649X - 0.1313X^2 + 0.8024X^3 - 1.986X^4) \times 10^{-6}$$
$$E = (1.237 - 0.753X + 0.1448X^2 - 6.964X^3 + 14.61X^4) \times 10^{-9}$$

The Haas formulation first relates the temperature of the brine, T_b (°C), to the temperature of H_2O liquid, T_0 (°C), at the same pressure, where x is the molality (mol salt/kg solution):

$$\ln(T_0) = m\ln(T_b) + c \tag{7}$$

where:

$$\begin{aligned} m &= (a + bT_b)^{-1} \\ a &= 1.0 + a_1x + a_2x^2 + a_3x^3 \\ b &= b_1x + b_2x^2 + b_3x^3 + b_4x^4 + b_5x^5 \\ c &= 0 \end{aligned}$$

The Haas formulation for vapor pressure, P^{HA} (bar), is then calculated as a function of the H_2O liquid temperature, T_0 (°C):

$$\ln(P^{HA}) = \frac{e_0}{t} + e_1 + \frac{e_2}{w}(10^{w^2} - 1.0) + e_3 10^{y^{1.25}} \tag{8}$$

where:

$$\begin{aligned} w &= z^2 - e_6 \\ y &= 647.27 - T_0 \\ z &= T_0 + 0.01 \end{aligned}$$

The constants used in the Haas vapor pressure equations are presented in Table 3.-1.

Table 3.-1: Constants for vapor pressure calculation by Haas Jr. (1976).

Constant	Value
a_1	5.93582×10^{-6}
a_2	-5.19386×10^{-5}
a_3	1.23516×10^{-5}
b_1	1.15420×10^{-6}
b_2	1.41254×10^{-7}
b_3	-1.92476×10^{-8}
b_4	-1.70717×10^{-9}
b_5	1.05390×10^{-10}
e_0	12.50849
e_1	-4.616913×10^{3}
e_2	3.193455×10^{-4}
e_3	1.1965×10^{-11}
e_4	-1.013137×10^{-2}
e_5	-5.7148×10^{-3}
e_6	2.9370×10^{5}

Liquid enthalpy is also a function of salt concentration. Here, we use the formulation of Sparrow (2003), where h is specific enthalpy (kJ/kg), T is temperature (°C), and X is mass fraction of dissolved salt in water (kg salt/kg solution),

$$h = A + BT + CT^2 + DT^3 + ET^4 \tag{9}$$

where:

$$\begin{aligned}
\mathrm{A} &= (0.0005 + 0.0378\mathrm{X} - 0.3682\mathrm{X}^2 - 0.6529\mathrm{X}^3 + 2.89\mathrm{X}^4) \times 10^3 \\
\mathrm{B} &= 4.145 - 4.973\mathrm{X} + 4.482\mathrm{X}^2 + 18.31\mathrm{X}^3 - 46.41\mathrm{X}^4 \\
\mathrm{C} &= 0.0007 - 0.0059\mathrm{X} + 0.0854\mathrm{X}^2 - 0.4951\mathrm{X}^3 + 0.8255\mathrm{X}^4 \\
\mathrm{D} &= (-0.0048 + 0.0639\mathrm{X} - 0.714\mathrm{X}^2 + 3.273\mathrm{X}^3 - 4.85\mathrm{X}^4) \times 10^{-3} \\
\mathrm{E} &= (0.0202 - 0.2432\mathrm{X} + 2.054\mathrm{X}^2 - 8.211\mathrm{X}^3 + 11.43\mathrm{X}^4) \times 10^{-6}.
\end{aligned}$$

3.1.2 Fully-coupled solute mass balance in PFLOTRAN

For flow of fresh water in aquifers, aqueous chemical species are typically dilute enough (i.e., low enough concentrations) to not significantly affect the properties of the water solvent, including its density and viscosity. This simplification forms the basis for decoupling fluid flow and reactive transport, as is typically done in PFLOTRAN or most other environmental flow and transport simulators. When the solute transport primary solution variables do not significantly impact the flow primary solution variables, then sequentially solving the flow and transport solutions can oftentimes be more efficient and sufficiently accurate.

An exception to this is the case of a brine flow system through a halite porous or fractured medium. If the pore water contains salt (as exemplified by pore water contained in a salt host rock where the rock itself can dissolve into the water), salt dissolves rapidly in high enough concentrations to meaningfully affect the density, viscosity, and saturation pressure of the pore water. It is therefore very important to consider this feedback between the solute and the liquid flow properties. Until now, modeling salinity effects on flow properties required modeling salinity development and migration as part of the transport equations and then handing off updated density and viscosity to the flow solution under the standard sequential flow and transport coupling scheme. This approach uses the brine properties from the previous timestep in each flow time step. Since these two systems are much more tightly coupled when salt comprises the porous medium and is a solute, sequential coupling in this manner requires taking very small time steps in order to avoid numerical artifacts. The developments described in this section for fully coupling a solute in PFLOTRAN's general mode (i.e., two-phase flow with energy), and are new capabilities to PFLOTRAN (Nole et al., 2022, 2023).

These additions are made to PFLOTRAN's general (two-component, multi-phase air/water flow) mode to accommodate solute transport as a third component either dissolved in the liquid phase or as a solid precipitate. GENERAL mode, in its prior formulation, implicitly solves two component mass balance equations for gas and liquid:

$$\frac{\partial}{\partial t}(\phi s_l \rho_l X^l + \phi s_g \rho_g X^g) + \nabla \cdot (\phi \alpha_l \rho_l q X^l + \phi \alpha_g \rho_g q X^g) - \phi s_l D_l \nabla X^l - \phi s_g D_g \nabla X^g = Q_l \tag{10}$$

and an energy balance equation:

$$\sum_{\alpha=l,g}\left(\frac{\partial}{\partial t}(\phi s_\alpha u_\alpha)+\nabla\cdot(q_\alpha H_\alpha)\right)+\frac{\partial}{\partial t}((1-\phi)\rho_r c_r T)-\nabla\cdot(k\nabla T)=Q \tag{11}$$

for components i = water, air and phases α = liquid, gas. See the PFLOTRAN documentation (`https://www.pflotran.org/documentation/`) for more detailed description of the variables and constitutive laws.

The newly implemented, fully implicit solute transport mode includes an additional solute component mass balance equation:

$$\frac{\partial}{\partial t}(\phi s_l \rho_l X^{l,s}+\phi s_p \rho_s X^s)+\nabla\cdot(\phi\alpha_l\rho_l q X^{l,s}-\phi s_l D_l\nabla X^{l,s})=Q_{solute} \tag{12}$$

In this new formulation, the vapor pressure of the solute is assumed negligible, and therefore it is only present in the liquid phase. The solute can also form a solid precipitate phase (α = s), which is immobile in the pore space. Diffusion through the solid phase is considered negligible on the timescales used in our simulations and is therefore not present in this mass balance equation.

Primary variable switching is used to track phase transitions. The phase states used depend on whether the rock matrix is comprised of a soluble or insoluble material. For example, a quartz sandstone rock matrix is largely insoluble in water, therefore the possible phase states are any combination of liquid, gas, and solid precipitate. In halite rock matrix, on the other hand, readily dissolves in water, which changes the porosity of the rock matrix (Table 3.-2). The concentration of salt in the pore water is held at solubility and as salt comes out of solution, or the rock matrix dissolves, the porosity changes.

Table 3.-2: Phase states and primary variables for soluble rock matrix.

State	Primary variables
Liquid	P, X_{air}, X_S, T
Gas	P_g, P_{air}, T
Liquid/Gas	P_g, X_{air}, X_S, T
Liquid/Precipitate	P, X_{air}, X_S, T
Gas/Precipitate	P_g, P_{air}, X_S, T
Liquid/Gas/Precipitate	P_g, S_S, S_S, T
Precipitate	P_g, T^*

3.1.3 Thermal Characteristic Curves

Recent developments in PFLOTRAN have focused on implementing temperature-dependent thermal conductivity by way of thermal characteristic curves (TCCs), (Mariner et al., 2020). TCCs express thermal conductivity as a function of temperature for a given material. In the input files, this description resembles the way “characteristic curves” are implemented. A prototype of this capability was created to allow more physically realistic heat conduction modeling in salt, affiliated with the RANGERS Project and the Brine Availability Test in Salt (BATS) heater test at the Waste Isolation Pilot Plant (Kuhlman et al., 2020).

Salt is well known to have thermal conductivity that decreases with increasing temperature (e.g., see lab test data in Kuhlman et al. (2020)). The prototype capability developed for Salt R&D was expanded in scope and is now widely used in PFLOTRAN for other applications. Thermal conductivity of a salt host rock, for instance, is understood to be heavily influenced by temperature in the relevant thermal regime for repository applications (Gilliam and Morgan 1987; Vosen and Schellschmidt 2003).

The previous implementation of thermal conductivity (k_r) for use with PFLOTRAN non-isothermal flow models involved using wet (k_{wet}) and dry (k_{dry}) thermal conductivity values in a function with saturation (S) from Somerton et al. (1974). In the context of the current version, this equation is still used as the default (D) for effective thermal conductivity.

$$k_T(S) = k_{dry} + \sqrt{S}(k_{wet} - k_{dry}) \tag{13}$$

A linear resistivity thermal conductivity model, where thermal conductivity is also a function of temperature. This model assumes that the reciprocal of thermal conductivity can be modeled as a linear function with temperature. This form was suggested by Birch and Clark (1940) and fitted empirically by Blesch et al. (1983) for granite, basalt, shale, and salt. The latter study was a far-field thermal analysis of a repository that intended to evaluate environmental impact based on temperature changes in various regions. In the linear resistivity function, a is the resistivity shift parameter and a_2 is the scaling factor with the change in temperature. The temperature change is defined with respect to a reference temperature (T_{ref}), such that when $T = T_{ref}$, k_{dry} and k_{wet} are assumed to be evaluated at 0 °C as well.

The linear resistivity model is

$$k_T(S, T) = k_T(S)/[a_1 + a_2(T - T_{ref})] \tag{14}$$

where $k_T(S)$ is given by (13) and a_1, a_2 are coefficients, and T_{ref} is a reference temperature.

To model the change in thermal conductivity of the granular salt during compaction, a special form of the linear resistivity TCC was implemented. The expression was developed for reconsolidation of granular salt with air-filled porosity (see Table B.4, see “Saltgrus” of Bollingerfehr et al. (2012)),

$$k_T(S, T, \phi) = k_T(S, T)\left(1 - \frac{\phi}{\phi_{ref}}\right)^{\xi} + \left(\frac{\phi}{\phi_{ref}}\right) \cdot (b_1 + b_2 T) \tag{15}$$

where ϕ is porosity, ξ is a porosity exponent, ϕ_{ref} is a reference porosity, b_1 and b_2 are coefficients and $k_T(S, T)$ is given by (14). At $\phi = 0$ this function gives the intact thermal conductivity associated with the linear resistivity model (specified by a_1 and a_2, and proportional to $1/T$). At $\phi = \phi_{ref}$ this function gives the porosity associated with a linear conductivity model (specified by b_1 and b_2 and proportional to T). At porosity values between these two end members, the function linearly interpolates between the two thermal conductivity values.

3.1.4 Implementation of Non-Darcy flow into PFLOTRAN

In low-permeability materials, a threshold gradient can become important (Liu, 2017). This is a permeability-dependent gradient, which must be overcome before any flow can occur. Standard Darcy flow is given by

$$q = K\mathfrak{i} \tag{16}$$

where q is the water flux (m/s), K is the hydraulic conductivity (m/s), and $\mathfrak{i} = \frac{dh}{dx}$ is the hydraulic head (h) gradient (m/m; m of hydraulic head per m of distance). Liu (2014) presented a closed-form non-Darcy expression for water flux in very tight rocks in terms of a threshold gradient, $\mathfrak{I}$ (m/m), as

$$q = K\left[\mathfrak{i} - \mathfrak{I}\left(1 - e^{-\mathfrak{i}/\mathfrak{I}}\right)\right]. \tag{17}$$

Through a regression, Liu (2014) found the threshold gradient could be expressed in terms of the intrinsic permeability

$$\mathfrak{I} = Ak^B \tag{18}$$

where A = 4.0×10^{-12} and B = -0.78 are based on a fit to data from Liu et al. (2012).

3.2 Code Verification for performance assessment

3.2.1 Motivation

The presence of the gas phase in the repository under consideration of small amount of humidity in the host rock requires the consideration of two-phase-flow in the performance assessment of the salt repository system. Until now, the numerical investigations of two-phase flow in the repository in salt have been carried out at Sandia within a special flow mode especially developed for WIPP. Historically, WIPP was licensed with a two-phase flow simulator (BRAGFLO) for the repository that utilized a simplified flared 2D-mesh representation of the repository (DOE, 2019). WIPP uses two-phase immiscible flow under isothermal conditions. Because a 3D representation of the repository and the consideration of the heat propagation from waste (non-isothermal) are required for state of the art and performance assessments for heat-generating waste, PFLOTRAN was further developed in order to perform the assessment of a salt repository under two-phase flow assumption with energy transport.

To ensure the advancements made within PFLOTRAN are robust and to establish its capability for conducting non-isothermal multiphase simulations, it is imperative to conduct a comprehensive testing phase before advancing to performance assessment. For this purpose, one of the modeling test scenarios designed in the BenVaSim project was selected for evaluation in the RANGERS program. The BenVaSim project's objective was to provide a benchmark for various THM coupled simulators using well-defined, simplified modeling tasks that target fundamental processes, particularly flow phenomena in porous media. The upcoming study is driven by the need to compare PFLOTRAN's performance with that of other simulators, especially since PFLOTRAN was not included in the original array of codes validated by BenVaSim.

3.2.2 Methodology

The test under consideration involves assessing the hydraulic response within an EBS seal under two-phase flow conditions with specific boundary constraints. The addition of a gas

fluid phase introduces more realistic conditions, considering the interplay between gas and liquid phases within the repository. The disposal drifts are air filled at the time of repository closure. Following the disposal of radioactive waste, chemical reactions may occur within the repository environment, such as interactions between the metal of the waste container and the humidity of the host rock, potentially leading to gas generation. The emergence of additional gas can create pressure build-up, influencing the system's behavior and potentially inducing fracturing in the host rock.

The benchmark problem is depicted in Figure 3.-1, showcasing a model geometry of 10 m in length and 1 m in height, focusing exclusively on horizontal process dynamics. Boundary conditions are indicated by arrows, with dark blue representing liquid and light blue indicating gas boundary conditions, while black denotes mechanical effects (Czaikowski and Friedenberg, 2020).

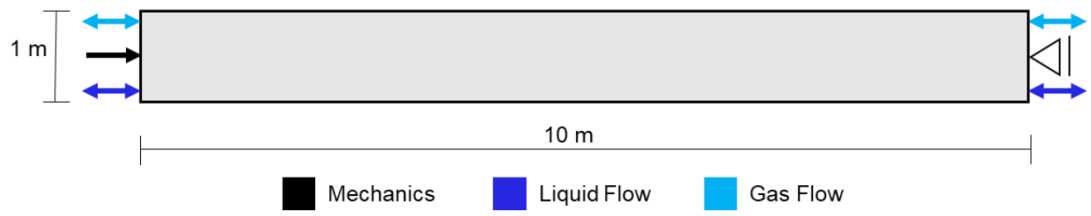

Figure 3.-1: Model geometry and considered processes (Czaikowski and Friedenberg, 2020).

The original BenVaSim problem also incorporated mechanical effects that cannot be computed in PFLOTRAN. In the selected benchmark, the mechanical process class is decoupled from the hydraulic processes. Thus, the base scenario as specified in BenVaSim was carried out in PFLOTRAN without mechanical effect and the results were compared with simulation results with OpenGeoSys (OGS) and against those obtained by GRS in the BenVaSim project, both considering mechanical effects.

3.2.3 Benchmark results

The benchmark scenario selected in this study shows a two-phase flow within a model representing partial saturation and with boundaries that allow fluid transfer. Coupling the hydraulic scenario with mechanical stress, the latter is exerted at the model's right edge, as illustrated in Figure 3.-2. Details about material properties, along with initial and boundary conditions, are summarized in Table 3.-3. Throughout the projected simulation duration of 100,000 years, these boundary conditions remain constant. The models do not include the effects of diffusion of dissolved gas in the liquid phase or diffusion of humidity in the gas phase. Initial model conditions are set with a 63% liquid saturation corresponding to a suction pressure of -13.63 MPa, alongside a gas pressure of 0.2 MPa and mechanical stress of 4 MPa. At the model's left boundary, a 50% saturation level is stipulated (resulting in a suction pressure of -16.58 MPa), with a gas pressure of 3 MPa and identical mechanical stress. The model's right boundary is mechanically fixed, with a constant gas pressure of 0.5 MPa and an anticipated saturation level of 90% (equating to a suction pressure of -4.89 MPa).

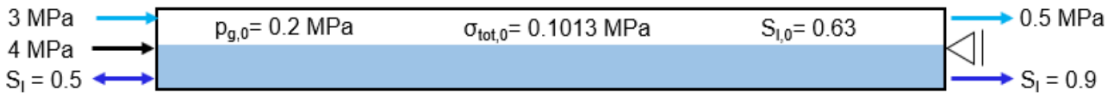

Figure 3.-2: Initial and boundary conditions for the immiscible two-phase flow benchmark Czaikowski and Friedenberg (2020).

Table 3.-3: Material parameters for the base scenario (Czaikowski and Friedenberg, 2020).

Parameter	Value	Unit
Young's modulus	650	[MPa]
Poisson's ratio	0	[-]
Porosity	0.33	[-]
Intrinsic permeability	2.5E-21	[m^2]
Biot coefficient	1	[-]
Liquid viscosity	1.0E-9	[MPa·s]
Liquid bulk modulus	2200	[MPa]
Residual liquid saturation	0.02	[-]
Residual gas saturation	0	[-]
Van Genuchten parameter	0.5	[-]
Van Genuchten pre-factor	11	[MPa]
Pore connectivity parameters	0.5	[-]

Figure 3.-3 shows the results for the gas pressure and saturation evolution problem. The figure shows the comparison of results obtained with OpenGeoSys and PFLOTRAN and those computed with CODE_BRIGHT by GRS taken from Czaikowski and Friedenberg (2020) for different locations along the seal model. A good agreement in the results obtained using the three codes is evidenced in the figure. Results with OpenGeoSys and PFLOTRAN are identical. A small discrepancy to the GRS results for the saturation evolution might be related to a different spatial and time discretization as well as in the difference in the implementation in Code_Bright. Nevertheless, all the results are similar enough to consider this benchmark conclusive.

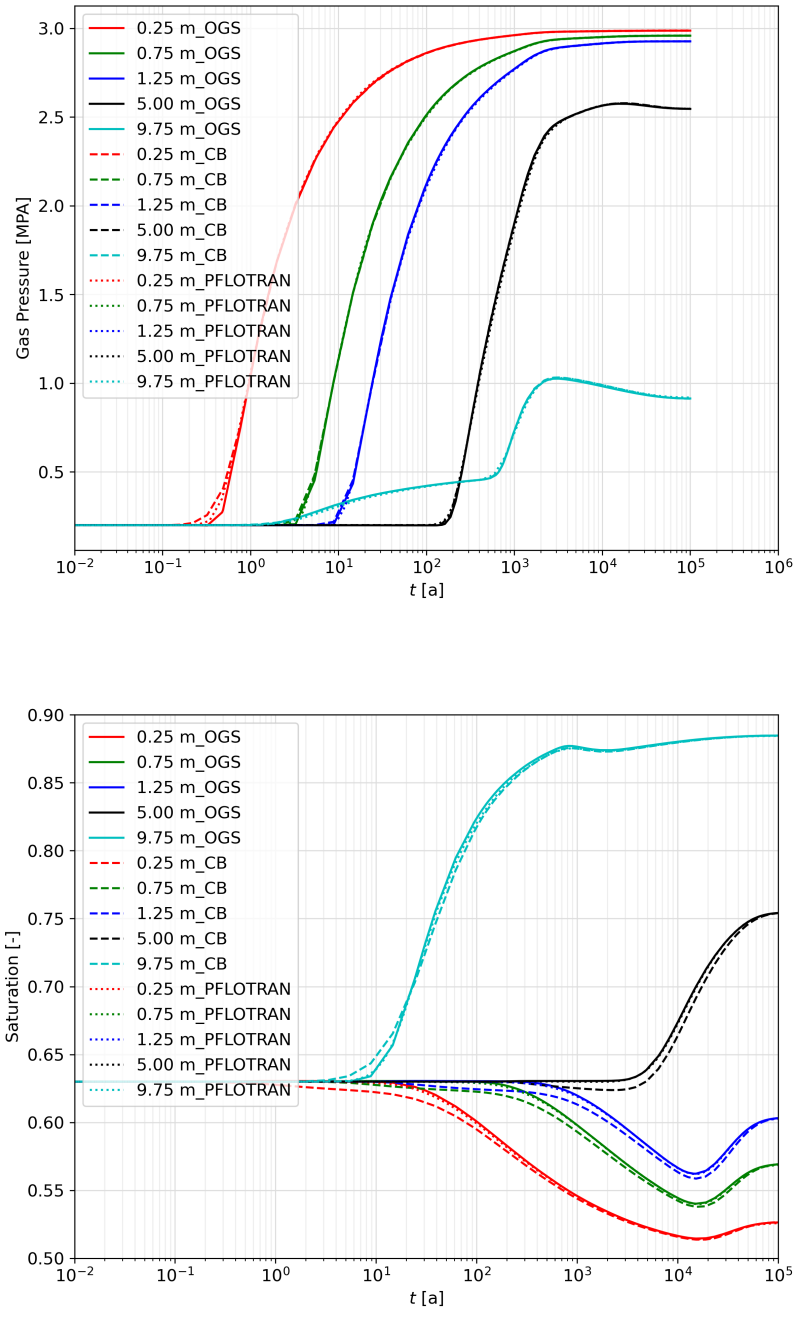

Figure 3.-3: Comparison between OpenGeoSys and PFLOTRAN results (this study) and CODE_BRIGHT results from Czaikowski and Friedenberg (2020).

4. Temperature Evolution in the EBS

High temperature can affect the long-term performance of the EBS materials. As part of the assessment of the long-term stability of the geomaterials used in the EBS, the temperature evolution in the repository is evaluated. The aim of the simulation is to estimate the temperature increase in the EBS over the course of the repository. Based on this, the effect of temperature increase on the materials from which the EBS are made can be evaluated. The present analysis serves also as input for further simulations aiming at verifying other aspect of the design and performance assessment of the EBS. This is for instance the case for the thermomechanical integrity analyses for the shaft and drift seals and the TH²C performance assessment. The results of the analysis also serve as input in the geochemical assessment as it is well known that temperature increases the rate of chemical reactions.

4.1 Repository system

The generic repository system developed in the context of the RANGERS project is based on the generic geological model developed in the KOSINA project prior to RANGERS. The generic geological model of the salt pillow from the KOSINA project is located on the southern crest of the North German Basin. This geological model consists of twelve homogenized geological layers. Homogenized because those layers were combined from smaller layers with similar properties. The thicknesses of the cover rock consisting of lithostratigraphic units Quaternary (Q), Tertiary (T), and Bunter Sandstone (S) vary in thickness across the model area from approximately 800 m to 140 m. The evaporitic host rock consists of Stassfurt (K2), Leine (NA3), Aller (NA4), and Ohre formations and reach a thickness of more than 800 m in the center of the salt pillow. No modeling was undertaken of possible cap rocks at the top of the salt. The model does not incorporate fault tectonics or salinar tectonics. The fault characteristics of the below-salt horizons, as well as the fragmentation of the main anhydrite into blocks, are not part of the reference profile and thus not included in the 3D model based on the profile.

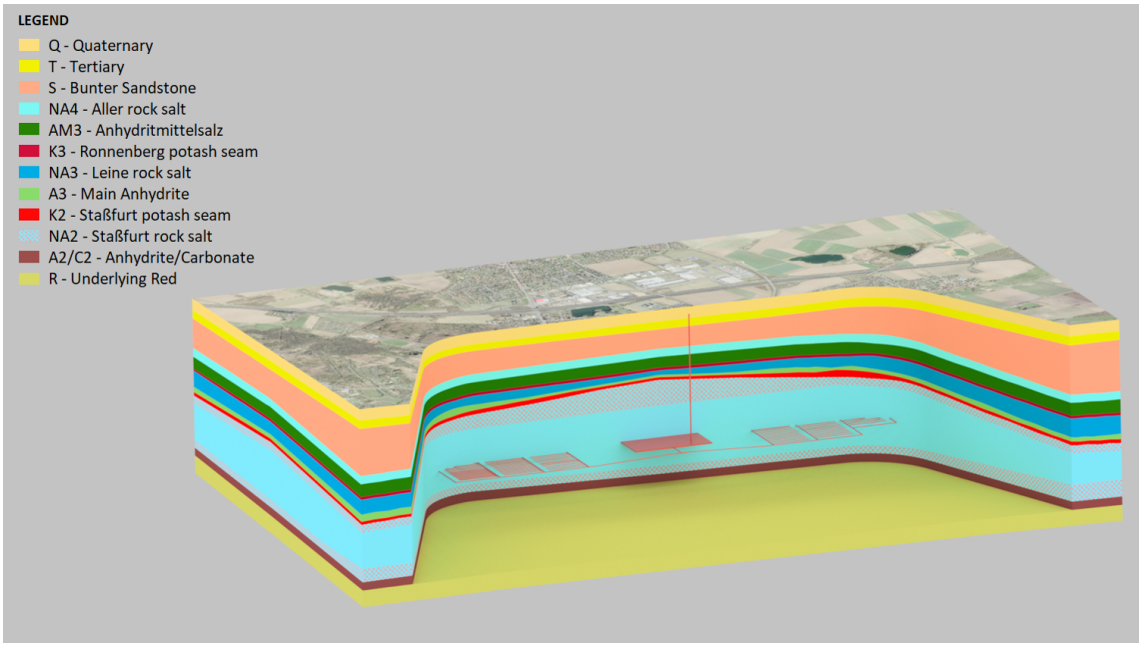

Figure 4.-1: Generic repository system for RANGERS (with courtesy of BGR **?**).

The repository mine is strategically situated at the core of the salt pillow, where the salt layer attains its maximum thickness, ensuring optimal geological stability and integrity. A minimum safety distance of 200 m to the overburden or at least 750 m to the surface were respected. Figure 4.-1 shows a stylized 3D representation of the repository system comprising the generic salt pillow and the repository.

The repository design considers the disposal of self-shielded casks in horizontal emplacement drifts which are later backfilled with crushed rock salt. The repository mine is composed of two main emplacement wings that have a width of 800 m and a central infrastructure area that hosts two shafts. Each wing hosts three emplacement fields. The infrastructure area and the emplacement fields are separated by at least 300 m of undisturbed rock salt. Each access drift to the emplacement wings includes 500 m interval for the construction of drift seals. The shafts can be sealed within the thickest part of the salt pillow.

In the southern section, the three emplacement fields are occupied by POLLUX®-10 containers, each housing spent fuel elements from pressurized water reactors (PWR). A similar setup is replicated in half of the northern section. A big part of the northern wing is dedicated to containing reprocessed waste in POLLUX®-9 containers. Additionally, one-third of the final disposal zone is allocated for the disposal of CASTOR® containers, which safely encase waste from prototype and experimental reactors. Complementing these arrangements, two separate drifts have been allocated for the storage of structural components from spent fuel assemblies, encapsulated within MOSAIK-II containers. These are strategically positioned in two disposal fields adjacent to the infrastructure area, see Figure 4.-2. The disposal operational time was assumed to be 30 years in the planning of the repository.

The repository planning assumes a maximum temperature of 200 °C at the surface of the waste casks. To meet this temperature requirement, the repository was first thermally designed to optimize the spacings between the drifts and between the disposal casks within the drifts. The engineered barrier systems of this repository consists of four horizontal closure systems installed in the main drifts near sealing the two emplacement wings and of two shaft closure systems installed in both shafts. Each of these horizontal closures is 600 m long and is divided into two abutments made of magnesia (i.e., Sorel) concrete with a length of 50 m. Between the abutments, the 500 m long backfill seal is made of a mixture of crushed salt and clay, which itself seals after reconsolidation and compaction, taking over the long-term sealing function of the repository. For up to 50,000 years, the Sorel concrete abutments should limit any potential fluid migration within the repository mine and should protect the crushed salt seal against hydromechanical loads. The shaft closure system is made of several material following the concept of diversity and redundancy. The shaft closure is redundant to the drift closure. The sealing elements made of Sorel concrete, salt clay, and bentonite ensure the diversity and the redundancy of the closure system. If one seal loses its function, other seals made of different material will significantly reduce the chance that the same deficiency occurs in multiple elements.

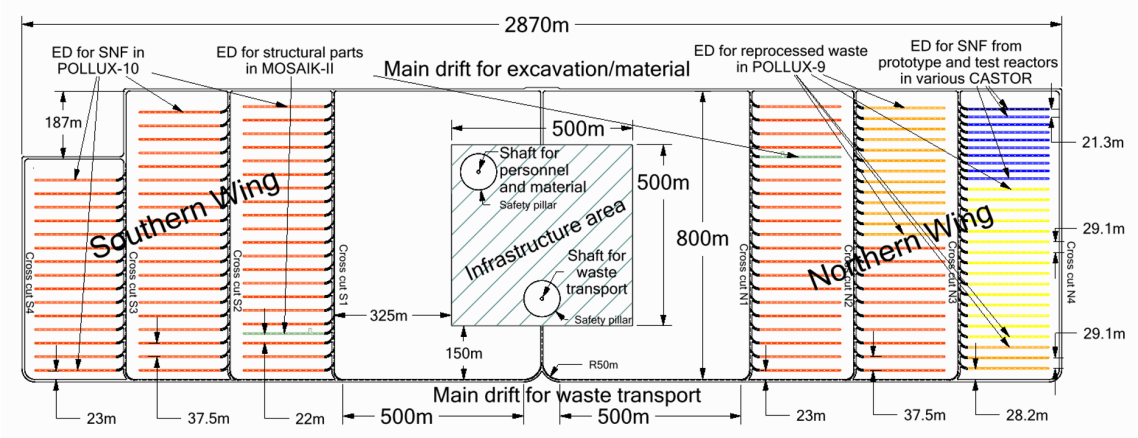

Figure 4.-2: Repository layout and waste stream distribution.

4.2 Waste inventory and thermal power

The POLLUX®-10 containers can be optionally loaded with fuel rods from 10 fuel assemblies of Western design pressurized water reactors (PWR), 30 fuel assemblies of Western design boiling water reactors (BWR) or 25 fuel assemblies from Russian design pressurized water reactors (WWER). The different container loadings are because the fuel rods from BWR fuel assemblies are two-thirds shorter than those from PWRs, allowing for triple loading in a container. The WWER fuel rods are thinner than their Western counterparts, which allows for a two-and-a-half times loading capacity.

In Western-designed PWR and BWR reactors, uranium oxide (UO_2) and mixed oxide (MOX) fuel elements included both Uranium-235 and Plutonium. Only UO_2 fuels were used in Russian-designed reactors. The decay heat of these fuels was adopted according to the burn-up calculations described in Bollingerfehr et al. (2013). These burn-up calculations apply to each characteristic decay heat per waste type without considering the burn-up and enrichment of the fuel elements.

For the storage of MOX fuel elements, which have a high heat production compared to UO_2 fuel elements, a container loading was developed that predominantly consists of fuel rods from PWR fuel assemblies and to a lesser extent from MOX fuel assemblies (Amelung et al., 2005). The ratio used in Bollingerfehr et al. (2013) in the container loading of 89% UO_2 content and 11% MOX content corresponds to the mixing ratio that results from the ratio of the total quantities of PWR-UO_2 fuel assemblies and PWR-MOX fuel assemblies. Figure 4.-3 shows the thermal power of the individual fuel element types in a loading equivalent to loading with PWR fuel elements. The mixed loading with 89% UO_2 and 11% MOX conservatively covers the heat release of the UO_2 fuel elements from BWR and WWER reactors. The thermal power for pure loadings from MOX fuel elements can also be seen in the figure. Containers with such loading are difficult to implement while maintaining the temperature criterion of 200 °C.

The reprocessed wastes are stored in POLLUX®-9 containers. Such a container can be loaded with nine high-level waste (HLW) casks. The thermal power of a reprocessed cask is also shown in Figure 4.-3. It displays a different burn-up behavior compared to the fuel elements. The thermal power of such wastes initially remains at the level of the UO_2 fuel elements and then declines more significantly after 50 years post-reprocessing.

In the thermal calculations, the temporal development of the heat output for the various waste categories shown in Figure 4.-3 is simplified via a reduced thermal nuclide spectrum. This spectrum includes four key nuclides, with parameter values provided in Table 4.-1.

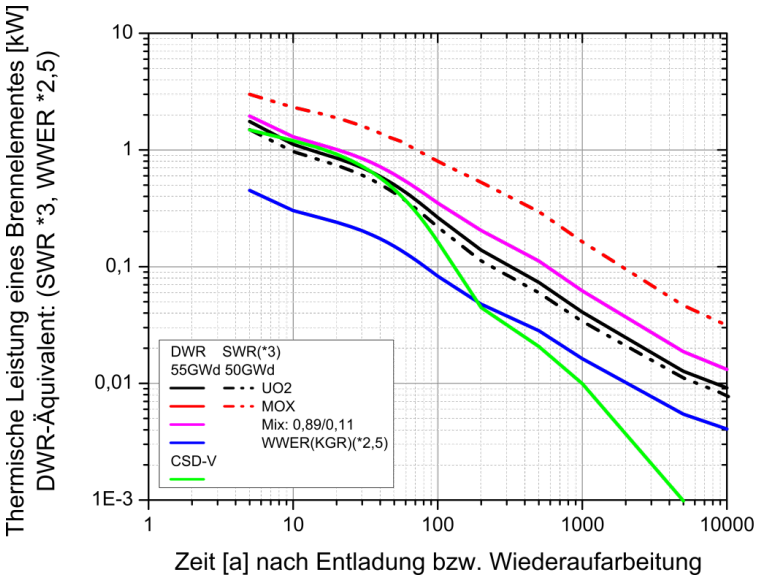

Figure 4.-3: Thermal output of a fuel element over time, loading equivalent to a PWR fuel element, as well as the thermal output of a CSD-V (Bollingerfehr et al., 2013).

Table 4.-1: Key nuclides of spent fuel elements and reprocessed radioactive waste.

	PWR-Mix 89/11	**CSD-V**	**VVER**
Nuclide 1:			
Power p [kW]	1,156	1,480	$1,126 \cdot 10^{1}$
Half-life $t_{1/2}$ [y]	$3,220 \cdot 10^{1}$	$2,799 \cdot 10^{1}$	$3,242 \cdot 10^{1}$
Nuclide 2:			
Power p [kW]	$2,267 \cdot 10^{1}$	$4,468 \cdot 10^{2}$	$2,034 \cdot 10^{2}$
Half-life $t_{1/2}$ [y]	$3,968 \cdot 10^{2}$	$4,172 \cdot 10^{2}$	$4,306 \cdot 10^{2}$
Nuclide 3:			
Power p [kW]	$2,151 \cdot 10^{2}$	$9,507 \cdot 10^{4}$	$2,402 \cdot 10^{3}$
Half-life $t_{1/2}$ [y]	$1,367 \cdot 10^{4}$	$9,649 \cdot 10^{3}$	$1,701 \cdot 10^{4}$
Nuclide 4:			
Power p [kW]	$9,466 \cdot 10^{4}$	$1,289 \cdot 10^{4}$	$8,243 \cdot 10^{5}$
Half-life $t_{1/2}$ [y]	$7,593 \cdot 10^{5}$	$2,952 \cdot 10^{4}$	$1,090 \cdot 10^{6}$

According to the final report of the German Commission for the Storage of High-Level Radioactive Waste Materials, the earliest start of storage is assumed to be the year 2050 (Endlagerkommission, 2016). At this point, the interim storage time of the wastes is up to 60 years, depending on the type of waste and the date of origin. With an assumed storage duration of 30 years, the shortest interim storage time for the fuel elements of Western design can be calculated as 57 years. For reprocessed wastes, a conservative interim storage time of 53 years is assumed.

4.3 Numerical model

The temperature evolution within a final repository is primarily determined by the existing geothermal gradient and the heat input from high-level radioactive wastes. The geothermal gradient dictates the naturally prevailing temperature at the storage horizon as a function of depth.

In the disposal drift, the thermal conductivity of the selected backfill material plays a significant role in the peak temperature. In contrast, the thermal conductivity of the host rock is crucial for heat distribution in the far field. The thermal conductivities of the overlying geological layers can also affect the temperature distribution in the far field, especially if they are significantly lower than that of the host rock. In this case, there is a delay in heat transfer to the overlying layers, resulting in a corresponding increase in temperature within the host rock layer.

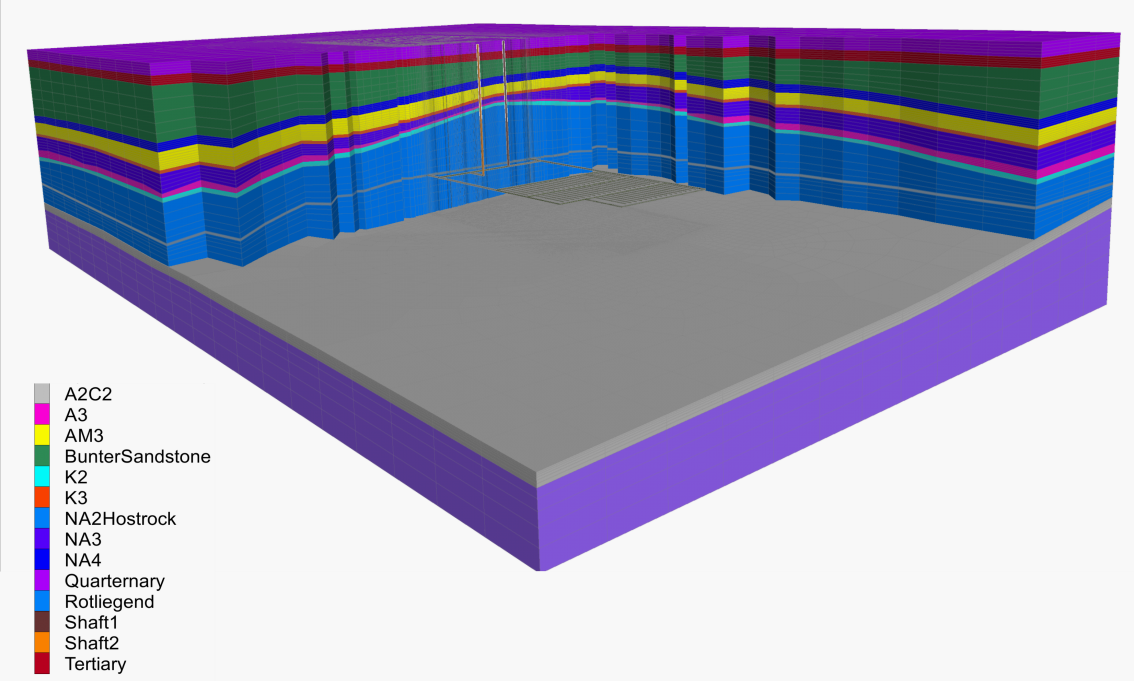

Figure 4.-4: Numerical model for the heat propagation in the entire repository system.

The numerical model developed for the present analysis is aimed at assessing the temperature evolution in the far field. Thus near field effects can be simplified. These effects were already considered in the thermal design of the repository as part of the optimization of the spacings between the drifts and between the casks, see Simo et al. (2024). Therefore, it is not necessary to resolve individual casks in the drifts (i.e. they are not explicitly modeled). Taking into account this simplification, a numerical model with a high fidelity of the drifts and seals in the repository system is realized and depicted in Figure 4.-4. In this model, all drifts were resolved and the geometrical form of each geological layers were respected. The model was parameterized in such a way that the mesh size can be easily change in the three dimensions for mesh convergence studies. The model adopted for the present analysis is about 4000 m wide, 5900 m long and extends up to 3000 m in the depth. It consists of 3.5 million elements.

At the upper boundary of the model, a constant air temperature of 9 °C is assumed. At the ground surface, a convective heat flux q_c is considered with a heat transfer coefficient of

α = 8.7 $Wm^{-2}K^{-1}$ according to Bertrams et al. (2020). The temperature at the lower model boundary is calculated using the geothermal gradient of 30.0 K per kilometer to be approximately 100.0 °C and is consistently applied along the entire lower boundary of the model. Thermally, the disposal of waste is represented by a transient heat source. In the model each disposal drift acts as a heat source. The thermal load has been homogenized in each drift based on the heat power of the radioactive waste disposed in each drift. One refers to the methodology report for more details about the repository planning (Simo et al., 2024).

The thermal parameters used are compiled in Table 4.-2, sourced from Liu et al. (2017).

Table 4.-2: Thermal Properties of Geological Layers (Liu et al., 2017).

Homogeneous zones	**Symbol**	**Thermal conductivity** λ (W/(m · K))	**Specific heat capacity** c_p (J/(kg · K))	**Thermal expansion coefficient** α (1/K)
Quaternary	Q	2.3	950	$1.0 \cdot 10^{-5}$
Tertiary	T	2.1	905	$1.0 \cdot 10^{-5}$
Bunter	S	2.6	760	$1.0 \cdot 10^{-5}$
Aller rock salt	NA4	5.2	860	$4.0 \cdot 10^{-5}$
Anhydritmittelsalz	AM3	5.0	860	$3.5 \cdot 10^{-5}$
Potash seam Ronnenberg	K3	1.5	903	$2.5 \cdot 10^{-5}$
Leine rock salt	NA3	5.2	860	$4.0 \cdot 10^{-5}$
Main anhydrite	A3	4.2	860	$1.6 \cdot 10^{-5}$
Potash seam Staßfurt	K2	1.5	903	$2.5 \cdot 10^{-5}$
Staßfurt rock salt	NA2	5.2	860	$4.0 \cdot 10^{-5}$
Anhydrite/carbonate	A2/C2	4.2	860	$1.6 \cdot 10^{-5}$
Underlying red	R	2.7	760	$1.0 \cdot 10^{-5}$

The calculations were carried out using numerical codes FLAC3D (Itasca Consulting Group, Inc., 2021) based on the finite difference method and OpenGeoSys based on the finite element method (Naumov et al., 2024). A benchmark was carried out between the two codes showing nearly identical results for the problem at hand.

4.4 Numerical results

The numerical model for this assessment includes a detailed representation of the whole repository system with a bounding model domain box that has an extent of several km on each side. Due to the homogenization of the thermal load in each drift and reduction in the ability to represent steep temperature gradients between the cask and surrounding material, the maximum temperature in the homogenized drift is about 130 °C compared to 200 °C at the surface of the cask when individual disposal casks are represented in the numerical model. Nevertheless, this discrepancy only occurs in the near field and the developed numerical model is believed to be precise enough for the temperature evolution in the far field.

Figure 4.-5 shows the thermal evolution of the system at 500 years, by which time the repository is reaching its maximum temperature. In the figure, one can see how the heat propagates

through the geological formation. This propagation is asymmetric between the two emplacement wings due to the different heat power of the different families of radioactive waste emplaced in the repository at different times.

The subsequent analysis for periods of time over 500 years was performed with OpenGeoSys. Based on the repository concept, it is assumed that an emplacement field is filled every five years starting with the fields in the northern wing of the repository mine. The effect of this activation sequence can be seen in figure 4.-6. Figure 4.-6 shows a map view of the temperature evolution at a slice taken through the disposal horizon in the model. The first emplacement field in the northern wing is mostly filled with cold wastes from the prototype and test reactors (subplot at t = 9.1 a). In this field, only three drifts filled with reprocessed waste in POLLUX-9 are heat producing. In the next activated field (subplot at t = 9.1 a) where 13 drifts are filled with reprocessed waste followed by two drifts with PWR spent fuel and the rest with VVER spent fuels (from top to bottom in subplot at t = 9.1 a), the heat generation in this field follows the thermal power characteristics of the waste as displayed in Figure 4.-3 with higher temperature to be observed in the drifts with PWR spent fuel. Drifts with VVER fuels produce less heat in this field.

The last field in the northern wing as well as all fields in the southern wing are filled with PWR spent fuels. The thermal propagation follows the activation sequence of 5 years between the fields (subplot at t 13.1, 17.1, 21.1 and 25.1 a in Figure 4.-6) with the two drifts that are reserved for the disposal of the structural elements that remains thermally inactive and only are heated from the waste in neighboring drifts.

In the post closure phase, the temperature in the repository increases significantly (Figure 4.-7) reaching a maximum value of about 130 °C in the third field of the northern wing (subplot t = 115.1 a). Almost 500 years after the start of the waste disposal, the repository is now cooling down especially in the northern wing. In the southern wing, where a higher concentration of high heat generating waste packages are disposed, the temperature remain stable at values over 120 °C in the center of the emplacement wing. At 755 years, the temperature decrease in the repository is now remarkable at all point in the repository. The cooling process is clearer at 955 years. At this time the temperature is already below 100 °C. 2055 years after the begin of disposal, the repository system is trending back towards the initial conditions dictated by the geothermal gradient.

Line plots of the temperature evolution along the length of the engineered barriers are shown in Figure 4.-8 and Figure 4.-9. The figures show the temperature profiles along the drifts and the shafts at different times. The results for the seals installed in the material drift and in the waste transport drift are similar Figure 4.-8. This is also the case for the two shaft seals temperature profile Figure 4.-9. In the drift seals, the temperature increase from the sides that are located near the emplacement fields and propagates along the length of the seals. Higher temperature increases are observed in the southern wing compared to the northern wing. There, the maximum temperature increase at the edge of the seal emplacement side is about 20 °C (about five 3 K less in the northern side drift seal). The maximum temperature occurs at approximately 500 years and remains almost stable at the edges (emplacement side) of the seals up to 1000 years later. Near the shafts, the temperature in the seal increases only to 5 K with a maximum observed around 5000 years. At 5000 years the temperature in the drifts is almost homogenised at a value of 5 K higher than the initial conditions. 8000 years later the drift seal further cool down to about 1 to 2 K above initial conditions.

During the simulation, a new steady state is computed based on the different material properties of the different geological layers. This is noticeable by a deviation from the otherwise smooth gradient of temperature with depth. The temperature profiles show an increase of temperature along the shaft over the time up to about 5000 years. The maximum of temperature increase is less than 5 K after 5000 years. At 8000 years, one can observe that the cooling process has begun within the shafts (Figure 4.-9).

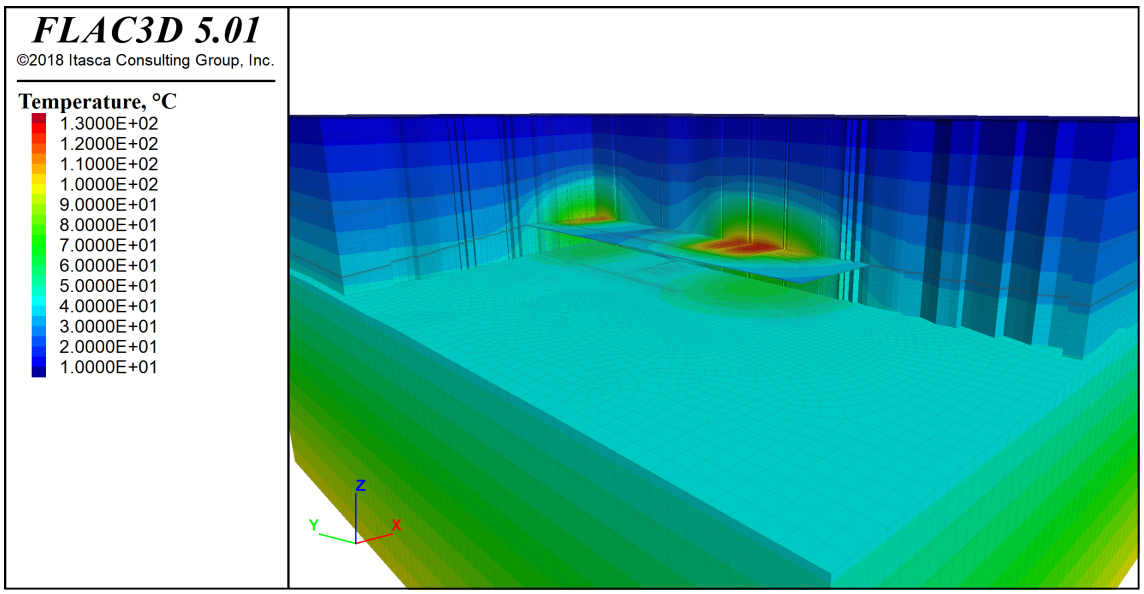

Figure 4.-5: Thermal evolution in the repository system at 500 years.

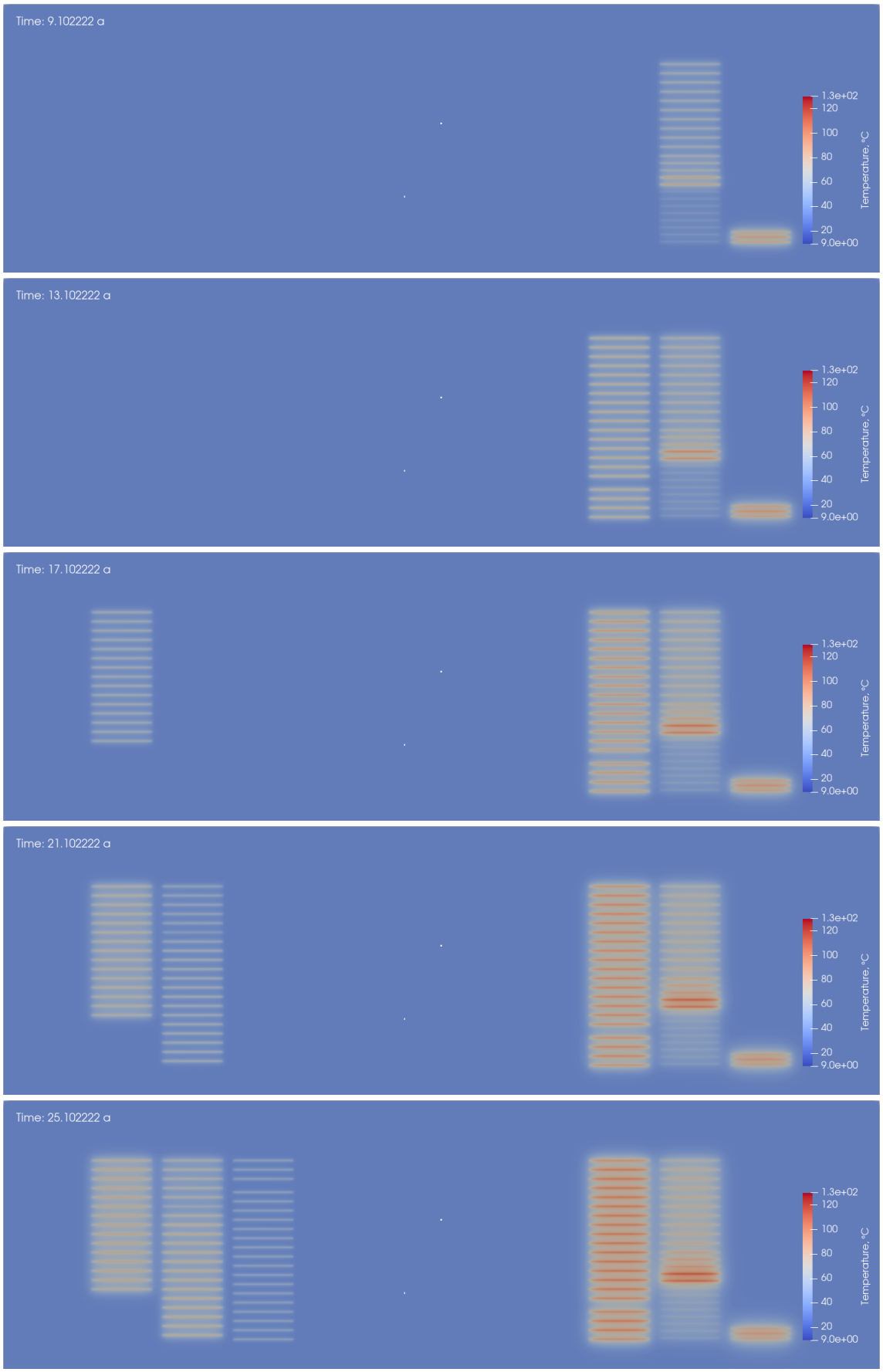

Figure 4.-6: Temperature evolution during the disposal phase, first 30 years.

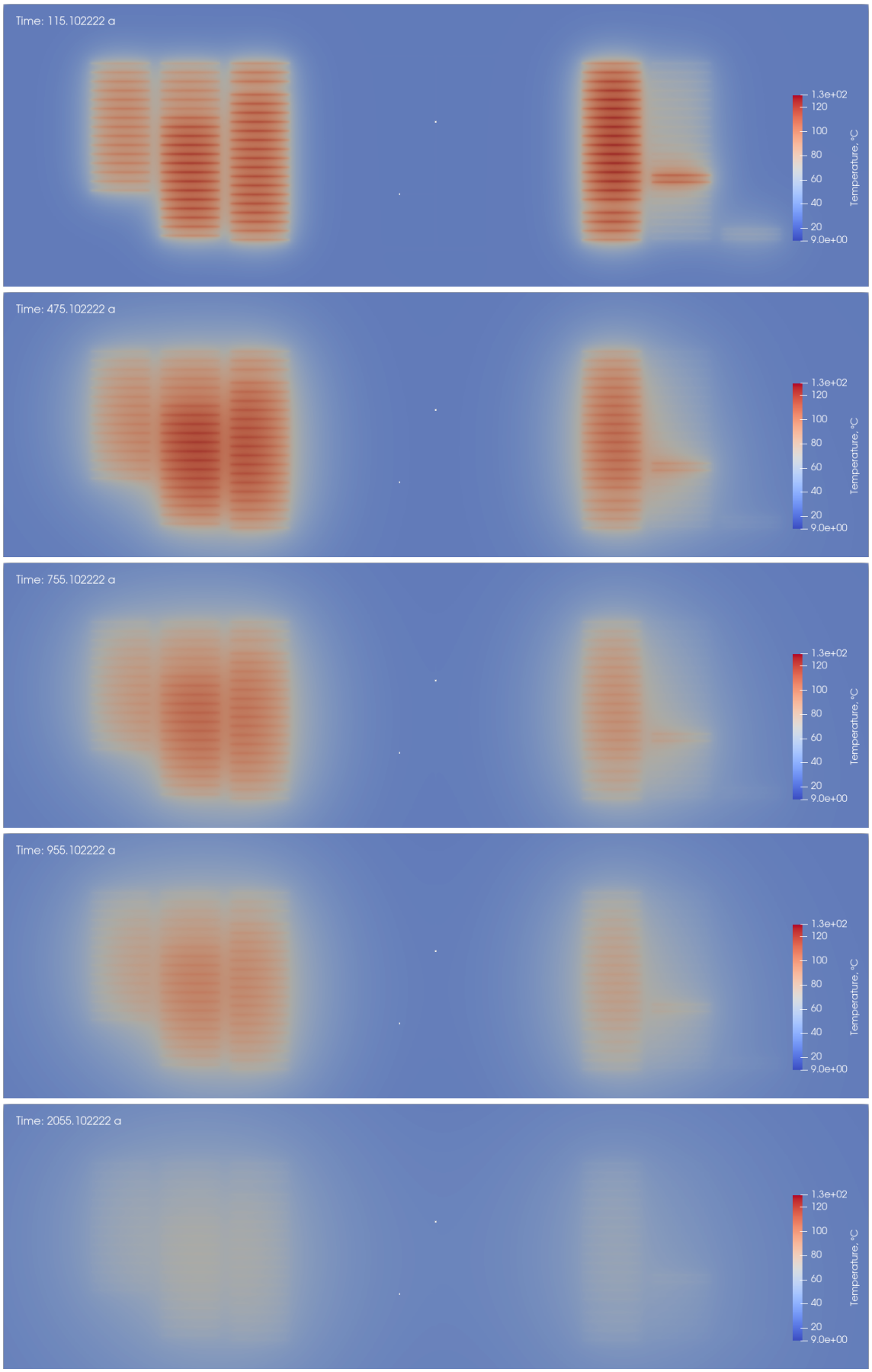

Figure 4.-7: Temperature evolution in the post closure phase up to 2,000 years.

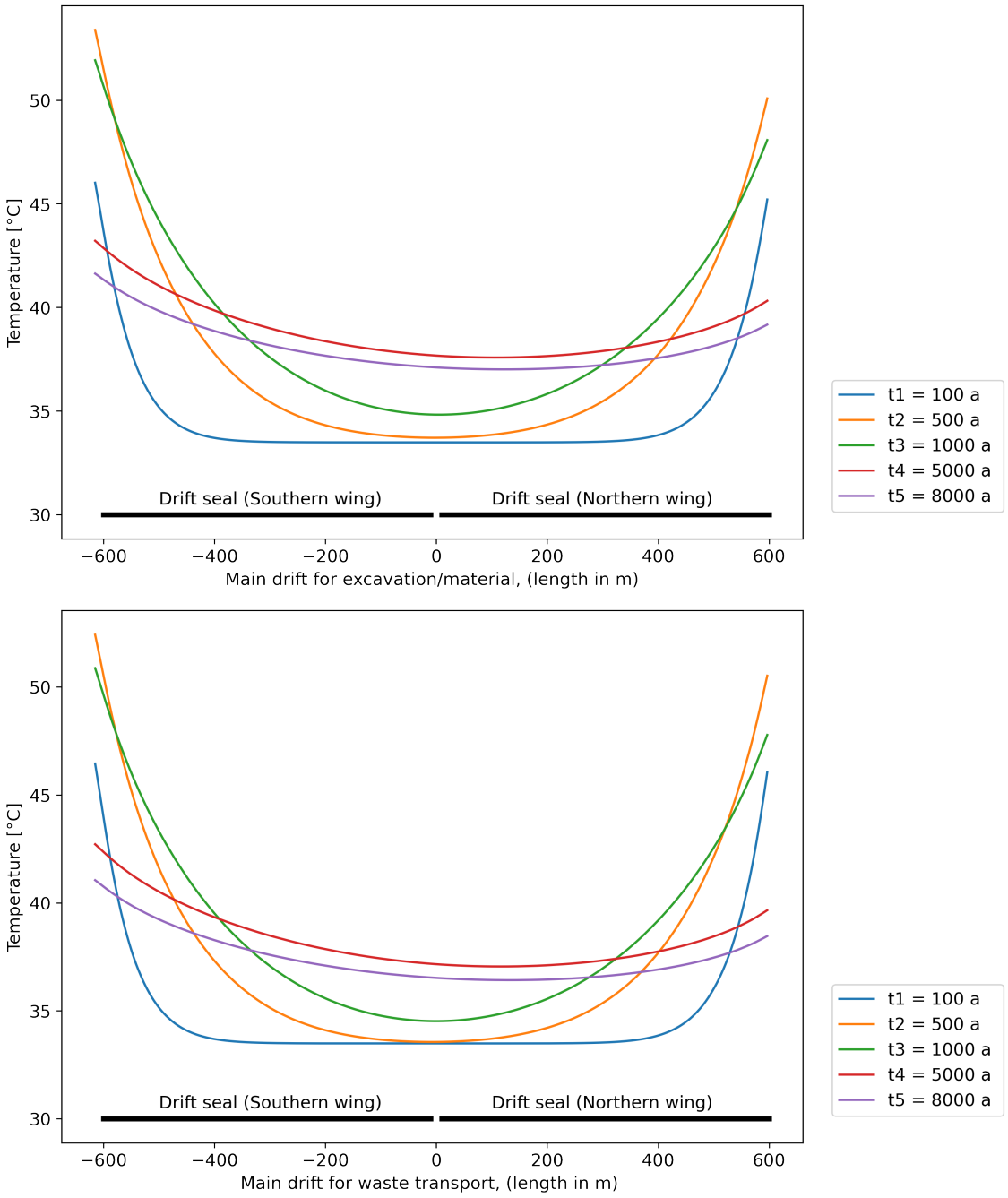

Figure 4.-8: Temperature evolution in the drift seals (top is material drift, bottom is waste handling drift). See Figure 4.-2 for the location of the seals in the repository.

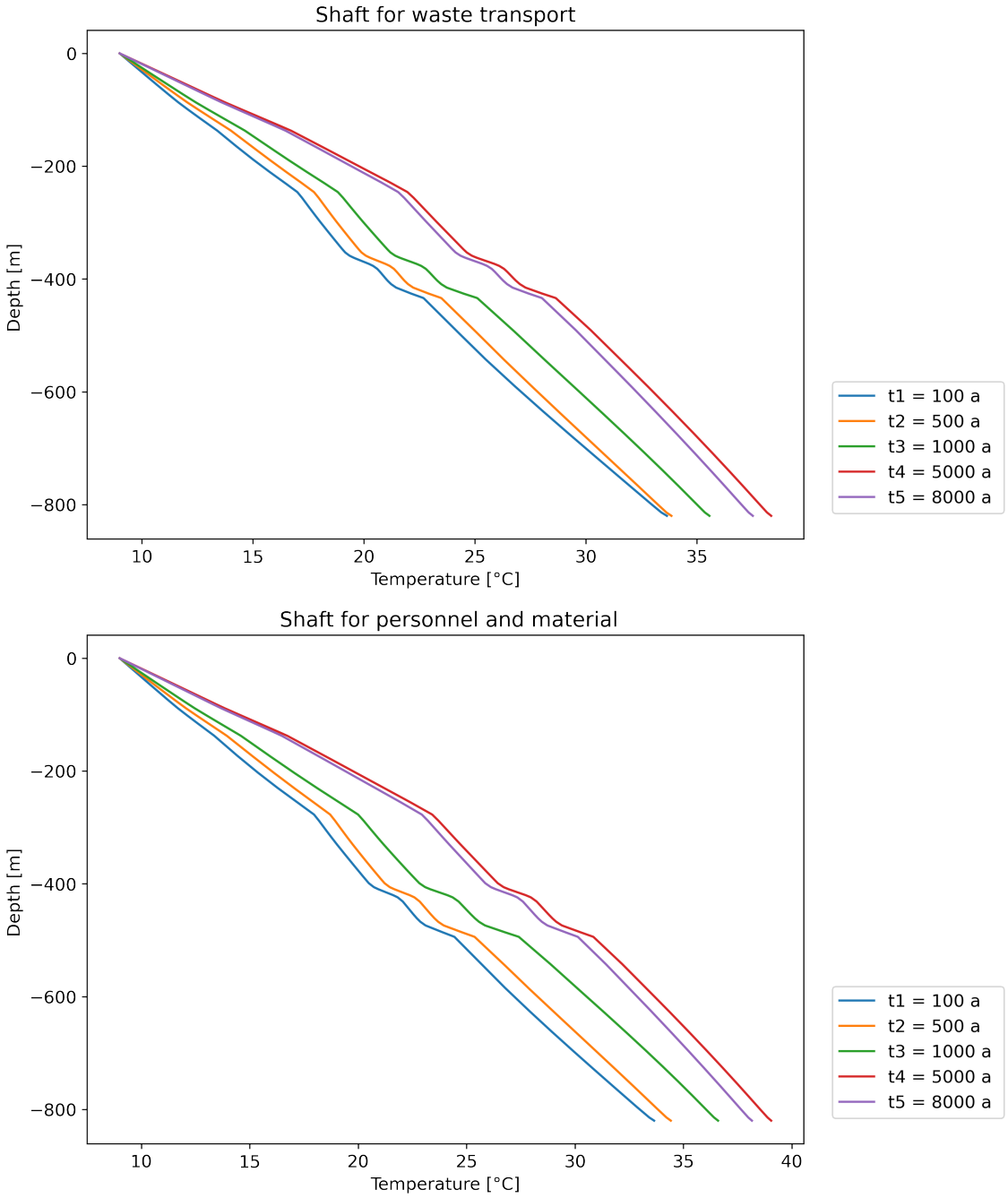

Figure 4.-9: Temperature evolution in the shafts. See Figure 4.-2 for the location of the shafts in the repository.

4.5 Discussion

In regard to the long-term stability of the EBS components, one can conclude that due to the negligible temperature increase in the EBS, the temperature evolution will not endanger the long-term stability of the geomaterials used in the EBS. For instance, the sealing properties of clays and bentonite do not deteriorate when exposed to temperature up to 100℃ (Villar et al., 2023). Rock salt from bedded salt formation in Germany with a water content of 0.02 up to 2% - only shows disintegration (“decrepitation”) linked to the formation of microcracks above approx. 250℃, (Bräuer et al., 2016). Sorel and salt concretes are stable up to 90℃. This temperature limit increases with the in situ confining pressure that is to be expected in repository conditions. Higher confining stress will reduce the development of fractures.

5. Long-Term Geochemical Stability of the EBS

5.1 Scenarios

Two shaft seal leakage scenarios were investigated:

1. brine leaks down the shaft seal from a penetrated overlying formation to the repository, and

2. brine enters the repository at depth and is driven up the shaft seal due to convergence and gas generation in the repository.

The overlying formation can either be a fresh water aquifer, or water from a fractured anhydrite caprock.

The geochemical materials considered are either shaft seal materials (e.g., MgO) or the geological materials surrounding the shaft seal and making up the excavation damaged zone (EDZ) around the emplaced seal (e.g., Halite - NaCl and Sylvite - KCl). It is assumed that the salt layers that surround the shaft seal materials are much more soluble and reactive than the shaft seal materials like clay, asphalt, and gravel (Figure 5.-1).

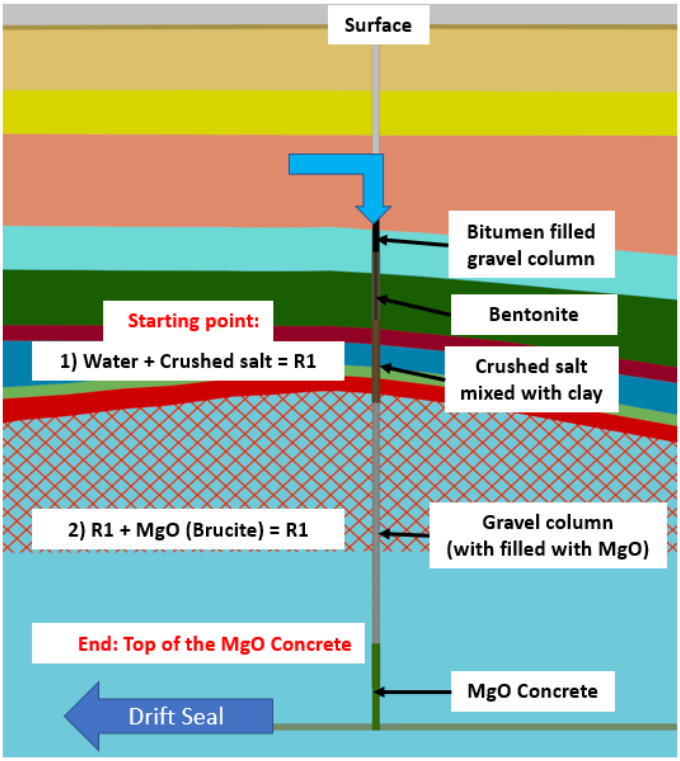

Figure 5.-1: Schematic of the shaft seal system and surrounding geology.

We used geochemical modeling to determine the stability of the solid phases with the brine as it progresses down (scenario 1) or up (scenario 2) the shaft seal/natural barrier system.

5.2 Methods

EQ3/6 version 8.0a was used to perform geochemical modeling (`https://github.com/llnl/eq3_6`). It is a reaction path simulator for isothermal batch reactions (Wolery, 2010). EQ3/6 is split into two functions that work in series: EQ3 and EQ6. EQ3 equilibrates a starting solution and computes the charge balance, accounting for formation of complexes. It can also force a charge balance by adjusting the concentration of an ion of the modeler's choice (in these models, Cl^-). Starting from the EQ3 output, EQ6 then computes the desired reaction on the equilibrated solution, dissolving and precipitating solids when necessary.

The approach for the implementation of EQ3/6 was to run an EQ3 equilibration and EQ6 reaction path simulation for the fluid as it reacts with each layer of the salt barrier. That is, the output from the reaction path calculation for a single layer, was used as the input for the equilibration and subsequent reaction path reaction for the next layer, and so on. This simulates slow flow of the fluid through the shaft seal and EDZ, assuming there is adequate time for the reactions to occur at each stage. Arbitrary kinetics have been assumed, such that the fluid reacts completely with each layer and reaches equilibrium.

EQ3/6 requires a reference thermodynamic database for its calculations. The database used for the modeling presented here (titled YMP) is included with the v8.0a release of EQ3/6 and was used previously in the Yucca Mountain Project, is currently used in the WIPP project, and has been used in generic spent fuel disposal research (Kuhlman et al., 2018). This database includes formation reactions for a wide variety of minerals and complexes, Pitzer interaction parameters, and reaction log equilibrium constants as a function of temperature.

Initial fluid compositions have been constrained as shown in 5.-1. Three representative waters have been chosen: A low-salinity surface water, a saline cap rock water, and halite-saturated Gorleben brine (Müller-Hoeppe et al., 2012b).

Table 5.-1: Initial compositions of reacted fluids.

Species	**Concentration (mol/kg H_2O)**		
	Surface Water	**Cap Rock Water**	**Gorleben Brine**
Na^+	8.07E-05	4.96E+00	5.98E+00
K^+	1.90E-06	3.61E-02	-
Ca^{2+}	1.98E-04	3.52E-02	2.00E-02
Mg^{2+}	-	5.64E-02	2.00E-02
Cl^-	8.07E-05	5.07E+00	5.98E+00
SO_4^{2-}	1.98E-04	5.15E-02	4.00E-02
SiO_2(aq)	-	5.49E-04	-
Al^{3+}	-	1.19E-05	-
HCO_3^-	3.19E-06	2.10E-03	-
pH	5.81	6.3	5.9

The shaft seal penetrates through five geologic layers. Each layer is a mixture of either two or three different salts. Below the final salt layer the shaft seal is comprised of MgO; in the

model, MgO has been represented as periclase in the thermodynamic database. In the first scenario, for both the cap rock and surface waters, reactions occur sequentially down. In the second scenario, the layers are reacted in the reverse order; Gorleben brine starts in the MgO layer and moves up. Figure 5.-2 shows the constituents of each layer and the order of reactions. Each set of reactions was simulated at 25 °C and 40 °C (isothermal), to span the range of expected geologic disposal conditions in the shaft seal.

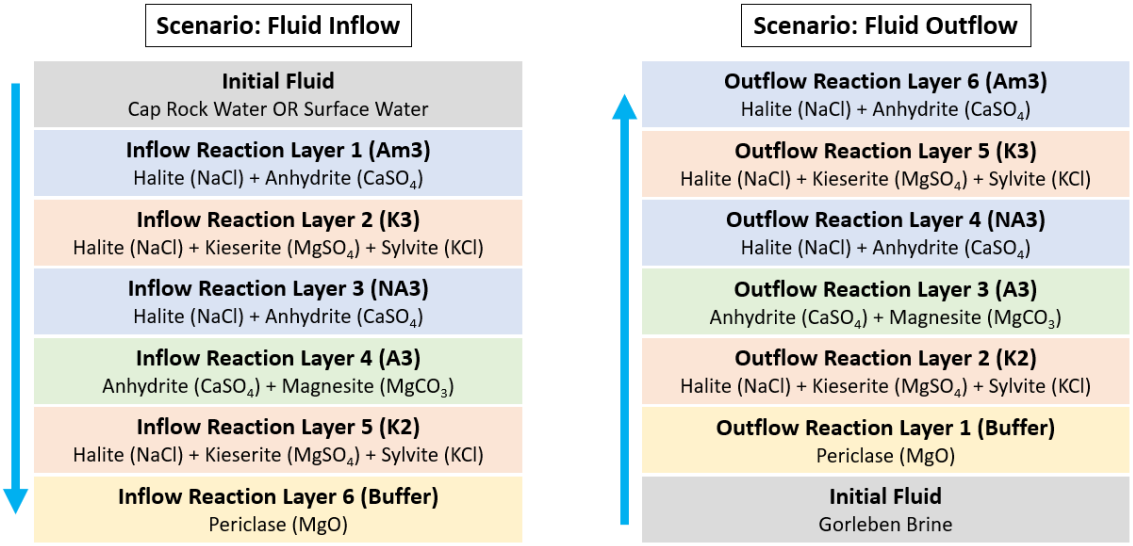

Figure 5.-2: Layers of the simulated shaft seal and salt EDZ.

EQ6 requires the mass of reacting solids to be specified and the solid phase is titrated into the liquid phase; an excess mass was specified for each salt reacted. 15 moles of each salt in each layer is titrated into 1 kg of fluid. This arrangement is like a titration into a beaker in the lab, where the liquid and solid phase salts that precipitate are all kept in equilibrium with one another. This was done to ensure the reactions progressed to completion (i.e., there was always more than enough salt available). This is similar to the approach used during brine evaporation calculations (Kuhlman et al., 2018) and by other common geochemical codes, like PHREEQC (Parkhurst and Appelo, 2013).

Additionally, EQ6 has an input option that establishes the reaction in a “fluid-centered flow-through open system.” With this, solids that precipitate as the reaction proceeds are removed; that is, they do not participate in the reaction any further. This can be likened to solids being left behind as the fluid flows through the salt mass. In this flow-through approach, the added solid phases dominate the system chemistry, rather than the precipitated solid phase (which tend to dominate in the titration mode). It was believed that this flow-through behavior is more similar to what would be expected in the field.

5.3 Results and discussion

The inlet and outlet compositions of each water type at each model temperature are shown in Figure 5.-3. Composition changes over the course of reaction steps are discussed in further detail hereafter. Notably, the composition of the surface water sees the most marked change by the end of reaction with the seal.

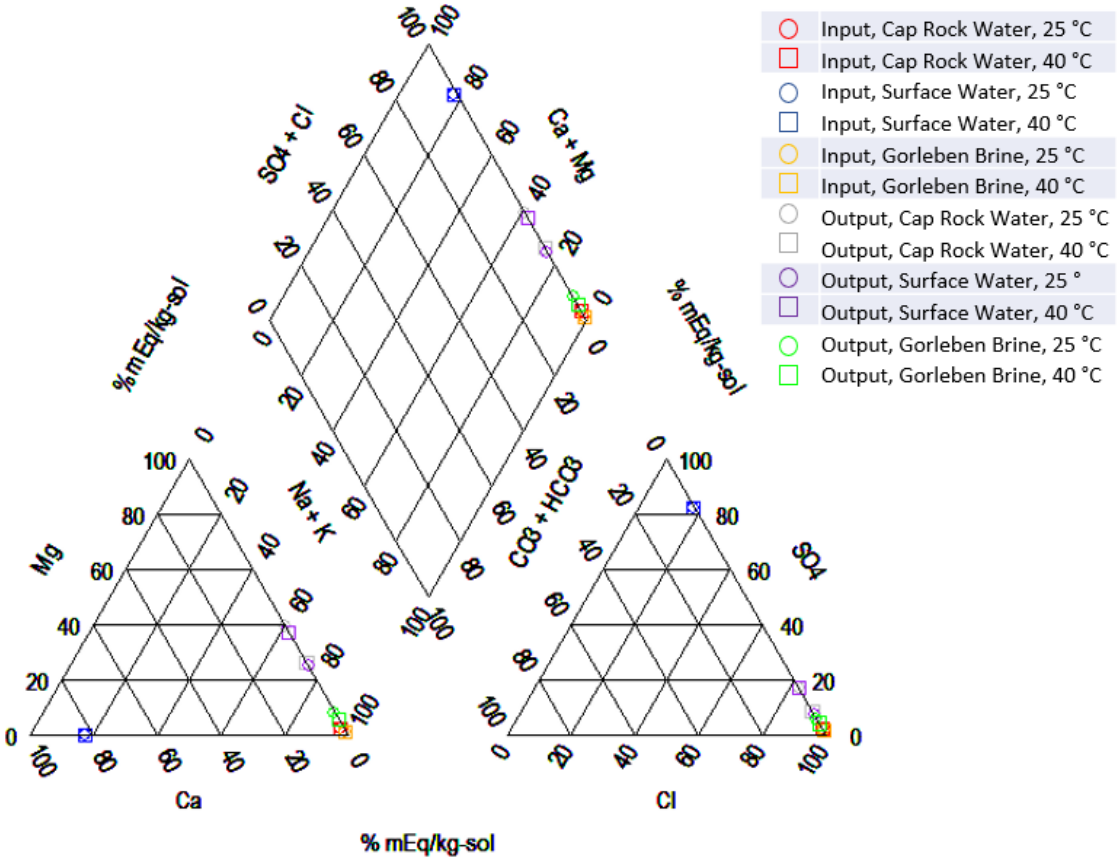

Figure 5.-3: Piper plot showing distribution of inlet and outlet waters to seal system in model.

5.3.1 Scenario: Downward flow starting with cap rock water

Reaction of the salt barrier with cap rock water at 25 °C results in the solute profiles shown in Figure 5.-4. After the first reaction step, the dissolved concentrations of Na^+ and Cl^- increase. As additional cations are introduced in subsequent layers, the concentration of Na^+ decreases; however, this change is not as notable in the concentration of Cl^- as more anions are added. By the final reaction step, the most prominent cations in the solution are Na^+, K^+, and Mg^{++}. Solution pH decreases at most steps, though it increases at step 2 (layer K3) and step 6 (MgO buffer) for a final pH in the alkaline range. Ionic strength trends upwards, increasing from an initial value below 6 molal to a final value of ~10 molal.

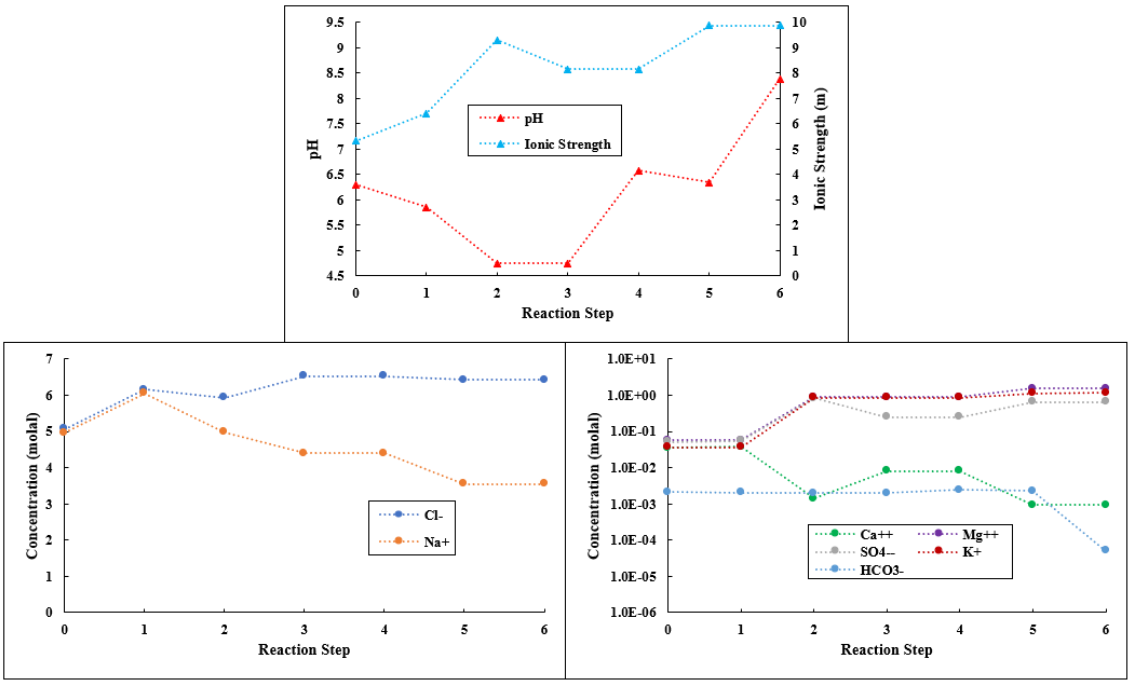

Figure 5.-4: EQ3/6 simulation results for caprock water inflow down the shaft seal system at 25 °C.

In the case where reactions are computed at 40 °C, previous observations hold (Figure 5.-5). No major differences in solute profiles are seen at elevated temperature; the same general trends persist, and the orders of magnitude of results stay the same. Some absolute values are slightly different, and there are minor differences in the later time behavior.

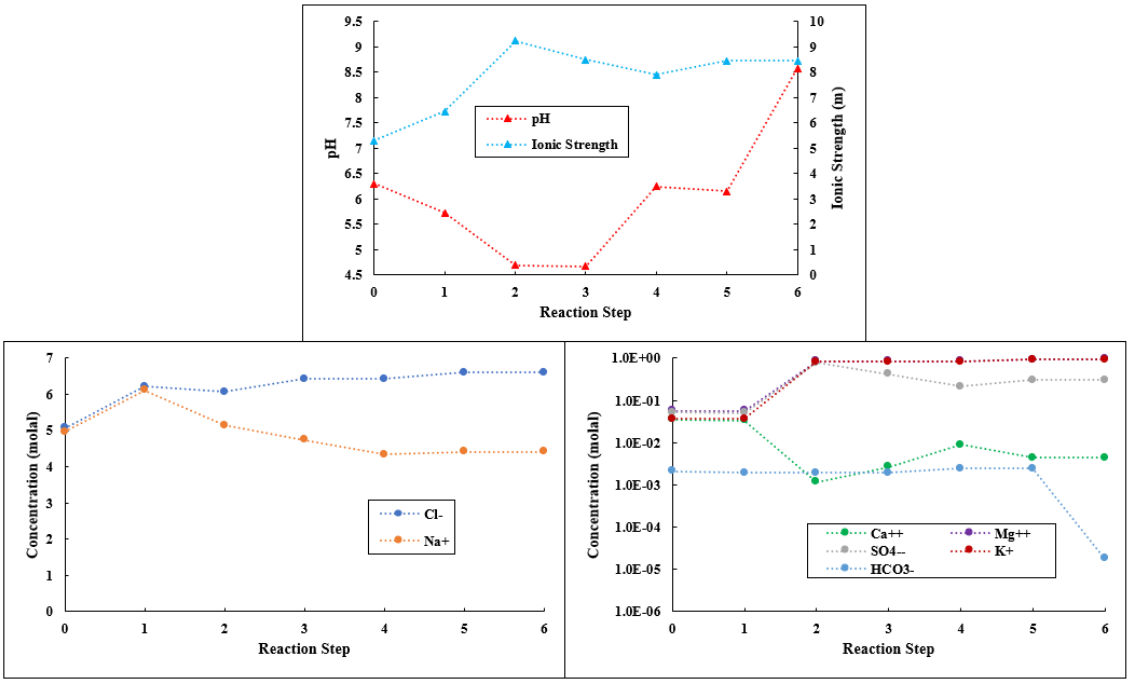

Figure 5.-5: EQ3/6 simulation results for caprock water inflow down the shaft seal system at 40 ℃.

5.3.2 Scenario: Downward flow starting with surface water

Trends for the reaction of surface water with the salt barrier follow those observed in the case of the cap rock water (Figure 5.-6). There is a notable uptick in Na^+ and Cl^- concentrations. It is worth observing that the final K^+ and Mg^{++} concentrations are higher in this case than in final cap rock water step, despite starting with a lower concentration in the initial fluid. As before, increasing reaction temperature from 25 ℃ to 40 ℃ results only in minor changes in trend shapes and absolute values (Figure 5.-7).

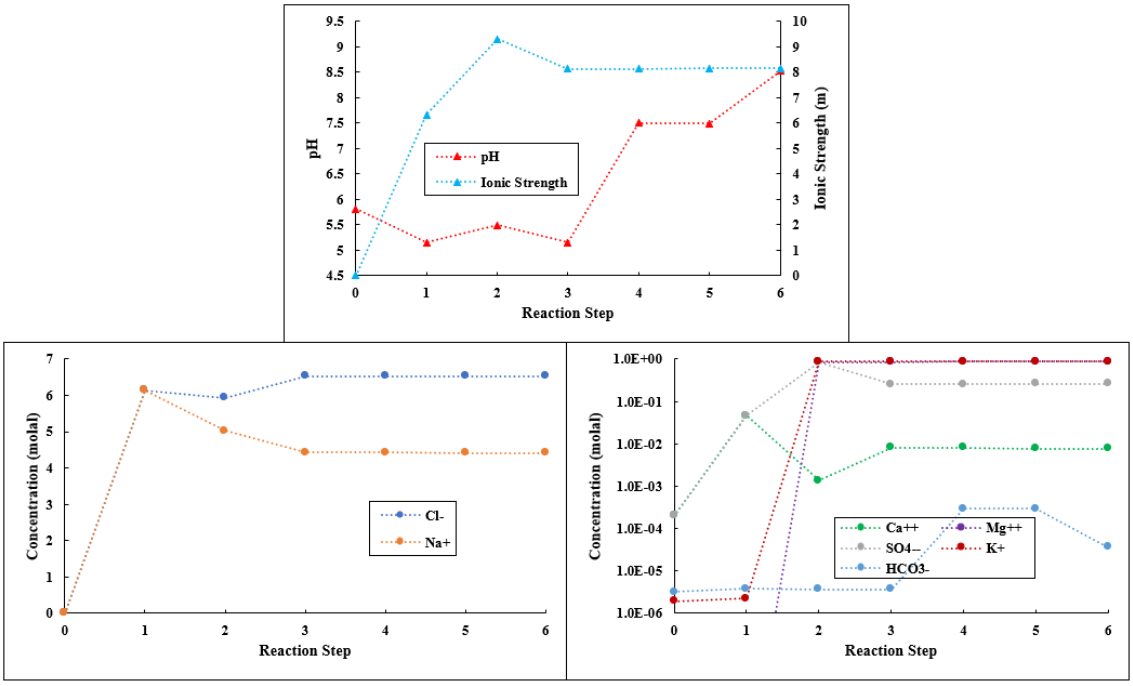

Figure 5.-6: EQ3/6 simulation results for surface water inflow down the shaft seal system at 25 ℃.

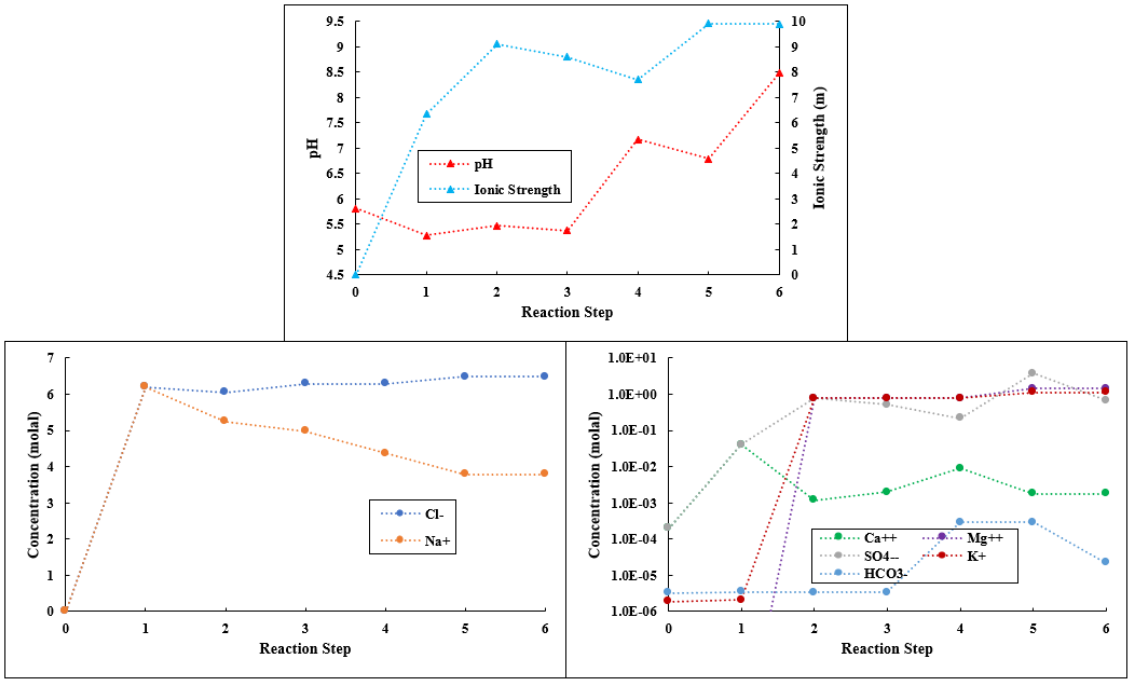

Figure 5.-7: EQ3/6 simulation results for surface water inflow down the shaft seal system at 40 ℃.

5.3.3 Scenario: Upward flow of Gorleben brine

Trends observed in the reaction of Gorleben brine with the salt barrier in reverse order are shown in Figure 5.-8. Solution pH spikes due to contact with the MgO layer in the first reaction, but then stabilize at slightly alkaline pH (~8.5). The concentrations of Na^+ and Cl^- initially present in the solution remain mostly unchanged – thus, the final brine remains primarily a halite-saturated brine. The ionic strength increases, but not to the degree observed in the inflow cases. At elevated temperature, (Figure 5.-9), very minor differences are seen; trends and final values are approximately the same.

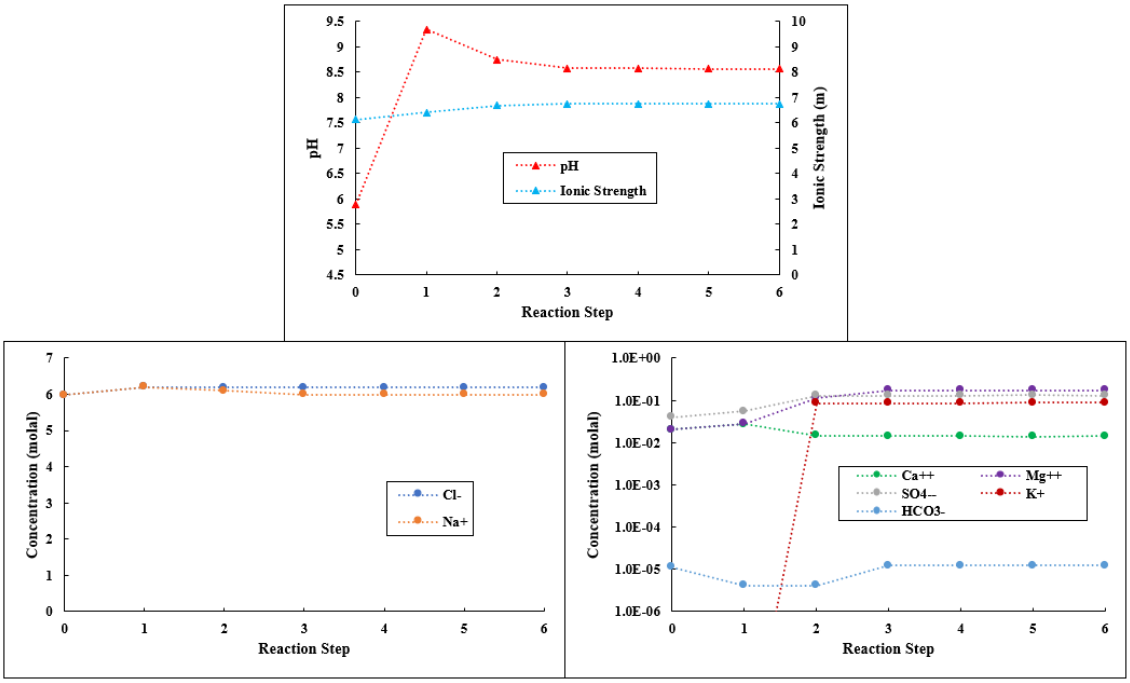

Figure 5.-8: EQ3/6 simulation results for Gorleben brine outflow up the shaft seal system at 25 ℃.

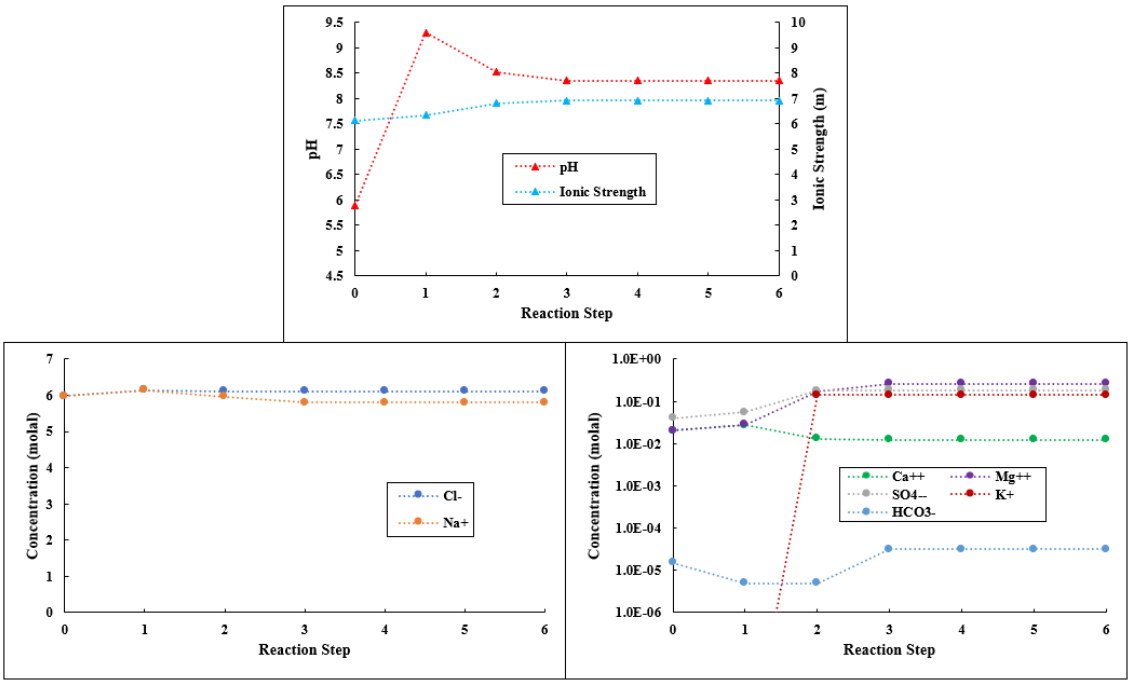

Figure 5.-9: EQ3/6 simulation results for Gorleben brine outflow up the shaft seal system at 40 ℃.

5.4 Conclusions

The reaction of each of three geologic fluids with the anticipated salt barrier produces solutions with high ionic strength and moderately alkaline pH, that consist primarily of halite. This is irrespective of the direction by which the fluid travels through the barrier. This was the anticipated behavior and function of the barrier as designed. Thus, the salt barrier could reasonably be expected to mitigate a canister breach. Further developments on this work could assess the time-dependence of this behavior, alternate configurations for the salt barrier, or minor interactions with the largely inert sealing materials.

6. Evolution of Crushed Salt Compaction in a Repository Mine

In addition to the initial barriers (drift and shaft sealing systems), further barriers contribute to the long-term containment of radionuclides in the effective confinement geological area. They do this by either delaying the access of solutions to the waste packages (e.g., crushed salt backfill) or by preventing or hindering the release of radionuclides from the effective confinement geological area (e.g., crushed salt backfill and waste matrix). The initial barriers must remain sufficiently impermeable until the hydraulic resistance of the compacting crushed salt is high enough to prevent or significantly limit the inflow of solutions to the wastes (Kock et al., 2012). In the safety assessment of salt repositories, it is crucial to determine the time when the crushed salt will gain its function as long term seal. The understanding of the compaction behavior of crushed salt has been the scope of several research project in the last four decades. Recent research projects such as KOMPASS focused on remaining issues regarding the compaction at low porosities (Czaikowski et al., 2023). Nevertheless, constitutive models are available to predict the compaction behavior of crushed salt numerically. In the scope of the present study, we intend to analyze how crushed salt will compact over the course of the repository evolution under the thermal-mechanical conditions of the repository.

The modeling crushed salt compaction in the repository must take into account the development of stresses and the creeping behavior of the rock salt as well as the thermal evolution in the emplacement fields. Different modeling approaches were used to accurately predict the compaction at different locations of the repository mine. They will be discussed in the following section.

6.1 Material parameters

In the following simulations several materials are present that need to be described thermal-mechanically. Table 6.-1 summarizes the thermal material properties used in the model to simulate thermal propagation in the near field - rock salt. The crushed salt considered in the calculation model is compacted over time under the influence of lithostatic stresses, changing its thermal properties, particularly its thermal conductivity.

Table 6.-1: Density and thermal parameters of the components in the near field of the disposal zone (Bollingerfehr et al., 2013).

Components	**Heat Capacity [J/(kg K)]**	**Thermal Conductivity [W/(m K)]**
Container	515	15
Container basket	500	20
Crushed salt	$c_{p,CS} = c_{p,RS}(1-\eta)$ (1) where: $c_{p,CS}$: Specific heat capacity of crushed salt $c_{p,RS}$: Specific heat capacity of rock salt η : Current porosity	$\lambda_{CS} = \left(1-\frac{\eta}{\eta_0}\right)^m \cdot \lambda_{RS} + \frac{\eta}{\eta_0} \cdot \lambda_G$ where: m : exponent m = 1.14 η : Current porosity η_0 : Initial porosity η_0 = 0.35 λ_G : Initial thermal conductivity $\lambda_G = \lambda_{0,CS} + c_{T,CS} \cdot \theta$ $\lambda_{0,CS} = 0.42 \frac{W}{m \cdot K}$ $c_{T,CS} = 0.0027 \frac{W}{m \cdot K^2}$
Rock salt	864	$\lambda_{RS} = \frac{\lambda_{0,RS}}{1 + c_{T,RS} \cdot \theta}$ where: $c_{T,RS}$: Temperature parameter $c_{T,RS} = 0.0045 \frac{1}{K}$ $\lambda_{0,RS}$: Thermal conductivity $\lambda_{0,RS} = 5.2 \frac{W}{m \cdot K}$ θ : Temperature in °C

In Table 6.-2 the elastic material parameters as well as the densities of the components are given. The density and elastic properties of crushed salt depend on the compaction behavior of the material and necessitates advance constitutive model for accurate estimation.

Table 6.-2: Densities and elastic material parameters of the components in the near field of the disposal zone (Bollingerfehr et al., 2013).

Material	**Density**	**Young's modulus**	**Poisson's ratio**
	[kg/m^3]	GPa	–
Salt rock	2,200	25	0.27
Crushed salt	f(η)	f(η)	0.27
POLLUX®	7,000	150 GPa	0.25

The compaction of the crushed salt, dictated by the material properties of the rock salt, exhibits a viscosity-dependent deformation behavior influenced by stress and temperature, and therefore is time-dependent. The viscoplastic behavior can be expressed by a volumetric strain component and its deviatoric counterpart. For the mechanical material model of the crushed salt considered in this study, the "CWIPP" model by (Itasca Consulting Group, Inc., 2021) that has been modified by BGE TEC is considered. In this flavor of the model, the volumetric and deviatoric strain are given in Table 6.-3 and the material parameters are taken

from Bollingerfehr et al. (2013).

Table 6.-3: Viscoplastic material model for crushed salt based on CWIPP (Bollingerfehr et al., 2013).

viscoplastic total strain rate:

$$\dot{\varepsilon}^{vp}_{CS} = \dot{\varepsilon}^{vp}_{v,CS} + \dot{\varepsilon}^{vp}_{d,CS}$$

volumetric part:

$$\dot{\varepsilon}^{vp}_{v,CS,ij} = \frac{1}{3}\dot{\varepsilon}_{v,CS}\delta_{ij}$$

$$\dot{\varepsilon}^{vp}_{v,CS} = A_0 e^{-\frac{Q}{RT}} e^{B_2\rho}\left(1 - e^{-\left(B_1\frac{(\sigma_0-\sigma_v)}{B_3}\right)^{B_4}}\right)$$

deviatoric part:

$$\dot{\varepsilon}^{vp}_{d,CS,ij} = \frac{3}{2}\left(\frac{\dot{\varepsilon}^{vp}_{d,CS}}{\sigma'}\right)\sigma'_{ij}$$

$$\dot{\varepsilon}^{vp}_{d,CS} = A\left(\frac{\sigma'}{\sigma(1-\eta)}\right)^{n} e^{-\frac{Q}{RT}}$$

δ_{ij} : Kronecker delta
A_0 : Structure factor
$A_0 = 1.909 \cdot 10^{13}$ kg/d/m^3
$B_{1..4}$: Material parameters
$B_1 = 0.789$ 1/MPa
$B_2 = -19.5 \cdot 10^3$ m^3/kg
$B_3 = -26.0$ MPa
$B_4 = 1.8$
Q : Activation energy
$Q = 36.4$ kJ/mol
σ'_{ij} : Deviatoric stress
A : Structure factor
$A = 0.18$ 1/d

The corresponding porosity dependent Young's modulus assumed in the mechanical law is given in Table 6.-4

Table 6.-4: Porosity dependent elasticity Young's modulus for crushed salt (Bollingerfehr et al., 2013).

$$E_{CS} = E_{CS,f} \cdot e^{\frac{-c_E(1-\eta_0)}{\eta}}$$

$E_{CS,f}$: Young's modulus at full compaction
$E_{CS,f} = E_{RS}$
c_E : Material parameter

$$c_E = \frac{\eta_0 - 1}{\eta} \cdot \ln\left(\frac{E_{CS,0}}{E_{CS,f}}\right)$$

$E_{CS,0}$: Initial Young's modulus
$E_{CS,0} = 1$ GPa
η : Current porosity
η_0 : Initial porosity
$\eta_0 = 0.28$
$\nu_{CS} = 0.27$ (Poisson's ratio)

Several approaches have been developed over the years to describe the thermomechanical creep behavior of rock salt (**?**). In this study, the constitutive material model BGR-EB, taking into account two independently effective deformation mechanisms for a better capture of creep at higher temperatures is considered. This model formulated in Table 6.-5.

Table 6.-5: BGR-EB creep mechanical law for rock salt (Bollingerfehr et al., 2013).

$$\dot{\varepsilon}_{RS}^{vp} = V_k A_0 \left(A_{1e} \exp\left(-\frac{Q_1}{RT}\right) + A_{2e} \exp\left(-\frac{Q_2}{RT}\right) \left(\frac{\hat{\sigma}}{\bar{\sigma}}\right)^n \right)$$

V_K : Creep class factor = 5.872

A_0 : Multiplier = 5.872

$A_{1,2}$: Structure factors

$A_1 = 2.3 \cdot 10^{-4} \cdot \frac{1}{d}$

$A_2 = 2.1 \cdot 10^{-6} \cdot \frac{1}{d}$

$Q_{1,2}$: Activation energies

$Q_1 = 42 \frac{kJ}{mol}$

$Q_2 = 113.4 \frac{kJ}{mol}$

R : Universal gas constant

$R = 8.314 \frac{J}{mol \cdot K}$

T : Absolute temperature

m : Stress exponent = 5

$\hat{\sigma}$: von Mises equivalent stress

$\bar{\sigma}$: Reference stress = 1MPa

6.2 Crushed salt compaction in the near field of the emplacement fields

The first model consists of analyzing the compaction behavior in a single drift located in the middle of an emplacement field where the thermal output is maximum reaching the temperature limit of 200℃. The numerical model developed for this purpose takes into account the thermal superposition and the resulting temperature increases coming from the neighboring drifts. Such representation can be achieved by considering thermal symmetry boundary conditions as a quarter model of a cask embedded in a partial model of the rock formation, allowing the simulation of a large disposal field. In this model, the distance from the drift axis to the model boundary in the transverse direction of the drift equals half the drift spacing, and the distance from the cask's end face to the model boundary in the drift direction equals half the cask spacing. The resulting thermal superpositions are conservative and only occur in disposal fields with very long drifts and a large number of such drifts.

This modeling approach has the advantage of not requiring the entire repository to be modeled, reducing time and numerical effort. The calculation model is depicted in Figure 6.-1, showing a drift filled with crushed salt in a salt formation where a final disposal cask is stored. The cask in the model comprises two components: an outer casing for shielding against radioactive radiation and a container basket holding the high-level radioactive wastes, acting as a heat source in the model. The computations was carried out thermal-mechanically with FLAC3D Version 9 (Itasca Consulting Group, Inc., 2021).

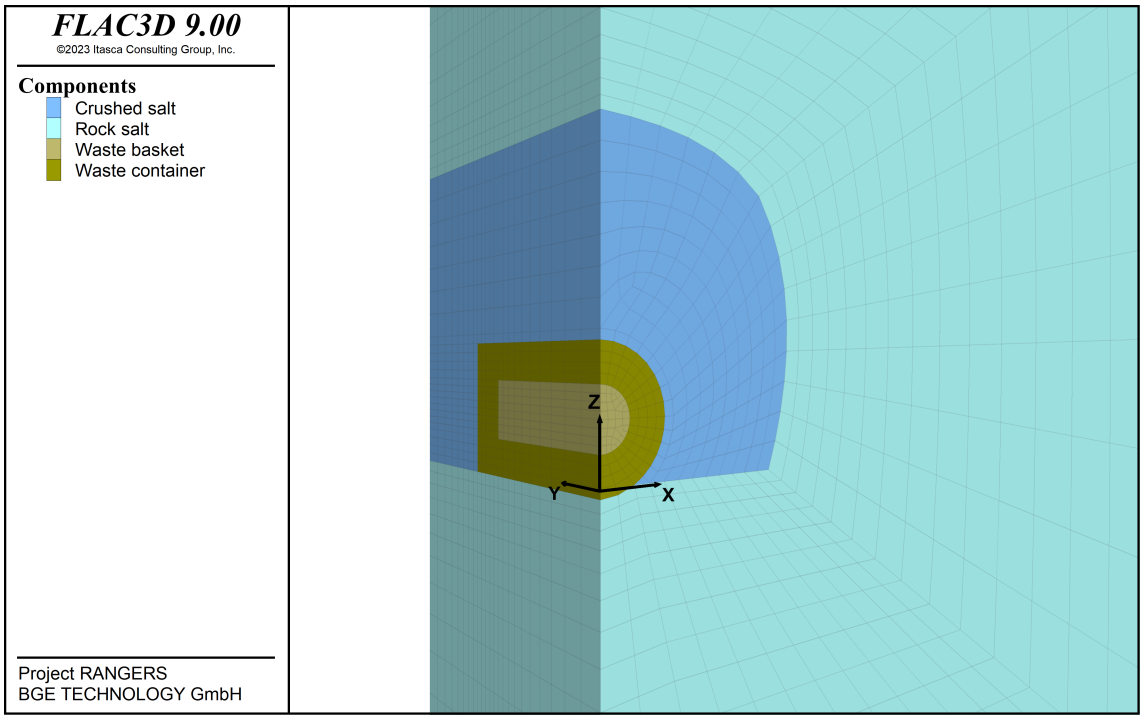

Figure 6.-1: Numerical model for the thermal-mechanical compaction in disposal drifts with heat generating waste.

The results of this simulation are depicted in Table 6.-6. The sub-figures in this table show the evolution of the temperature, displacements and porosity in the first 10 years after the disposal of the waste and the backfilling around the waste with crushed salt. Over this period of time, the temperature rises quickly to almost 200 °C in the cask and near the waste package. At five years, a slight decrease is observed that is due to the increase of thermal conductivity in crushed salt due to compaction. Because of the higher heat power in waste package, the temperature rises again at t = 10 years. The displacement presented here as the magnitude value, which is the square root of the sum of the displacement components, shows that high displacement occur around the cask. A region above the cask with almost no displacement can be observed. In that region, the porosity decrease is the highest, whereas region with high displacement show high porosity value, see porosity at t = 1 year. As a result, The analysis of the displacement in the model gives an idea about the compaction kinetics in the drift. Less displacement is found where compaction occurs first and vice-versa. At t = 5 years, the compaction process is completed as the porosity in the drift reaches zero in all finite zones. This rapid compaction is the result of the high temperature of up to 200 °C occurring in the drift. This high temperature environment helps the crushed salt to gain its sealing function faster and the disposed waste to be already confined even though the repository is still in operation.

Table 6.-6: Temperature, displacement (magnitude), and porosity evolution in a hot disposal drift.

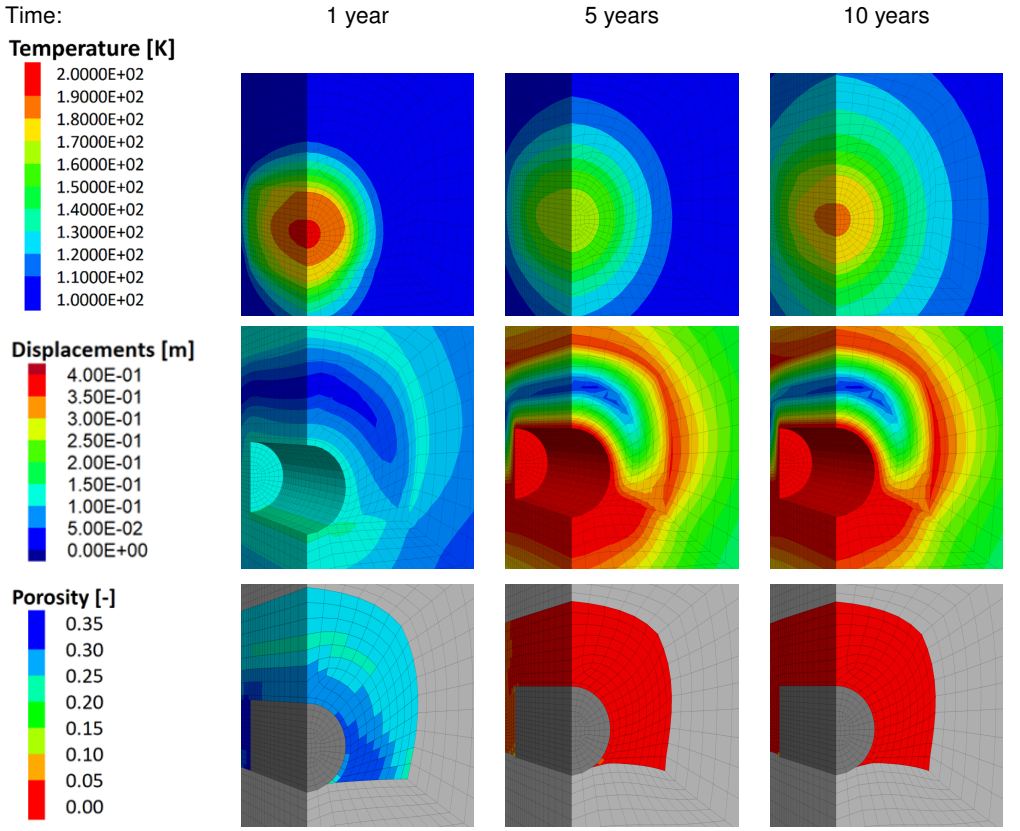

6.3 Crushed salt compaction in a cross-section of an emplacement field

The previous analysis already gives an idea how the compaction of crushed salt in the hot drifts with heat generating waste in the repository will take place. In order to analyze the compaction in the relatively colder drifts of the repository, such as the main drifts which are the pathways for a potential inflow of fluids into the repository mine, a modeling approach consisting of plain strain analysis on representative cross-sections of the repository mine was considered. This model allows to consider the thermal-mechanical effect due to the heat generation coming from the adjacent disposal drifts with PWR spent fuel.

The numerical model of the representative model region is depicted in Figure 6.-2. It consists of a cross section along the middle of the first emplacement drift in the Northern wing of the repository mine. This field has 22 disposal drifts filled with PWR spent fuel waste in POLLUX casks. One additional disposal drift is also present in this field where structural parts in MOSAIK-II casks are emplaced. The two main drifts for excavation and waste transport are also considered in the model. The geological layers at the location of the cross section were extracted from the 3D geological model. The K2 layer was merged into the salt pillow because of its negligible thickness. The disposal casks in the 22 disposal drift with POLLUX are resolved in the model. Those casks are surrounded with crushed salt backfill. The remaining drifts are fully backfilled with crushed salt. Because of the plain strain assumptions, The model represents an infinitely long repository in the longitudinal direction. The heat source in the casks are adjusted accordingly. For that, the heat source of all the casks in each disposal

drift was homogenized along the drift effective length. The right and left model boundaries are placed far enough away from the disposal area to minimize any boundary effects. The minor heat dissipation in the longitudinal direction of the repository is taken into account using adiabatic boundary conditions at the front and back model boundaries. The computation is performed with FLAC3D in the version 7.

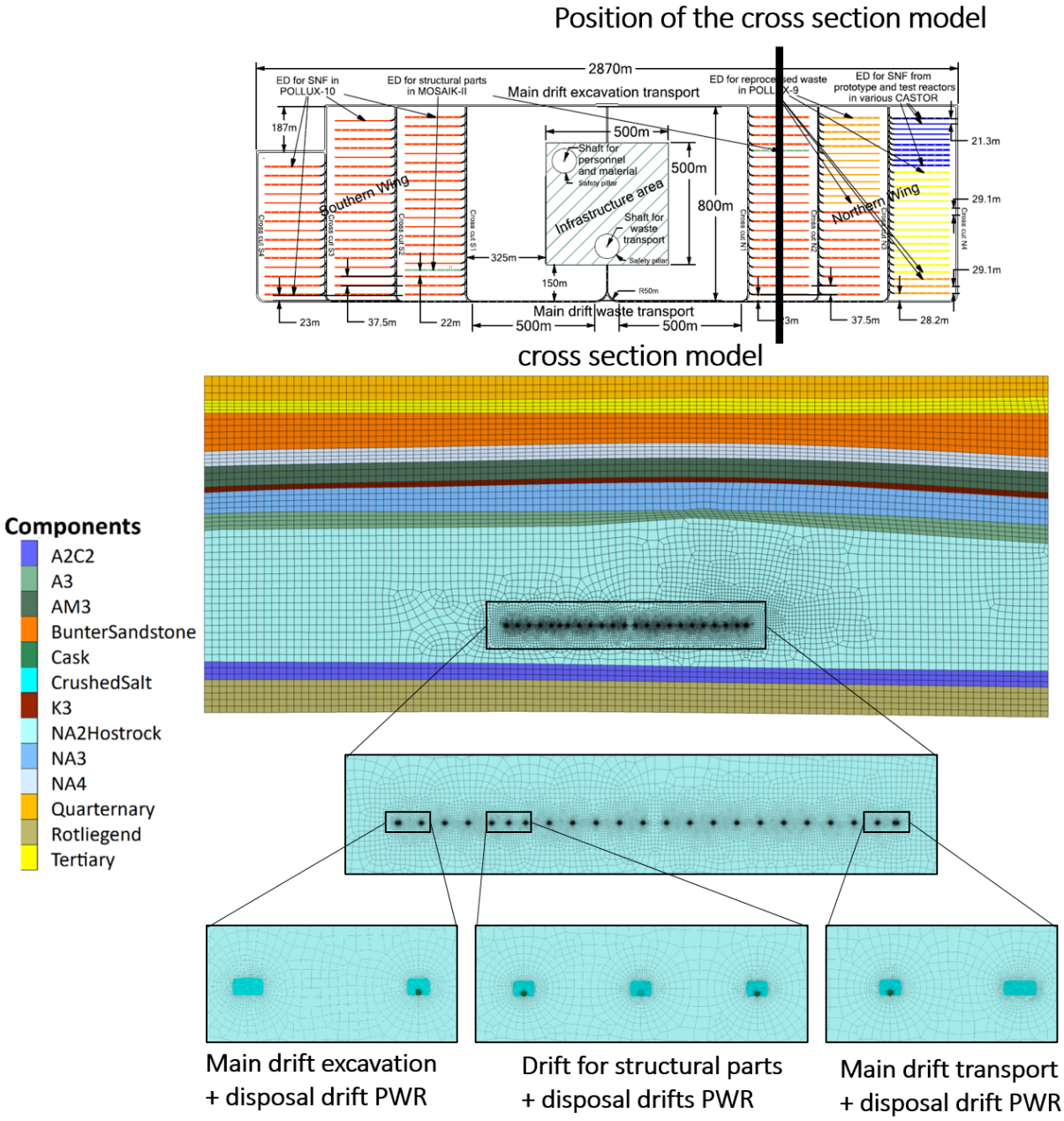

Figure 6.-2: Numerical model for the thermal-mechanical design of disposal drifts with heat generating waste.

Because of the homogenization of the heat source, the temperature evolution in the model reaches a maximum of around 100℃ in the middle of the cross section, see Figure 6.-3. An

increase of approximately 15 °C is observed in the main drift.

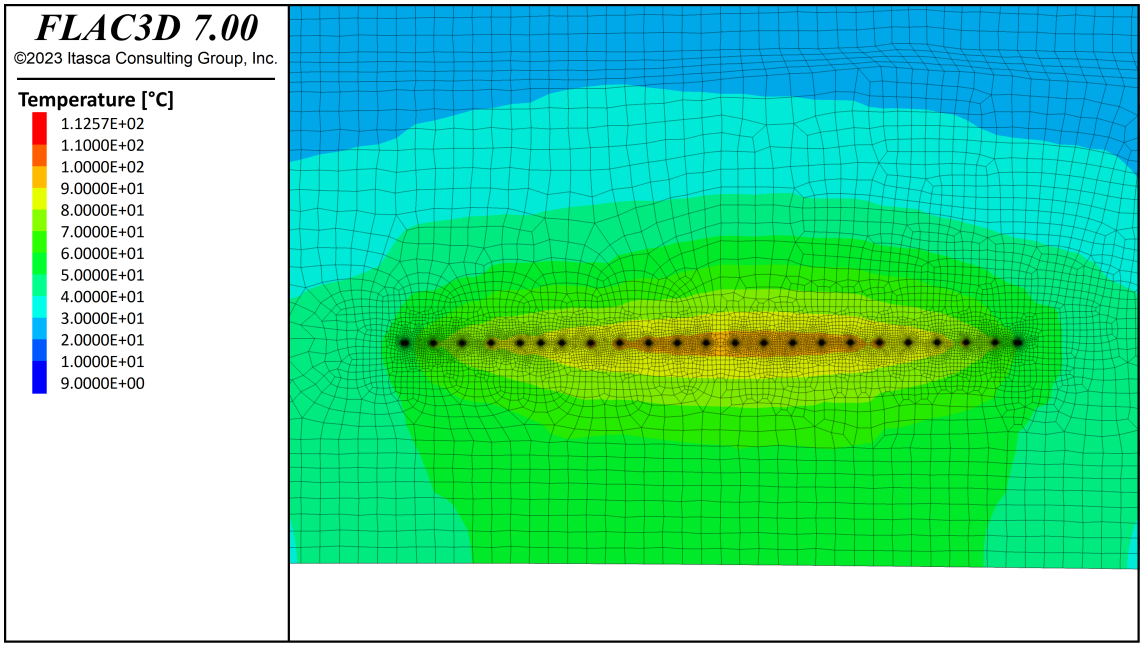

Figure 6.-3: Temperature distribution in the cross section at t = 200 years.

Table 6.-7 illustrates the porosity evolution in the crushed salt in four selected drifts along the cross-section. In the disposal drift with POLLUX cask and PWR spent fuel, the porosity decrease from 0.35 to approximately 0.2 in the first ten years of heating. Within the next 10 years, the porosity decrease reaches less than 5%. At 30 years, the crushed salt is fully compacted with computed porosity of 0. A similar evolution can be seen in the disposal drift for structural parts with a time delay. There, the porosity at 10 years is about 0.2 and decreases to 0.1 at 20 years. 30 years after heating, is the crushed salt in that drift also fully compacted. This means that the heat coming from the adjacent drift is sufficient to help the crushed salt in this thermally inactive drift to compact as almost fast as the disposal drift with heat generating waste.

The porosity distribution in the two main drifts is similar five years after heating. The compaction does not occur uniformly across the entire cross-section. In the subsequent time, the compaction in the main drift for waste transport is faster as in the main drift for excavation. The bigger dimensions of the main drift for waste transport leads to comparatively higher convergences as in the main drift for excavation. As it can be seen in Figure 6.-3, the main drift for waste transport is also comparatively warmer as the drift for structural part limits the heat propagation towards the main drift for excavation. It results from this different compaction evolution that 30 years after the disposal, the porosity reaches 0.1 in the main drift for waste compared to 0.15 in the main drift for excavation. Nevertheless, the compaction is completed in the two main drifts at time=50 years.

Table 6.-7: Computed porosity in different drifts in the cross section.

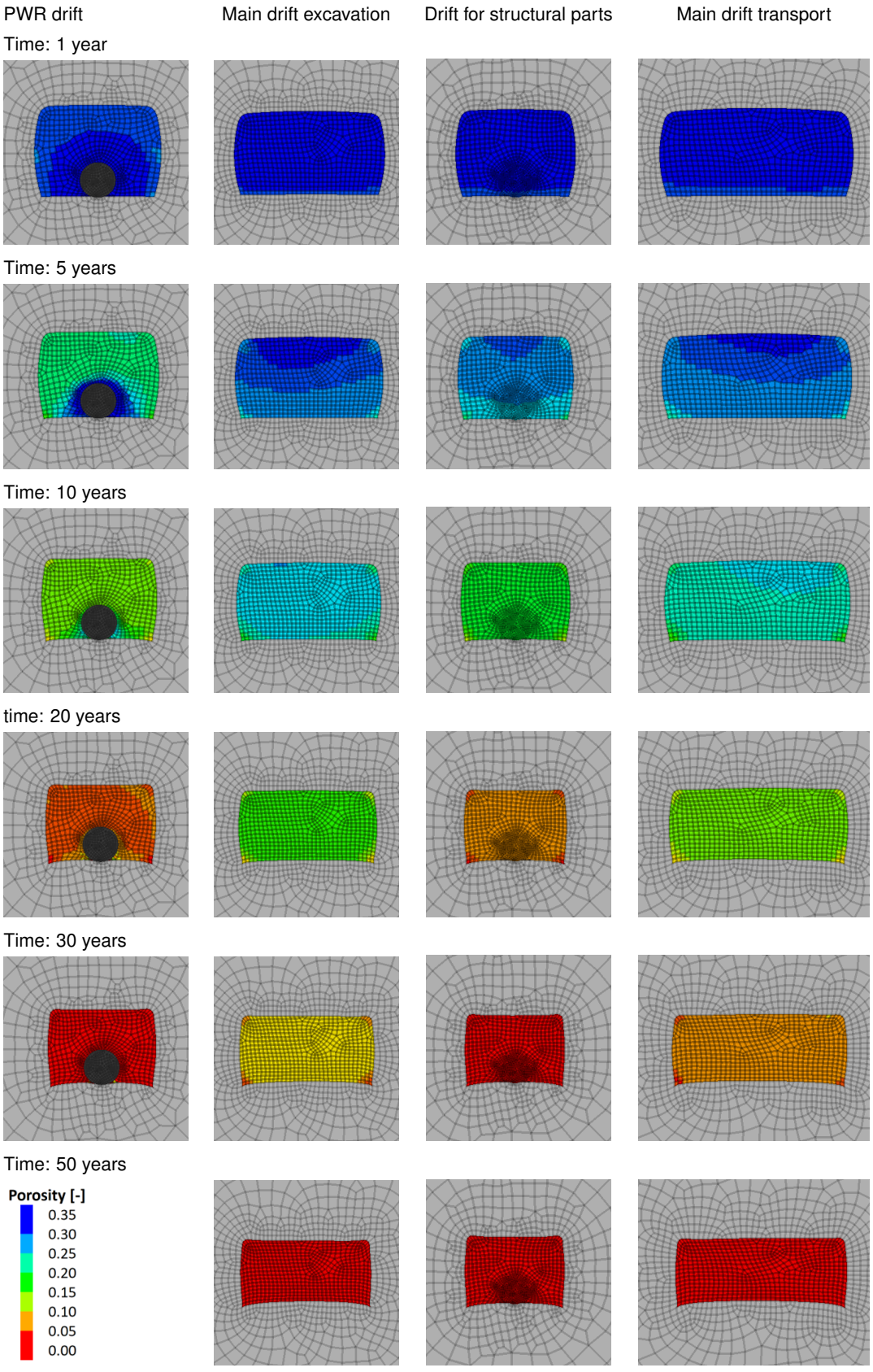

Figure 6.-4 shows the quantitative evolution of the porosity evolution over the time in all the drifts in the considered cross section. For comparison, the porosity results of the analysis of a PWR disposal drift (previous section) is also plotted in the figure. The figure shows that faster compaction for PWR drifts are obtained using single drift model as using the cross section. The reason for this discrepancy lies in the homogenization of the heat power required for this 2D plain strain analysis leading to a temperature maximum of around 100℃ compared to 200℃ in the more precise single drift modelling. All disposal drifts with PWR in the cross section compact similarly as can be seen in the narrow band under which all porosity curves fall. Only the two disposal drifts located at the edges of the emplacement field next to the main drift take comparatively longer to compact. This clearly shows the effect of temperature as the only reason of this time delay in the compaction of these two drifts is due to the fact that these two drifts remains relatively colder due to their location. The figure also shows that the crushed salt in the drift for structural drift will take longer to compact compared to the PWR drifts. Some decades are necessary to complete the compaction in the main excavation drift and the transport drift. These results show that in the repository concept considered in this study a fast compaction is to be expected due to the the high temperature in the repository. It should be mentioned that the results from this simulation are pessimistic compared to a more precise 3D modeling as the comparison with the PWR single disposal drift modeling shows. Nevertheless, considering the repository lifetime of one million years, it can be derived from this simulation that the compaction process will be accomplished in the very early phase of the repository evolution. This means that the repository will be sealed and the radioactive waste will be confined quite early.

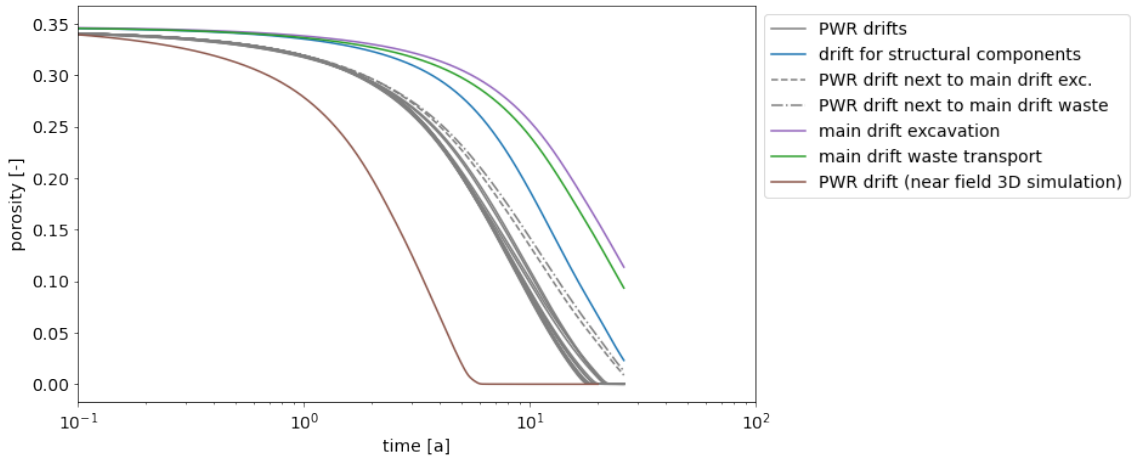

Figure 6.-4: Porosity evolution in all drift present in the considered cross section and in the single PWR disposal drift (previous section).

6.4 Crushed salt compaction in a whole repository mine

With the previous 2D approach, it is not possible to determine the compaction evolution in the drifts located away from the disposal fields. This is especially the case for the cross cuts, the main drifts or the long term seal in the drift sealing system. The compaction at this location are of importance to characterize when the repository will be ultimately sealed. To better estimate of the spatial evolution of the compaction in the repository, a 3D modeling approach was considered.

The model uses of a domain representing one-quarter of the repository system. This domain includes the half of the three emplacement fields located in the Southern wing of the repository, where PWR spent fuel waste packages are disposed. The model domain also includes one of the four drift sealing systems allowing estimation of when this seal will take on its sealing function. The model domain is limited to one-quarter because of the huge computational cost associated with this simulation. In fact, the numerical model to be developed should accurately capture both the stress development and thermal expansion in the near field of the drifts backfilled with crushed salt. At the same time, it is also necessary to model the geological layers surrounding the salt pillow. The interaction between the geological layers capable of creep and those that behave rigidly, especially taking into account the complexity of the geological formation under consideration, is important to better account for the convergence of the rock. This requires a model that spans several square kilometers yet consists of centimeter-sized finite elements in relevant areas. To handle this complexity, several simplifications were made.

The containers themselves are not modeled discretely. Instead, the total heat output from all containers within a disposal drifts is summed and applied as a thermal volume load. The assumed volume is equivalent to the volume of the drift. All drifts are modeled with a rectangular cross-section. The geological units above and below the shallow rock salt formation are discretized as coarsely as possible while still allowing the different stiffnesses of the layers to be taken into account. A uniform density of 2200 kg/m³ is considered in the model, while symmetrical boundary conditions are applied, modeling only a quarter of the repository. Standard displacement and adiabatic boundary conditions were applied at the model boundaries. The lateral boundaries are 1.5 to 2 km away from the repository to avoid boundary effects. The numerical model contains 3 million elements. The finite element sizes range from 20 cm near the drifts to 100 m in the overburden. In Figure 6.-5, the numerical model is shown.

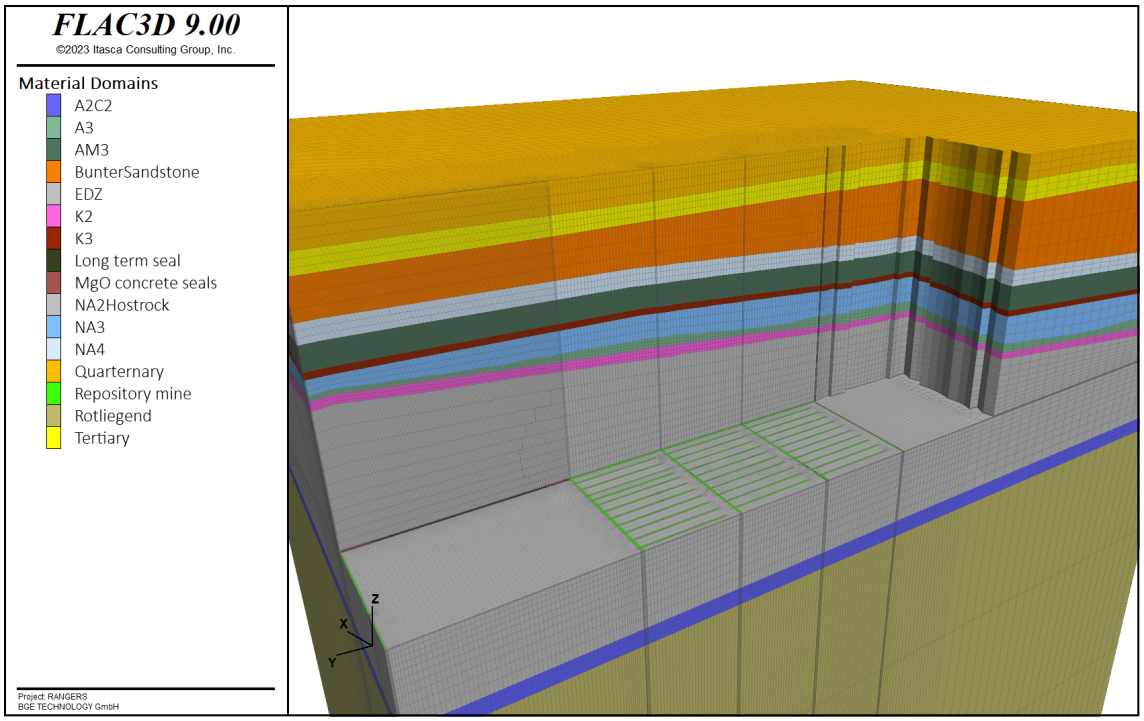

Figure 6.-5: Isometric view of the numerical model with ≈ 3 million elements for the analysis of the compaction of the crushed salt backfilled in the repository.

The material behavior of rock salt and crushed salt was implemented according to the material models presented in section 6.1. The other model units were modeled elastically or elasto-plastically, with their stiffnesses considered accordingly. The mechanical material parameters of those layers will be described in more detailed in Chapter 7.. The thermal parameters of the geological units were already reported in Table 4.-2.

The simulation begins by initializing the primary state, followed by the instantaneous excavation of the drifts in the mine. Sequential backfilling continues until the mine is completely closed. The backfilling starts 20 years after excavation for the Southern emplacement wing, as prescribed in the repository concept. Every five years, one emplacement field is backfilled and thermally activated. After the backfilling of the disposal drifts, the cross drifts and the section of the main drift are closed 30 years after the beginning of the excavation.

An isotropic primary stress state is presumed, with a consistent density of 2200 kg/m³ for the overlying layers. This results in an estimated depth pressure of about 18.5 MPa at the disposal level. For undisturbed rock temperature, a temperature gradient of 9 K per 100 m is used, leading to a disposal depth temperature of 38.67 °C. A constant air temperature of 9 °C is maintained at the upper boundary of the model. On the ground surface, a convective heat flux (q_c) is incorporated with a heat transfer coefficient (α = 8.7 W m^{-2} K^{-1}) according to Bertrams et al. (2020).

The results of this simulation are presented in Figure 6.-6 and Figure 6.-7.

In Figure 6.-6, the distribution of porosity across the repository mine is depicted. At 30 years, the emplacement fields have been backfilled with crushed salt. Initially, the porosity in the

drifts after backfilling is approximately 35%. The effect of sequential backfilling is particularly evident in the first emplacement drift on the right-hand side, where porosity begins to decrease, showing values below 30% in the center of the field where the temperature is highest. This drift was the first in the wing to be backfilled, 20 years after the start of the backfilling operations. The middle emplacement field, backfilled at year 25, does not yet show significant compaction, and similarly, the most recent field, just backfilled at year 30, exhibits no notable compaction.

Ten years later, the compaction in all fields has significantly progressed. In all fields, porosity has reduced to at least 20%. The lowest porosity values, ranging from 5% to 10%, are observed in the center of the fields where heat generation is most intense. Similarly, in the main and cross drifts, which were backfilled right after the emplacement fields were closed, porosity evolution mirrors that of the emplacement drifts. In the cross drifts, the porosity follows a pattern similar to that at the edges of the emplacement drifts, while in the main drift, the lowest porosity values are observed along the center of each field.

By year 69, compaction has largely completed in most of the drifts, with porosity reaching near-zero values, except for the drifts at the edges of the emplacement fields and the drift containing non-heat-generating structural components. After 100 years from the start of backfilling, compaction across the emplacement zone is nearly complete. Only in the main drift and its intersections with cross drifts does porosity continue to evolve, showing values between 5% and 10%.

In Figure 6.-6, it is evident that the porosity in the long-term seal at the edge of the emplacement zone is progressively decreasing, reaching values between 15% and 25%, 100 years after backfilling. A detailed view of the porosity evolution in the long-term seal is provided in Figure 6.-7 shows the reconsolidation of the crushed salt seal between the MgO seals (in magenta) from 100 to 750 years after backfilling. The figure illustrates the compaction progression from the emplacement side (right) toward the shaft side (left). This is clearly noticeable in the porosity distribution at 200 and 300 years. This compaction progression reflects the heat propagation from the emplacement fields. By year 400, porosity in the seal has nearly reached zero. After 700 to 750 years, compaction of the long-term seal is effectively complete, with only small pockets near the MgO seals showing porosity above zero, likely due to the assumed rigid contact between the MgO concrete and the crushed salt/clay mixture. A more accurate representation of this interface would require the use of interface elements in the model.

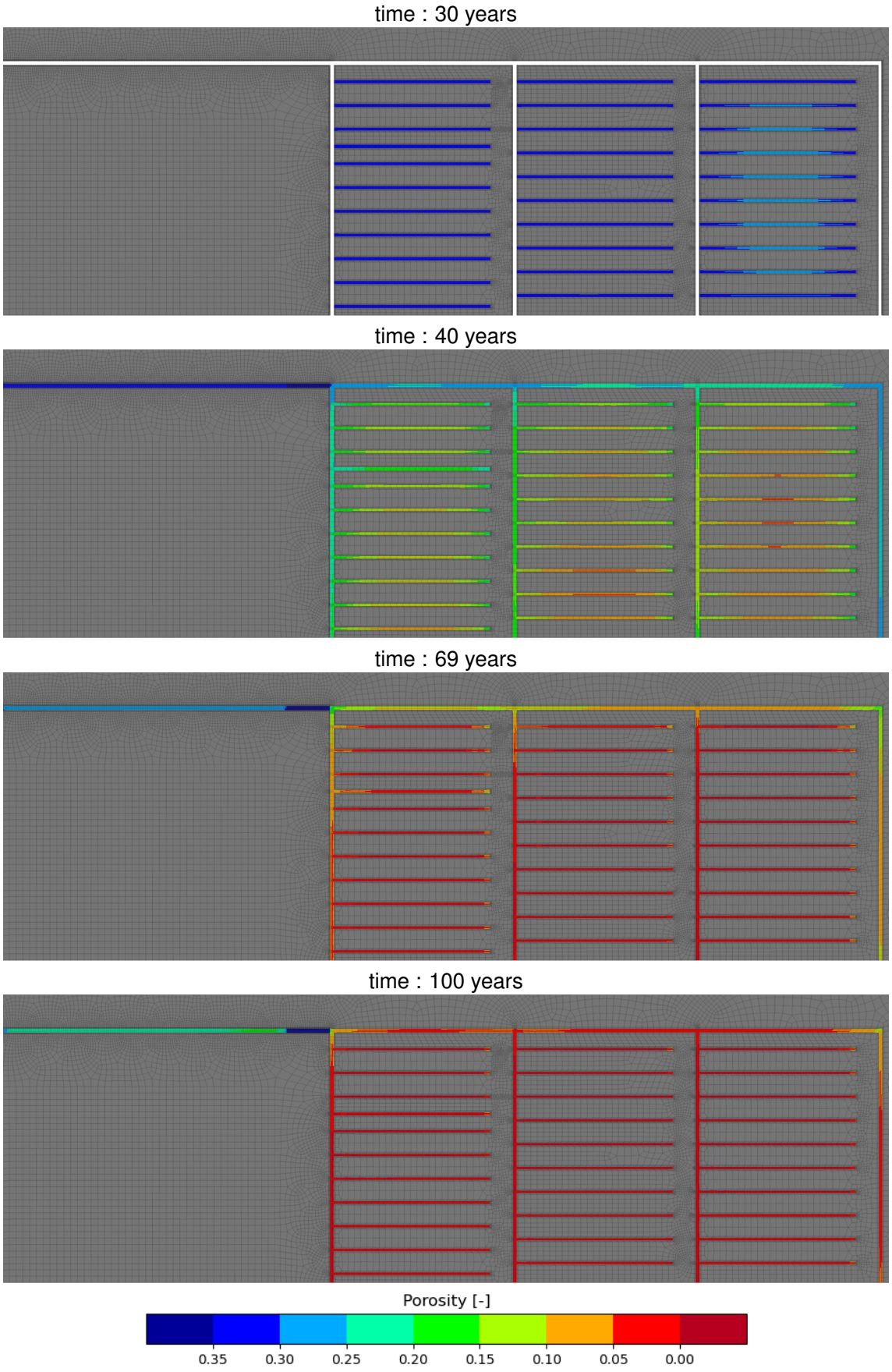

Figure 6.-6: Compaction evolution in the repository after 100 years.

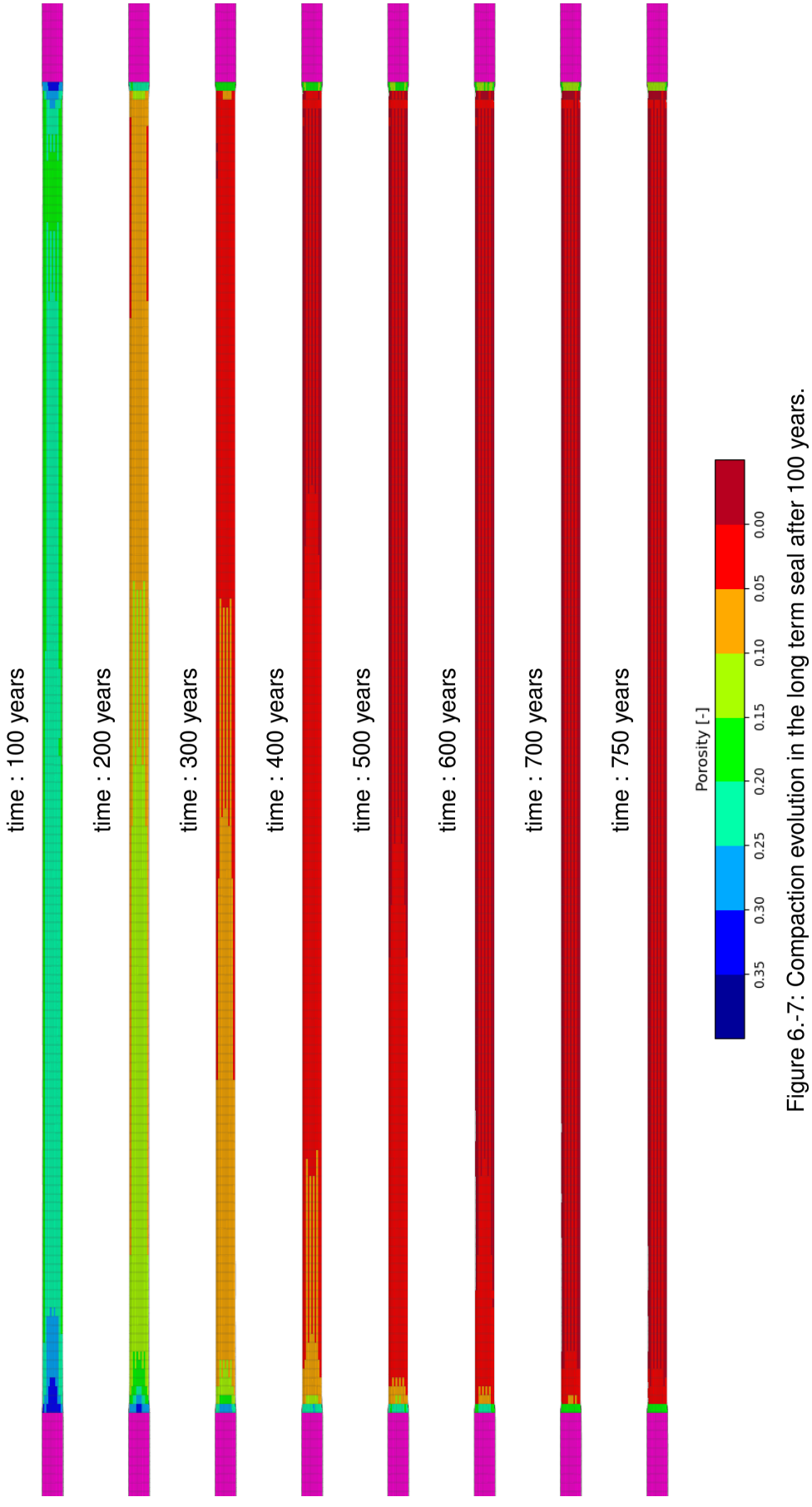

Figure 6.-7: Compaction evolution in the long term seal after 100 years.

A quantitative analysis of the porosity through time in the 3D model is presented in Figure 6.-8. The figure shows the average porosity in all modeled drifts. All drifts from each emplacement field are put in a category and are plotted with the same color.

to be continued

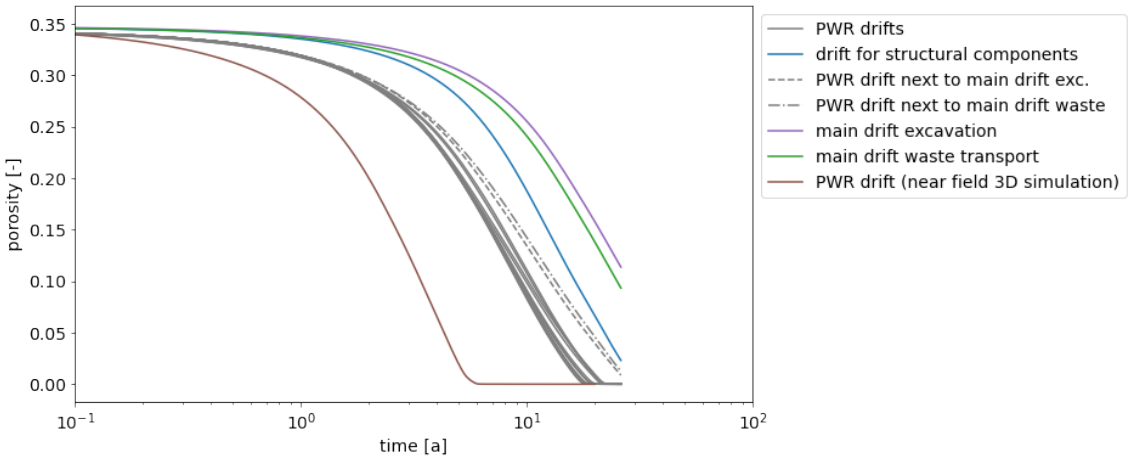

Figure 6.-8: Porosity evolution in all drift present in the considered cross section and in the single PWR disposal drift (previous section).

6.5 Summary: Evolution of crushed salt compaction in a repository mine

The long-term containment of radionuclides in a salt repository relies heavily on the effectiveness of multiple barriers, including the reconsolidating crushed salt backfill, which serves as a long-term sealing element. The crushed salt gradually compacts due to lithostatic pressure, eventually reducing its porosity and permeability to levels that prevent the inflow of solutions to the waste packages. Understanding the compaction behavior of crushed salt is crucial for safety assessments.

This study analyzed the compaction behavior of crushed salt under the thermal-mechanical conditions of a repository. Various modeling approaches were employed to predict how crushed salt compacts over time in different areas of the repository mine. The compaction was assessed for both hot and cold repository zones, including disposal drifts and main drifts.

Key findings include:

- **Early compaction**: In drifts containing heat-generating waste (e.g., POLLUX casks), compaction occurs rapidly due to high temperatures (up to 200℃). In these areas, porosity can decrease from 35% to near zero within 5 to 30 years depending on the modeling approach, completing the compaction process relatively quickly.
- **Gradual compaction in colder drifts**: In drifts with structural components and main access drifts, where heat is less intense, compaction occurs more slowly. These areas may take several decades to reach full compaction, but the process still occurs well within the repository's operational timeline.
- **Long-term seal**: After 100 years, the long-term seal at the edges of the repository also shows substantial compaction, with porosity nearing zero after 700 to 750 years. This

compaction ensures the repository's effective sealing over the long term, aiding in the isolation of radioactive waste.

The results from these simulations highlight that the compaction process in salt repositories is well-understood and predictable. The use of crushed salt as a backfill material provides an effective long-term sealing mechanism, significantly contributing to the repository's overall safety and containment performance. Moreover, the rapid compaction of the crushed salt in thermally active zones suggests that sealing functions are achieved early in the repository's life cycle, providing confidence in the long-term isolation of radioactive waste.

This study confirms that the compaction process, although influenced by varying thermal and mechanical conditions, is completed early in the repository's operational phase, thereby ensuring the long-term safety and containment of radioactive waste in salt-based repositories.

The primary result of this analysis is that the confinement of radioactive waste in salt repositories is achieved relatively early in the repository's life cycle. This has several important implications:

- Since the long-term seal is projected to achieve its full functionality within less than 1,000 years, based on the simulation results, the required functional lifetime of the EBS could potentially be reduced to just a few thousand years, rather than the previously assumed 50,000 years.
- To better define the requires lifetime of the EBS, it is essential to use advanced and highly accurate constitutive material models for crushed salt and crushed salt clay mixtures. Only with precise modeling can the uncertainties regarding the longevity of the EBS be minimized.
- To further reduce uncertainty, it is advisable to use a high temperature limit in the repository design. The current limit of 200 °C has proven effective and is therefore recommended for future salt repositories.
- Given that a substantial portion of the repository reaches an advanced state of compaction during the operational phase, it is feasible to implement a monitoring system to ensure that the repository behaves as expected over time.
- Additionally, the early compaction behavior suggests that it can be tested under real conditions through field experiments in salt mines, spanning several decades. Similar long-term field experiments, such as those on bentonite seals, are already underway in various underground research laboratories around the world.

7. Mechanical Integrity Assessment of the Drift Seal

In the following section, the design and integrity of the drift sealing system in salt repositories are assessed based on the methodology developed within the RANGERS project. This exercise is an example performed for the specific drift sealing system designed in generic repository system developed in RANGERS, see (Simo et al., 2024).

7.1 Safety function

According to Kock et al. (2012), the drift seal as part of the EBS should prevent or limit the inflow of solutions until the crushed salt has compacted to the extent that it can take over the sealing function. Conservative estimates of the required period for salt compaction are up to a few thousand years. To cover this period, a significantly longer duration of functionality for the sealing structures is assumed. in actual considerations, the drift seals can remain their function up to the point where significant changes in the hydrogeological and hydrochemical conditions are taking place. Such significant changes in the boundary conditions can be expected in the next ice age (Müller-Hoeppe et al., 2012b). Under such conditions, the evolution of the sealing system is no longer predictable. Statements about the function of the shaft seals are therefore only possible for a period of about 50,000 years, and this period is assumed for the functional duration in the proof.

7.2 Design of the drift sealing system

The drift sealing system as designed in the scope of RANGERS consists of an assembly of abutments, drift seals, and the long-term crushed salt seal. In the repository presented here, four drift sealing systems are designed and are located in the two main drifts closing all access to the emplacement wings, see Figure 7.-1. The drift seals consider two sealing elements made of MgO-concrete. Both are bounded with concrete-based abutments to guarantee mechanical stability and fix their positions. Here also, for reason of geochemical stability, MgO-concrete is considered for the abutments. All elements are placed in a row, with direct contact to the rock. Kock et al. (2012) recommends the EDZ is removed to the extent possible immediately before the installation drift sealing system. In the construction location, the extent of the EDZ is expected to be between 10 and 30 cm. The possibly remaining residual damage zone can also be sealed by injections if necessary. In between the sequence of sealing elements and abutments, an additional long-term sealing element is considered. This sealing element is made of crushed salt that has been enriched with some clay admixtures. This clay partially fills the pores in the crushed salt, reduces its permeability at the early stages of compaction, and help the mixture to reach a fully compacted state much faster. The effectiveness of this novel material made of crushed salt and clay still need to be shown. For this study, the behavior of pure crushed salt is assumed for the long term seal. The long term seal is installed over a length of 300 m between the drift seals. The MgO concrete seals themselves have a length of 115 m including the abutments. Figure 7.-2 illustrate the design of the proposed drift sealing system install in the main drifts.

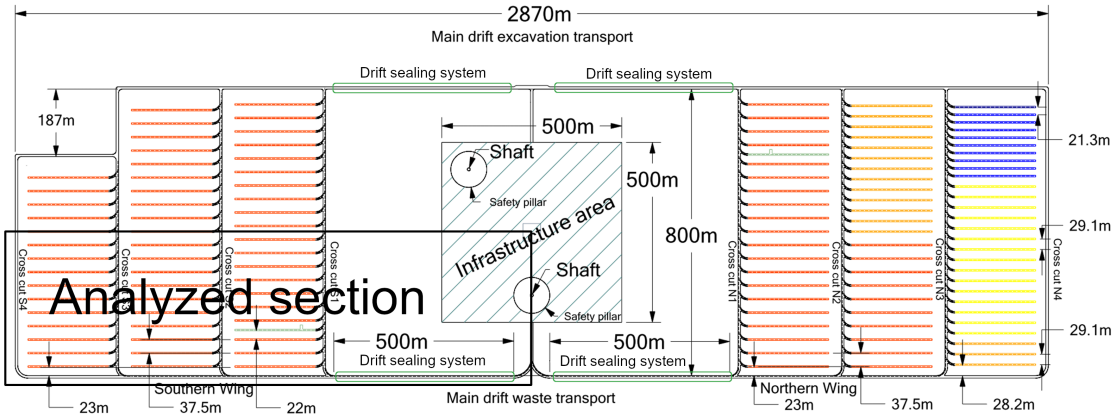

Figure 7.-1: Location of the drift sealing system in the repository mine.

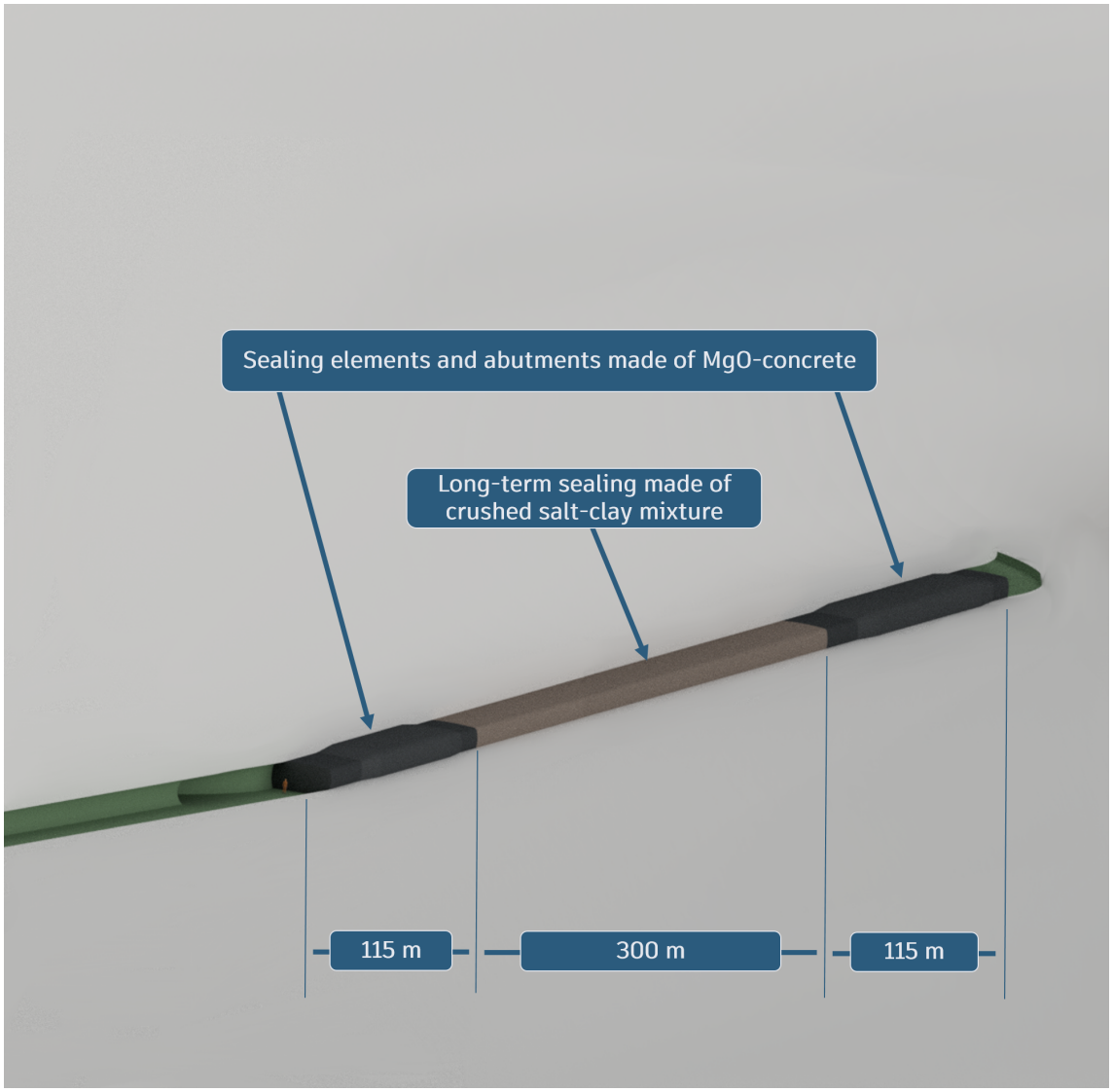

Figure 7.-2: Illustration of the drift sealing concept as designed for the RANGERS case study.

7.3 Modeling cases

The integrity assessment is based on the loads derived from the scenario and Features, Events, and Processes (FEP) development. The FEPs relevant for the mechanical integrity of the EBS were already discussed in Section 2.. These FEPs are summarized again for the drift sealing system in Figure 9.-1.

Thermal expansion and contraction, resulting from heat propagation within the repository, are among the primary loading conditions on the drift sealing system, aside from lithostatic load. The combination of heat flow and the convergence of the surrounding rock leads to mechanical stress changes throughout the repository, creating significant load scenarios that must be accounted for in the integrity assessment. Additionally, time-dependent processes such as swelling, shrinking, and creeping of the MgO-concrete used in the seals affect their resistance and must also be considered.

Over the course of the repository's evolution, hydraulic changes may arise due to gas pressure build-up caused by the compression of enclosed mine air and gas generation (in the reference scenario). Alternatively, a failure of the shaft seal and subsequent water inflow through the shaft or host rock (in an alternative scenario) could also lead to significant hydraulic pressure changes. These hydraulic changes are mainly driven by liquid and gas flow processes and liquid inflow into the repository. Seismic events, such as earthquakes, must also be considered, especially given the long functional lifetime of the EBS (50,000 years), during which even rare events are eventually likely to happen. In the case of gas explosions or deflagrations, the dynamic forces generated would propagate through the rock in a manner similar to that of a seismic event, exerting comparable mechanical stresses on the repository and therefore on the drift sealing system.

The FEPs in gray in the figure are considered not relevant for the integrity proof of the drift sealing system for the following reasons:

- Thermal degradation of carnallite: This process is specific to certain minerals that are not present in the drift seals and in the host rock at the disposal depth, and therefore it does not directly affect the integrity of the sealing system.
- Liquid flow processes: While hydraulic pressure changes are relevant, liquid flow through pathways that do not directly intersect the seals is not a primary concern for the mechanical integrity of the drift sealing system.
- Gas flow processes: Although gas pressure build-up is considered, the actual gas flow mechanisms through other parts of the repository do not significantly impact the integrity of seals.
- Metal corrosion: This is relevant for metallic components within the repository, but not for the drift seals themselves, which are made of MgO-concrete and other non-metallic materials.
- Solution, transformation of clay minerals: This process concerns the alteration of clay minerals, which are not a component of the MgO-concrete used in the drift seals.
- Microbial processes: Microbial activity is unlikely to have any meaningful impact on the structural integrity of the drift seals, as it primarily affects organic materials or metals,

not concrete-based sealing systems.

- Alteration of bentonite: Bentonite, commonly relied upon in other repository designs, is not part of the drift sealing system in this context, making its alteration irrelevant for the seals.
- Colloid generation and filtration: This concerns the behavior of colloidal particles in solution, which does not directly affect the mechanical integrity of the drift seals.
- Dissolution and precipitation of salt minerals: These processes primarily affect the surrounding rock salt and do not directly influence the integrity of the concrete drift seals.
- Asphalt migration: Asphalt is not a material used in the drift seals, and thus, its migration does not affect the integrity of these barriers.

By excluding these gray FEPs, we focus on the processes and scenarios that are expected to have a direct impact on the mechanical integrity of the drift seals and are most critical for the long-term safety of the repository.

From the discussions of the FEPs relevant for the drift seal, one can derive the following modeling cases to be considered in the design and integrity assessment of the drift sealing system:

- Modeling case 1: Thermal-mechanical loading on the drift seals: consideration of the FEPs heat flow, thermal expansion/contraction, mechanical stress changes, and convergence
- Modeling case 2: Thermal-mechanical loading of the drift seals with alteration of concrete: in addition to the already enumerated FEPs, the FEP swelling, shrinking and creeping of MgO-concrete are considered
- Modeling case 3: Thermal-mechanical loading with gas pressure built up: consideration of gas effects acting on the drift seal (FEPs: hydraulic pressure change)
- Modeling case 4: Thermal-mechanical loading combined with an earthquake event
- Modeling case 5: Thermal-mechanical loading with hydrostatic loading following the failure of the shaft seal (alternative scenario)

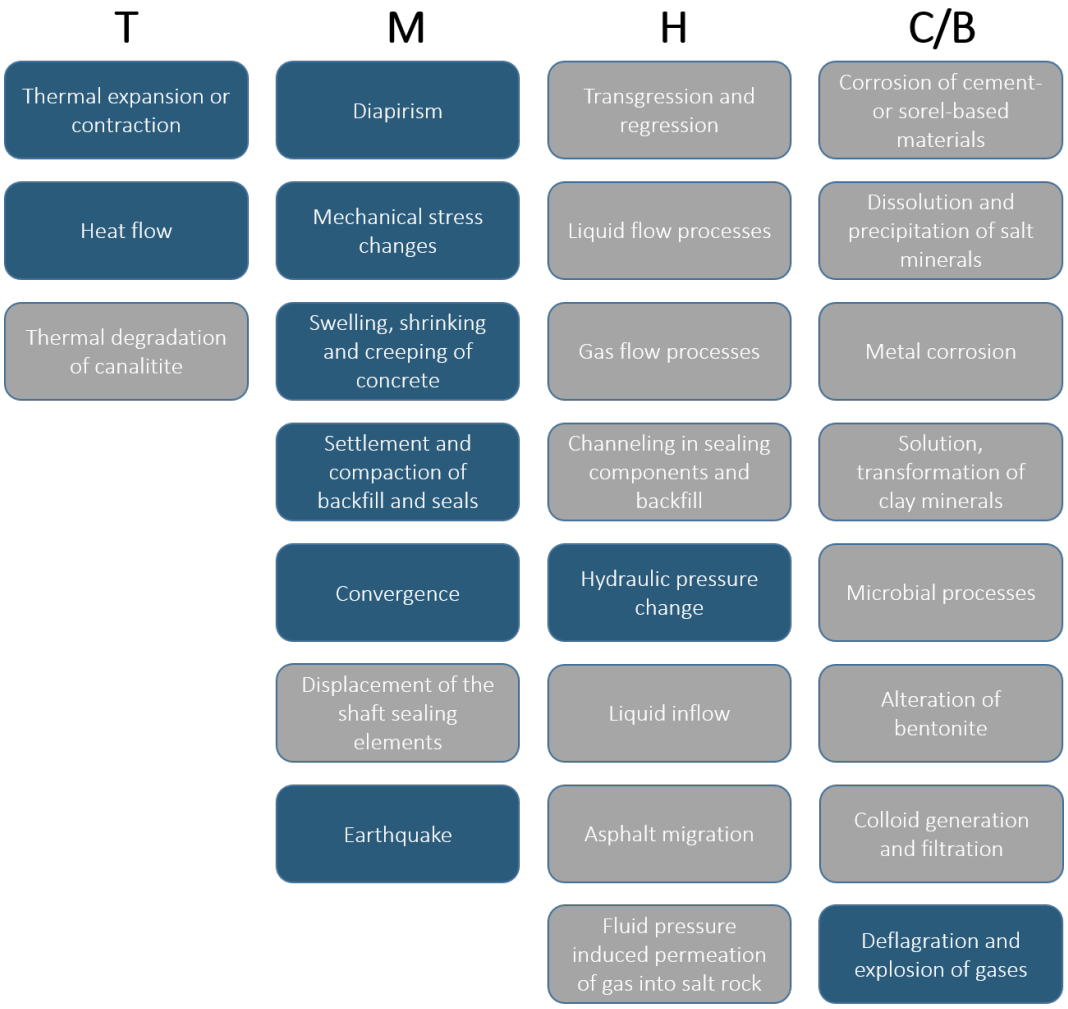

Figure 7.-3: Initial FEPs of relevance for the mechanical integrity proof of the drift seals.

Other modeling cases can be derived as the combination of the selected ones above. The thermal-mechanical evolution, which is the integral effects resulting from gravitational forces, convergence and creep of the host rock as well as the heat propagation, can be considered as the permanent design situation and serves as the basis for combination with other FEPs or modeling cases. The interaction between the drift sealing system and the surrounding rock belongs also to the permanent design situation. Especially, Stresses and strains resulting from temperature increases at the contact zone need to be addressed.

In the presence of the adequate constitutive models, the time dependent behavior of the concrete materials can be also added to the permanent design situation. Autogenous swelling of the Sorel concrete is attributed to the construction phases and is therefore not considered. Solution-induced swelling does not occur, as there is only a negligible amount of solution present. (Müller-Hoeppe et al., 2012a).

The (hydraulic) load cases are occurring gradually over the time for the case of gas pressure build up. As the shaft seal is assumed to retain its function over the verification period, an inflow of water followed by a rise of fluid pressure at the edge of the drift seal can only be

considered in the scope of the alternative scenario analysis. The occurrence of earthquakes should also be considered in integrity assessment as such events will probably occur over the considered verification period of time.

In this study, the design and safety assessment will be exemplary demonstrated for the modeling case 1. Additional hydraulic analyses are required before modeling cases 3 and 5 can be analyzed. Adequate constitutive modeling is needed for the modeling of case 2. Dynamic analyses beyond the scope of RANGERS are needed for the seismic simulations in case 4.

7.4 Integrity safety concept and criteria

Five individual verification criteria have been formulated for the demonstration or verification of structural integrity. There are (Müller-Hoeppe et al., 2012b):

- Structural Stability (commonly referred to as “Load-bearing Capacity”)
- Crack Limitation
- Deformation Restriction
- Filter Stability
- Long-term Stability (also known as “Durability”)

From these criteria, the first two apply for the sealing material and can be combined by using adequate constitutive model for Sorel concrete which is the sole sealing material used in the drift sealing system. This will be described in more detail later on. The criterion of deformation restriction does not apply because there is no seal made of granular material that needs a confining volume to exercise its sealing function.

The absence of granular material also eliminates the need to verify the filter stability criterion. It should be mentioned that the long term seal made of crushed salt is installed in a granular state. This seal gains its function when it reaches a fully compacted solid state. No need to check the filter stability.

The long-term stability is covered in Chapter 5..

Specific requirements for the geological barriers in § 5 (2) of EndlSiAnfV (2020) applies for the contact zone between the elements of the drift sealing system and the host rock. The contact zone represents a critical path that need to be verified in order to secure the safe containment of the CRZ. Therefore the dilatancy criterion should be verified for the contact zone along the drift sealing system.

7.5 Numerical model

7.5.1 Modeling concept

The numerical model necessary to investigate the evolution of the drift seals accurately represent both the stress development and thermal propagation in the near field of the drift sealing system. Because the thermal sources are located in the emplacement field from which the

heat starts to propagate within the repository, it's necessary to have a model that explicitly consider the emplacement fields. Thus, the model must cover an area of several square kilometers while consisting of finite elements that are only centimeters in size in key areas. To handle this complexity, the following simplifications were made.

First, all the drifts in the model are simplified with a rectangular cross-section. The drift seals are instantaneously backfilled. This means that the pouring of the Sorel concrete made seals and the transient effects due to concrete hydration are not considered. The geological units above and below the rock salt formation are coarsely discretized which is sufficient to account for their weight and stiffness. Symmetrical boundary conditions were used, and only a quarter of the repository was modeled. The size of the finite elements varies in the model, ranging from 20 cm in the drift seals and gradually increases in the emplacement fields and in the overburden. The lateral boundaries are 1.5 to 2 km away from the repository, ensuring that minimal boundary effects are expected. The standard displacement and adiabatic boundary conditions were applied to the model boundaries.

The numerical model considered in this analysis is the one already used for the compaction analysis which also contains the drift sealing system. The cross section of the drift seal in this model consists of 11 by 5 subdivisions. In this model, all the drifts are resolved and are used as heat sources with the corresponding thermal power of all waste packages disposed in each drift. The model has been already presented in Figure 6.-5. A top view of this model at the level of disposal depth is shown in Figure 7.-4 with an emphasis on the drift sealing system.

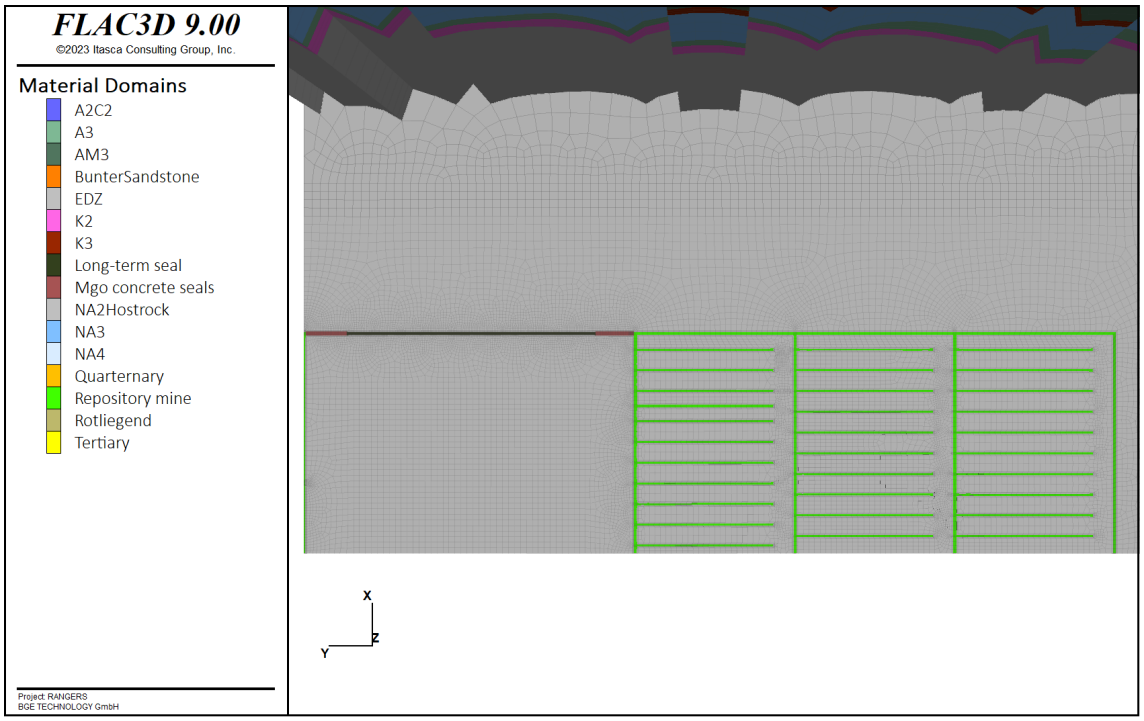

Figure 7.-4: Top view of the numerical model for the analysis of the mechanical integrity of the drift sealing system for the section depicted in Figure 7.-1.

The modeling stages account in the simulation starts with the initialization of the primary state. It follows the excavation of the drifts in the mine, which is carried out instantaneously. A sequential backfilling is realized up to the complete closure of the mine. Thus, the main

drift remains open over 30 years before the construction of the drift sealing system. Over the time, the convergence of the rock due to creep will compact all materials in the mine. This convergence process is further enhanced by the thermal propagation also considered in the model.

To limit the computational cost, the simulation was carried out thermal-mechanically over 1,200 years. This corresponds approximately to the end of the thermal phase of the repository evolution. Subsequently, the thermal phase is deactivated and the simulation continue in the mechanical process class. This allowed us to speed up the simulation by a factor of 10. The residual heat still present in the model at 1,200 years will enhanced the creeping behavior of the rock leading to more deformations and stresses on the drift sealing structure. This assumption is therefore conservative for the design of the drift seals.

7.5.2 Initial conditions

The drift sealing system is planned at the disposal level at a depth of 810 m in the Staßfurt sequence. An isotropic primary stress state is assumed, with an integral density of the overlying layers assumed to be 2.200 kg/m³. This results in a calculated depth pressure of approximately 18.5 MPa at the level of the disposal level. For the undisturbed rock temperature, the temperature gradient of 9 K/100 m is assumed resulting in a temperature of 38.67℃ at the disposal depth. At the upper boundary of the model, a constant air temperature of 9℃ is assumed. At the ground surface, a convective heat flux q_c is considered with a heat transfer coefficient of α = 8.7 $Wm^{-2}K^{-1}$ according to Bertrams et al. (2020). Thermally, the disposal of waste is represented by a transient heat source. Each disposal drift serves as heat source with the thermal power of the sum of the heat power of the disposal waste emplaced in each drift.

7.5.3 Constitutive models

Different constitutive models are essential to accurately represent the complex behavior of the repository system, with a specific focus on the drift sealing system. Figure 7.-5 illustrates a cross-sectional view of a geological repository, where various geological layers and materials are assigned distinct constitutive models based on their mechanical properties.

The overburden, composed of Quaternary, Tertiary, and Bunter sandstone layers, is modeled using the Mohr-Coulomb failure criterion, appropriate for sandy materials. For the salt formations, different creep laws derived from the WIPP creep law are applied to capture the viscoplastic behavior of the salt under long-term loading conditions. FLAC3D is used for this analysis, the WIPP creep law is implemented in it already.

The main anhydrite layer, which is typically found in a fractured or broken state due to stresses caused by salt diapirism, is modeled using a reduced stiffness to reflect its brittle nature. Its plastic behavior is also simulated using the Mohr-Coulomb model, which is suitable for materials that undergo shear failure under stress.

The underburden below the salt is treated with an elastic constitutive model. Since this region is located far from the point of interest — the drift sealing system — modeling it elastically is a sufficient and efficient approximation for the purposes of this analysis.

Table 7.-1 summarizes the different constitutive models for the geological layers with their elastic material properties. The recommended creep classes for the different salt layers are given in Table 7.-2. The parameters for the creep laws BRGa and BGRb are summarizes in Table 7.-3 and in 7.-4. The Mohr-Coulomb parameters of the overburden layers and main anhydrite can be found in Table 7.-5.

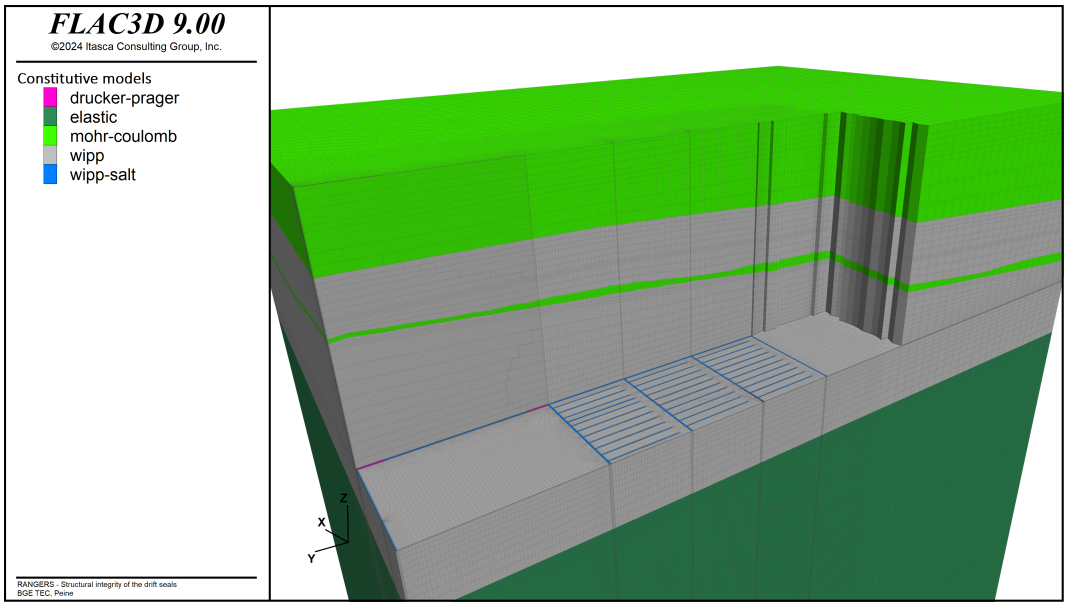

Figure 7.-5: Distribution of constitutive models used in the numerical model for the integrity assessment of the drift seals.

Table 7.-1: Mechanical properties and density of geological layers.

Model zones	**Symbol**	**Constitutive Model**	**Density** ρ (kg/m^3)	**Young's modulus** E (GPa)	**Poisson ratio** ν
Quaternary	Q	Mohr-Coulomb	2000	0.1	0.33
Tertiary	T	Mohr-Coulomb	2100	0.5	0.33
Bunter	S	Mohr-Coulomb	2500	15	0.27
Aller rock salt	NA4	wipp, BGR[a]	2235	25	0.27
Anhydritmittelsalz	AM3	wipp, BGR[a]	2275	30	0.27
Potash seam Ronnenberg	K3	wipp, BGRSF	1850	16	0.26
Leine rock salt	NA3	wipp, BGR[a]	2160	25	0.25
Main anhydrite	A3	Mohr-Coulomb	2700	60	0.25
Potash seam Staßfurt	K2	wipp, BGRSF	1850	17	0.28
Staßfurt rock salt	NA2	wipp, BGR[b]	2160	33	0.25
Anhydrite/carbonate	A2/C2	elastic	2700	30	0.27
Underlying red	R	elastic	2500	17	0.27

Table 7.-2: Recommended formula for geological zones.

Homogeneous zones	**Symbol**	**Recommended formula (with Prefix Factor)**
Aller rock salt	NA4	$\frac{1}{8} \cdot$ BGR[a]
Anhydritmittelsalz	AM3	$\frac{1}{16} \cdot$ BGR[a]
Potash seam Ronnenberg	K3	BGR[a]
Leine rock salt	NA3	$\frac{1}{4} \cdot$ BGR[a]
Potash seam Staßfurt	K2	BGR[a]
Staßfurt rock salt	NA2	$2 \cdot$ BGR[b]

Table 7.-3: BGR[a] parameters for rock salt.

Material parameter	**Symbol**	**Value**	**Unit**
Gas constant	R	8.31441	[J/mol*K]
Activation Energy	Q	5.40E+04	[J/mol]
WIPP_Model constant	A	0	[-]
WIPP_Model constant	B	0	[-]
Critical steady-state creep rate	-	-0.01	[1/s]
Strukturfaktor WIPP_Model constant	D	0.18	[MPa^{-n-d-1}]
WIPP_Model exponent	n	5	[-]

Table 7.-4: BGR[b] parameters for rock salt.

Material parameter	**Symbol**	**Value**	**Unit**
Creep rate	crfac	$2 * 5.872$	[-]
Activation Energy	Q1	4.20E+04	[J/mol]
Activation Energy	Q2	1.13E+05	[J/mol]
WIPP_Model constant	A	0	[-]
WIPP_Model constant	B	0	[-]
Critical steady-state creep rate	ε_{dot}	-0.01	[1/s]
Structural factor D	dwipp	0.18	[-]
WIPP_Model constant	d1wipp	2.30E-04	[$MPa^{-n} \cdot d^{-1}$]
WIPP_Model constant	d2wipp	2.10E+06	[$MPa^{-n} \cdot d^{-1}$]
WIPP_Model exponent	nwipp	5	[-]

Table 7.-5: Mohr-Coulomb parameters of the overburden layers and main anhydrite.

Homogeneous zones	**Symbol**	**Cohesion, c** [MPa]	**Friction angle,** ϕ [°]	**Tension limit,** σ_t [MPa]
Quaternary	Q	2	27.5	0.1
Tertiary	T	5	30	0.1
Bunter	S	4	15	0.1
Main anhydrite	A3	20	35	0.1

The repository mine will be backfilled with crushed salt. It is also planned to use a mixture of crushed salt and clay for the main sealing element in between the Sorel concrete seals. In the absence of experimental data and model available to describe this novel material, we assume for the time being that the behavior of this material is similar to crushed salt (but it will likely have lower permeability at early times). In this regard, the crushed salt model presented in Table 6.-3 is also used here for the materials in the model made of crushed salt.

An advanced constitutive model for Sorel concrete has been developed at BGE and BGE TECHNOLOGY for the license application of the Morsleben mine. This model assumes a Drucker-Prager yield surface for plasticity. The viscoelastic part of the model is described rheologically by the Burgers model. The Burgers model consists of a Maxwell element and a Kelvin element. The Maxwell element is a series connection of spring and damper elements and describes the instantaneous elasticity along with the basic creep, while the Kelvin element is a parallel connection of spring and damper elements and describes the transient creep. The rheology of the model is presented in Figure 7.-6. An associated thermal part is described in (Itasca Consulting Group, Inc., 2021). The solution of thermal and mechanical process classes is based on a weak coupling, meaning there is not a single system of equations to be solved, but rather two separate systems of equations, each solved independently. The model has been validated against experimental data, see Figure 7.-7.

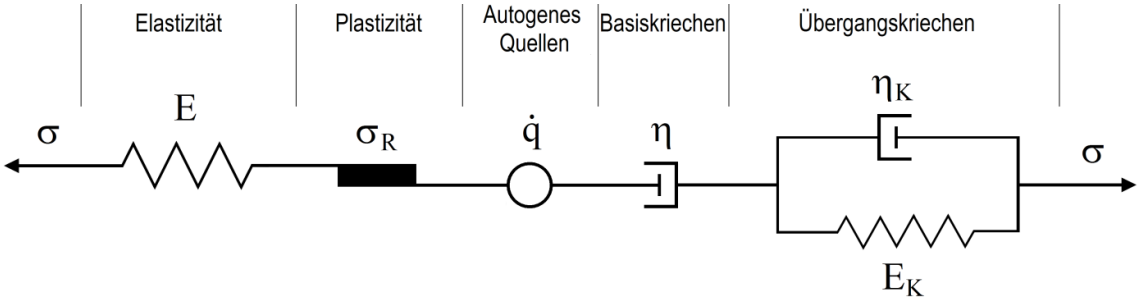

Figure 7.-6: Rheology of the constitutive model M2 for Sorel concrete.

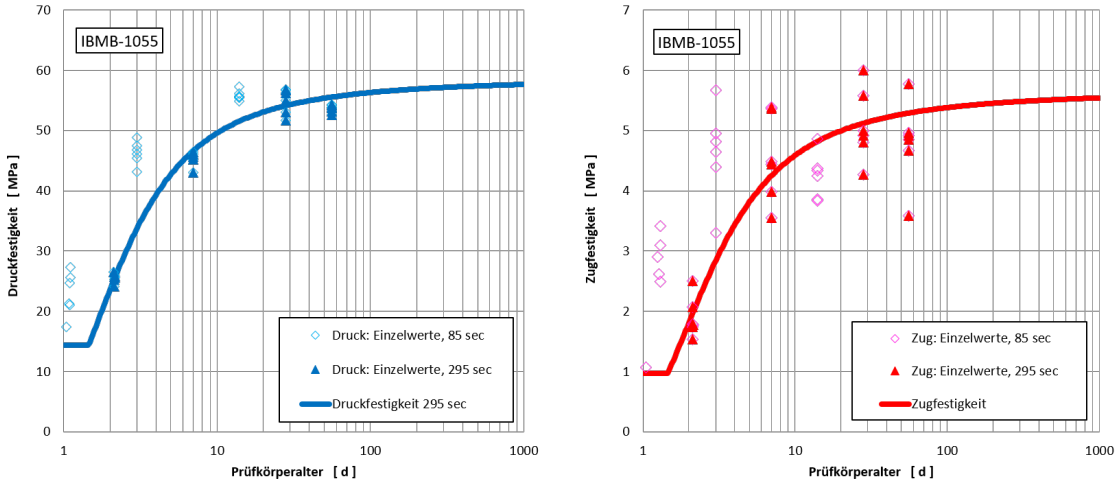

Figure 7.-7: Comparison between the model computation of compressive and tensile strength against experimental data for Sorel concrete.

The present analysis does not consider the transient effects occurring in the Sorel concrete from the pouring of the seal to its hardened state. We focus only on the long-term evolution

which is relevant for the safety case. In this case, the Drucker-Prager model from which the model is based can be used for this analysis. We therefore extracted from the initial model the Drucker-Prager parameters representing a concrete strength after 56 days which represent the long term strength of the Sorel concrete, see Table 7.-6. Further increase of concrete strength as it can be seen in Figure 7.-7 are conservatively neglected.

Table 7.-6: Drucker-Prager mechanical properties for Sorel concrete.

Property	**Value**
Density, ρ [kg/m^3]	1,900
Young's modulus, E [MPa]	20,333
Poisson's ratio, ν, [-]	0.372
Bulk modulus, K [MPa]	26,475.26
Shear modulus, G [MPa]	7,409.985
Friction-drucker, φ_φ	1.43
Cohesion-drucker, k_φ	5.6
Dilation-drucker, d_ψ	0
Tension limit, σ_t [MPa]	1.763333333

7.6 Numerical results

The loads acting on the drift sealing structures are the results of the thermal-mechanial evolution of the repository system. In order to understand how does load evolve, we will describe how each variable are evolving over the time.

7.6.1 Global displacements

The impacts of heat generated by the radioactive waste is one of the primary processes, alongside excavation-induced stress redistribution, that significantly affects the repository system. This was discussed in detail in chapter 4.. The impact of heat propagation on the displacement evolution at the disposal level is illustrated in Figures 7.-8, 7.-9, and 7.-10.

Figure 7.-8 presents the y-displacement in space at three times. Due to the heat generated in the disposal drifts, thermal expansion causes the surrounding rock to expand, which is evident from the displacement patterns in the first and third emplacement fields. The first emplacement field, located on the right side of the image, shows a clear expansion of the rock mass away from the emplacement. This results in displacement opposite to the y-axis for the first emplacement field, while for the third emplacement field, the displacement occurs along the positive y-axis.

In contrast, the second emplacement field shows minimal expansion. This is because the expansion of the adjacent first and third emplacement fields constrains the second field, effectively canceling out any significant deformation.

Over the time period from 100 to 1,400 years, the expansion of the rock mass becomes more pronounced, reaching its peak when the temperature is at its highest, as shown in Figure 4.-7. As the temperature starts to decrease, the expansion subsides, and the displacement gradually reduces.

The displacement along z-direction in Figure 7.-9 shows that the thermal expansion will cause an uplifting of the rock mass towards the surface. This uplifting process is concentrated over the emplacement fields and does not significantly affect the location where the drift sealing system is installed. Although the uplifting is still ongoing in the middle of the formation at 1,400 years, a recovery (i.e., decrease of displacement) can be observed at the disposal level at the emplacement fields between the time points of 700 and 1,400 years. Along the main drift, negative values of displacement are observed. They indicate the convergence of the rock compacting the crushed salt and long term seal in the drift.

The displacement along the x-direction, as shown in Figure 7.-10, highlights the effect of thermal expansion in that axis. Similar to the y-displacement, the rock mass expands at the disposal level, with the largest displacements occurring at the boundaries of the emplacement fields along the x-axis. This expansion extends towards the region where the drift sealing structures are installed, though moderate displacement values are observed there, gradually decreasing as the distance from the emplacement fields increases.

Notably, no displacement is seen at the center of the emplacement field located at the front of the model, which serves as a symmetrical boundary. At the top of the formation, significant displacements in the x-direction are observed, which result from the uplift process occurring in the z-direction. The presence of the anhydrite layer—a non-creeping material with high stiffness—appears to decouple the mechanical processes in the repository mine from those at the top of the formation.

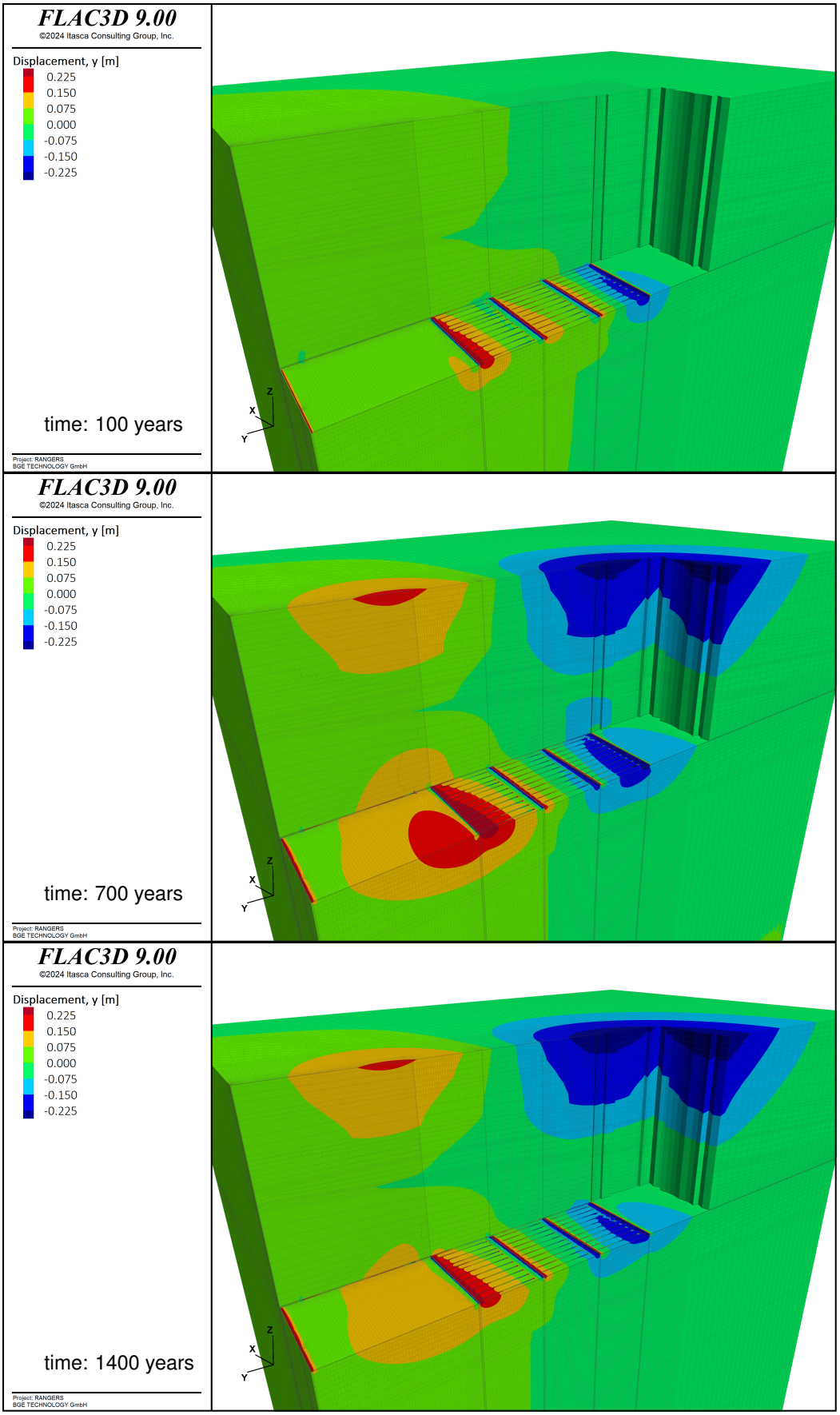

Figure 7.-8: Displacement distribution along the y-axis over time.

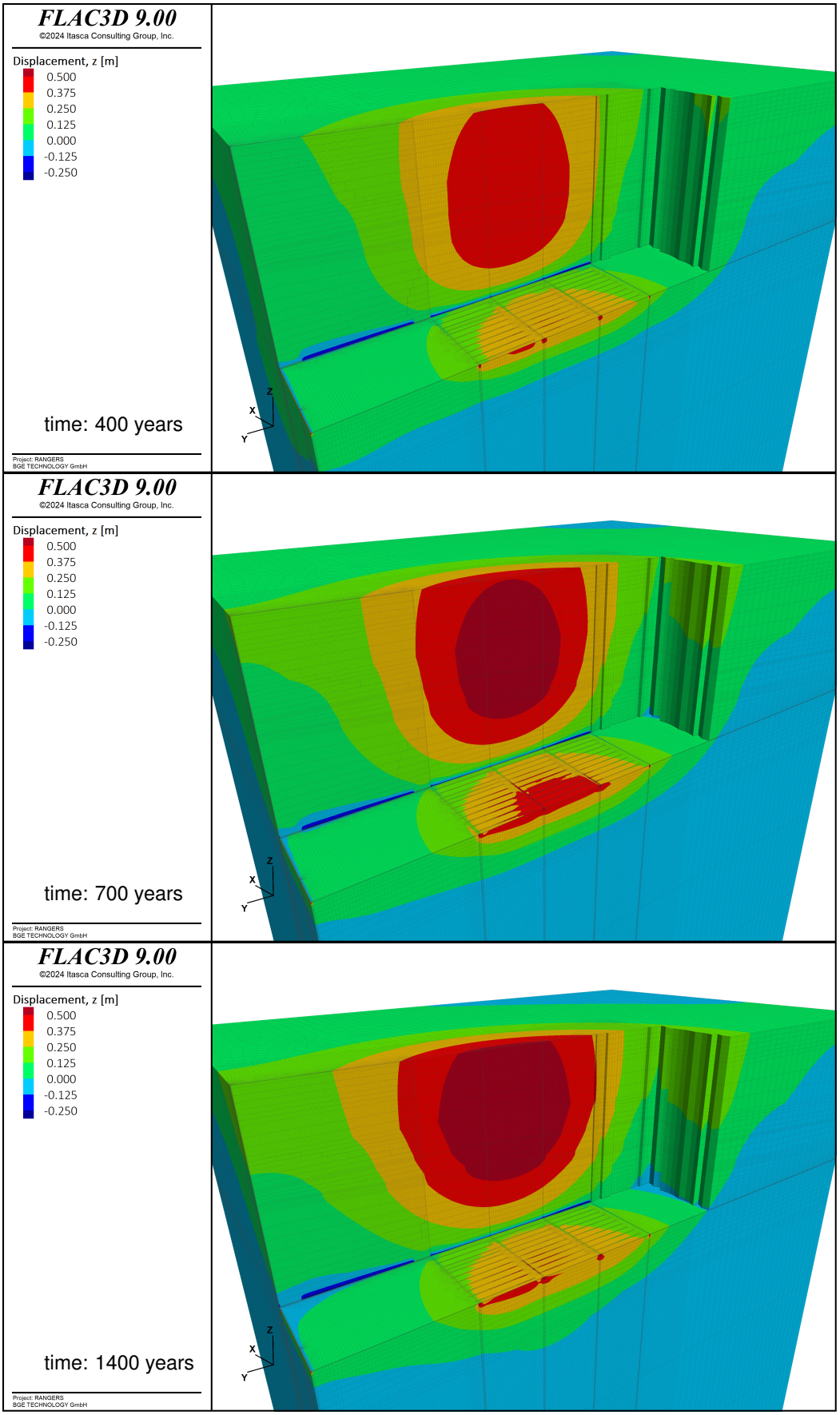

Figure 7.-9: Displacement distribution along the z-axis over time.

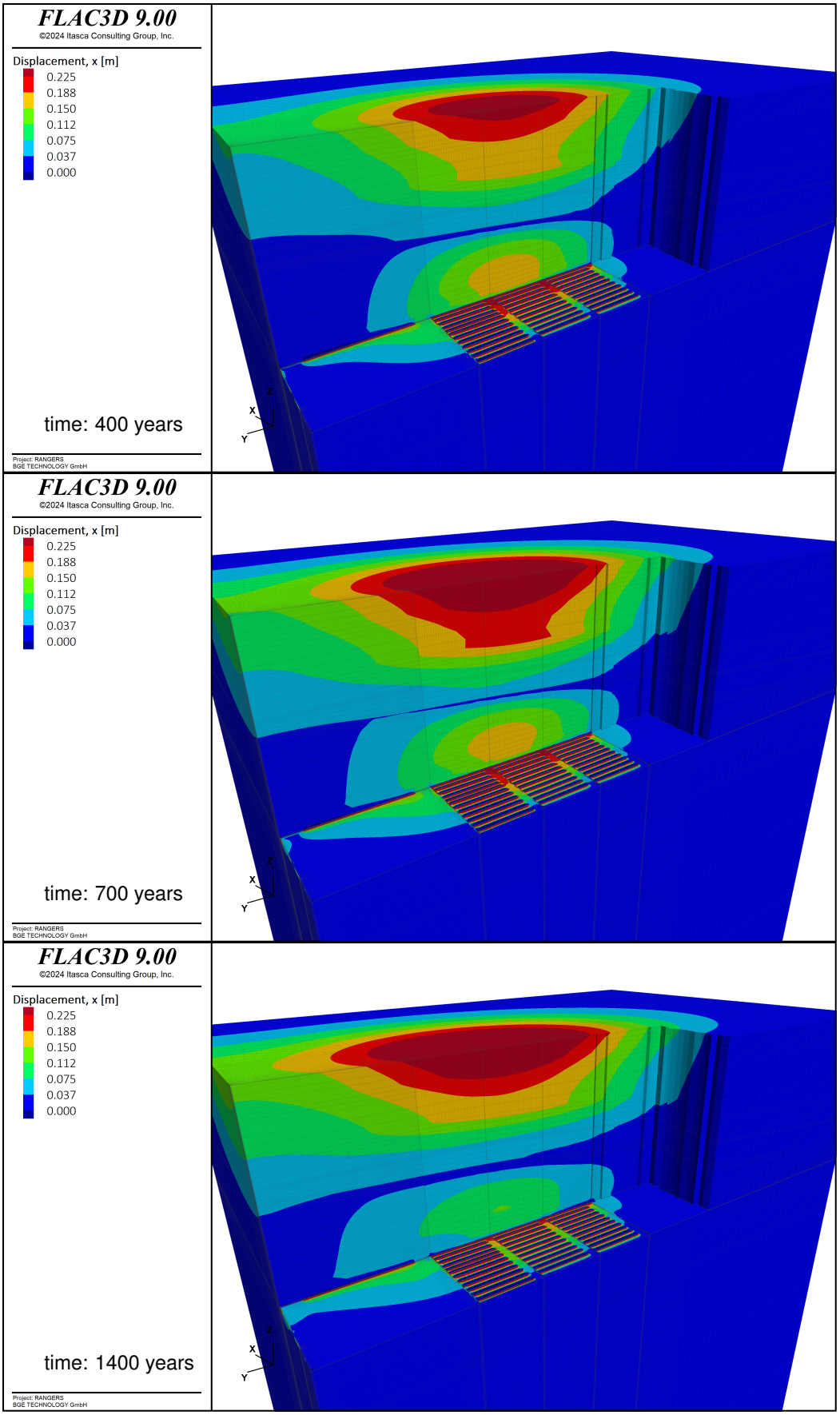

Figure 7.-10: Displacement distribution along the x-axis over time.

7.6.2 Displacements and strains in the seals

Figure 7.-11 illustrates the displacement vectors around the first Sorel concrete seal near the emplacement fields at the disposal level. The vectors represent the projected displacements on the x-y plane, with the z-component excluded. As shown in the figure, the rock mass predominantly moves in the y-direction at the level of the seal. This movement becomes most pronounced at around 700 years, coinciding with the peak temperature in the repository. At 100 years, there is minimal rock mass movement near the seal, as indicated by the small size of the vectors. By 1,600 years, the rock mass continues to move in a similar direction as at 700 years, but the smaller vector size suggests that the velocity of this movement is gradually decreasing. Due to the viscous and creeping nature of salt, which causes it to deform more rapidly than the stiffer concrete seal, it can be anticipated that rock mass movement will generate lateral skin forces along the surface of the seals. These skin forces, in turn, induce tensile loading in the seals.

This phenomenon is also observed in geotechnical applications to pile foundation. The so called negative skin friction (negative Mantelreibung in German) is a phenomenon that occurs in pile foundations when the surrounding soil settles and exerts a downward frictional force on the surface of the pile. Normally, the skin friction between the pile and the soil acts upwards and helps support the load carried by the pile. However, in certain conditions, this friction reverses, becoming negative, and adds an additional load on the pile rather than providing support. The settling of the surrounding soil generates a downward force along the pile's surface. This downward force acts against the pile, essentially pulling it down by applying a tensile force.

To test this hypothesis, we closely examine the displacement experienced by the seals over the course of the simulation. Table 7.-7 and Table 7.-8 display the displacement along the y- and x-directions, respectively, for the two drift seals — one located near the shaft and the other near the disposal side. In Table 7.-7, it is evident that the seal near the emplacement fields experiences greater displacement compared to the seal near the shaft. For both seals, displacement increases from the disposal to the shaft side, creating a heterogeneous distribution. This uneven displacement leads to an elongation or extension of the seals. For the seals to experience this extension, they must be subjected to tensile stresses, thereby validating the hypothesis.

The seal near the disposal side exhibits a maximum elongation ranging from 12 to 15 cm, occurring between 500 and 600 years after the disposal of radioactive waste. This period coincides with the thermal peak in the repository, as previously mentioned. Meanwhile, the extension of the seal near the shaft is more moderate, with the maximum displacement not yet reached even after 1,400 years.

In Table 7.-8, where the displacements of the seal along the x direction is displayed, a more homogeneous displacement distribution is observed. Here also the seal at the disposal side experiences higher displacement compare to the seal at the shaft side. The observed displacements may result also into an extension along the width of the seal. This is however limited to less than 2.5 cm for both seals. This also confirm the observations gained from the displacement vectors in Figure 7.-11 where it has been shown that the seals are mostly stressed along the y direction.

The extension of the seals discussed above can also be observed in the strain distribution within the seals, as shown in Table 7.-9, which presents the maximum principal strain in both seals over time. Only positive strain values are computed, indicating extension. Higher strain levels are reported in the center of the seal compared to the boundary regions, likely due to the tight contact with the surrounding rock. The maximum strain in the main part of both seals is less than 7.5×10^{-3}. This value remains constant over the time up to 1,400 years indicating that the rock mass movements around the seals are still active.

However, the highest strain values are observed at the edges of the seal, which is a numerical artifact. This occurs because, in the model, the seal is rigidly connected to the crushed salt. As the crushed salt compacts due to convergence, tensile forces develop at the interface with the seal, as the seal cannot accommodate the deformation of the compacting salt. This results in elevated strain at the ends of the seal.

To address this effect, interface elements or similar numerical techniques should be used to prevent such artifacts. Nonetheless, these high strain values remain localized at the seal edges and do not propagate further into the seal over time.

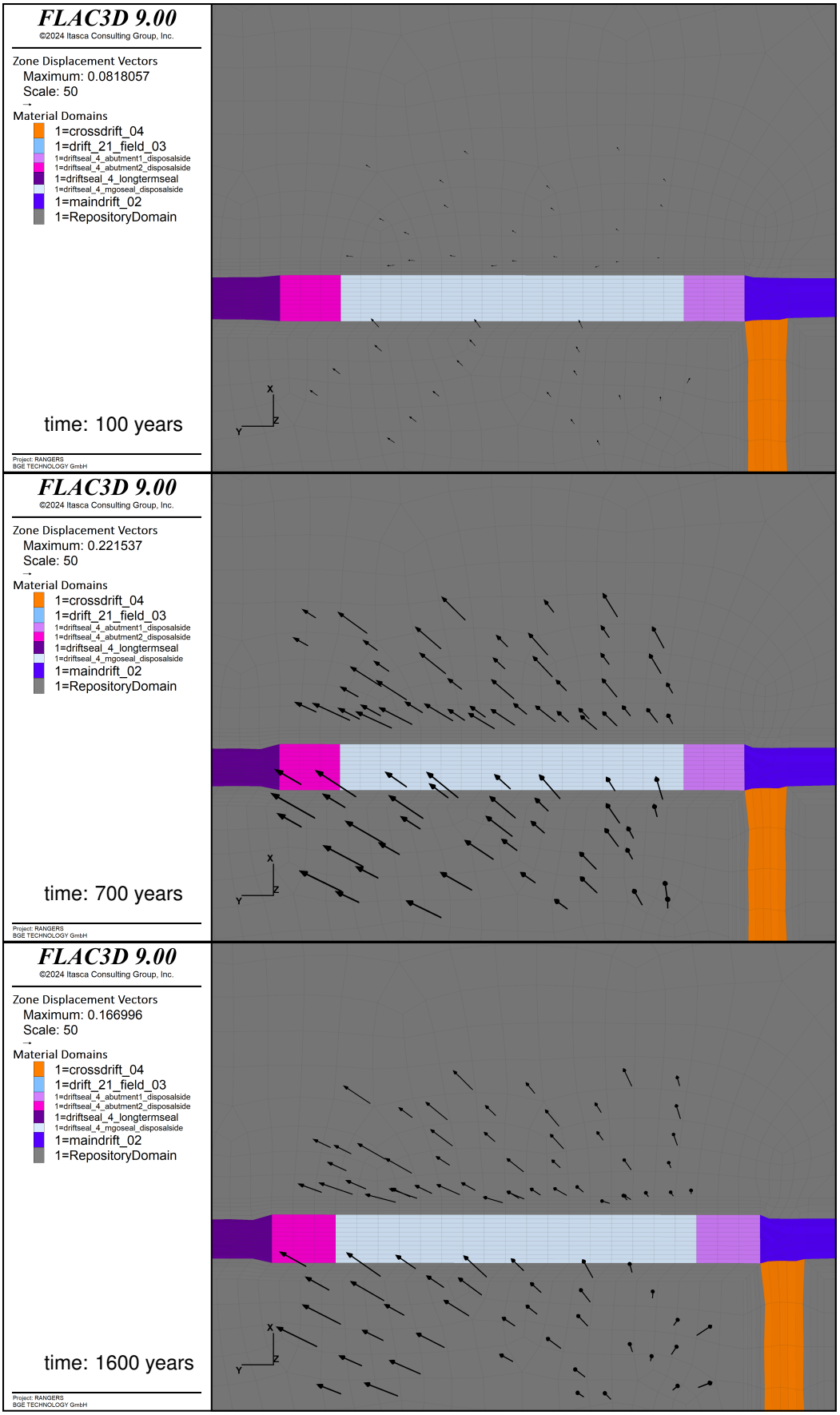

Figure 7.-11: Displacement vectors around the seal over time.

Table 7.-7: Displacement distribution in the drift seals the y-axis over time.

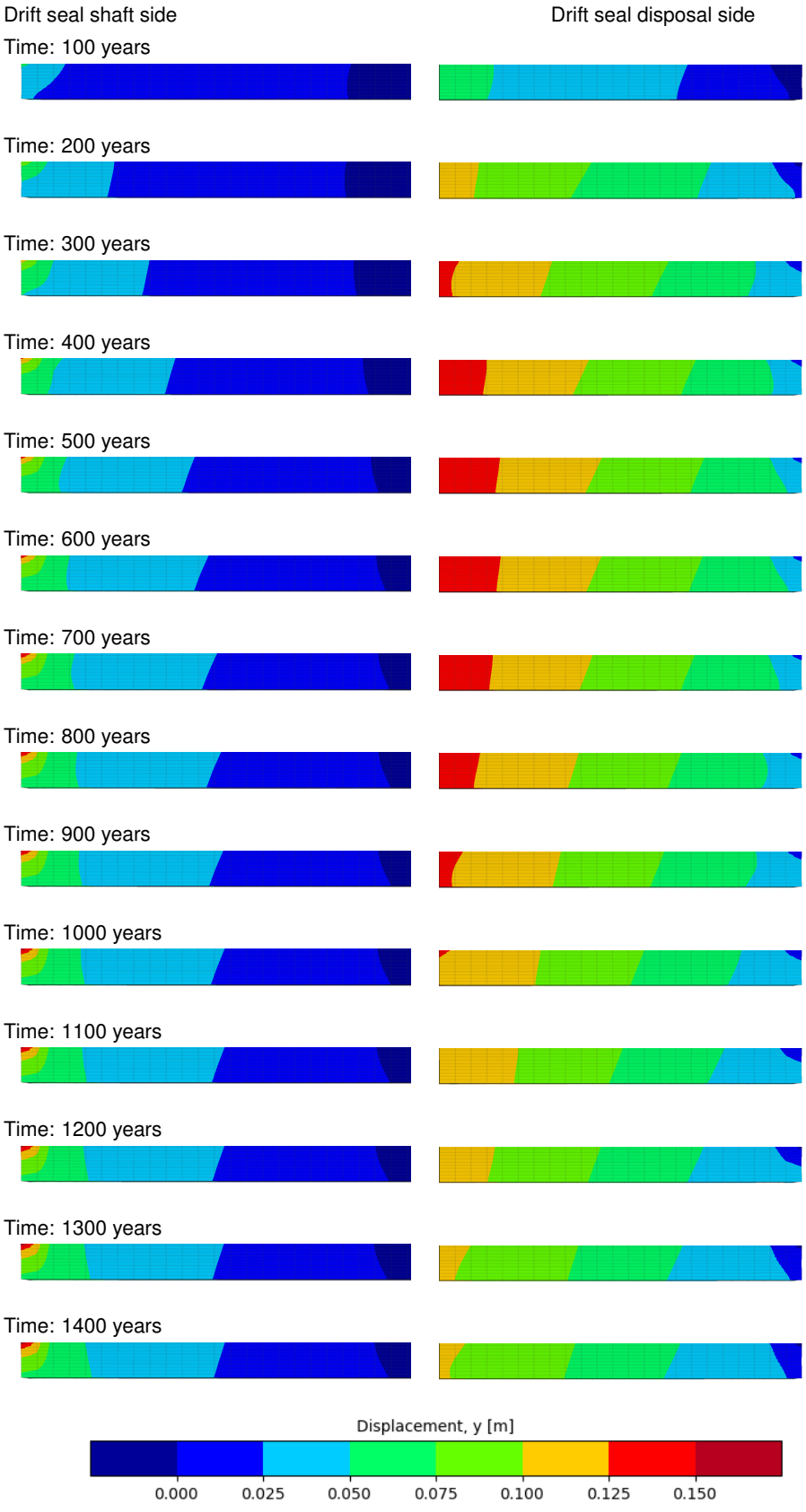

Table 7.-8: Displacement distribution in the drift seals the x-axis over time.

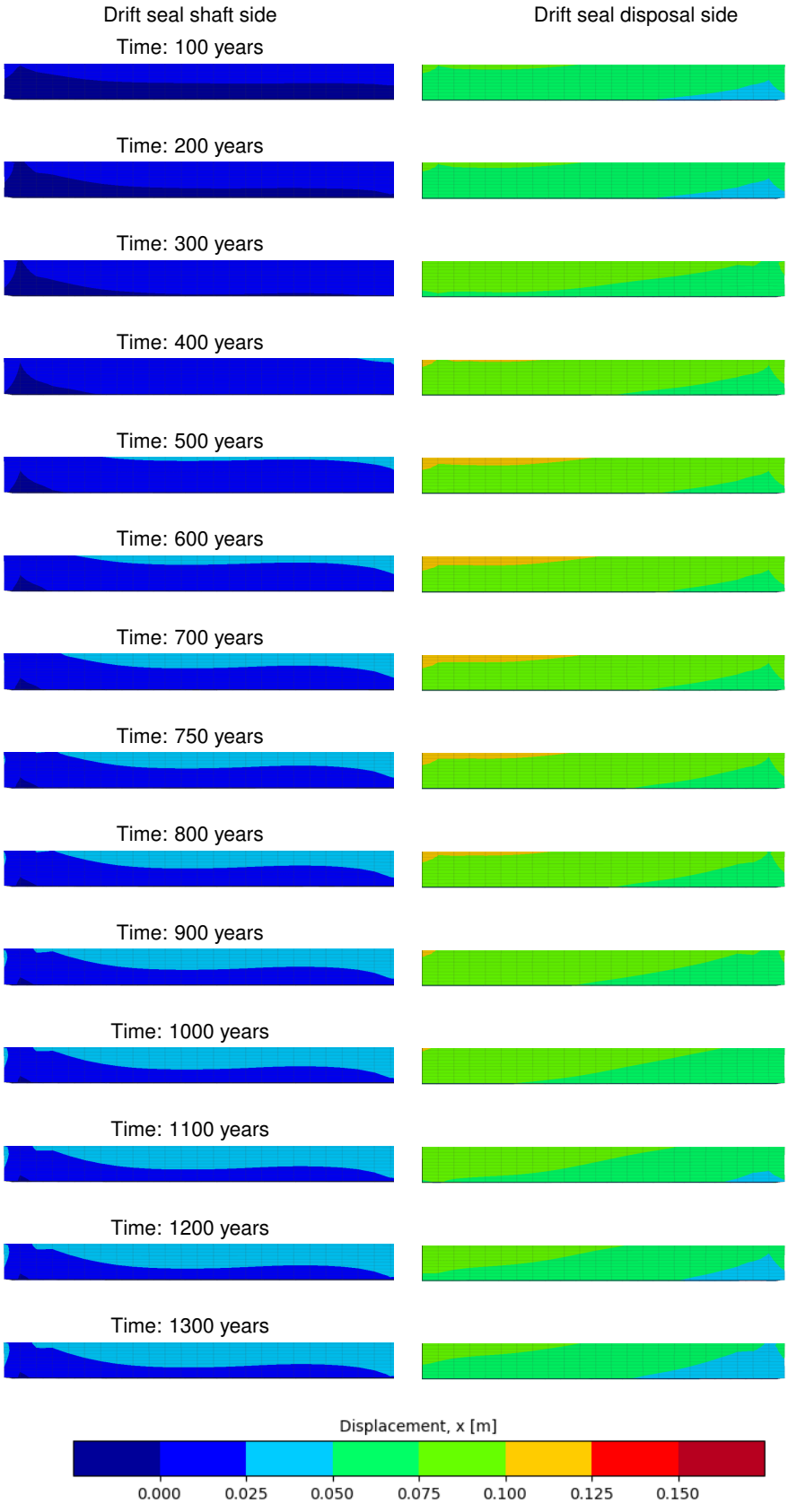

Table 7.-9: Strain distribution in the drift seals over time.

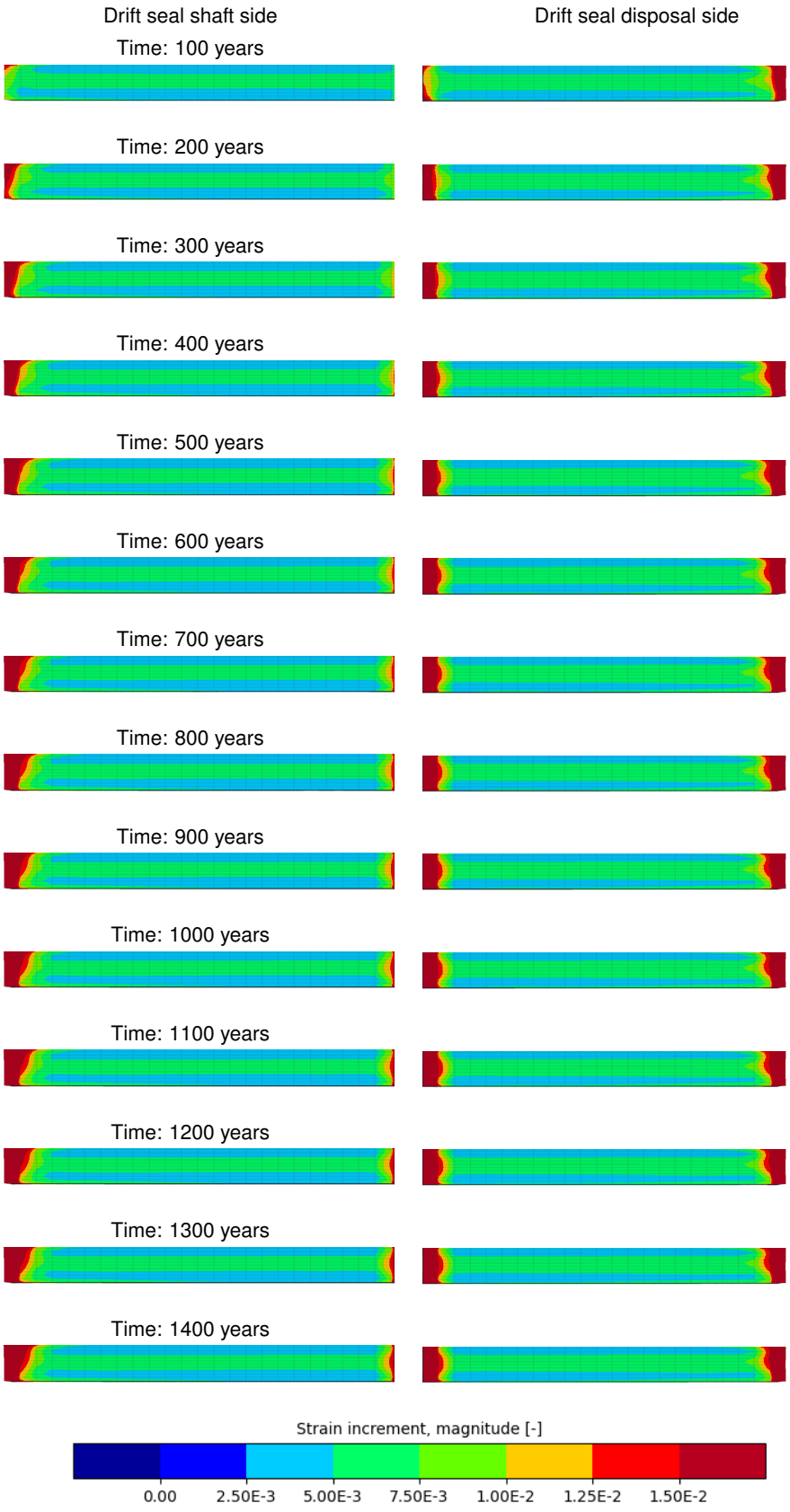

7.6.3 Stresses in the seals

The stresses responsible for the observed extension of the seals are exemplified in Figure 7.-12, which shows the distribution of the maximum principal stresses in the seal, along with the vectors indicating the direction of these stresses. It is clearly noticeable from the figure that the maximum principal stresses are primarily in the tensile region at the evaluated time, and their direction aligns with the y-axis — the same direction in which the extension of the seal has been observed. These findings further support the hypothesis that thermal expansion of the rock mass induces skin forces at the seal boundaries, leading to the development of tensile stresses and, consequently, the extension of the seals.

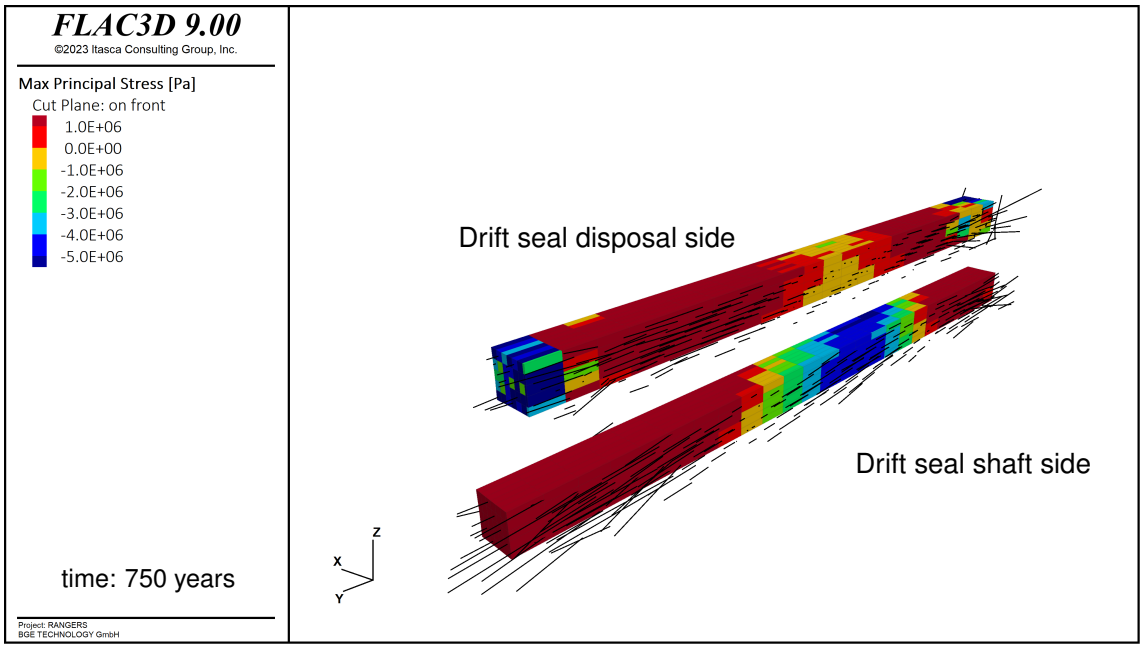

Figure 7.-12: Maximum principal stress distribution and vectors in the drift seals at 750 years.

The stresses in the seals resulting from the rock mass expansion are shown in Table 7.-10, which illustrates the evolution of maximum principal stresses in both seals at several time points. As can be expected, tensile stresses develop in the seals. The seal located near the disposal side experiences higher stress compared to the one near the shaft, due to its proximity to the heat source, where thermal expansion is more pronounced.

In the early stages of the simulation, tensile stresses begin to form at both ends of each seal. Over time, these stresses propagate toward the center of the seals. By around 800 years, the entire seal at the disposal side is subjected to tensile stresses, with this condition intensifying until around 1,400 years, when stresses exceed 1 MPa in the center. A recovery begins at the seal ends around 500 years, where the seal gradually returns to a state of compression.

The behavior of the seal near the shaft is similar to that of the seal near the disposal side, with tensile stress accumulation observed at the edges. However, unlike the disposal-side seal, there is no propagation of tensile stresses toward the center. This indicates that the thermal expansion of the rock mass near the shaft is insufficient to significantly impact the seal further. The stress state remains largely unchanged from 500 years onward, except for a stress recovery observed at the right end of the seal.

Table 7.-10: Maximum principal stress distribution in the drift seals over time.

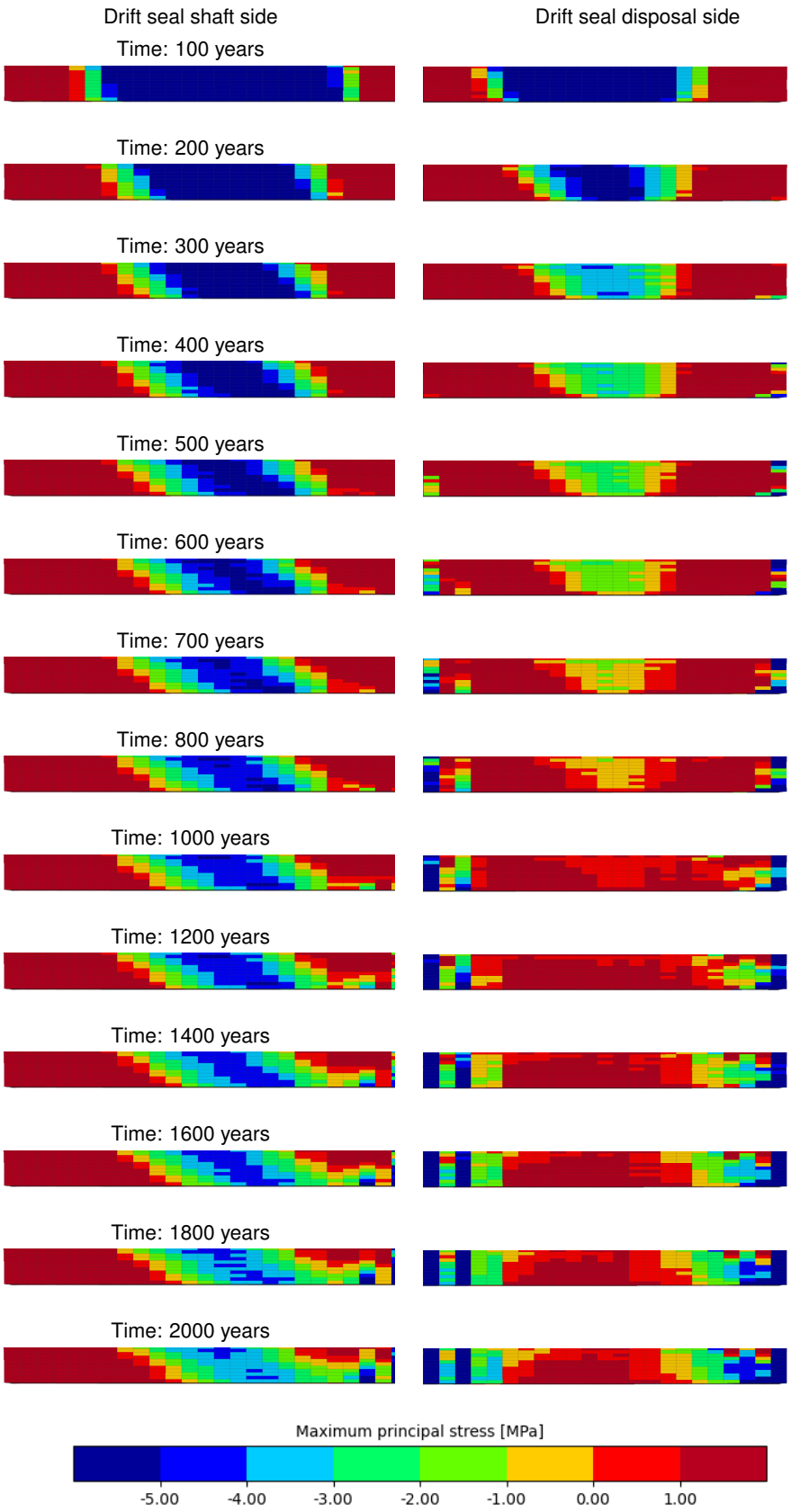

7.7 Verification of integrity

To assess the integrity of the drift sealing structure, the verification criteria discussed in section 7.4 need to be evaluated. Those criteria are Structural Stability, Crack Limitation, Deformation Restriction, Filter Stability and Long-term Stability. Additionally, the dilatancy criterion is considered to verify that the contact zone remain tight along the drift sealing system over time.

The performance of the long term seal was already discussed in section 6.4. There has been already shown that the long term seal will gain its function quite early in the repository lifetime. From the criteria mentioned above, the deformation of the seals that constrain the long term seal may affect its performance. This is fortunately not the case as the compaction of the long term seal as presented in section 6.4 already account for the deformation of the seals discussed in section 7.6.2. Both analyses were combined in a single simulation. This means the the deformation experienced by the seals did not have a negative effect on the compaction evolution of the long term seal

For the seals, we use a qualified constitutive material model that has been validated and calibrated against experimental data. The evaluation of the damage state of the sorel concrete based on this model allows us to quantify the criteria of structural stability and crack limitation.

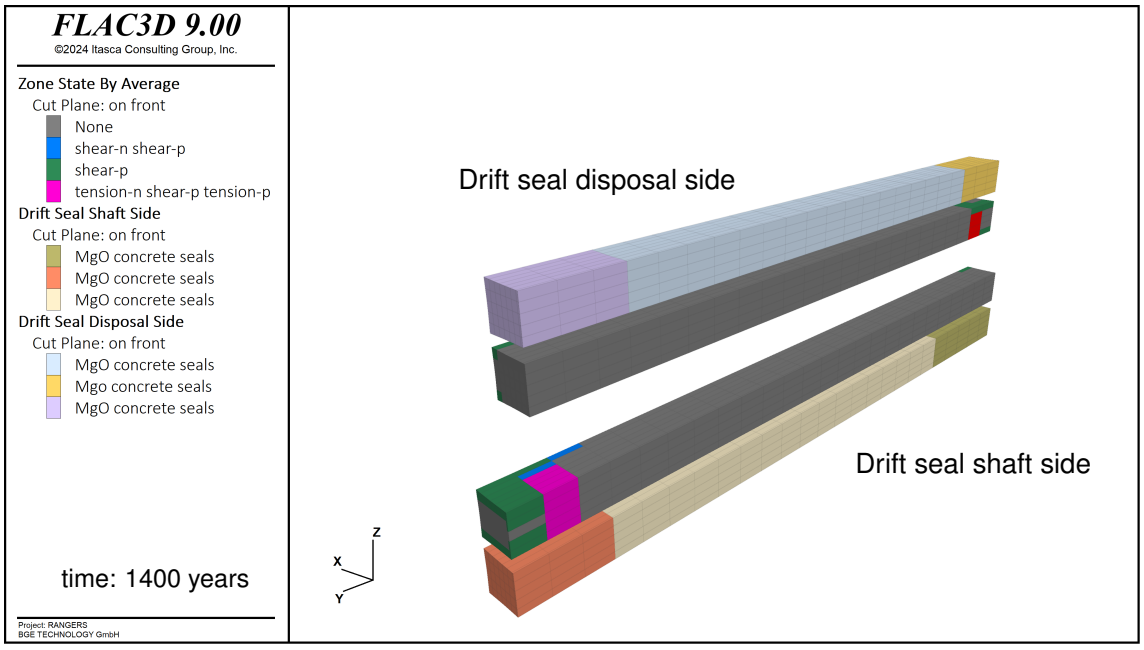

Figure 7.-13: Damage in the drift seals at the end of the simulation.

Figure 7.-13 illustrates the damage in the seals due to the thermal-mechanical behavior of the surrounding rock mass, shown along a vertical cut through the middle of the seal. As observed, the damage is confined to the ends of the seals. This damage results from the numerical artifact previously identified in the strain distribution, caused by the rigid contact assumption between the seal and the crushed salt. As the crushed salt compacts, it exerts traction on the seal that would not occur in reality. As previously discussed, using interface elements or introducing thin layers with weak thickness would better model the interaction between the seal and crushed salt.

It is also important to note that the damage is located in the abutment sections of the seal, which do not serve a sealing function but instead protect the sealing section, which remains undamaged. The amount of damage in the abutments is particularly related to the coarse mesh used for this analyses. This was necessary to limit the computational effort for the analysis. Using a finer mesh will to reduce the amount of damage in the abutments. This damage must be concentrated at the interface to the crushed salt. As already mentioned. By employing an adequate numerical technique to realistically modeled the interface crushed salt/Sorel concrete, one should not expect any damage at all.

Although the seals are subjected to tensile stresses, these stresses are not sufficient to cause any damage. As stress recovery progresses toward the compressive regime and the repository continues to cool, no further damage is expected in the long-term evolution of the repository. On the contrary, due to the compressive stresses that the seals will experience in the long term, the triaxial strength of the Sorel concrete is likely to increase, making the seals mechanically stronger than they were in the early phase after disposal.

The dilatancy criterion is a crucial parameter for assessing the mechanical behavior of rock salt under varying stress conditions. When the stress in the salt exceeds a certain threshold, the material begins to dilate, forming microfractures and increasing its permeability. This increase in permeability can create potential pathways for fluid ingress into the repository, particularly along the drift sealing system.

Figure 7.-14 presents the evaluation of the dilatancy criterion over time. At the end of the backfilling operation (at 30 years), the rock mass surrounding the drifts experienced significant dilatancy. However, 70 years later, the model shows signs of recovery due to the creep behavior of the salt, although areas around the long-term seal were still undergoing dilatancy. By 400 years, the affected areas had largely recovered, and by 1,000 years, no dilatancy was observed in the model.

The infrastructure drift connecting the shafts also exhibited dilatancy but recovered at a similar rate to the long-term seals. Notably, no dilatancy was observed along the MgO seals, indicating that the sealing function was effective immediately after the installation of the seals. By 500 years, it is expected that the long-term seal had fully gained its intended function. From this point onward, the drift sealing system operates as designed, following the principle of diversity and redundancy to ensure long-term containment.

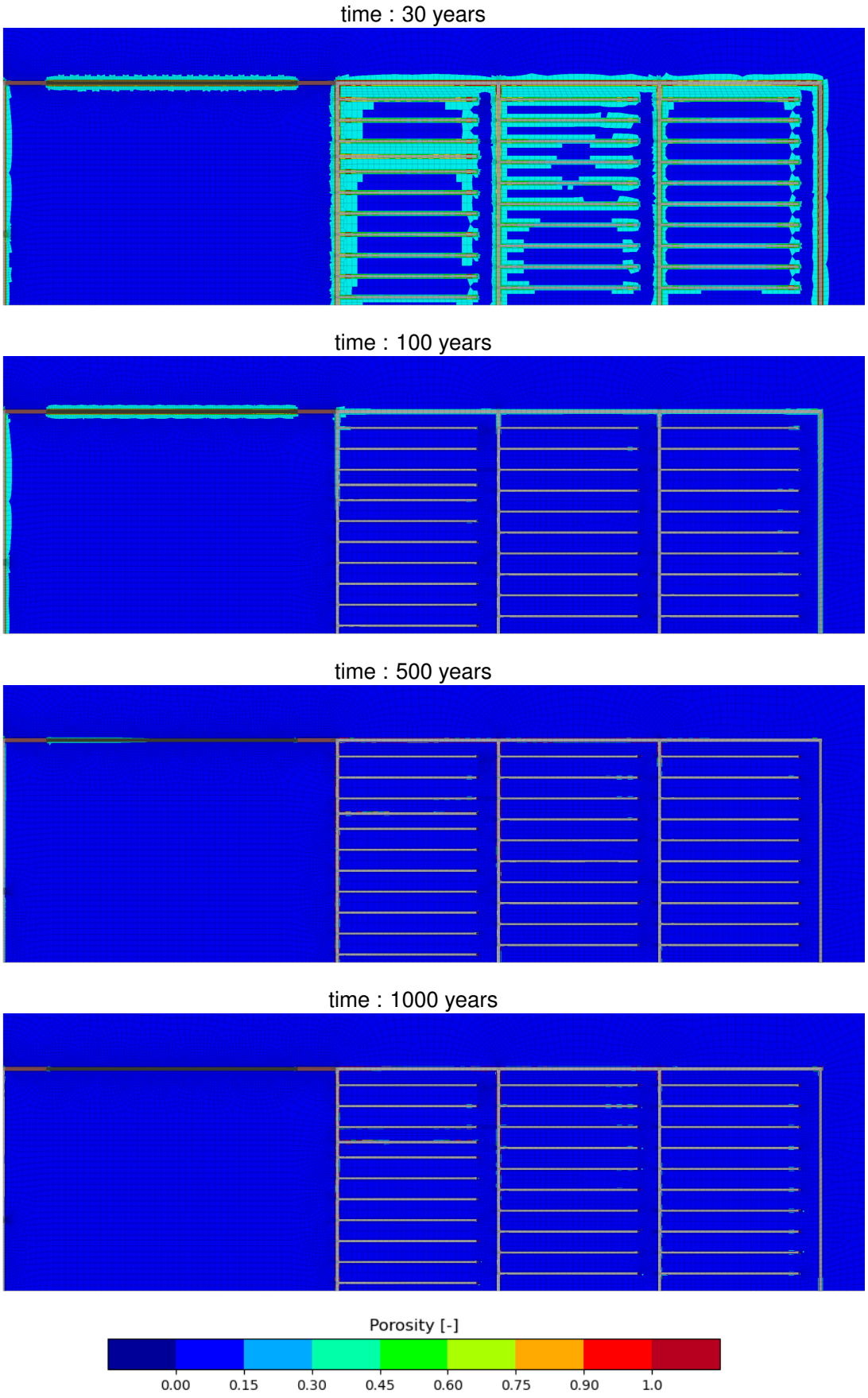

Figure 7.-14: Evaluation of the dilatancy criterion in the repository over time.

8. Mechanical Integrity Assessment of the Shaft Seal

In the following section, the design and integrity of the shaft sealing system in salt repositories are assessed based on the methodology developed within the RANGERS project. This exercise is exemplary performed for the two shaft sealing systems designed in generic repository system developed in RANGERS.

8.1 Safety function

According to Beuth et al. (2012), the function of the shaft sealing system is to limit the inflow of solutions from the overburden and adjacent rock formations to such an extent that only small amounts of solutions can penetrate the repository mine. The shaft seals are designed to withstand the expected fluid pressures (hydrostatic pressure of the water column in the overburden and adjacent rock formations). The design of the shaft seals assumes a functional duration of 50,000 years, during which their effectiveness must be maintained. After more than 50,000 years, for the reference scenario, increased hydraulic permeabilities of the shaft seals are assumed, resulting in enhanced solution inflow into the infrastructure area. If solutions reach the drift sealing system, partial dissolution of the seal materials or precipitation of dissolved material in the pore space may occur. At this time, the crushed salt backfilled between the drift seals as well as in the repository mine will take the function of the long term seal of the repository.

8.2 Design of the shaft sealing system

Shaft sealing systems are engineered barriers that are designed based on the diversity principle. The diversity principle is fulfilled by several seals installed in the shaft made of different materials. The shaft sealing system is redundant to the drift sealing system. Both together in addition to the technical barrier represented by the waste packages form a multi-barrier system. In RANGERS, two different designs has been elaborated inspired by prior research and development projects and have been tailored to the generic repository system used in this project.

In both designs, a first MgO concrete element is installed in the shaft sump, the deepest parts of the shaft as well as the subsurface landing station. At this depth, the MgO-concrete fulfills an abutment function. Above, a second MgO-concrete element is considered serving this time as sealing element. It follows in both designs, a gravel column is installed that fill the part of shaft that is in the rock salt layer. To guarantee chemical stability of the MgO-concrete, the gravel column is enriched with Mg-salt (e.g. Brucite). Water intakes from above will be saturated with Mg when it passes the gravel column. The gravel column represents also an abutment for the seal that comes next. The two designs diverges by the adjustment of the seals. In the first design, a bentonite seal is emplaced at the top of the gravel column followed by a column of compacted salt-clay mixture. The location of the bentonite below the crushed salt/ clay mixture should ensure a saturation of intake water with Na and provide a stable chemical composition of the brine entering the bentonite. At the salt top a bitumen filled gravel column will be installed, covering surrounded anhydrite and clay layers too. In the area of the overburden a simple gravel column will be installed.

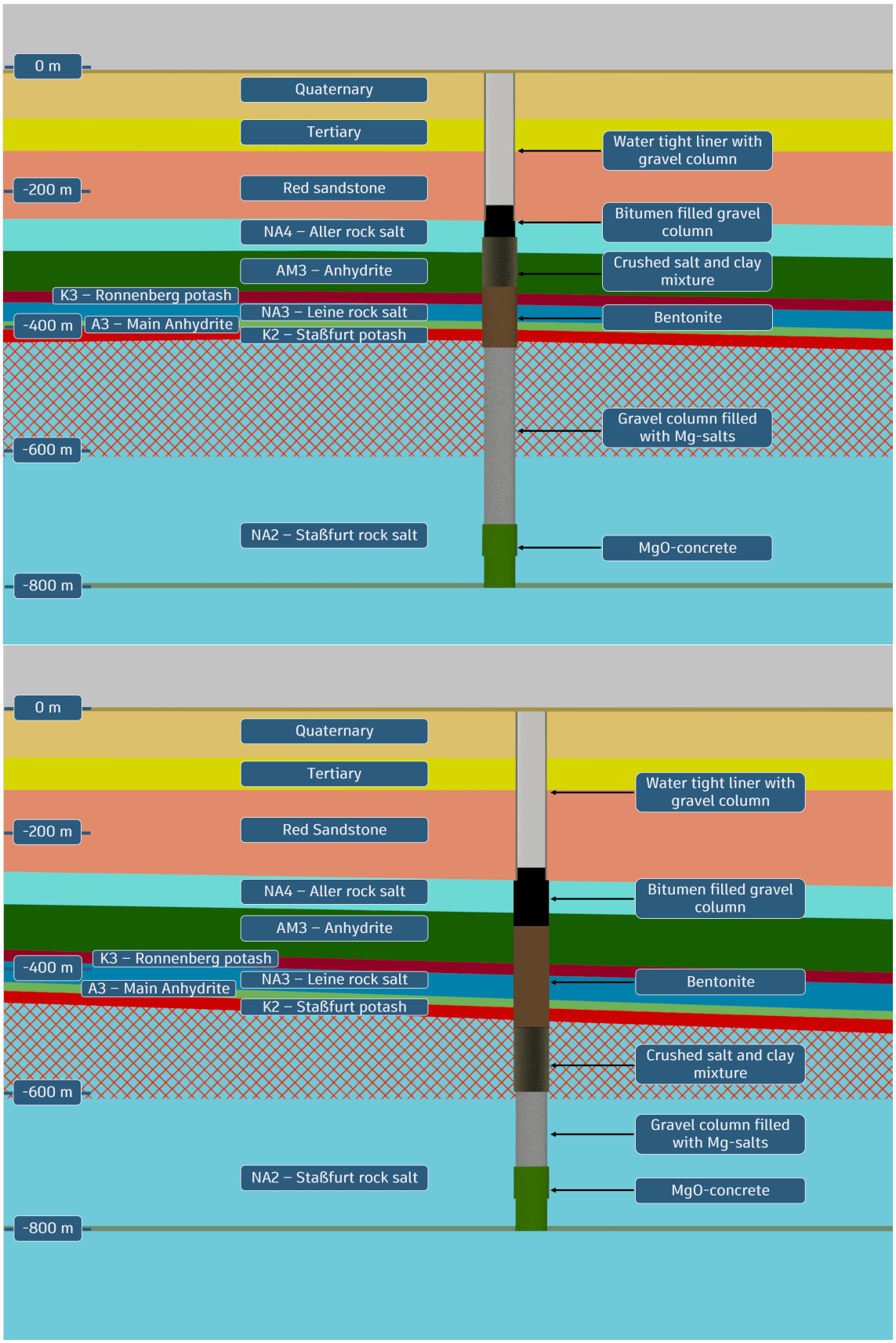

Figure 8.-1: Illustration of both shaft sealing concepts in the geological model used in RANGERS.

In the alternative design, the bentonite and salt-clay seals are permuted. This is motivated by the fact that the convergence of the rock helps to reseal the EDZ. The convergence rate increases with depth. Because bentonite due to its swelling capacity is able to close the EDZ itself, it is adequate to install the bentonite higher in the shaft and the salt/clay mixture deeper to let the convergence increase the sealing capacity of the this latter seal. Above the bentonite seal, the third seal made of bitumen gravel is installed followed by the gravel column up to the ground surface as it is the case for the reference design. The location of the two shaft sealing systems in the geological formation is illustrated in Figure 8.-1.

8.3 Modeling cases

The integrity assessment for the shaft seal design is based on the loads derived from scenario development and Features, Events, and Processes (FEP) analysis. The FEPs relevant for the mechanical integrity of the engineered barrier system (EBS) are discussed here in the context of the shaft seal design, as shown in Figure 8.-2.

Thermal expansion and contraction resulting from heat propagation in the repository are among the key loading conditions affecting the shaft sealing system. Heat flow, coupled with the convergence of the surrounding rock enhanced by creep, induces mechanical stress changes within the repository, creating significant loads that must be considered for the long-term safety and integrity of the shaft seal.

Time-dependent processes, such as the swelling, shrinking, and creeping of the sealing materials (e.g., bentonite and salt-clay mixtures), also play a critical role in the system's resistance over time and must be factored into the design. The swelling of bentonite may also induce some damage in the rock contour leading to potential pathways for water migration. The compaction of the seals that is expected to occur due to converge helps to compensate the deformation to be expected due to shrinkage and creep of the seals.

Furthermore, hydraulic pressure change results from the liquid inflow in the shaft starting with the saturation of the upper gravel column and the subsequent infiltration through the sealing components. The resulting hydrostatic loads need to be considered in the integrity of the shaft sealing system.

Due to its granular nature, the gravel columns in the shaft are prone to settling. This settlement can lead to subsidence within the shaft, potentially affecting the performance of the sealing materials and creating new pathways for water inflow. This issue becomes more pronounced in the event of seismic activity. To address these concerns, dedicated analyses were conducted as part of the ELSA project (Herold et al., 2018), utilizing various numerical approaches to quantify the settlement both immediately after backfilling the gravel material and following seismic events.

The settlement quantification from the ELSA project demonstrated that the applied seismic impulse was insufficient to cause significant particle rearrangement or settlement. The maximum vertical displacements recorded were approximately 2 cm, while horizontal displacements reached up to 4 cm. Following the seismic loading, subsidence of around 1 cm was observed. A second identical seismic event, delayed in time, resulted in similar settlements of less than 2 cm.

However, the earthquake did influence the stress distribution within the gravel column, leading to the observation of a silo effect, which caused an increase in both horizontal and vertical stresses. The effect of the seismic event on the porosity of the gravel was minimal, indicating no significant compaction or particle rearrangement occurred.

Based on these findings, the current shaft sealing design can be considered robust and largely unaffected by the FEP “Settlement and compaction of backfill”.

The results obtained in ELSA also cover the FEP “displacement of the shaft sealing elements”. A displacement of the sealing element can occur only if the settlement of the gravel columns serving as abutment for these elements is large enough. This is fortunately not the case.

Seismic events, such as earthquakes, must also be incorporated into the design considerations, especially given the expected long functional lifetime of the shaft seals (50,000 years and beyond). They are of relevance especially in the contact zone between sealing material and rock. This should be adressed in the scope of dedicated numerical investigations.

The gray FEPs in the figure represent processes that are not relevant to the integrity proof of the shaft sealing system for the following reasons:

- Thermal degradation of canallite: This process pertains to certain minerals that are not present in the shaft seals, making it irrelevant to the integrity of the sealing system.
- Dissolution and precipitation of salt minerals: While this affects the surrounding rock salt, it does not directly impact the concrete or clay-based shaft seals.
- Gas flow processes: there is no gas in the shaft and no gases is to be expected in the salt formation. In the potential presence of gas inclusion will certainly be discovered during the excavation of the shaft and can be eliminated as a potential risk to the mechanical integrity of the shaft seal.
- Metal corrosion: This process affects metallic components within the repository but is not relevant for the non-metallic materials used in the shaft seal system.
- Solution, transformation of clay minerals: This concerns the alteration of clay minerals. This is FEP may affect the long term sealing performance of the shaft but not its mechanical integrity. The effect of such degradation results in an increase of permeability of the clay based seals and should be considered in the scope of the hydraulic assessment.
- Microbial processes: Microbial activity is unlikely to significantly impact the shaft seals, which are primarily composed of concrete and clay.
- Alteration of bentonite: The rational for the FEP “Solution, transformation of clay minerals” applies also here
- Colloid generation and filtration: This process relates to the behavior of colloidal particles in fluid, which is not directly relevant to the mechanical integrity of the shaft seal.
- Asphalt migration: Asphalt is not used in the shaft seals, so this process is not applicable.

- Thermal degradation of carnallite: This process pertains to certain minerals like canallite, which are not present in the shaft seals or the surrounding rock formations. Therefore, it does not directly affect the mechanical integrity of the sealing system.
- Diapirism: This geological process involves the upward movement of material through overlying rock, typically salt, due to buoyancy. While diapirism can occur in some salt formations, the mechanical integrity of the shaft sealing system would not be influenced by this process, as diapirism primarily affects large geological timescales and is not relevant to the short- to medium-term behavior of the shaft seals.
- Transgression and regression: These are large-scale geological processes related to changes in sea level. Since the repository is designed in a stable geological setting and such processes would occur far above the repository level, they do not pose a risk to the mechanical integrity of the shaft seals.
- Corrosion of cement- or Sorel-based materials: While corrosion could affect certain materials, the shaft seals use materials that are non-metallic (such as concrete or clay), and therefore, this FEP does not apply to the integrity of the shaft sealing system.
- Dissolution and precipitation of salt minerals: While this process affects the surrounding rock salt, it does not directly impact the concrete or clay-based shaft seals. If there is a potential for such processes, they would be monitored and controlled in the salt formation itself, with little to no effect on the seal materials.
- Gas flow processes: No gas is expected in the shaft or the salt formation. Any potential gas inclusions would be detected and mitigated during shaft excavation, ensuring that gas-related processes do not pose a threat to the mechanical integrity of the shaft seal.
- Metal corrosion: Metal corrosion could affect metallic components within the repository, but this FEP is not relevant for the shaft seals themselves, which are constructed from non-metallic materials such as concrete and clay.
- Solution, transformation of clay minerals: This FEP concerns the alteration of clay minerals, which may influence the long-term sealing performance of the shaft but not its mechanical integrity. The degradation of clay-based seals could lead to increased permeability, which should be addressed in hydraulic assessments rather than in mechanical integrity assessments.
- Microbial processes: Microbial activity typically affects organic materials or metals. The shaft seals, being composed of concrete and clay, are not significantly affected by microbial processes, making this FEP irrelevant to their mechanical integrity.
- Alteration of bentonite: This FEP is similar to the “Solution, transformation of clay minerals.” Bentonite, if used, may experience some transformation over time, which could affect its sealing performance but not the mechanical integrity of the shaft seal. Any permeability changes due to this FEP should be considered in the hydraulic assessments.
- Colloid generation and filtration: This process refers to the behavior of colloidal particles in solution, which is not relevant to the mechanical integrity of the shaft seals. While it might affect the movement of contaminants, it has no direct impact on the structural stability of the sealing system.
- Asphalt migration: Since asphalt is not used as part of the shaft seals, this process does not apply and is irrelevant for the integrity assessment of the shaft sealing system.

- Deflagration and explosion of gases: While gas explosions could have dynamic impacts similar to seismic events, no significant gas presence is expected in the shaft area. Any gas inclusions would be identified and removed during excavation, ensuring that this FEP does not affect the mechanical integrity of the shaft seals.

By focusing on the relevant FEPs, we can address the processes that directly impact the shaft seal's mechanical integrity and ensure its long-term functionality.

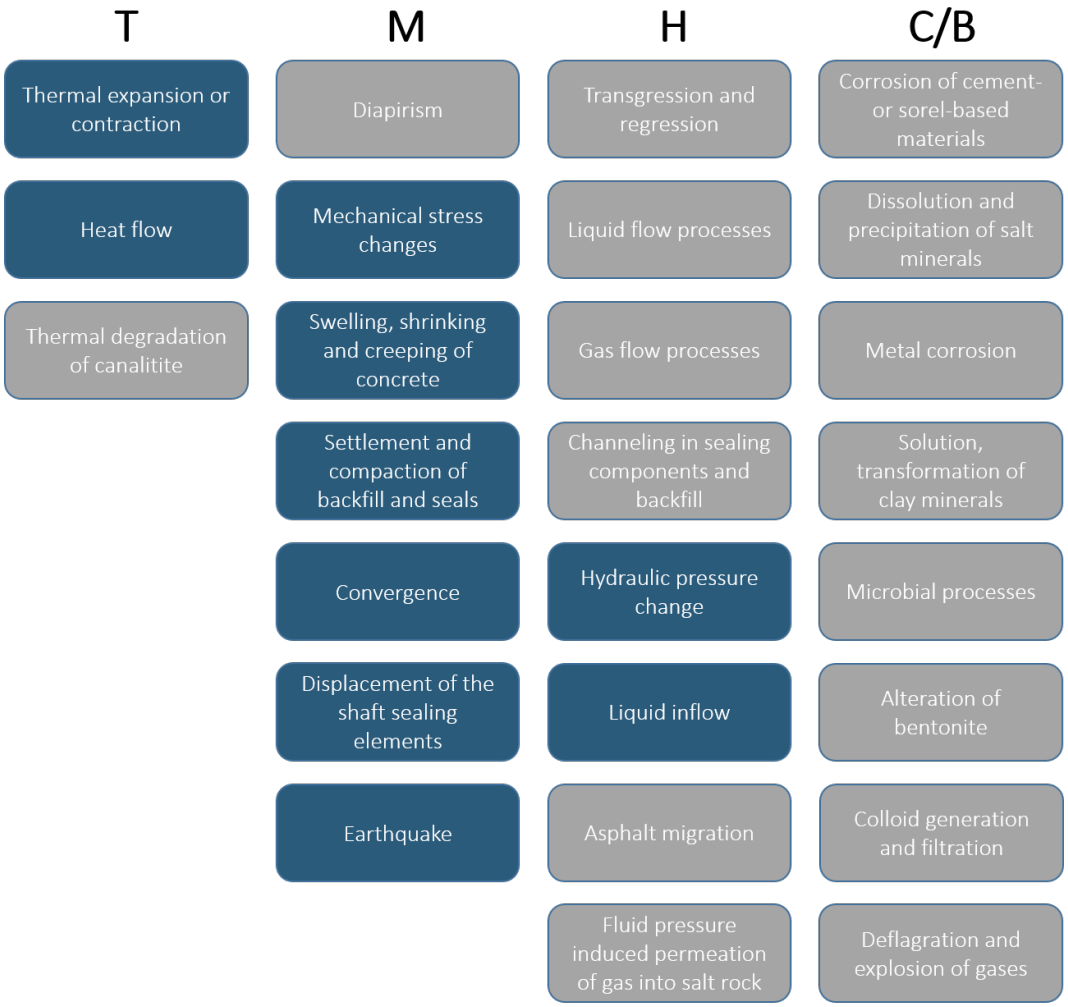

Figure 8.-2: Initial FEPs of relevance for the mechanical integrity proof.

From these discussions, we derive the following modeling cases for the shaft sealing system:

- modeling case 1: Thermal-mechanical loading: This scenario considers the combined effects of heat flow, thermal expansion/contraction, mechanical stress changes, and rock convergence.
- modeling case 2: hydrostatic pressure build-up in the shaft: This case analyzes the effects of water pressure on the shaft seal (FEP: hydraulic pressure change).
- modeling case 3: Earthquake events: Seismic activity is combined with thermo-mechanical loading to assess the impact of seismic loading at the contact zone seal/rock. system.

The interaction between the shaft seal system and the surrounding rock is part of the permanent design situation, where processes like gravitational forces, convergence, and creep of the host rock are always considered. In combination with other FEPs or modeling cases, the long-term thermal-mechanical evolution can be modeled to predict the system's performance.

Hydraulic load cases from water inflow, occur gradually over time and can be considered in the scope of the thermal-mechanical simulation as volumetric load acting in the shaft.

In this study, the design and safety assessment will be demonstrated using modeling case 1 and 2. Additional dynamic seismic analyses will be required to evaluate the effects of modeling case 3.

8.4 Numerical model

8.4.1 Modeling concept

The numerical model necessary to investigate the evolution of the shaft sealing systems is designed to accurately compute both the stress development in the near field of the shaft sealing systems and the heat propagation from the emplacement fields up to the shafts. A comprehensive model that considers both the shaft sealing components, the emplacement fields, and the surrounding geological layers is required for the integrity assessment. Thus, the model must cover several square kilometers, yet consist of finite elements that are only centimeters in size in key areas like the shaft and surrounding zones of interest.

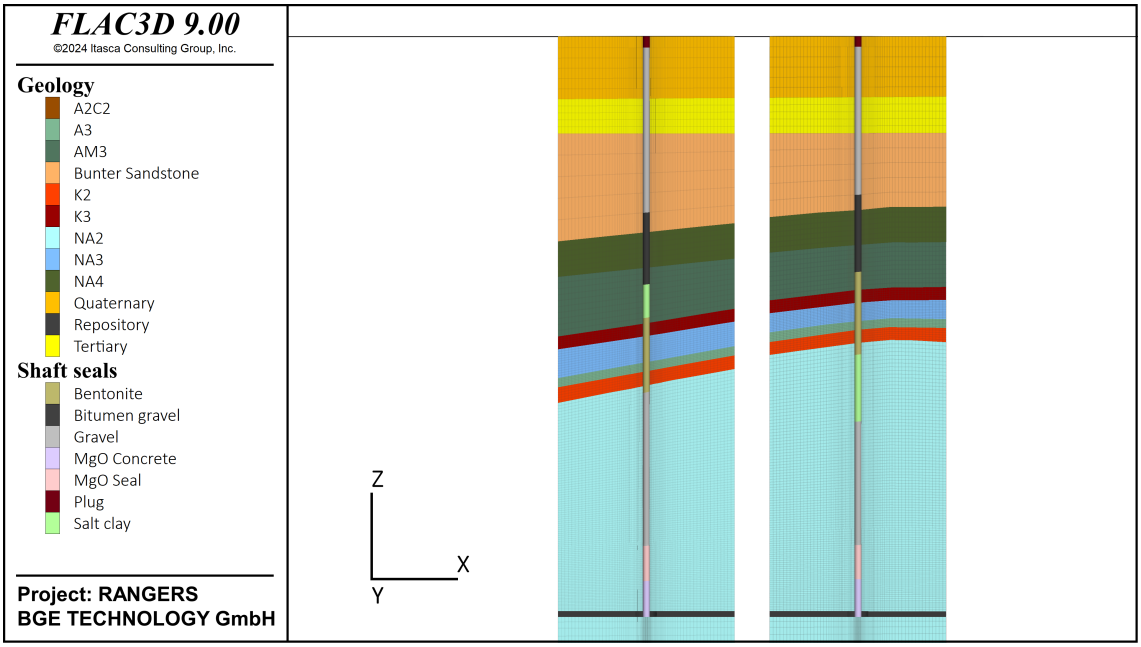

Figure 8.-3: Numerical model for the analysis of the mechanical integrity of the shaft sealing structures - near field.

To handle the complexity of the model, all disposal drifts are homogenized into disposal fields which act as heat sources. The thermal heat power of all disposal drifts is summed up and applied to these heat sources. This approach allows for the reduction of the computational burden while maintaining accurate heat propagation results in the model.

Figure 8.-3 shows the components of the two shaft sealing systems embedded in the geological layers. In this model, layers between the components were introduced to help mechanically decouple certain parts. In Figure 8.-4, the shafts and emplacement fields are shown within the context of the geology.

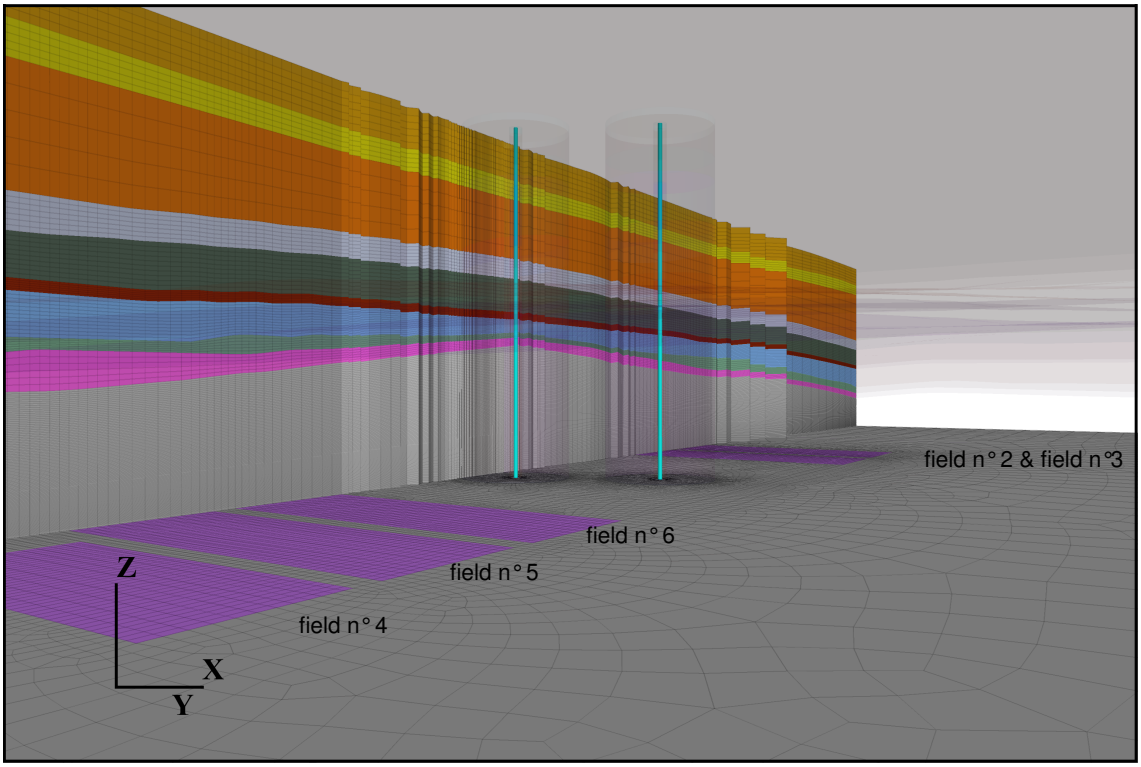

Figure 8.-4: Numerical model for the analysis of the mechanical integrity of the shaft sealing structures - far field.

The model is constrained in the normal direction at the lateral and bottom boundaries. The lateral boundaries are placed 1.5 to 2 km away from the repository, ensuring no edge effects are present. Adiabatic boundary conditions are applied to the model boundaries for thermal simulations.

The simulation stages begin with the initialization of the primary state, followed by the instantaneous excavation of the shafts and installation of a liner up to the upper boundary of the salt layers. Subsequently, sequential activation of the heat sources over 30 years is performed, simulating waste emplacement while keeping the shaft open. At year 32, the shafts are backfilled according to the sealing concept.

Due to the thermal-mechanical evolution of the repository system, the sealing components are subjected to external forces that need to be evaluated. The simulation runs for 1,200 years until the thermal phase is complete. After this point, the thermal processes are deactivated to allow the simulation to continue mechanically, speeding up the computational process and extending it to 25,000 years. This approach is conservative since the residual heat at the time of thermal deactivation still contributes to higher mobility of the salt up to 25,000 years. A realistic approach, where the heat gradually diminishes over time, would result in fewer thermal effects.

Besides the base case scenario described above, an alternative simulation was performed with interface elements introduced at the contact between the sealing components and the surrounding rock. In the base case scenario, this contact was assumed to be "tight-forced," meaning direct transfer of forces between the two materials. In reality, the strength at the contact interface is limited and can fail under specific conditions. Using interface elements allows for the modeling of this potential behavior.

It is expected that a silo effect will occur in the gravel columns. Therefore, a tight-force contact can be assumed there. The contact zone between the MgO concrete and the salt is well studied, with evidence showing that in most cases the contact zone remains intact after shearing, with cracks typically occurring in the Excavation Disturbed Zone (EDZ). Therefore, a rigid contact assumption is made between MgO concrete and rock salt. Bentonite, due to its swelling pressure over time, is also assumed to develop a tight-force contact with the rock, resulting in a rigid contact assumption for the bentonite/rock salt interface.

In contrast, the contact between bitumen and rock, and the contact between the crushed salt/clay mixture and rock, are expected to be more loosely connected. Due to the viscous nature of bitumen and the plasticity of the crushed salt/clay mixture, slip at the contact interface is more likely. In these cases, a frictional (slip) contact condition is applied.

In geotechnical modeling, the interaction between different materials at their interfaces plays a crucial role in defining the system's overall behavior. In the case of the shaft sealing system, various contact conditions exist between materials such as bentonite, MgO concrete, bitumen, and the surrounding rock salt. FLAC3D, being a robust numerical tool for simulating the mechanical behavior of geotechnical systems, allows the user to define both rigid and slip contact conditions between materials.

In the present analysis, the slip contact condition for interface were used.

The slip contact in FLAC3D is governed by Coulomb's friction law:

$$\tau = \mu \cdot \sigma_n$$

Where τ is the shear stress at the contact interface, μ is the coefficient of friction at the interface and σ_n is the normal stress acting perpendicular to the interface.

If the shear stress τ exceeds the critical value defined by the normal stress σ_n and the friction coefficient μ, relative slip occurs between the materials.

In this case, the relative displacement in the tangential direction $\mathbf{u}_\mathrm{t}$ is proportional to the shear stress as long as it remains below the yield condition:

$$\tau \leq \mu \cdot \sigma_n$$
$$\mathbf{u}_t \neq 0 \quad \text{if} \quad \tau = \mu \cdot \sigma_n$$

The coefficient of friction μ can vary depending on the materials in contact. For instance, in the case of bitumen and salt, a relatively low coefficient of friction might be assumed due to the

viscous nature of bitumen. On the other hand, the friction coefficient at the contact between crushed salt/clay mixture and rock can be higher.

The normal and tangential stiffness at the contact surface can be defined as:

$$K_n = E \cdot \frac{1-\nu^2}{h} \qquad K_t = G \cdot \frac{1-\nu^2}{h}$$

Where K_n is the normal stiffness at the interface, K_t is the tangential stiffness at the interface, E is the Young's modulus of the stiffer material,G is the shear modulus of the stiffer material, ν is the Poisson's ratio and h is the thickness of the interface element or the characteristic element size.

The result of this contact formulation is a realistic simulation of the interaction between the various sealing components and the surrounding geological materials, accounting for both tightly bonded and frictionally slipping interfaces, depending on the material properties and stress conditions.

The mechanical properties of interface at the contact between the materials in the shaft and the different geological layers are presented in Table 8.-1

Table 8.-1: Mechanical Properties of Interface Materials.

Interface Material	**Normal Stress,** σ_n [Pa]	**Shear Stress,** τ [Pa]	**Friction Angle,** φ [°]	**Cohesion,** c [Pa]
Gravel/Q	8.00×10^{10}	2.99×10^{10}	31	0
Gravel/T	1.33×10^{11}	5.08×10^{10}	31	0
Gravel/BunterS	8.11×10^{10}	3.07×10^{10}	31	0
Bitumen Gravel/BunterS	8.11×10^{10}	2.79×10^{10}	27	0
Bitumen Gravel/NA4	8.06×10^{10}	2.78×10^{10}	27	0
Bitumen Gravel/AM3	8.05×10^{10}	2.77×10^{10}	27	0
Bentonite/K3	1.98×10^{9}	7.99×10^{8}	6	50000
Bentonite/AM3	1.98×10^{9}	7.99×10^{8}	6	50000
Bentonite/NA3	1.98×10^{9}	7.99×10^{8}	6	50000
Bentonite/A3	1.98×10^{9}	7.99×10^{8}	20	50000
Bentonite/K2	1.98×10^{9}	7.99×10^{8}	6	50000
Bentonite/NA2	1.98×10^{9}	7.99×10^{8}	6	50000
Gravel/NA2	8.06×10^{10}	3.05×10^{10}	31	0
Salt Clay Mix/AM3	3.29×10^{11}	1.29×10^{11}	20	0
Salt Clay Mix/NA2	3.31×10^{11}	1.30×10^{11}	20	0
MgO Concrete/NA2	4.36×10^{13}	1.20×10^{13}	19	0

To simulate the effects of hydraulic loading in the shaft, a simplified approach was used. This approach consists of initializing a volumetric stress in the section of the shaft filled with water to mimic the effect of hydrostatic load. The initialization was carried out after 500 years in the base case simulation in the gravel column.

This allows for assessing the effects of water accumulation and hydrostatic pressure on the integrity of the shaft sealing system.

8.4.2 Initial conditions

An isotropic primary stress state is assumed, with an average integral density of the overlying geological layers of 2,200 kg/m³. This results in a calculated depth pressure of approximately 18.5 MPa at the repository level, which corresponds to the disposal depth. For the undisturbed rock temperature, a temperature gradient of 9 K per 100 m is assumed, leading to an estimated temperature of 38.67 °C at the disposal depth. At the upper boundary of the model, a constant air temperature of 9 °C is used as a boundary condition. A convective heat flux q_c is applied at the ground surface, with a heat transfer coefficient of α = 8.7 $Wm^{-2}K^{-1}$, following the methodology outlined in Bertrams et al. (2020).

The thermal evolution of the repository is primarily driven by the heat generated from the disposal of waste. In the model, this is represented by a transient heat source, where all the disposal drifts are homogenized into broader disposal fields, acting as the heat sources. The cumulative thermal output of all disposal drifts is summed and applied to these heat sources, capturing the thermal effects of waste disposal on the surrounding rock.

During the backfilling of the shaft, gravitational forces due to the weight of the material act as the primary driving forces. A lateral earth pressure coefficient of 0.5 is applied to account for horizontal stresses within the backfilled materials along the shaft. This coefficient represents the ratio of horizontal to vertical stresses and is crucial for understanding the stress distribution along the shaft.

Additionally, a silo effect is anticipated within the gravel column. The silo effect refers to the behavior of granular materials within a confined space, such as a column, where the material at the center of the column experiences less vertical pressure due to frictional forces at the walls, causing uneven stress distribution. This effect influences the way vertical loads are transferred down the shaft and contributes to the horizontal and vertical stress profiles along the column.

The silo effect is characterized by a reduction in vertical pressure due to the friction between the column walls and the backfill material, which supports part of the load. The vertical stress at any point in the gravel column can be calculated using Janssen's equation for silo pressures:

$$\sigma_v(z) = \frac{\rho g D}{2\mu(1-K)} \left[1 - \exp\left(-\frac{2\mu(1-K)z}{D}\right)\right]$$

Where:

- σ_v(z) is the vertical stress at depth z,
- ρ is the density of the backfill material (in kg/m³),
- g is the gravitational acceleration (9.81 m/s²),
- D is the diameter of the shaft,

- μ is the coefficient of wall friction,
- K is the lateral earth pressure coefficient, and
- z is the depth below the surface.

The results of this calculation provide a vertical stress profile showing a gradual reduction in stress with depth due to the silo effect. This stress distribution helps to explain the behavior of the gravel column in terms of load-bearing and settlement.

8.4.3 Constitutive models

The constitutive models applied to simulate the geological formations surrounding the repository have been described previously in Section 7.5.3. For the shaft sealing system, however, different constitutive models were used, each selected based on the specific mechanical and hydraulic behavior of the materials involved. Figure 8.-5 provides an overview of all constitutive models employed in the numerical model.

For the simplest material at the top of the shaft — the plug concrete — a linear elastic model was used. This is suitable for the plug concrete, given its limited deformation and the relatively low demands on its mechanical behavior compared to other components.

Gravel Column and Bitumen Gravel: The gravel column and bitumen gravel were modeled using the Mohr-Coulomb constitutive model. This model is appropriate for granular materials that exhibit significant plastic deformation once their yield criterion is met. The Mohr-Coulomb model captures the behavior of these materials under shear stress and accounts for the cohesionless nature of the gravel and bitumen gravel mixture.

Salt-Clay Mixture: Similarly, the salt-clay mixture was also modeled using the Mohr-Coulomb criterion. The presence of salt and clay minerals in this mixture introduces both cohesion and internal friction, characteristics well captured by the Mohr-Coulomb approach. This model accounts for the shear strength of the salt-clay mixture, which is important for understanding how the material behaves under loading, particularly when subjected to high stress and compaction conditions.

MgO (Sorel) Concrete: For the Sorel concrete (MgO concrete) at the bottom of the shaft, a more advanced constitutive model based on the Drucker-Prager criterion was used. This model was specifically adapted for MgO concrete using experimental results. The Drucker-Prager model extends the Mohr-Coulomb model by providing a smooth yield surface, making it more suitable for materials like MgO concrete that exhibit more complex plastic flow under triaxial stress conditions. The mechanical behavior of MgO concrete is crucial for the long-term performance of the sealing system, as it must resist deformation while maintaining its sealing function. This model, including its parameters, was detailed in Section 7.5.3.

Bentonite: The constitutive model for bentonite was selected based on its hydrological-mechanical properties. Bentonite, known for its swelling capacity when hydrated, was modeled using the Cam Clay constitutive model. The parameters for this model were derived based on a more advanced hydrological-mechanical model for bentonite, developed by **?**, which accurately captures the material's behavior under different saturation and stress conditions. This model is particularly effective in representing the swelling and plastic deformation of bentonite during

the hydration phase. After saturation, the behavior of bentonite resembles that of other clays, making the Cam Clay model an appropriate choice for simulating its plasticity under mechanical loading.

The Cam Clay model accounts for the nonlinear elastic behavior of bentonite under low stresses and its transition to plastic flow under higher stresses. It includes a yield surface that evolves with plastic strain and takes into consideration the consolidation behavior of bentonite as it absorbs water and increases its volume. This model allows for a realistic simulation of the stress-strain relationship of bentonite under both saturated and unsaturated conditions, capturing the essential hydrological-mechanical coupling that affects the sealing performance of bentonite over time.

Table 8.-2 provides an overview of the material properties and parameters used for each component in the shaft sealing system. These parameters are critical for ensuring that the numerical model accurately captures the behavior of each material under the expected loading and environmental conditions over the long-term evolution of the repository.

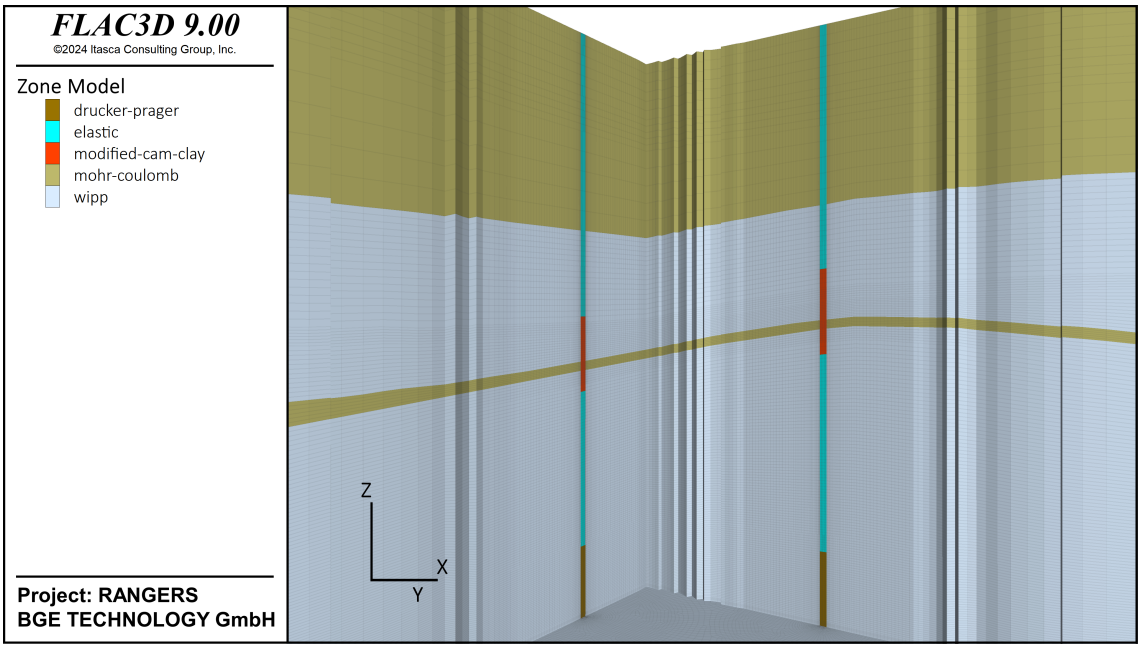

Figure 8.-5: Constitutive material models used in the numerical model.

Table 8.-2: Mechanical Properties of Backfill Materials.

Backfill	**Const. Model**	**Density,** ρ [kg/m^3]	**Young's modulus,** E [MPa]	**Poisson's ratio,** ν	**Cohesion,** c [MPa]	**Friction angle,** φ [°]	**Tension limit,** σ_t [MPa]
Bentonite	Mohr-Coulomb	1700	20	0.45	1.0	8	0
Gravel	MC	1700	200	0.32	0	40	0
Bitumen Gravel	MC	2238	200	0.45	0	40	0
Salt clay	MC	2300	800	0.27	0	40	0
Concrete	Elastic	3490	31.8	0.372	-	-	-

8.5 Numerical results

8.5.1 Reference modeling case

To illustrate the numerical results that highlight the thermal-mechanical impacts on the shaft sealing system, we begin by examining the overall thermal-mechanical evolution of the repository system. This foundational analysis provides insight into how thermal and mechanical processes interact within the repository, setting the stage for understanding their specific effects on the integrity and performance of the shaft sealing components.

Figure 8.-6 illustrates the temperature evolution along a longitudinal cross-section through the shaft 1 of the repository system over time, with time steps at 150, 500, 1,000, and 1,600 years. In the figure, we see the gradual propagation and dissipation of heat from the waste emplacement fields into the surrounding salt formation.

At a time of 150 years, the heat is concentrated around the waste emplacement fields where the temperatures reach 400 K (127 ℃). This temperature is lower than the temperature criterion of 200 ℃ due to the homogenization of the heat source all drifts in the emplacement field into a heat panel. The surrounding areas to the emplacement fields show temperatures in the range of 360 to 380 K near the waste. Beyond this zone, the region in green with temperature in the range of 320 to 340 K shows a temperature domain resulting from the thermal superposition of the heat coming from the different emplacement fields in each wing. Beyond this zone, the temperature decreases quickly, with blue areas indicating regions close to the baseline temperature of 282 K.

At a time of 500 years, the thermal impact has spread further from the waste emplacement areas, with a larger region affected by elevated temperatures. The red zones near the emplacement fields have started to reduce slightly in intensity, while surrounding areas in green and yellow show an expansion, now reaching temperatures between 320 and 360 K. The heat propagation shows a more extended impact in the salt formation.

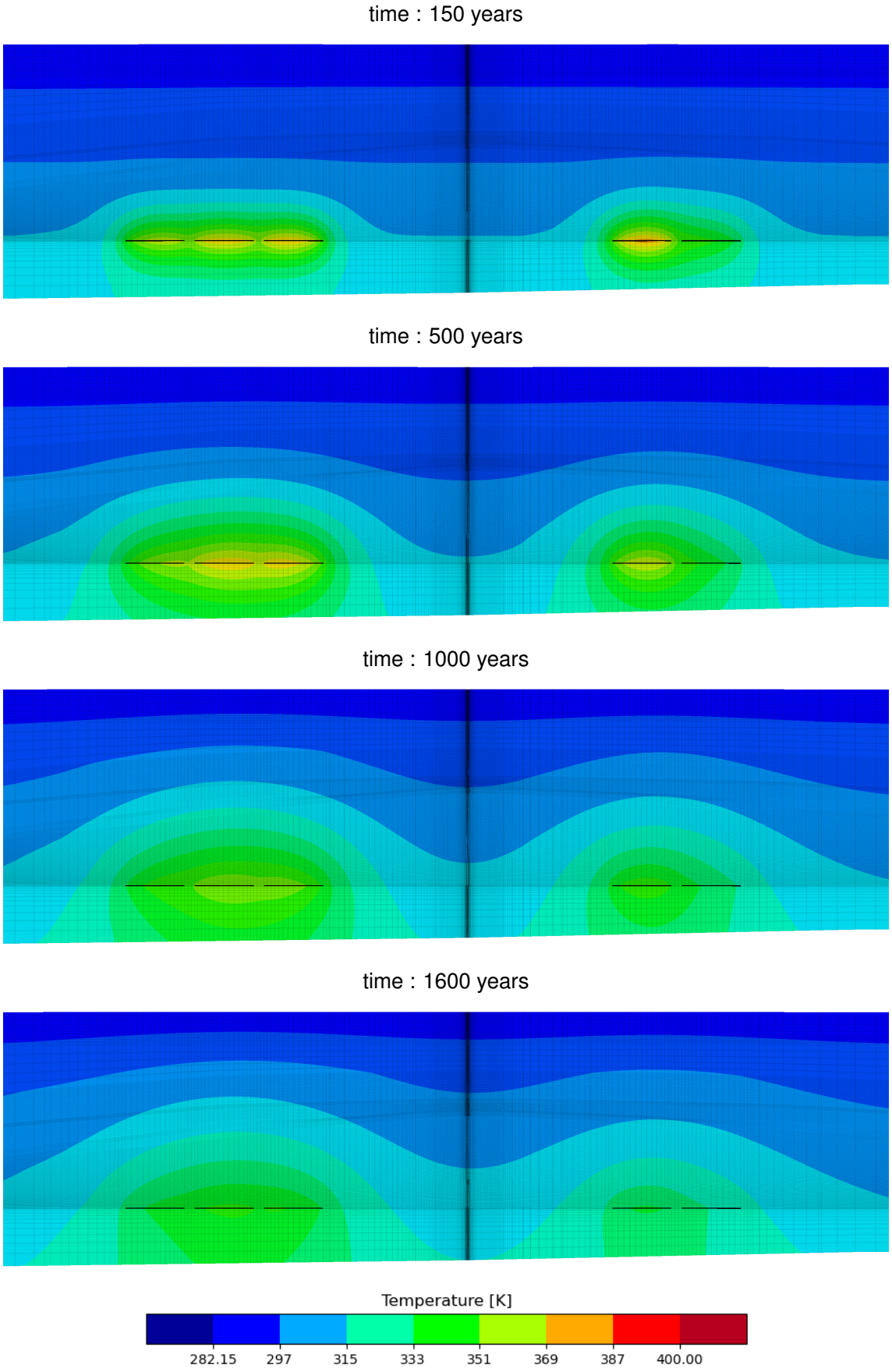

Figure 8.-6: Temperature distribution over time in the repository system.

At a time of 1,000 years, the peak temperatures in the emplacement areas have decreased further, with fewer red regions, and the dominant colors are now yellow and light green, indicating temperatures around 320 to 360 K. The surrounding salt formation is increasingly impacted by thermal diffusion, with a broader area experiencing elevated temperatures compared to earlier stages.

At a time of 1,600 years: The repository's heat impact has largely dissipated by this point. Temperatures throughout the cross-section are now predominantly in the green and blue range, indicating a decrease to the range 300 to 320 K near the waste and close to ambient temperatures further out. The heat source has significantly cooled, and the temperature across the repository system is approaching equilibrium with the surrounding formation. At this stage, the thermal process was deactivated, effectively "freezing" the remaining heat within the formation. This approach was implemented to reduce computational costs, allowing the simulation to proceed with a focus solely on mechanical processes. By doing so, the simulation was able to extend over a much longer period, reaching up to 25,000 years, while maintaining computational efficiency.

Overall, this temperature evolution illustrates the gradual cooling and dissipation of heat from the repository over time. Peak temperatures in the waste emplacement areas decline while the thermal impact expands outward initially, then diminishes as heat continues to diffuse into the salt formation. By 1600 years, the system is approaching thermal stabilization. Up to the end of the thermal simulation, the shaft region remains almost unaffected by the thermal evolution. At a time of 1,600 years, only the bottom experiences a minor temperature increase.

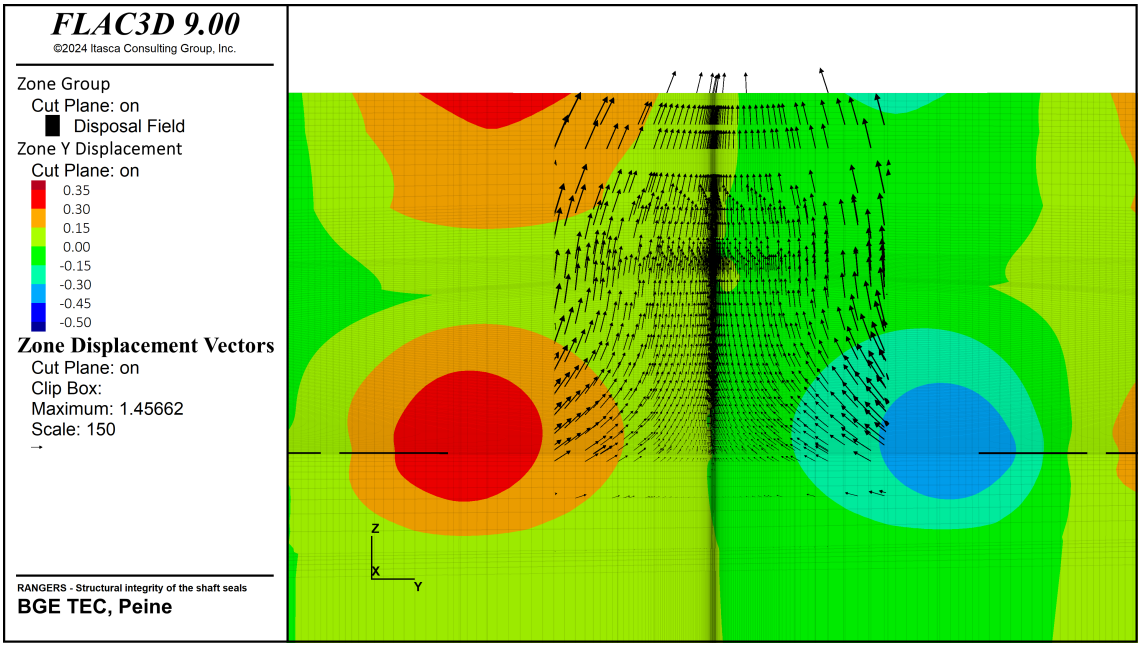

Figure 8.-7: Y-displacement distribution and displacement vectors near the shaft at 500 years.

The influence of temperature on the mechanical behavior of the rock is clearly illustrated by examining the displacement vectors in the cross-sectional view of the repository. This is shown in Figure 8.-7, which displays both the distribution of displacements along the y-direction and the displacement vectors within the rock formation surrounding the shaft.

In the disposal fields on either side of the central shaft, zones of significant displacement are observed in red and orange, indicating areas of intensified movement near the heat sources. This displacement is primarily due to thermal expansion resulting from the heat generated by the waste. The displacement vectors further illustrate the movement of the rock mass, showing a parabolic trajectory as the rock on both sides of the shaft is pushed outward due to thermal effects and then moves inward toward the shaft.

As the rock approaches the shaft, the displacement vectors shift direction, showing a nearly vertical movement near the shaft walls. This vertical trajectory suggests that the shaft itself is being lifted by the surrounding rock mass, indicating an upward displacement due to thermal expansion in the disposal fields. Additionally, this pattern implies a compaction in the horizontal direction, as the rock mass is forced inward toward the shaft.

This analysis reveals that the shaft is likely to experience vertical elongation, accompanied by horizontal compaction. These displacement patterns provide critical insight into the thermal-mechanical behavior of the rock formation and the resulting stress conditions within the shaft sealing system.

Figure 8.-8 illustrates the evolution of vertical displacement (z-direction) in a longitudinal cross-section of the repository system over several time periods. The figures reveal that thermal expansion of the rock mass causes significant uplift within the formation, with the effect most pronounced in the central region, particularly above the left emplacement wing. In this area, displacement values exceed 1.5 meters. This uplift is less prominent above the right emplacement wing, where predominantly lower heat-generating waste has been disposed, as indicated in the previous temperature evolution analysis.

At 500 years, the central part of the formation exhibits noticeable vertical displacement, forming a concentrated circular zone of high displacement values (shown in red and adjacent colors) that reaches up to 1.5 m. This red zone indicates a region of maximum displacement and suggests that the central area undergoes the most substantial vertical adjustment due to sustained thermal loading from the disposal fields. The displacement primarily results from thermal expansion of the rock mass, driven by heat generated by the waste.

As the simulation progresses to 1,000 years, the displacement in the central region intensifies, and the area with high displacement values expands, reflecting the continuing thermal and mechanical impact on the surrounding rock. The distribution of high displacement values suggests that the heat continues to exert a strong influence on the formation's mechanical response.

By 10,000 years, a shift is observed: the size of the high displacement zone begins to decrease in the vertical direction, while horizontally, the zone experiencing significant displacement (represented in green) expands. This suggests a redistribution of displacement as the thermal impact on the rock formation stabilizes.

At 25,000 years, this pattern persists because the thermal process in the model was deactivated at 1,600 years, freezing the heat distribution within the formation. Consequently, the remaining thermal energy maintains constant conditions, causing the displacement to stabilize while still exhibiting the lasting effects of the initial thermal expansion. Although the thermal effects remain constant, the mechanical evolution still evolves due to creep of the rock.

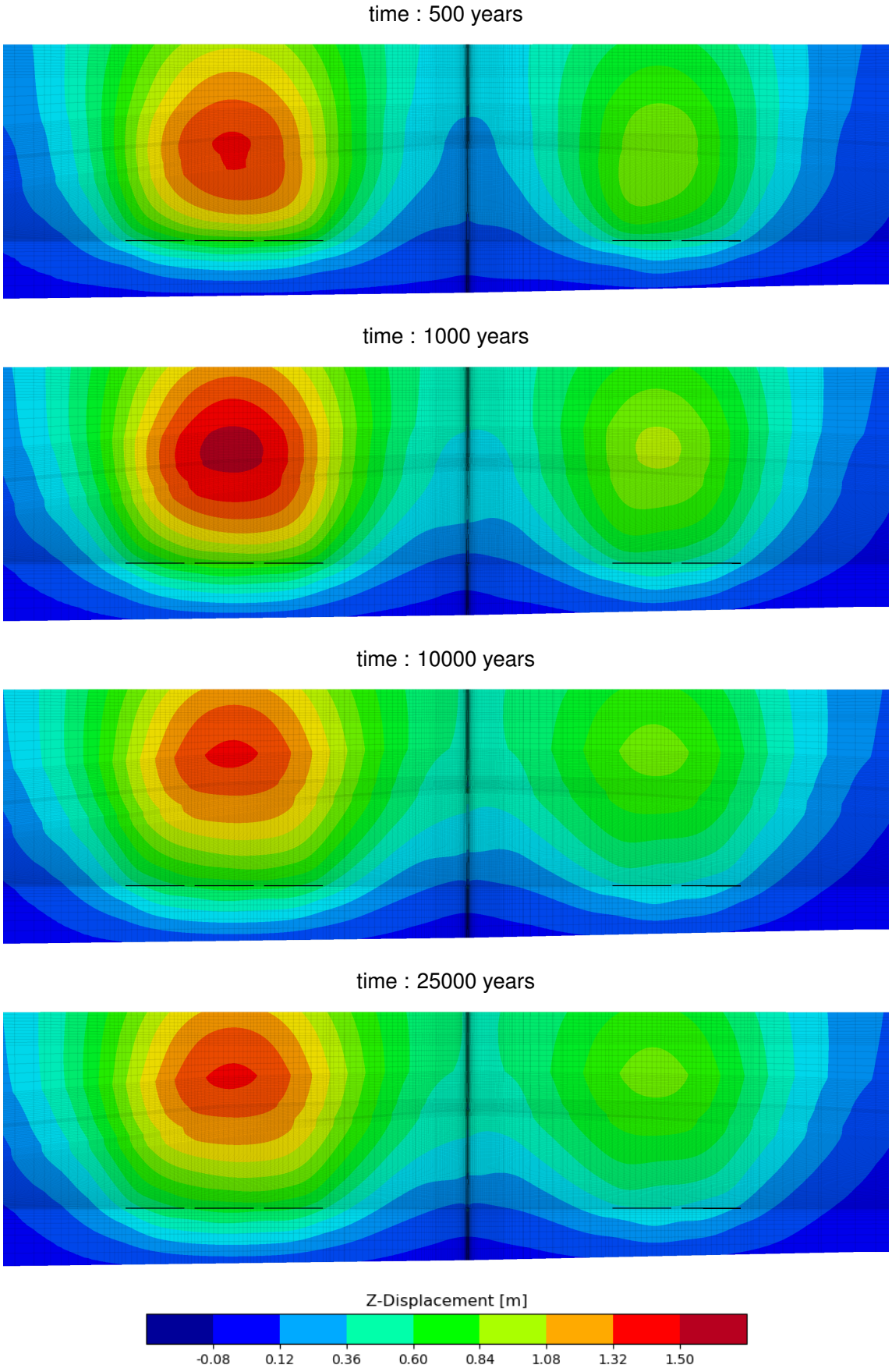

Figure 8.-8: Z-displacement distribution over time in the repository system.

Figure 8.-9 illustrates the evolution of octahedral stress along a longitudinal cross-section of the repository system over the simulation time periods. This stress distribution provides valuable insights into the mechanical response of the surrounding rock to thermal and structural loads over time, with the thermal impacts from the waste disposal fields causing significant stress variations in the salt formation.

At 500 years, regions of high stress, represented by red and orange tones (above 9.0×10^5 Pa), appear in the central part of the salt formation, forming a distinct shear band that extends diagonally from the region above the emplacement wing down towards the shaft. This shear band effect is more pronounced on the left side due to the higher thermal load generated by more heat-producing waste in that section. The observed stress concentration is primarily due to thermal expansion within the central rock mass. As the rock dilates under thermal influence, its expansion is constrained by the stiffer anhydrite layer, leading to significant shear stresses at the contacts with or near this layer.

At 1,000 years, the stress distribution shows a notable reduction in intensity, with the diagonal shear bands diminishing in the central region of the formation. This stress relaxation is a direct result of salt's natural creep behavior, which is highly accelerated by the elevated temperatures in the formation. The creep allows stress to dissipate more rapidly, reducing the overall stress concentrations. As the thermal expansion still evolves, new red and orange high-stress zones are formed at the upper salt layer at the boundary to the overburden layers. The expansion of the rock salt is hindered at the contact to the non creeping overburden layer of Bunter Sandstone leading to the formation of new shear stress concentration.

By 10,000 years, the stress distribution has continued to spread out and decrease in intensity. The previously dominant red and yellow colored areas have completely vanished in exception of the anhydrite that remains highly stressed as this material does not exhibit creep to help it dissipate the stresses. The transition into green and yellow zones, corresponding to stress values between 5.0×10^5 and 8.0×10^5 Pa reflects the ongoing creep-driven dissipation of shear stresses and suggests that the surrounding rock is gradually approaching mechanical equilibrium.

At 25,000 years, most of the cross-section is represented in blue and green (below 5.0×10^5 Pa), signifying a return to lower stress values across the rock formation. Any remaining stress concentrations are minimal, highlighting the long-term relaxation of the system. By this stage, the repository environment has largely stabilized, with the salt rock nearing a mechanical state similar to its original condition. The area surrounding the shaft still shows some moderate shear stresses due to the interaction between the rock mass and the components installed in the shaft.

In summary, the octahedral stress evolution in the repository system demonstrates the initial dominance of thermal impacts from the waste disposal areas, which lead to significant shear stress, especially near stiffer geological layers like the anhydrite. However, these stresses dissipate progressively over time due to the natural creep behavior of salt, particularly under elevated temperatures. This evolution indicates that thermal loads are impactful in the short term but lessen substantially over the long timescales considered, allowing the repository to achieve a stable, low-stress state that supports the long-term integrity of the containment system.

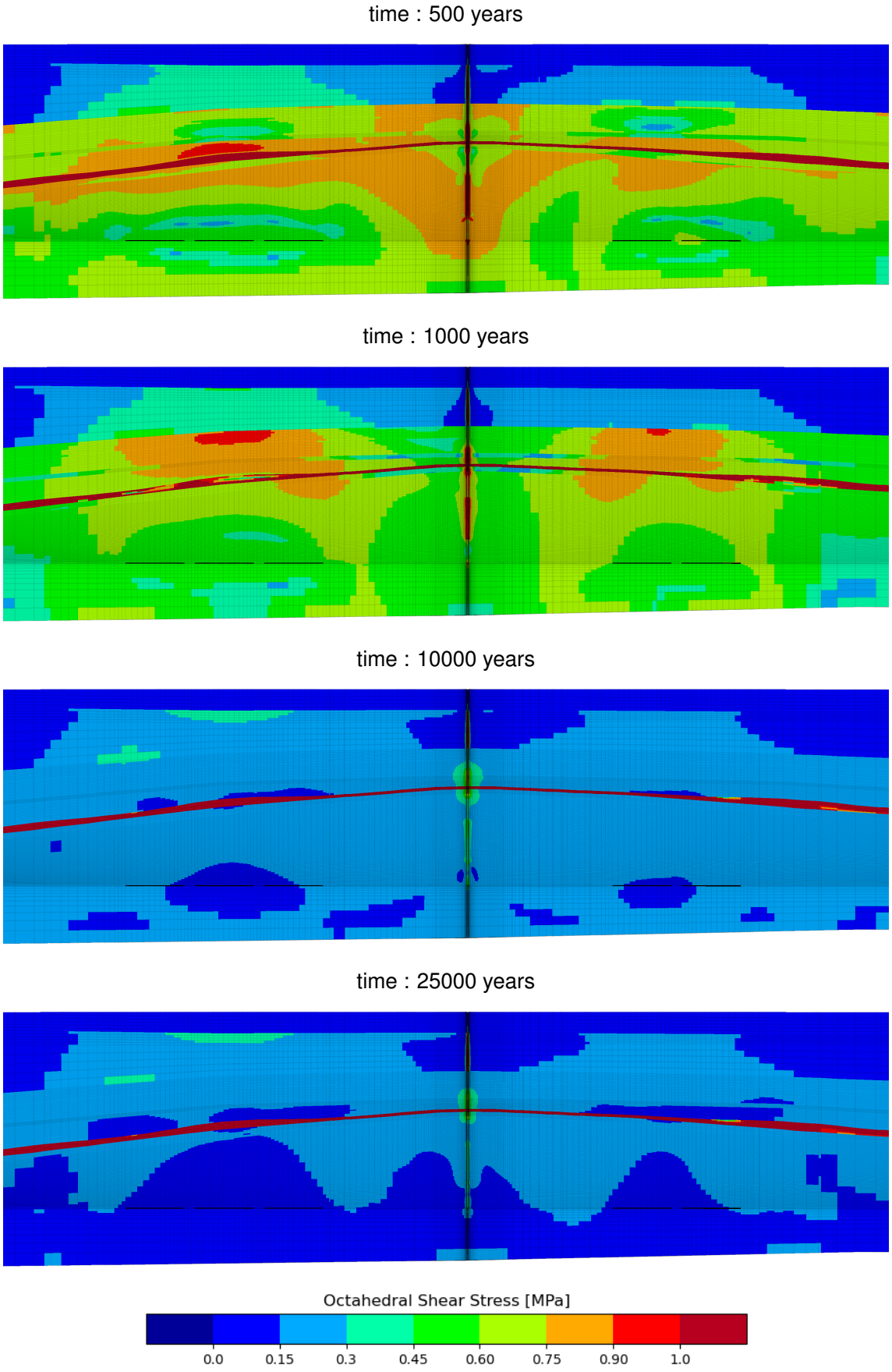

Figure 8.-9: Z-octahedral shear stress distribution over time in the repository system.

The modeling approach developed in the RANGERS project although intended for the integrity assessment of the engineered barrier system includes already all the necessary ingredients for evaluating the integrity of the geological barrier within the same model. This integrated approach enables simultaneous analyses of both the geotechnical and geological barriers, providing a more holistic view of repository stability over extended time periods.

To evaluate the geological barrier's integrity, we analyzed the dilatancy criterion across a longitudinal cross-section of the repository at various time intervals: 500, 1,000, 10,000, and 25,000 years, see Figure 8.-10. The dilatancy criterion serves as a key indicator of rock stability; it shows where the stress within the rock exceeds its threshold, leading to dilation, microfracturing, increased permeability, and, potentially, reduced confinement capability. A dilatancy criterion value of one or above signifies the onset of significant dilation, which could compromise the geological barrier's integrity.

In the early stages, at 500 and 1,000 years, minor dilatancy values of approximately 0.2 to 0.3 are observed in the upper layers of the salt formation. These zones correspond to areas of previously identified shear stress concentration, which likely results from thermal expansion effects generated by the repository's heat output. However, these dilatancy values remain well below the critical threshold of one, indicating that only minor dilation occurs, insufficient to create significant pathways for fluid migration or compromise the barrier's function.

Below these upper layers, the majority of the salt formation remains unaffected, as indicated by the blue color in the figure, representing a dilatancy criterion value close to zero. This suggests that most of the salt mass in the geological barrier remains stable and unlikely to experience dilation or increased permeability under the stress conditions modeled.

As the simulation progresses to 10,000 and 25,000 years, the entire rock mass shows a recovery in stress conditions, with no areas exceeding the dilatancy threshold. The absence of zones with elevated dilatancy values at these later stages demonstrates the self-healing potential of the salt formation, where creep and consolidation gradually reduce stress concentrations. By 25,000 years, the rock structure has stabilized, with no signs of dilatancy, confirming the long-term integrity of the geological barrier.

This finding supports the robustness of the geological barrier in maintaining containment of the waste. The ability of the model to simulate both the engineered and geological barrier systems within a unified framework provides a powerful tool for comprehensive safety assessments. The results underscore the stability and self-sealing properties of the salt formation, reinforcing its suitability as a host medium for radioactive waste disposal. This approach also highlights the potential for further refinement and extension to other repository designs, where simultaneous modeling of engineered and geological barriers may enhance understanding of long-term containment performance.

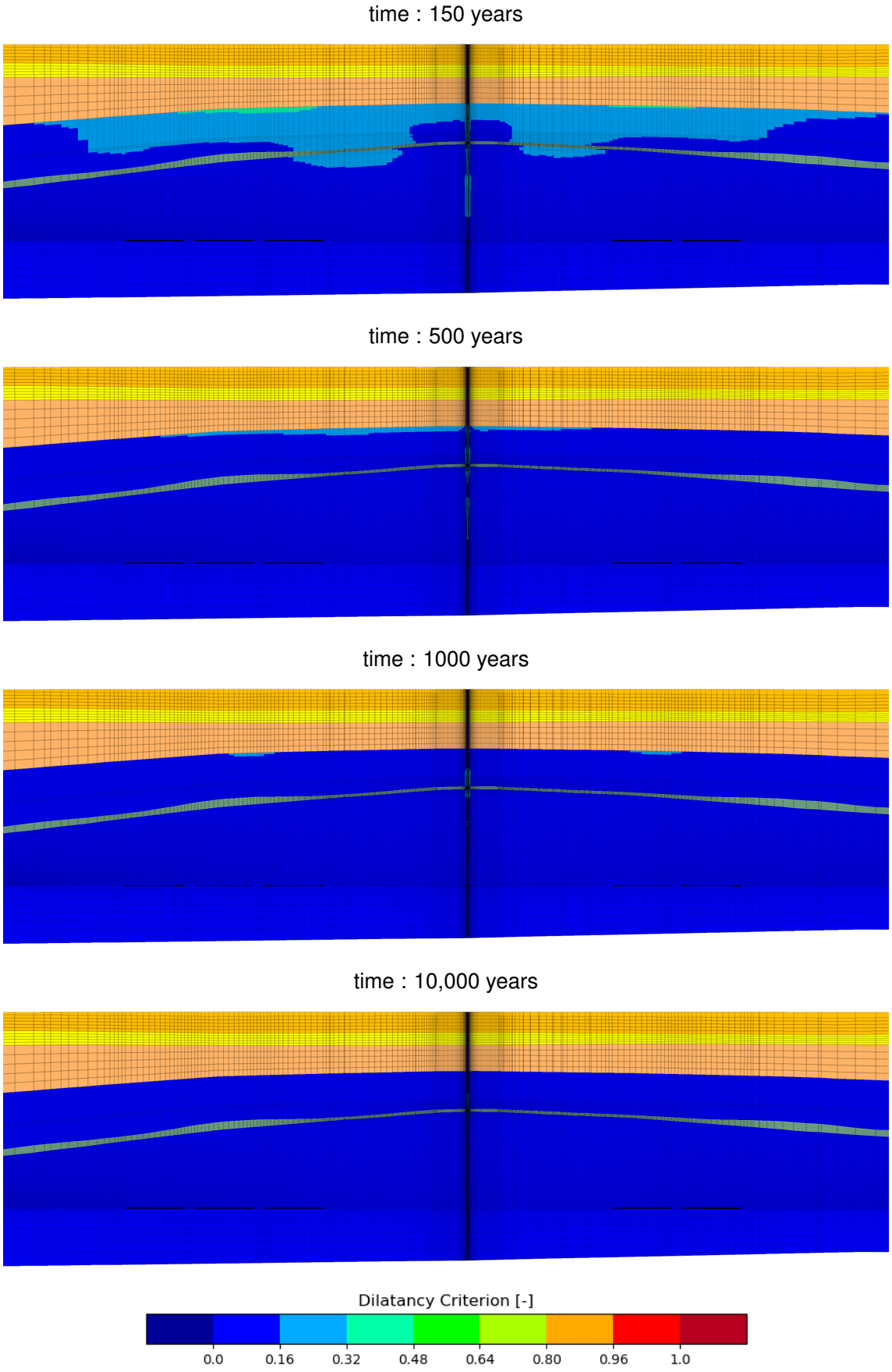

Figure 8.-10: Evaluation of the dilatancy criterion along a longitudinal cross-section of the repository system over different time periods.

In Figure 8.-11, the damage state in the non-creeping layers of the geological formation, specifically the overburden and anhydrite layers, is shown to evaluate the potential impact of thermal effects and salt thermal expansion. The analysis aims to determine if these non-creeping geological layers might experience structural damage due to the stresses induced by the repository's heat.

The figure reveals that the anhydrite layer, located above the emplacement fields, does indeed show localized damage, indicated by pink areas. This damage is confined to regions directly above the disposal areas, where thermal expansion of the salt leads to increased stress in the overlying anhydrite. Importantly, however, the damage remains limited in spatial extent, without extending across the full width of the formation. This localized damage suggests that while the anhydrite layer is affected by the thermal expansion, it does not create continuous fracture paths or secondary migration pathways for fluid movement through the anhydrite.

In conclusion, while thermal expansion generates sufficient stress to cause minor damage in specific zones of the anhydrite layer, this effect is spatially restricted and does not compromise the integrity of the geological barrier as a whole. The confinement of damage within localized areas minimizes the potential for fluid migration, indicating that the geological barrier remains effective in isolating the repository over the assessed period.

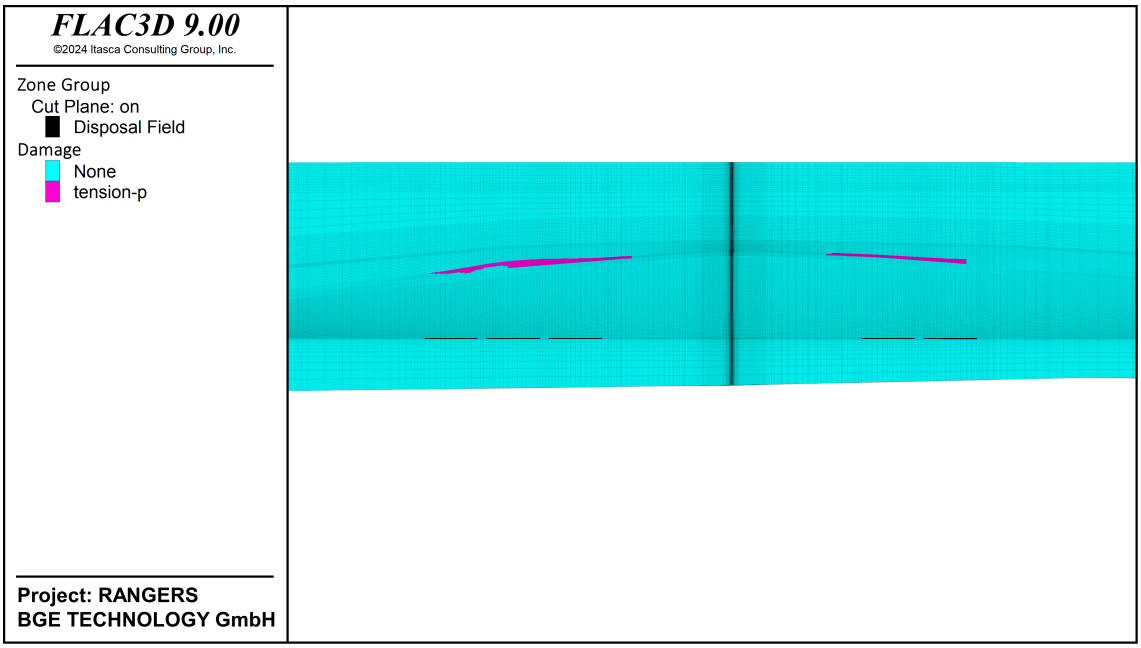

Figure 8.-11: Damage in the anhydrite layer at 25,000 years.

We now turn our focus to the thermal-mechanical evolution in the near field of the shaft to assess its impacts on the shaft sealing structure.

Figure 8.-12 illustrates the distribution of displacement in the x-direction within the near field around the shaft. In the upper part of the shaft, the x-displacement is primarily driven by the lateral expansion of the entire geological formation due to thermal effects. This thermal expansion of the rock mass induces outward displacement, which is evident in the shaft's surrounding regions. In contrast, the lower part of the shaft shows displacement patterns dominated by the lateral expansion of the salt rock itself, creating additional lateral pressures

on the shaft structure.

In this lower region, the displacement field around the shaft exhibits a symmetrical pattern, suggesting that the shaft sealing structure is subject to compaction forces from both sides. This compaction effect is critical as it influences the stability and integrity of the shaft sealing structure over time. Notably, along the length of the MgO seal, there is an absence of lateral displacement, attributed to the high stiffness of the MgO concrete, which effectively resists deformation and maintains stability in response to lateral pressures.

Overall, this displacement pattern indicates that the shaft and its immediate surroundings experience significant lateral stresses. These stresses, arising from thermal and mechanical expansion, have to be taken into account in the integrity and design of the sealing components in the shaft.

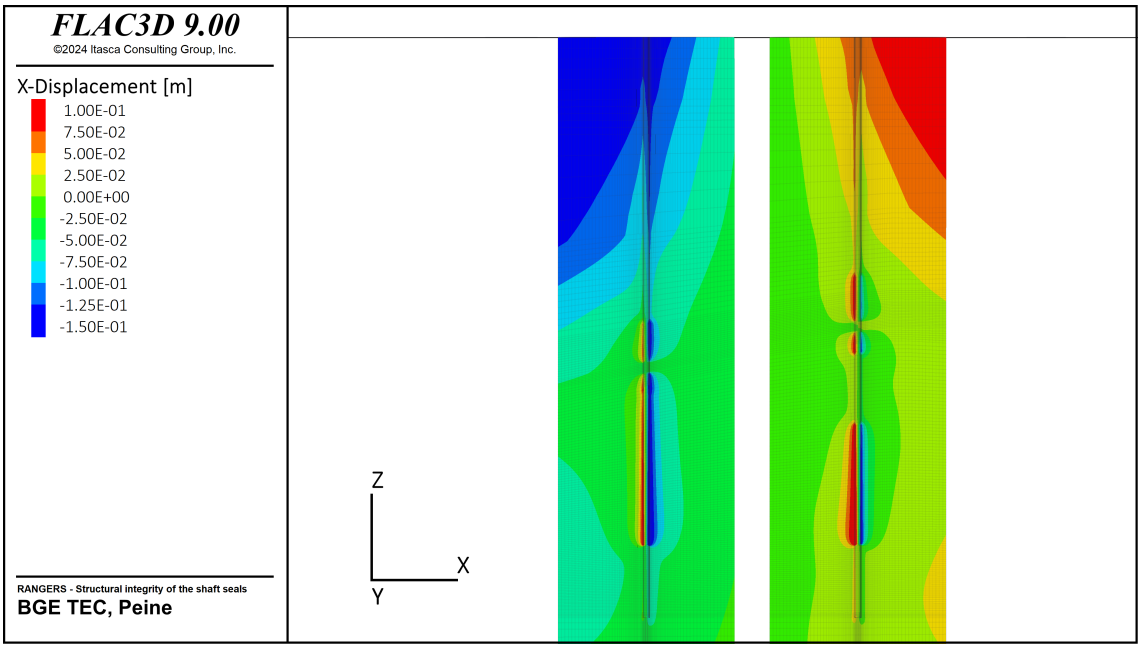

Figure 8.-12: X-displacement distribution in the near field of the shafts at 25,000 years.

Figure 8.-13 illustrates the distribution of displacement in the z-direction (vertical) within the near field around the shafts at the end of the simulation at 25,000 years.

In the upper part of the formation near the shaft, the displacement reaches substantial values exceeding 50 cm, with a near-symmetrical distribution along the shaft's length. The displacement is particularly high near shaft X, which is closer to the emplacement fields. This pronounced vertical displacement primarily results from the thermal expansion of the rock mass, which exerts upward pressure as it heats up over time. The upward movement is most intense near the surface, gradually diminishing with depth. This trend is illustrated by the transition from red and orange in the upper regions to yellow and green tones further down the shaft, indicating a reduction in displacement.

In contrast, the lower part of the shaft exhibits relatively minimal displacement, marked by blue and green areas with values up to 20 cm. This reduced displacement reflects the cumulative nature of rock expansion. Near the thermal source, where heat initially concentrates, expan-

sion is minimal, but it increases with distance from this focal point, leading to more significant displacement further along the shaft.

These observations indicate a generally uniform response to thermal expansion forces, with the shaft sealing structures experiencing vertical stresses that gradually lessen with depth. This displacement pattern suggests that the sealing components are primarily influenced by upward forces in the upper sections, where they are designed to provide stability, while facing reduced vertical displacement and stress in the deeper sections of the formation.

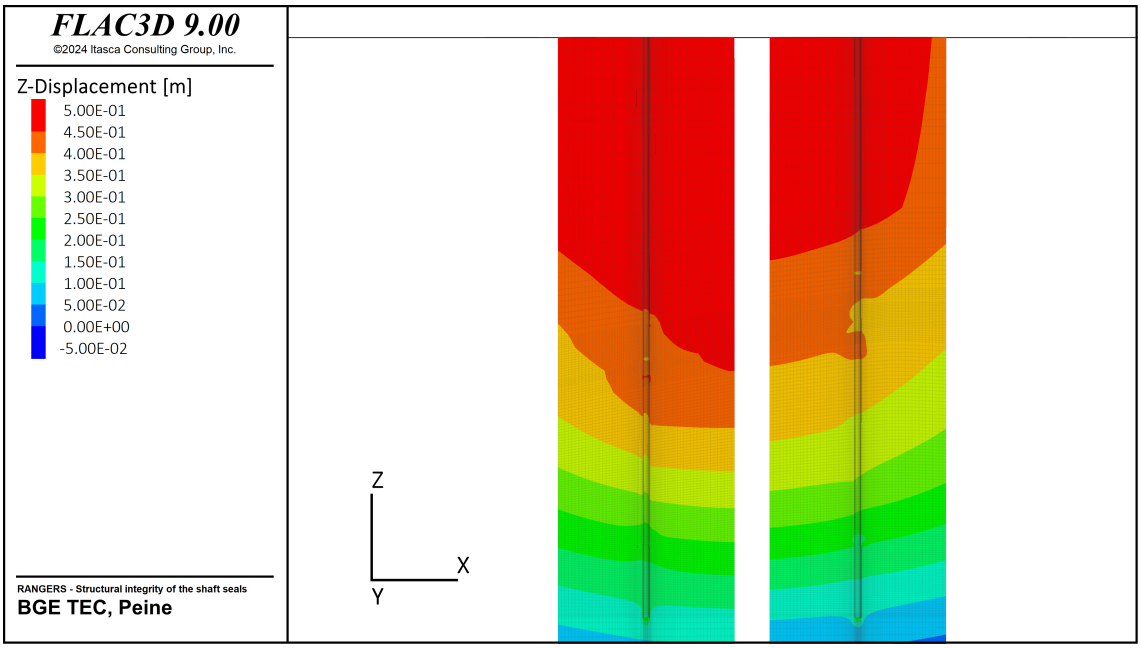

Figure 8.-13: Z-displacement distribution in the near field of the shafts at 25,000 years.

Figure 8.-14 illustrates the distribution of octahedral stress (Pa) within the shaft and surrounding rock, as observed in a cross-sectional view along the shaft's length. This distribution provides insights into how the shaft and its surrounding formations respond to thermal and mechanical loading over time.

In the upper part of the shaft within the overburden, there is a notable concentration of stress along the shaft contour, characteristic of an Excavation Damaged Zone (EDZ) typically induced by excavation processes. Moving into the upper portion of the salt formation, we observe a significant concentration of shear stress surrounding the bentonite sealing elements. This stress concentration is likely due to the bentonite being modeled as a highly plastic material, which lacks the structural rigidity to counteract the surrounding rock's deformations caused by the compression of salt as it undergoes thermal expansion. Consequently, the bentonite allows the rock's compressive movements, leading to elevated shear stress zones in its vicinity.

In contrast, the lower part of the shaft, where the sealing materials are primarily composed of gravel and MgO concrete, shows significantly reduced stress concentrations. The high stiffness of these materials effectively limits deformation, confining shear stress primarily to the immediate shaft contour and minimizing its spread into the surrounding rock. This rigidity allows the lower shaft components to better sustain the compressive forces exerted by the

expanding salt, helping to preserve the shaft's structural integrity.

Overall, the figure highlights how the combination of thermal expansion and overburden effects results in distinct stress zones within the shaft. Materials with low stiffness, such as bentonite, may contribute to increased shear stress zones due to their inability to fully resist the compressive forces of the surrounding rock. Conversely, high-stiffness materials like MgO concrete effectively reduce stress propagation, confining shear stress to a smaller area near the shaft contour. This stress distribution pattern provides valuable insights into the loading conditions the shaft sealing system is subjected to over time, informing material selection and structural design strategies for long-term shaft stability.

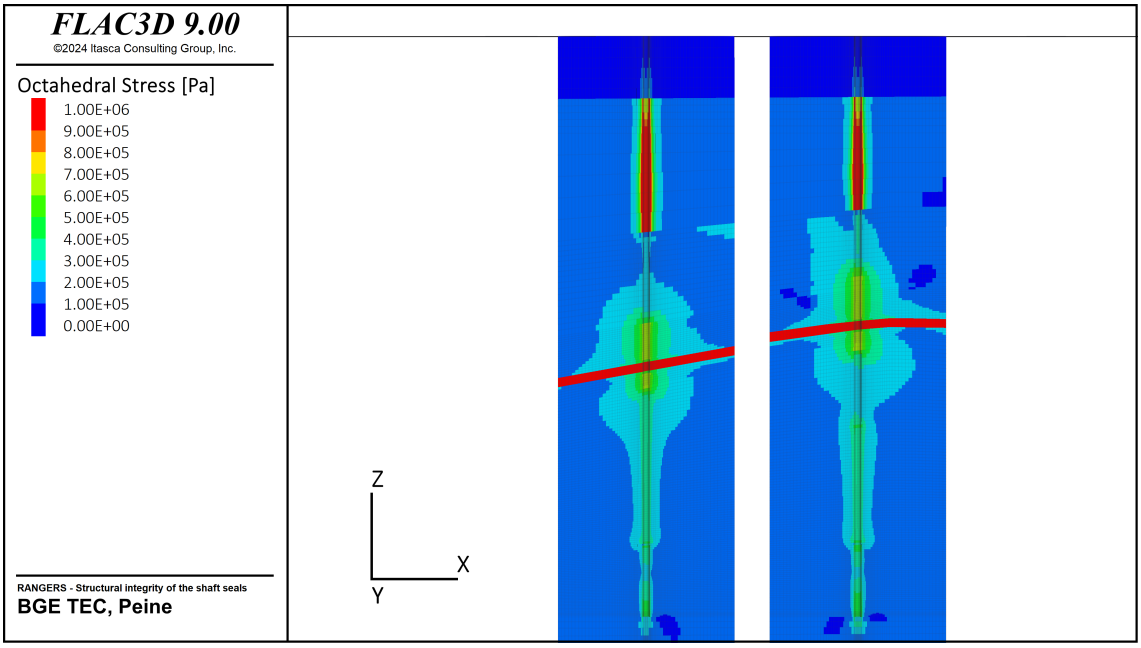

Figure 8.-14: Octahedral shear stress distribution in the near field of the shafts at 25,000 years.

Figure 8.-15 presents the distribution of the dilatancy criterion along the shaft and surrounding geological formations. This criterion indicates the regions where the rock has reached or surpassed its dilatancy threshold, signifying areas where micro-fracturing may begin, thus potentially increasing permeability and affecting stability.

The figure primarily highlights the salt formation itself, where dilatancy is a critical factor. In the vicinity of the shaft, particularly around the contact areas with the bentonite seals, we observe low dilatancy values in the range from 0 to 0.3. Outside of the bentonite length, no dilatancy is observed along the shaft. The low values of dilatancy along the bentonite seals correspond to the high shear concentration observed at this location. As previously discussed, this is due to the low stiffness of bentonite allowing movement of the rock. Nevertheless, these values indicate that the salt formation remains below the critical dilatancy threshold of 1, meaning it does not exhibit significant dilation or micro-cracking.

As time progresses, the salt rock at the contact zone to the shafts maintains its structural integrity with minimal changes in dilatancy values that is expected to vanish with time. This further demonstrating the stability of the salt formation under the applied thermal and me-

chanical loads. This stable condition in the salt formation indicates that the geological barrier remains intact, effectively preventing any secondary migration paths or zones of increased permeability along the shafts that could compromise the repository's containment function.

In conclusion, the results demonstrate that the salt formation can withstand the stress conditions surrounding the shaft without significant dilation, confirming its effectiveness as a long-term containment barrier.

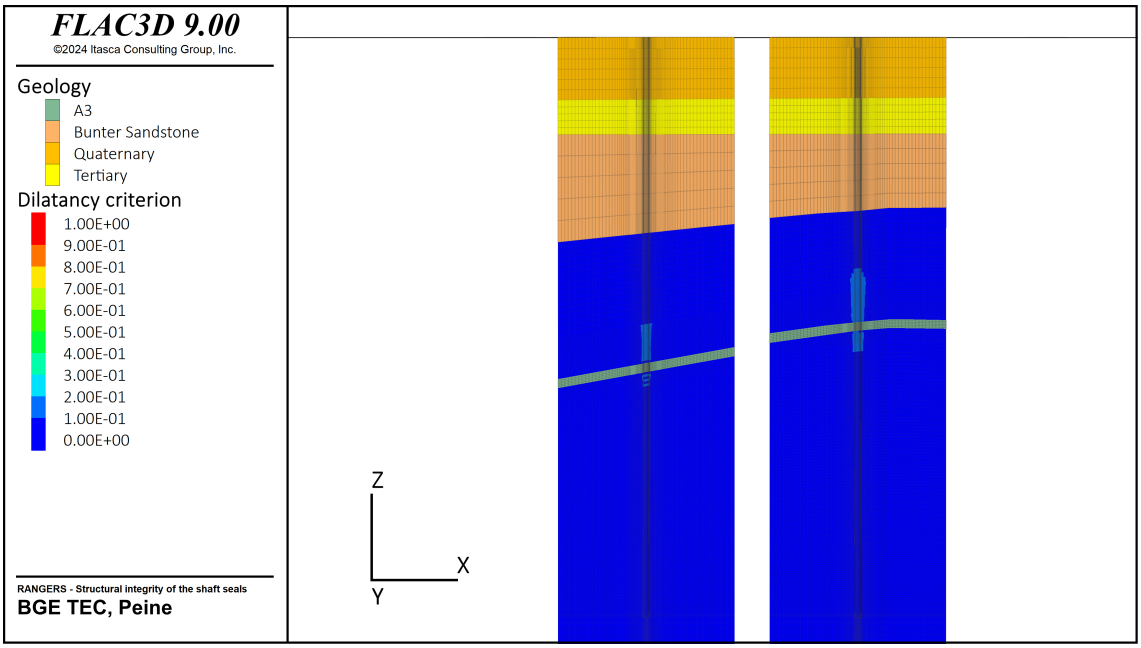

Figure 8.-15: Dilatancy criterion evaluation in the near field of the shafts at 25,000 years.

We now turn to analyzing the mechanical behavior of the shaft sealing system and its individual components in response to the thermal-mechanical evolution of the surrounding geological formation.

We have previously observed that the thermal expansion of the salt will cause a general upward displacement of the salt formation, extending up to the surface. This upward movement also affects the near-field area surrounding the shaft, as indicated in Figure 8.-13. Also it has been shown in Figure 8.-7 that the displacement vectors around the shaft are oriented upwards. Consequently, it is reasonable to conclude that the shaft sealing structure installed in both shafts will also undergo some degree of uplift.

Figure 8.-16 shows the vertical (z-direction) displacement distribution within the shaft sealing structure for both shafts. A displacement gradient is observed along the depth of each shaft, with the largest displacement occurring near the surface — up to 0.5 m — and decreasing to about 10 cm at the bottom of the shaft. This gradient indicates that thermal effects primarily impact the upper parts of the shafts, where the rock is undergoing significant vertical expansion. In contrast, the deeper sections of the shafts experience substantially less displacement. Similar patterns were noted for the near-field displacement around the shafts, as shown in Figure 8.-13.

The non-uniform displacement along the shaft implies that the shaft sealing structure is subject

to a stretching effect. As the salt formation undergoes thermal uplift, it effectively stretches the sealing structures within the shafts, leading to tensile forces along the shaft's length. This stretching indicates that tensile stresses are likely to develop within the shaft sealing system due to the differential displacement. This observation is crucial for the integrity assessment of the sealing system, as tensile stresses can potentially impact the sealing performance if not properly accounted for in the design.

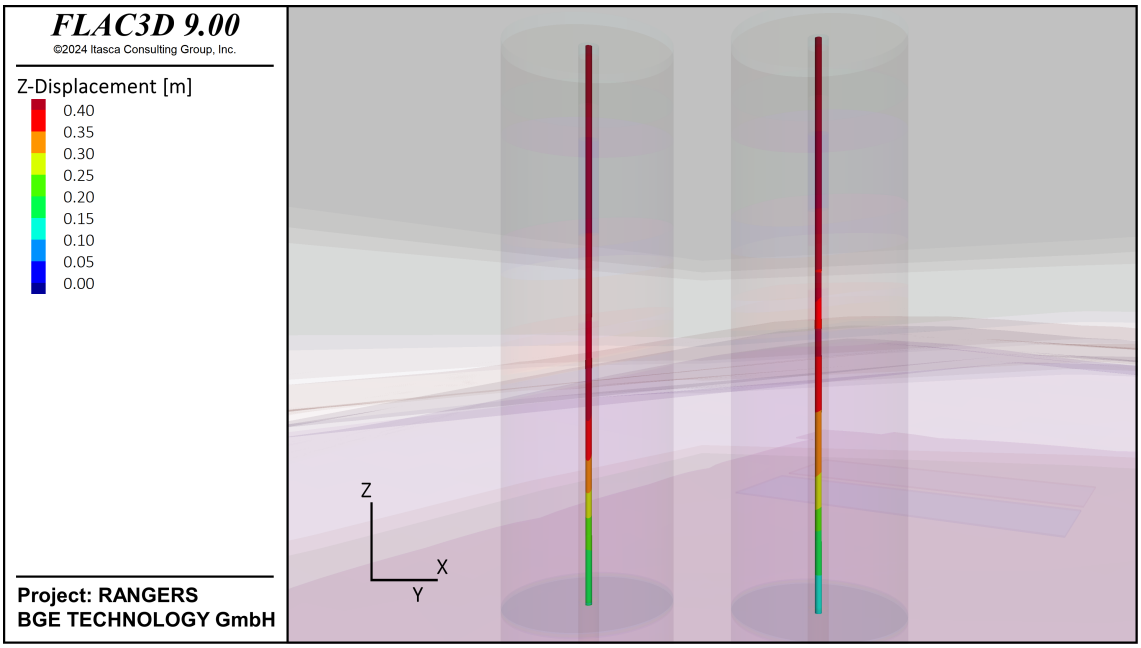

Figure 8.-16: Z-displacement distribution along the shaft sealing systems at 25,000 years.

To assess the impact of the stretching effect on the shaft sealing structures, we analyze the distribution of maximum principal stresses within the components installed in the shaft.

Figure 8.-17 presents the distribution of maximum principal stress (in Pa) along the shaft sealing structure in both shafts at the end of the simulation, at 25,000 years. This visualization provides insights into how stresses are distributed across the shaft sealing components, under the influence of thermal and mechanical effects from the surrounding rock formation.

In the upper sections of each shaft, where the gravel column is installed, the maximum principal stress reaches moderate values between 0 Pa and 2×10^6 Pa, indicating tensile stress in these areas. This tensile stress likely results from the thermal expansion and upward movement of the overburden rock. Notably, these tensile stresses are influenced by the modeling assumption of linear elasticity for the gravel column. In a real-world scenario, some loosening would likely occur within the gravel column, allowing it to accommodate the elongation due to stretching caused by the uplift of the surrounding rock mass.

Moving deeper into the shafts, the stress distribution becomes more nuanced. In the middle sections, the maximum principal stress generally decreases, falling within the range of -4×10^6 Pa to -6×10^6 Pa, indicating a shift from tensile to compressive forces. This transition is attributed to the low stiffness and probably the high confining pressure exerted by the surrounding salt formation, which counteracts tensile stresses and stabilizes the shaft structure.

At the lower end of the shafts, we observe a transition back to the tensile regime and a moderate development of tensile stresses in the MgO concrete seal in the right shaft. This effect is due to the high stiffness of MgO concrete, which cannot accommodate the uplifting forces generated at the shaft's boundaries, resulting in the buildup of tensile stresses. If these stresses exceed the material's tensile strength, they could lead to tensile failure, compromising the integrity of the sealing elements if cracks were to form.

Overall, the stress distribution reveals the potential for tensile stresses to develop within the shaft sealing structure as a consequence of the uplift of the surrounding rock due to thermal expansion. This mechanism poses a critical consideration for the design of shaft sealing systems, as it may necessitate material and structural adaptations to mitigate tensile stress and prevent potential failure within the shaft seals. This analysis underscores the importance of accounting for uplift-induced tensile forces in ensuring the long-term effectiveness and resilience of the shaft sealing system.

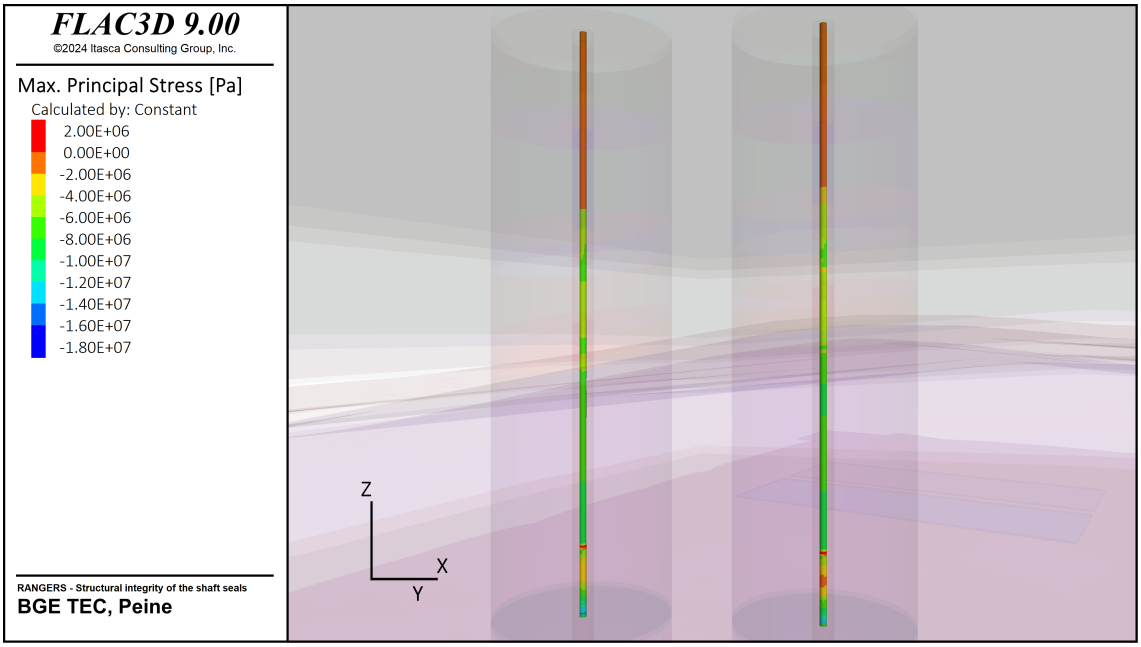

Figure 8.-17: Max principal stress distribution along the shaft sealing systems at 25,000 years.

Figure 8.-18 provides a view of the two shafts and their sealing structures, displaying the distribution of mean stress (in Pa) along the shaft length 25,000 years after the repository closure. The shafts are illustrated as vertical structures embedded within a semi-transparent representation of the geological model, allowing us to see the stress conditions within the context of the surrounding rock.

The figure reveals a clear distinction in confining pressure between the overburden and salt formation. In the overburden, consisting of sandy layers, the shaft sealing system experiences relatively low confining stresses. This is due to the non-creeping behavior of the sandy layers, which lack time-dependent deformation properties. However, in the salt formation, significantly higher confining pressures are observed, increasing with depth. This gradient reflects the combined effects of the surrounding rock's confinement and the thermal and mechanical loads exerted on the shaft, as previously discussed.

The results in the figure indicate that the main sealing elements — composed of bitumen gravel, a crushed salt/clay mixture, and bentonite — are subjected to confining pressures in the range of 4 to 10 MPa. Meanwhile, the MgO concrete seal and its abutment experience pressures between 12 and 18 MPa. These high confining stresses bring several advantages to the overall integrity and performance of the shaft sealing system.

Firstly, high confining stresses enhance the strength of the sealing materials, as it is well-known that the strength of materials increases under triaxial compressive loading conditions. This effect reduces the likelihood of failure in the sealing components, making them more resilient to various loading conditions. Secondly, the high confining pressures ensure that any potential micro-cracks or fractures within the sealing elements are likely to be closed or minimized. This includes closing of any voids that might have formed during installation or minor installation-related imperfections.

Furthermore, high confining stresses contribute to the long-term stability and robustness of the sealing system by compensating for potential human errors during installation. The pressure exerted on the materials aids in self-sealing processes, as it promotes compaction and densification of materials. This self-sealing effect, combined with the high confining pressure, creates an additional safety buffer that strengthens the barrier function of the shaft sealing system over time.

In summary, the presence of high confining pressures in the salt formation enhances the overall performance and reliability of the shaft sealing system. It increases material strength, promotes self-sealing of micro-cracks, and mitigates installation imperfections, thus reinforcing the shaft's role as a long-term containment solution for radioactive waste. It also emphasizes the quality of salt not as a host rock for radioactive waste but as a excellent medium for the installation of the EBS.

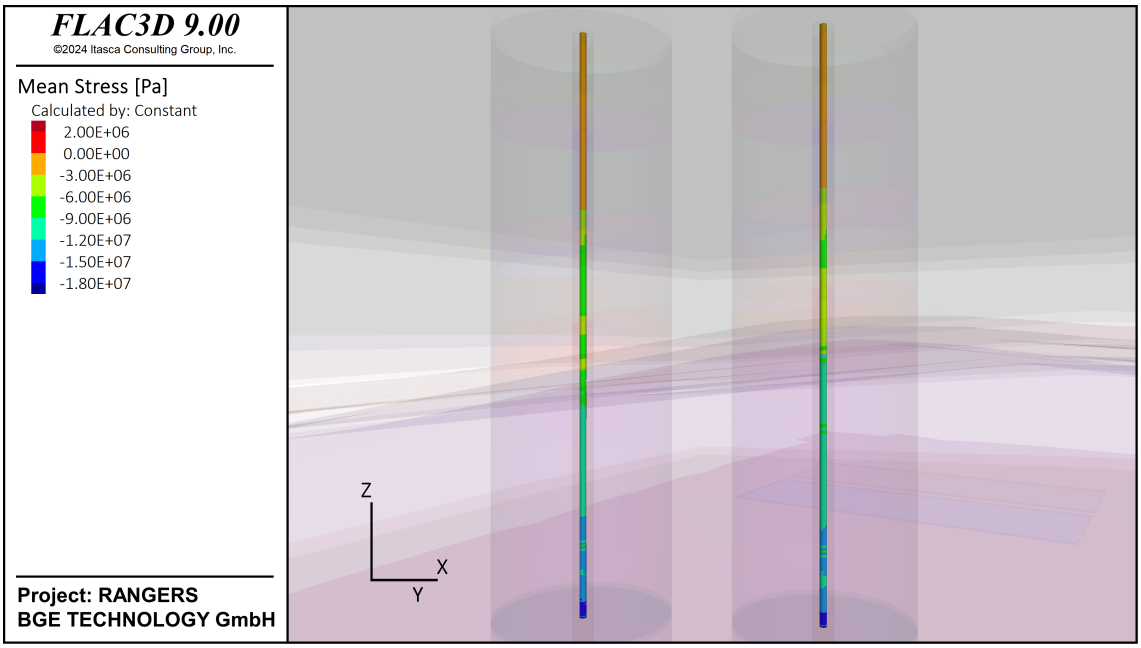

Figure 8.-18: Mean stress distribution along the shaft sealing systems at 25,000 years.

Figure 8.-19 also illustrates two distinct stress regimes concerning the development of shear

stresses along the shaft, which arise from similar factors as those discussed in the mean stress analysis. In the overburden, low shear stresses are observed due to the non-creeping, sandy nature of the upper layers. However, in the salt formation where the shaft sealing system is embedded, significantly higher shear stresses are present, distributed relatively uniformly along the depth of the shaft.

One notable exception is the bentonite element, which remains nearly stress-free. This is because bentonite, with its high plasticity, has been modeled to dissipate shear stresses through plastic yielding, effectively preventing the buildup of shear stress. The material's capacity to yield plastically allows it to absorb and redistribute mechanical loads, preventing stress concentration within this element.

Overall, the distribution of shear stress highlights the role of different materials within the shaft sealing system. For Stiffer materials in the salt formation, substantial shear forces are expected. They need to be designed to sustain those shear forces. For low stiff materials such as bentonite, their plastic behavior serves as a buffer, reducing stress transfer to other sealing components. This property enhances the system's overall resilience, as it helps prevent stress localization and potential damage to other elements within the shaft sealing structure. This balanced distribution of stresses contributes to the robustness and longevity of the sealing system under thermal-mechanical loads.

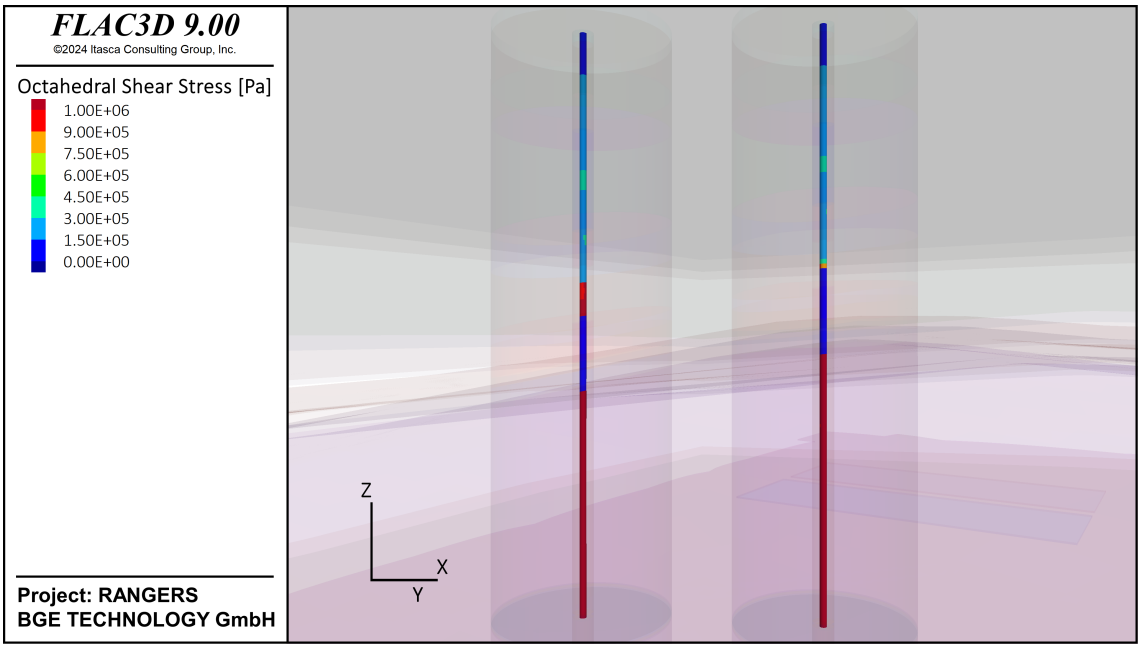

Figure 8.-19: Octahedral shear stress distribution along the shaft sealing systems at 25,000 years.

The effects of the stresses acting on the components installed in the shaft are reflected in the state of damage of these components, which is evaluated using constitutive models that describe their mechanical behavior. From the stress analysis discussed previously, two primary failure mechanisms emerge: tensile failure in the MgO seals, due to the tensile stresses arising from the extension of the shaft sealing structure, and shear failure in components experiencing high shear stresses. These potential failures are, however, mitigated by the high confining stresses acting on the materials, which help to counterbalance and contain these

stresses.

Figure 8.-20 illustrates the state of damage within the shaft sealing structure after 25,000 years. The results show that only the bentonite element undergoes plastic deformation, consistent with its design as a highly plastic material intended to yield and dissipate stress. All other sealing components remain structurally intact throughout the simulation period, indicating that the integrity of the system is preserved over the verification period. This outcome underscores the positive role of high confining stress, which enhances the triaxial strength of materials, thereby improving their resistance to both tensile and shear failures.

Overall, the results demonstrate that the engineered shaft sealing structure, under the given stress conditions, is capable of maintaining integrity over extended timescales.

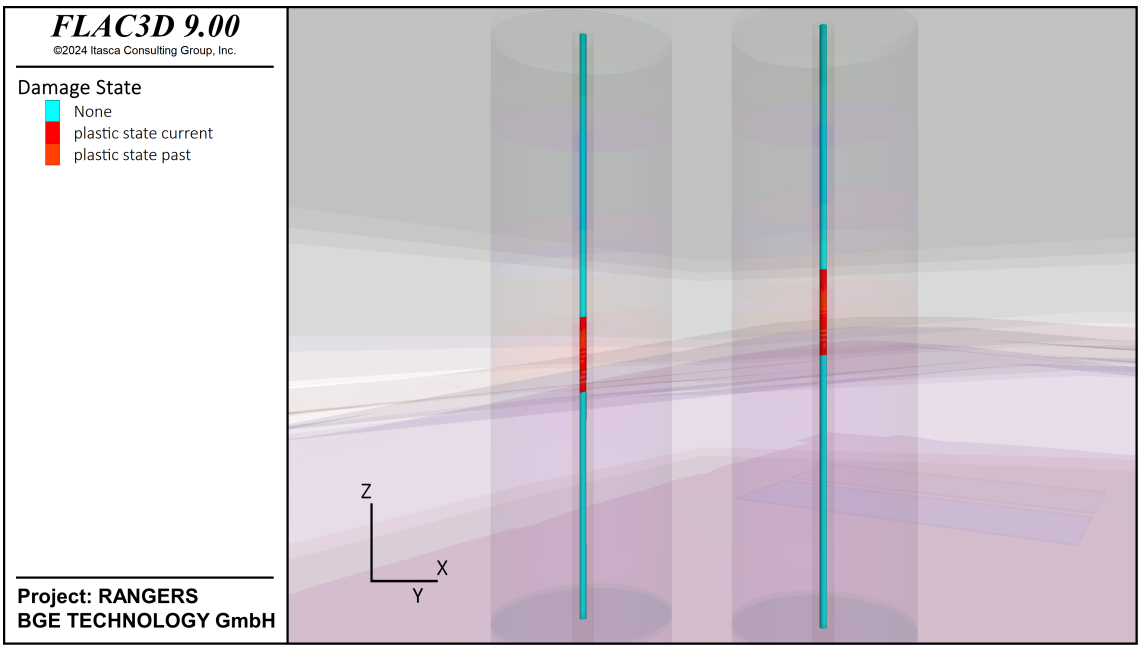

Figure 8.-20: Damage state in the shaft sealing systems at 25,000 years.

8.5.2 Modeling with Interfaces

A modeling case by using interfaces elements instead of rigid contact between the rock and the components in the shaft were carried out. This approach has the merit to be more realistic as the contact zone properties can be estimated through laboratory experiments.

Unfortunately using interfaces also bring another layer of numerical complexity and often fails when large deformation accumulate in the model. For this reason, we were able to run the simulation only for 150 years.

Fortunately, this period of time is good enough for benchmarking the reference approach using rigid contact and to understand what is going on at the contact zone.

For the benchmark, we compare the invariants of the stress tensor: mean stress of octahedral stresses. As it can be seen in figure 8.-21, only minor differences is remarkable between the mean stress distribution of the case with rigid contact, the case with interface. The same

can be concluded for the octahedral shear stress in Figure 8.-22. From this analysis on can conclude that the use of rigid contact which are numerically efficient are accurate enough to model the soil structure interaction at the interface between the shaft sealing structure and the salt.

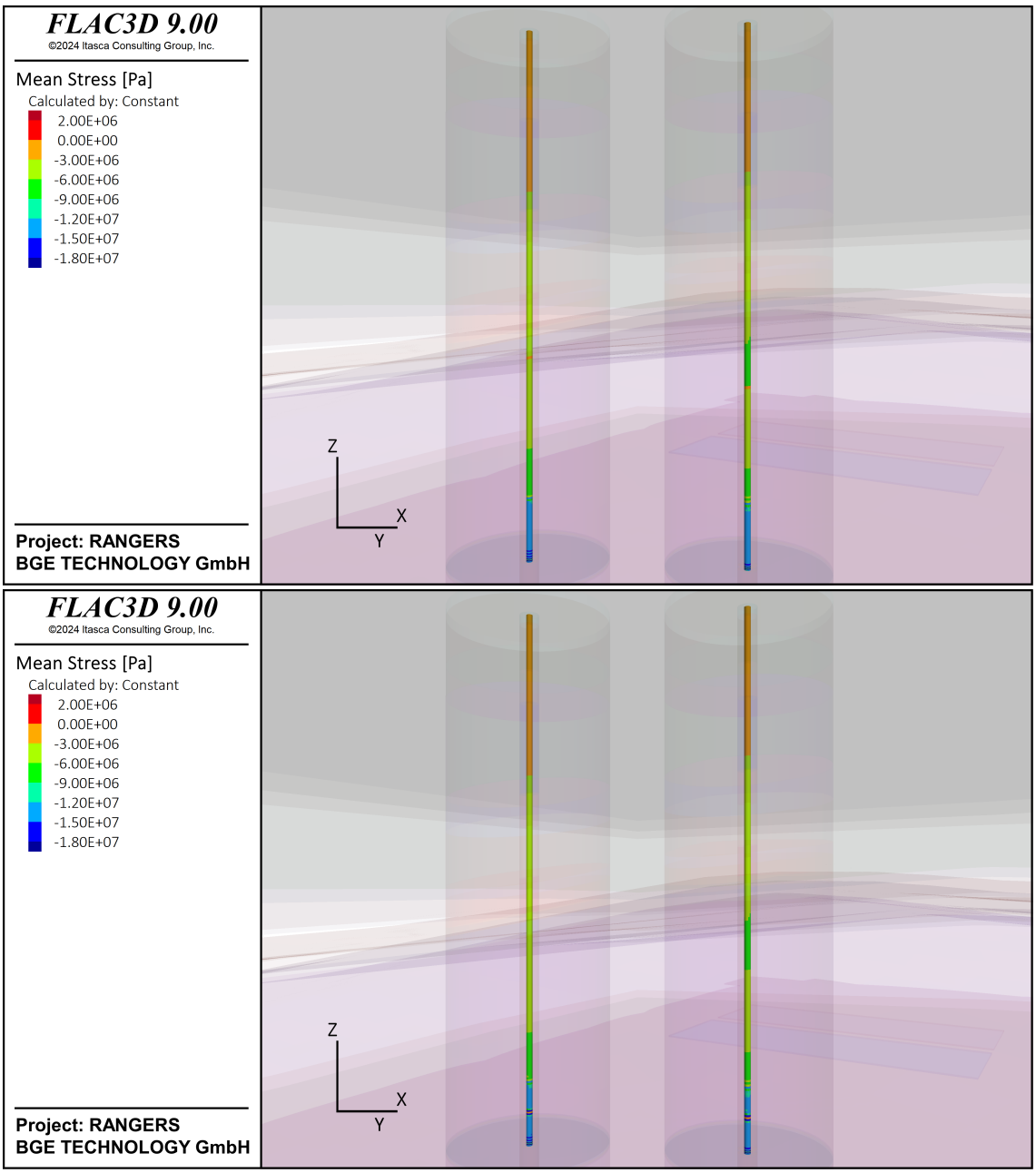

Figure 8.-21: Mean stress distribution along the shaft sealing systems at 150 years: simulation without interface (above), simulation with interface (below).

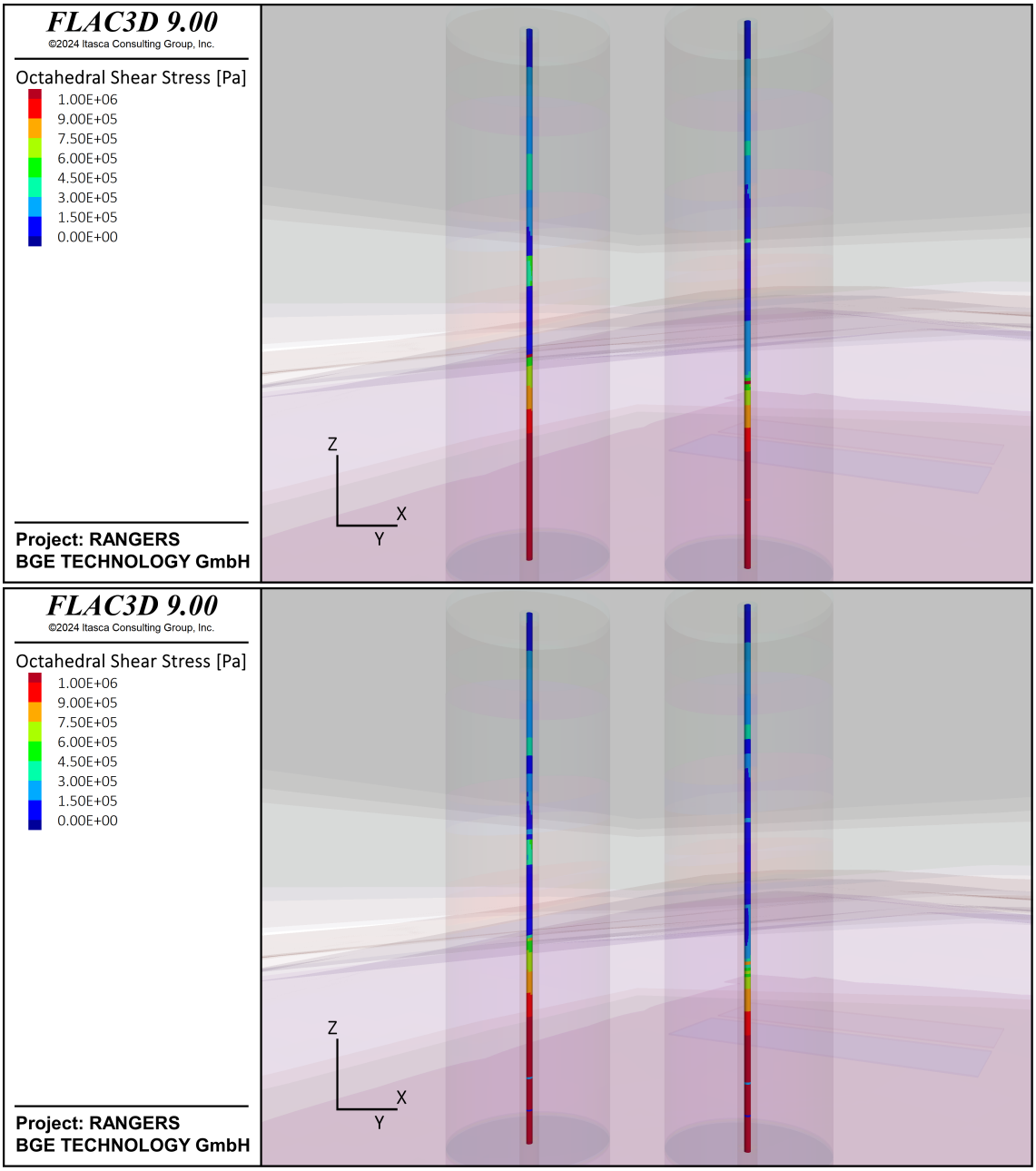

Figure 8.-22: Octahedral shear stress distribution along the shaft sealing systems at 150 years: simulation without interface (above), simulation with interface (below).

The modeling case with interface elements provides valuable insights into the behavior at the contact between the shaft sealing structure and the surrounding salt rock. In Figure 8.-23, which displays the distribution of shear stress at the interface, one can observe high shear stresses in the range of 1 to 1.5 MPa occurring specifically at the interface between the MgO concrete and the salt. In contrast, the shear stresses along the rest of the shaft interface are significantly lower, generally less than 0.5 MPa. The pronounced shear stress concentration at the MgO concrete contact is likely due to the high stiffness of this material, which restricts deformation and thus generates additional resistance against the surrounding rock's thermal expansion and mechanical movement.

In Figure 8.-24, the interface normal displacement along the shaft is presented. The results show a noticeable normal displacement, amounting to several millimeters, along the length of the bentonite seal. In contrast, the normal displacements along the other segments of the shaft are negligible. This observation is consistent with the high plasticity and low stiffness of the bentonite, which allows the surrounding rock to exert additional compressive force onto the shaft, further compacting the bentonite and, to some extent, allowing dilation of the rock near the interface.

These displacement and stress distributions highlight the balancing act between compaction of the bentonite and dilation in the rock. While the plastic behavior of bentonite facilitates this balance by yielding under stress and accommodating the rock's movement, it also provoke some dilation in the rock retarding the recovery of the dilatancy criterion as it has been discussed earlier. Also, In the case of MgO concrete, its high stiffness helps to limit deformation, maintaining a robust barrier but also concentrating shear stress at its interface. This dynamic indicates that the interface behavior is crucial in managing the interactions between the sealing materials and the salt. The evolution at the interface needs therefore thorough investigations in the scope of future safety and integrity assessments.

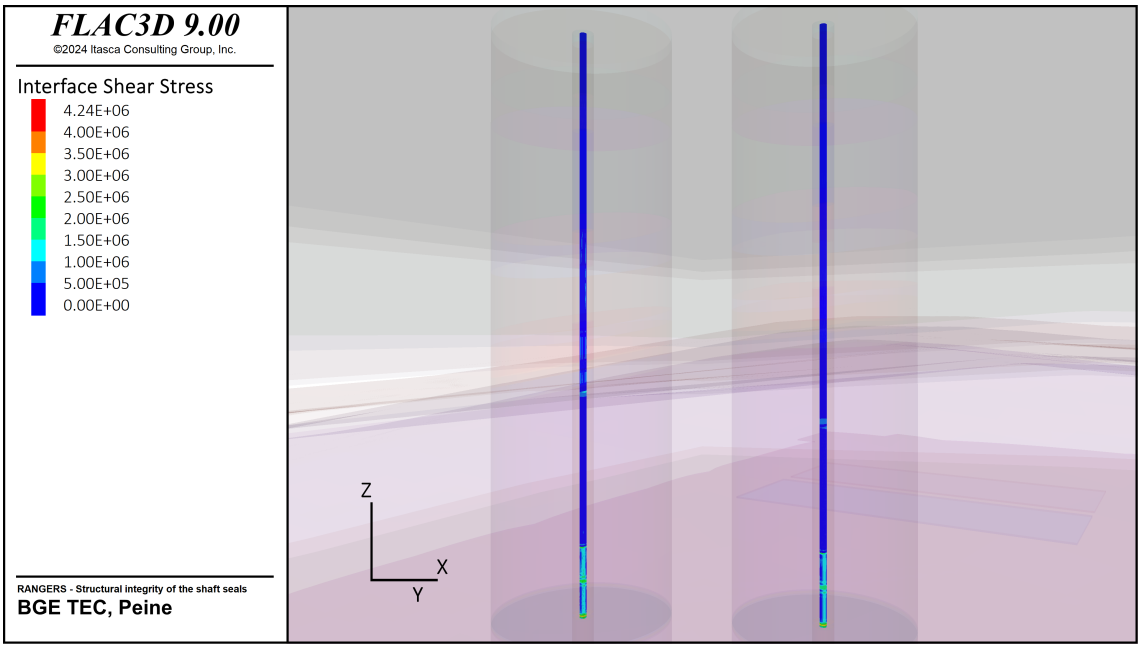

Figure 8.-23: Shear stress distribution in the interfaces at the shaft contours at 150 years.

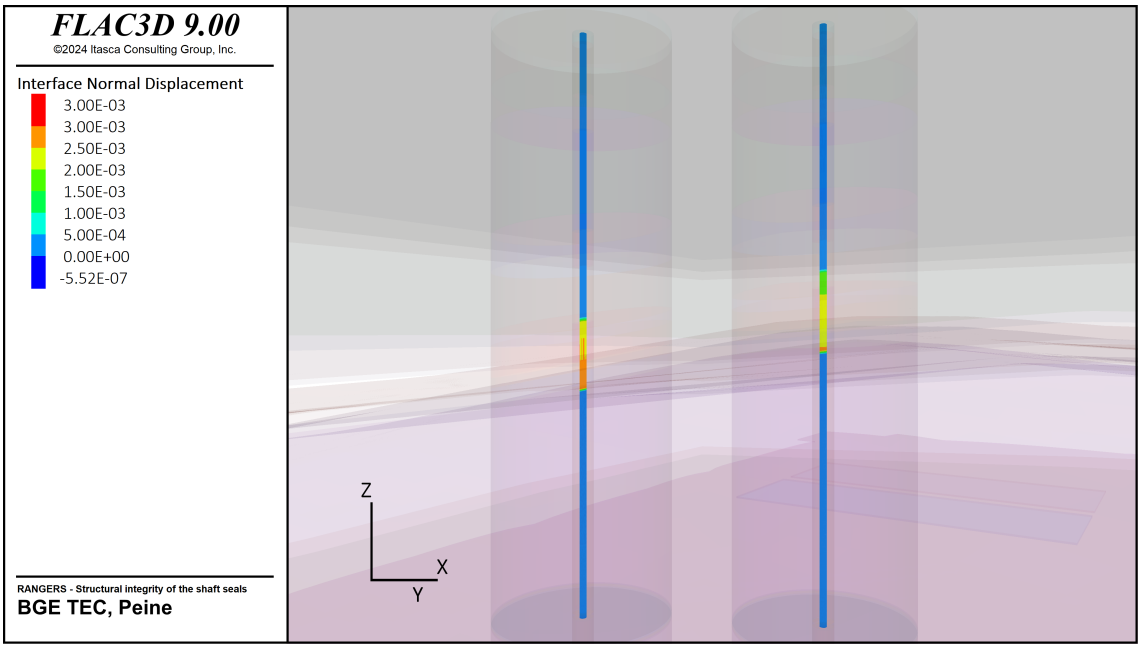

Figure 8.-24: Normal displacement distribution in the interfaces at the shaft contours at 150 years.

8.5.3 Effect of hydrostatic pressure in the shaft

Due to the high computational cost associated with running the full THM (thermal-hydrological-mechanical) simulation, it was not feasible to conduct a comprehensive analysis that fully accounts for the effects of infiltrating water into the shaft. However, a simplified approach was taken to evaluate the influence of hydrostatic pressure on the shaft structure, assuming that the upper gravel column becomes filled with water. Rather than a full THM simulation, hydrostatic loads were initialized as a volumetric load acting within the shaft, applied 500 years after repository closure, with the simulation then extending for an additional 500 years.

The results from this scenario are compared with the baseline case at t = 1000 years. Figure **??** and Figure 8.-25 show the mean stress distributions in the two shafts for the baseline and hydrostatic load cases, respectively. Comparing these two cases reveals that the introduction of hydrostatic pressure within the shaft significantly increases the confining pressure in the gravel column relative to the reference scenario. This additional confining pressure exhibits a stabilizing effect on the shaft structure, supporting the surrounding formation and enhancing the structural integrity of the shaft sealing system. Importantly, the presence of the hydrostatic load does not compromise the shaft's long-term integrity but rather contributes positively to its stability.

This approach, while simplified, provides valuable insights into the impact of hydrostatic pressure on the shaft's mechanical behavior, demonstrating that even in the absence of a full THM analysis, important conclusions can be drawn about the resilience and effectiveness of the shaft sealing system under variable hydrostatic conditions.

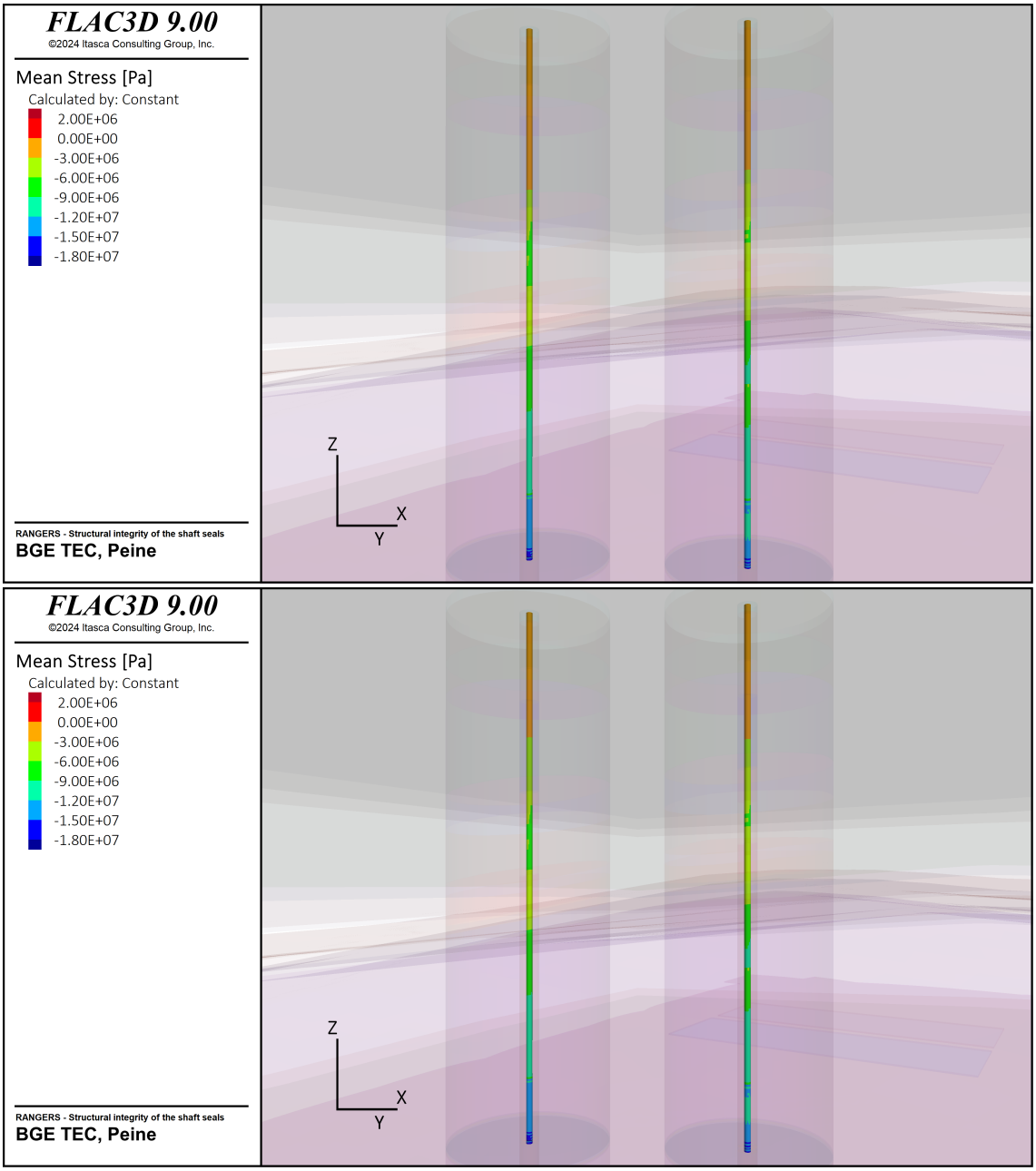

Figure 8.-25: Mean stress distribution along the shaft sealing systems at 1,000 years: simulation without (above) and with (below) hydrostatic pressure in the upper gravel column.

8.5.4 Conclusion and Barrier Integrity Assessment

The mechanical integrity assessment of the shaft sealing system demonstrates its capability to withstand thermal-mechanical and hydrostatic loads over extended periods, ensuring effective containment within salt repositories. By examining the system's response to thermal expansion, creep behavior, and pressure buildup, we have validated that the sealing system's design and material choices are suitable for maintaining structural stability under the anticipated repository conditions. Importantly, the results confirm that the shaft sealing structure remains damage-free throughout the simulation period, underscoring its robustness and resilience.

The integrity of the shaft sealing system is reinforced by several key findings:

- High Confining Pressure Advantage: In the salt formation, the high confining pressure significantly enhances the strength of sealing materials, leading to greater resistance against tensile and shear stresses. This pressure also helps to close micro-cracks and voids, maintaining the continuity and robustness of the seal, even under variable loading conditions. The high confining pressure plays a crucial role in ensuring that the system remains damage-free over time.
- Material Behavior under Thermal Expansion: Thermal expansion of the salt creates an upward displacement, generating tensile stresses in the shaft sealing structure. Materials with high stiffness, such as MgO concrete, experience localized tensile stresses that could lead to cracking if not managed appropriately. However, the high confining pressure helps mitigate these stresses, contributing to the damage-free status of the shaft. These findings emphasize the importance of selecting materials that can tolerate such stresses or adapting the design to accommodate them.
- Interface and Contact Zone Stability: The simulation of interfaces between sealing components and surrounding rock highlights the importance of realistic contact modeling. While rigid contact assumptions are efficient and adequate in many cases, certain materials with a definite contact shear strength such at the interface salt/MgO concrete require careful consideration of shear and normal stress distribution. This is particularly critical for maintaining seal stability under differential thermal expansion, ensuring that the sealing system remains intact and damage-free.
- Resilience to Hydraulic Pressure: The assessment shows that the shaft sealing system can accommodate additional hydrostatic loads without compromising its integrity. Introducing hydrostatic pressure within the shaft stabilizes the gravel column and augments confining pressures, thereby reinforcing the sealing structure and preventing damage.
- Long-term Stability and Self-healing Properties of Salt: The salt formation, with its natural creep behavior, demonstrates an ability to dissipate stress over time, contributing to the overall containment function. The salt's self-healing properties further enhance barrier integrity by closing any minor fractures that may occur over time, thereby supporting the damage-free status of the sealing structure.

In summary, the shaft sealing system in salt repositories, as evaluated in this chapter, exhibits sufficient resilience and durability to meet the stringent containment requirements of

radioactive waste repositories. The high confining pressures, combined with strategic material selection and design configurations, provide a robust barrier that maintains its integrity and remains damage-free even under prolonged stress conditions. This analysis confirms that salt formations not only serve as an excellent geological barrier but also create an ideal environment for engineered sealing systems, ensuring long-term containment and isolation of radioactive waste.

9. Hydraulic Integrity Assessment of the EBS

Following the verification concept, the hydraulic resistance against inflowing fluids has to be verified for the EBS. According to Müller-Hoeppe et al. (2012b), the hydraulic assessment should focus on two main aspects. Initially, it examines whether the EBS meets the design objectives under the likely conditions of the reference scenario. Subsequently, it assesses if the EBS can still effectively prevent the inflow of liquids from the overburden to the radioactive wastes even in the event of shaft closure failure of the less probable conditions of the alternative scenario. In this case, it crucial to determine whether, there is sufficient temporal delay when the inflowing brine will reach the drift sealing system, ensuring that the compaction of the crushed salt has advanced sufficiently to take its long term sealing function in the repository (Müller-Hoeppe et al., 2012b). The subsequent effect of the brine at the edge of the drift sealing system need to be investigated to ensure that the drift sealing system provides a sufficient hydraulic resistance against the brine.

The shaft sealing system is so designed that the fluids that will ingress through the shafts will accumulated at the bottom of the shaft. For that it is planned to backfill the infrastructure area with non-compactable gravel made of basalt or serpentinite. In contrast to the crushed salt, this non-compactable backfill is only slightly compacted by the convergence and support pressure builds up quickly. By backfilling with non-compactable backfill, the infrastructure area forms a reservoir for the solutions entering via the shaft and from the host rock. This reservoir has the positive effect to retard the hydrostatic pressure build up at the edge of the drift seal. A hydrostatic pressure associated with the repository depth will only be reached after the reservoir is full and all shaft components are saturated. Therefore, depending on the amount of fluid to be expected over the lifetime of the EBS and the repository, one can design the volume of the reservoir to retard any pressure build-up in the repository.

The present study aims to provide an example hydraulic assessment for the generic repository system considered in RANGERS. For that, The fluid dynamics through the EBS will be analyzed for the reference and the alternative scenario.

9.1 Hydraulic integrity assessment of the shaft sealing system

9.1.1 Numerical model

The model considered for the analysis of the hydraulic evolution through the shaft sealing system was extracted from the numerical model used in the mechanical integrity assessment of the shaft sealing system. It consists of a column surrounding a shaft with a diameter of 250 m. This column contains all the geological layers around the shaft with their natural curvature as in the generic geological model. The materials in the shaft are considered in the model in accordance with the sealing concept. Their geometrical representations were carefully respected. The EDZ and the contact zone around the shaft are not explicitly considered. Instead the analyses are carried out by taking into account the resulting system permeability made of sealing components, their contact zone to the host rock, and the surrounding EDZ in the host rocks. Since the infrastructure area was not yet designed, the area at the disposal level around the shaft was homogenized in the model column to mimic the volume of the infrastructure area. The volume was assumed to be higher than necessary to avoid that the pressure build up in the infrastructure area influence the fluid pressure evolution in the shaft. Depending on the amount of brine that would eventually reach the infrastructure area,

its volume can be adequately designed.

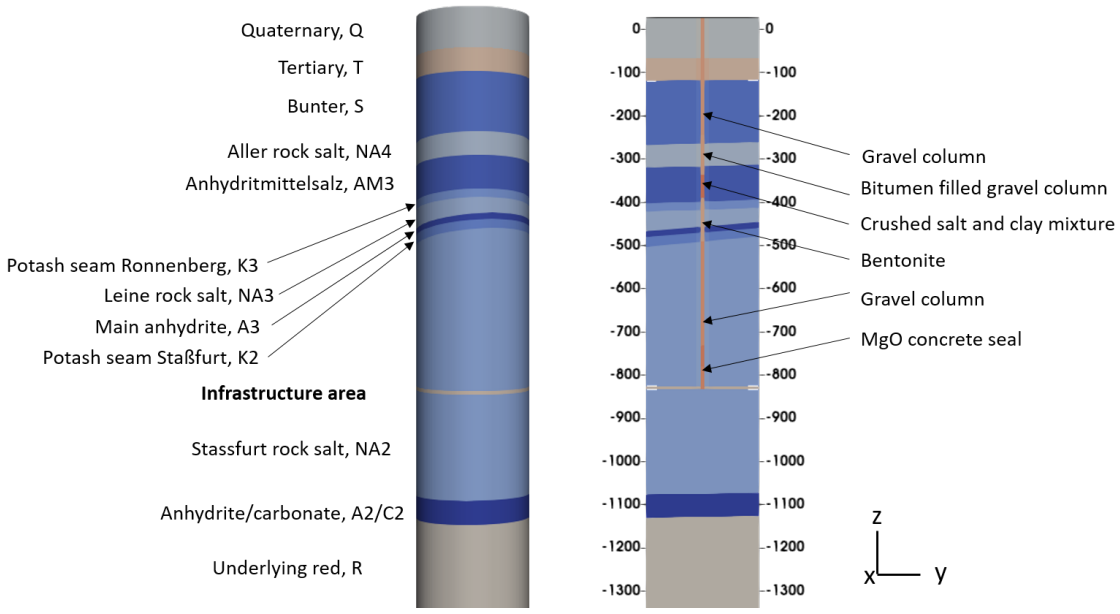

Figure 9.-1: Numerical model for the analysis of the hydraulic evolution in the shaft closure.

The materials in the shaft are partially saturated. Their initial saturation values was taken into account according to the details provided in Müller-Hoeppe et al. (2012b). For each material, a water retention curves needs to be defined that controls the saturation process. The necessary (van Genuchten, 1980) model parameters are summarized in Table 9.-1. The gravel mixture to be used for the shaft is not yet defined. Assumptions were made regarding its water retention curve. For gravel, which is generally coarse-textured with large pore spaces and rapid drainage, the residual water content close to 0.05 or lower is assumed, as gravel has low residual moisture due to large pore sizes. The saturated water content typically ranges from 0.25 to 0.35, associated with the high porosity of the gravel. A low value for the air entry suction, reflecting the high air entry value of coarse materials is assumed. This indicates gravel is likely the first material to be drained, and the last to fill. the pore-size distribution parameter is $\geq$ 2.0, indicating a less steep retention curve appropriate for materials with larger pores.

Table 9.-1 also lists the hydraulic parameters of the materials in the shaft according to the design requirements specified in the methodology report.

Table 9.-1: Hydraulic properties of shaft sealing components.

Material	**Density** [kg/m^3]	**Permeability** [m^2]	**Porosity** [-]	**Gas Entry Pressure** [Pa]	**van Genuchten Parameter** n	S_{ini} [%]
Gravel Column (bottom)	2200	10^{-9}	0.326	1.0×10^4	2	0.4
Bitumen-Gravel	2200	1.3×10^{-18}	0.1	8.85×10^5	1.492	85
Salt Clay Mix	2200	10^{-14}	0.1	1.0×10^5	2	21
Bentonite	2200	7.8×10^{-18}	0.3	1.0×10^6	1.82	45
MgO-concrete	2200	5.0×10^{-17}	0.2	2.2×10^5	1.492	80
Infrastructure (Gravel)	2200	10^{-9}	0.38	1.0×10^4	2	0.2

The permeability as well as the porosity of each of the geological layers is given in Table .

Table 9.-2: Hydraulic properties of the geological layers.

Material	**Density** [kg/m^3]	**Permeability** [m^2]	**Porosity** [-]	**Gas Entry Pressure** [Pa]	**van Genuchten Parameter** n	S_{ini} [%]
Quaternary	2000	10^{-14}	0.25	1.0×10^6	2	100
Tertiary	2100	10^{-14}	0.25	1.0×10^6	2	100
Sandstone (Bunter)	2500	10^{-14}	0.15	1.0×10^6	2	100
Anhydrite	2700	10^{-20}	0.01	1.0×10^4	2	0.2

Because salt is almost impermeable (i.e., no Darcy flow) compared to the other formations intersecting the shaft, no hydraulic transport was assumed in the salt layers for this analysis. A hydrostatic pressure is assumed in the water bearing layers of the overburden up to the end of the Bunter Sandstone. The anhydrite located between the intermediary salt layers and the salt pillow is assumed to be dry. Those salt layer prevent any water flow to reach the anhydrite layer. The same assumption is being made for the layers below the salt pillow, that are considered to be dry.

The temporal starting point of the calculations is the end of closure of the shaft. Figure 9.-2 shows the initial saturation and liquid pressure in the model. The saturation distribution in the shaft results from the pore pressure distribution based on the assumed water retention parameters.

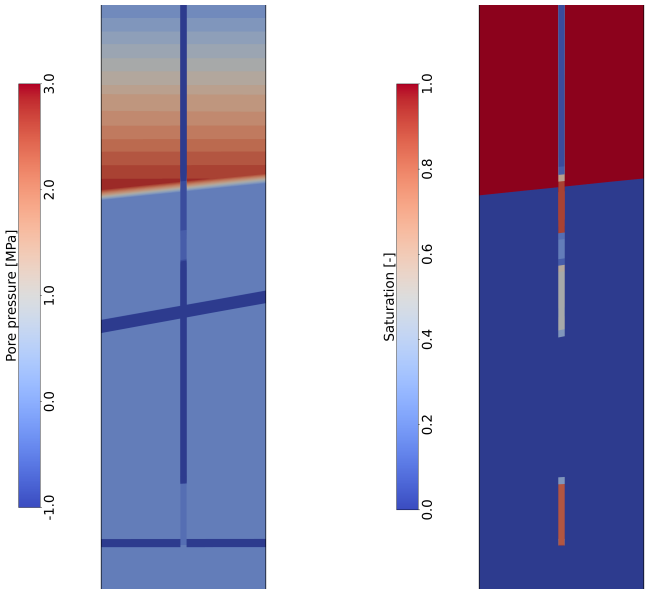

Figure 9.-2: Early-phase pore pressure distribution in the shaft and near field over time.

9.1.2 Modeling cases

For the assessment of the hydraulic integrity of the shaft sealing system, different modeling cases need to be defined covering the reference and and the alternative scenario. All modeling cases take a different assumption about how the sealing elements in the shaft will behave over the repository lifetime. For the design of the EBS, a functional lifetime of the EBS of about 50,000 years (Müller-Hoeppe et al., 2012b) was assumed. However, to better estimate the hydraulic resistance of the shaft sealing system, we start by considering the case where the shaft seals remain intact over the verification period of one million years (modeling case 1). In the second step, we assume that the shaft sealing system is functional over 50,000 years and a damage is expected afterwards (modeling case 2). Finally, we define a more severe case that can happen if the shaft closure does not meet the design requirements necessary for the shaft to be functional over the functional time of 50,000 years. For this case an exemplary analysis with a sudden damage at 5,000 years is performed. These latter modeling cases covers the expectation of the alternative scenario.

9.1.3 Numerical results for modeling case 1

Hydraulic flow evolution

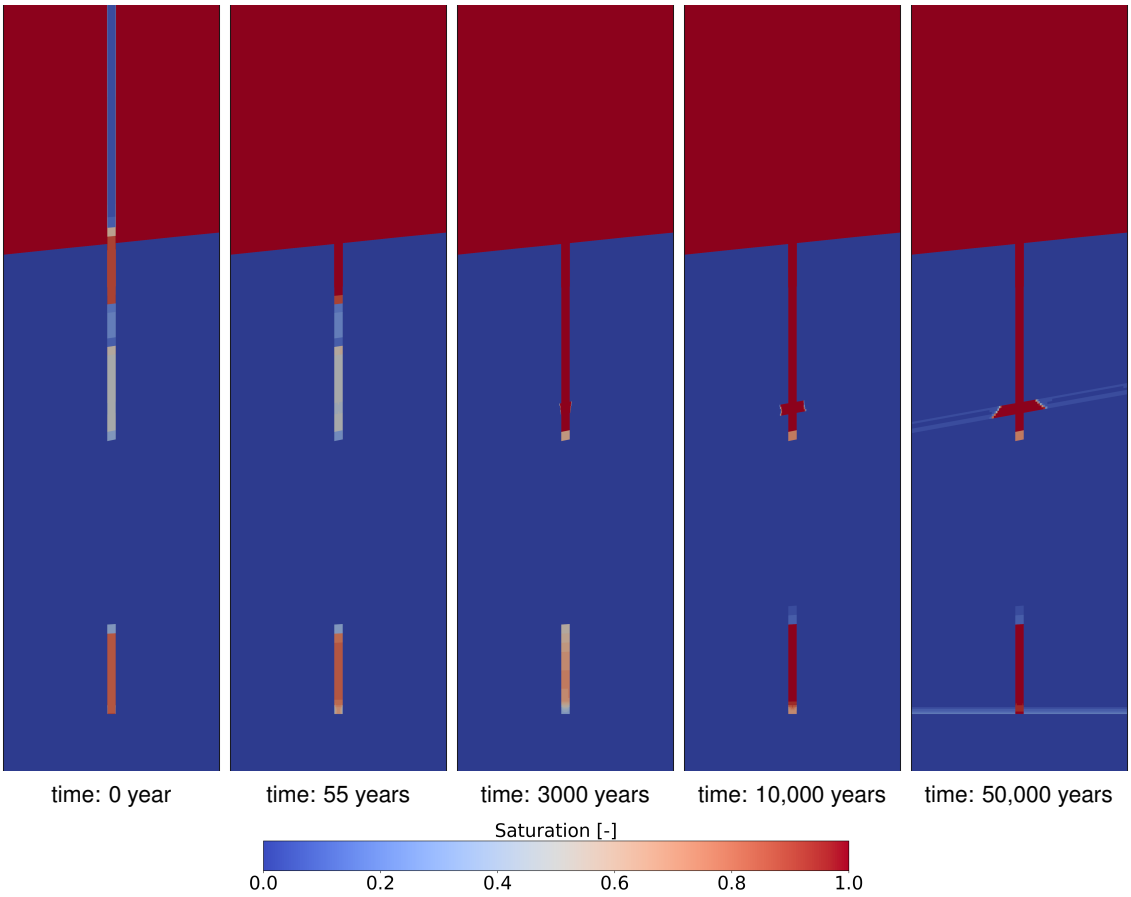

Figure 9.-3: Early-phase saturation distribution in the shaft and near field over time.

In Figure 9.-3, the saturation distribution in the shaft and its near field over time is presented up to the end of the 50,000-year verification period. At the beginning of the simulation (0 years), the materials in the shaft are partially saturated, with the gravel columns completely dry. The overburden, acting as a water-bearing layer, is fully saturated, while the salt, functioning as an impermeable non-Darcy medium, remains dry and does not participate in the hydraulic processes.

By 55 years, the upper gravel column becomes fully saturated. This occurs without accounting for the tightness of the liner in this section of the shaft. At the same time, saturation begins to increase in the bitumen-filled gravel column seal, marking the onset of fluid infiltration into the shaft seals. By 3,000 years, saturation is nearly complete in the three seals installed at the top of the salt pillow. This phase signifies the transition from localized saturation within the seals to a broader distribution, driven by the hydraulic gradient and the permeability of the materials. Interestingly, the MgO seal becomes drier over time due to the prevailing dry conditions in the repository environment, while the lower gravel column remains unsaturated.

At 10,000 years, the MgO seal shows substantial saturation across most of its length. Infiltration into the surrounding anhydrite layer is also observed, particularly around the bentonite seal. In this region, Darcy flow becomes evident, with the bentonite seal's permeability controlling the rate of water migration into the anhydrite layer. Despite this infiltration, the gravel column remains dry, as water flowing out of the bentonite seal quickly traverses the high-

permeability gravel column and infiltrates the MgO seal instead.

By 50,000 years, the saturation distribution within the shaft appears similar to the conditions observed at 10,000 years, with a more pronounced increase in saturation within the anhydrite layer. Additionally, there is a slight rise in saturation within the infrastructure area, although the lower gravel column remains unsaturated. At the end of the verification period, the saturation distribution indicates that minimal water has infiltrated the infrastructure area, suggesting limited flow into this region.

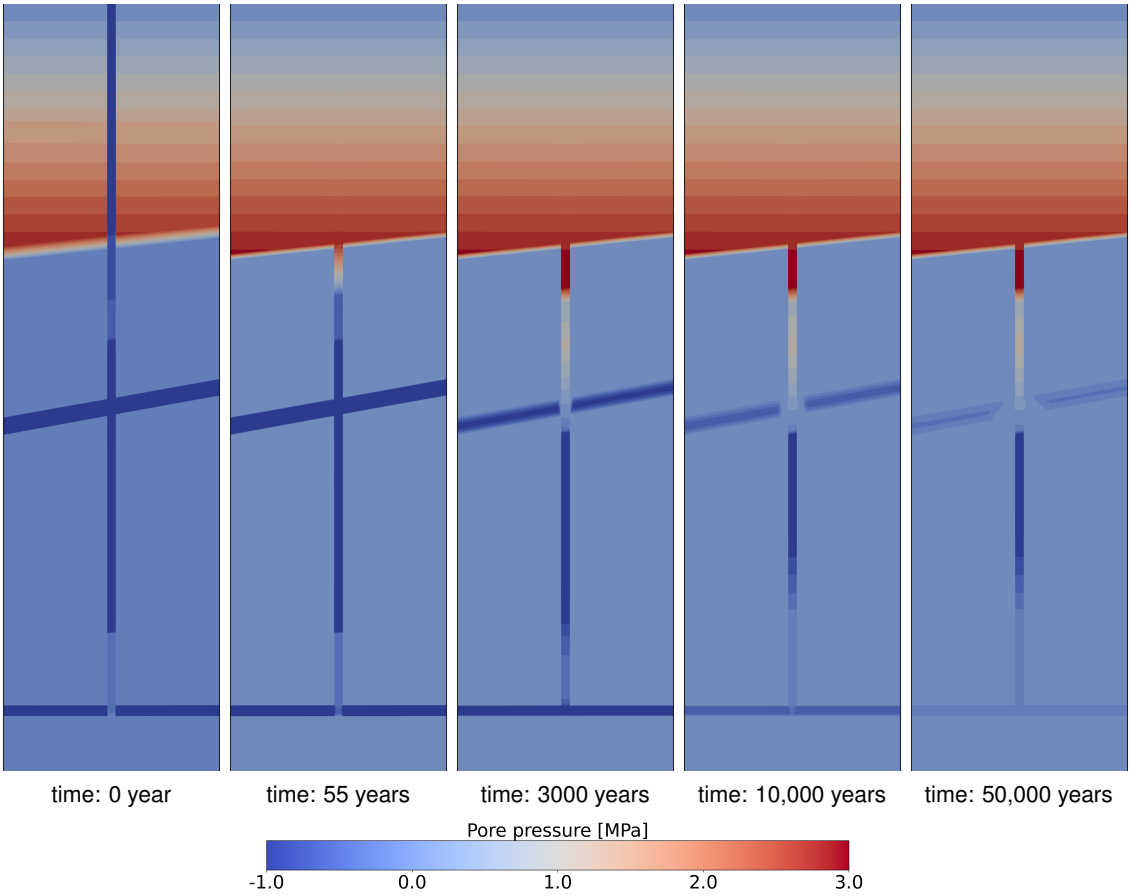

Figure 9.-4: Early-phase pore pressure distribution in the shaft and near field over time.

The progression of pore pressure over time, as shown in Figure 9.-4, highlights the evolution of hydraulic conditions within the shaft and its surrounding environment throughout the 50,000-year verification period.

At the start of the simulation (0 years), the pore pressure distribution shows a stark contrast between the water-bearing overburden and the surrounding salt and shaft components. The overburden exhibits positive pore pressure, indicative of its saturated state, while the shaft components and the surrounding salt layers exhibit minimal or negative pore pressure due to their unsaturated or impermeable nature.

After 55 years, a hydrostatic pressure is acting in the upper gravel column as a result of its saturation. There is a noticeable increase in pore pressure in the bitumen gravel seal at the onset of the salt pillow. This corresponds to the saturation observed earlier, as the

infiltration of water into this seal leads to a rise in hydraulic pressure. The salt layers and surrounding infrastructure remain unaffected, maintaining their low or negative pore pressure values, reflecting their impermeable and unsaturated characteristics.

By 3,000 years, the pore pressure increases significantly in the upper seals. The hydraulic gradient drives fluid migration, causing increases in pore pressure in these elements. The MgO seal, under the dry conditions of the repository environment, maintains lower pore pressure compared to the other seals.

At 10,000 years, the pore pressure distribution is similar to the situation observed at 3,000 years. We observe a pore pressure increase in the anhydrite layers as a result of the localized saturation that was observed earlier. There is also a decrease of suction in the infrastructure area. The MgO seal shows a moderate increase in pore pressure along its length, while the lower gravel column remains largely unaffected, reflecting its high permeability and the quick dissipation of infiltrated water.

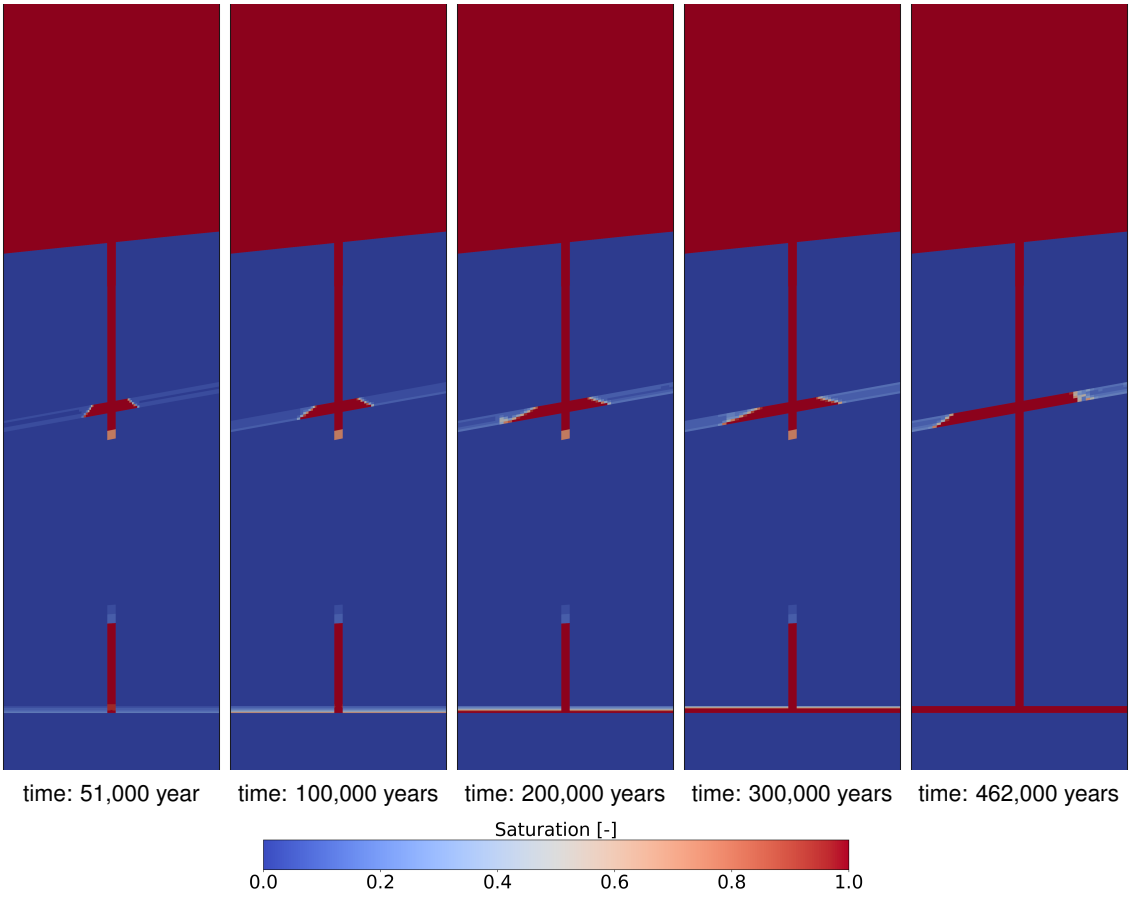

Figure 9.-5: Saturation distribution in the shaft and near field over time.

By 50,000 years, the pore pressure distribution reaches a near steady-state condition. The anhydrite layer exhibits more pronounced pore pressure, likely due to long-term infiltration from the shaft seals. The bentonite and bitumen-filled gravel seals maintain high pore pressure, indicative of their saturated states and roles in controlling fluid movement. The infrastructure area shows a slight increase in pore pressure over time, while the lower gravel column continues to exhibit negligible pore pressure due to its permeability and role in dissipating

water flows. Overall, the evolution of pore pressure demonstrates the interplay of material permeability, hydraulic gradients, and long-term fluid migration processes in the shaft and its surrounding environment.

In this modeling case, it is assumed that the seals remain intact beyond their planned service lifetime. The hydraulic behavior of the system is analyzed over a prolonged period, extending to nearly half a million years under these conditions.

The saturation distribution shown in Figure 9.-5 highlights the continued evolution of fluid movement within the shaft and its near field, extending the timeline previously studied.

Between the end of the verification period of the engineered barrier system (EBS) at 50,000 years and 300,000 years, there is a progressive increase in saturation within the infrastructure area. This clearly indicates that the pore volume in the gravel installed within the infrastructure region is gradually being filled by water inflowing through the shaft. During this period, the surrounding anhydrite layer also exhibits increasing saturation, reflecting prolonged interaction with fluids migrating from the shaft. Despite this, the lower gravel column remains unsaturated, as water continues to flow through it without being retained.

By 462,000 years, the shaft becomes completely saturated. Saturation of the lower gravel column occurs only after the infrastructure region is fully saturated. At this stage, the system appears to have reached a near-equilibrium condition. The saturation in the anhydrite layer remains the only transient phenomenon, but its progression is fortunately limited. The saturated domain of the anhydrite layer shows a gradual but restricted evolution, extending no more than 200 m in diameter around the shaft.

Overall, the results indicate a gradual yet controlled spread of saturation over hundreds of thousands of years. The engineered shaft components effectively regulate water flow, while the surrounding geological layers demonstrate long-term adjustments to fluid migration. Steady-state conditions emerge in the later stages of the simulation, confirming the stability of the system over extended timescales.

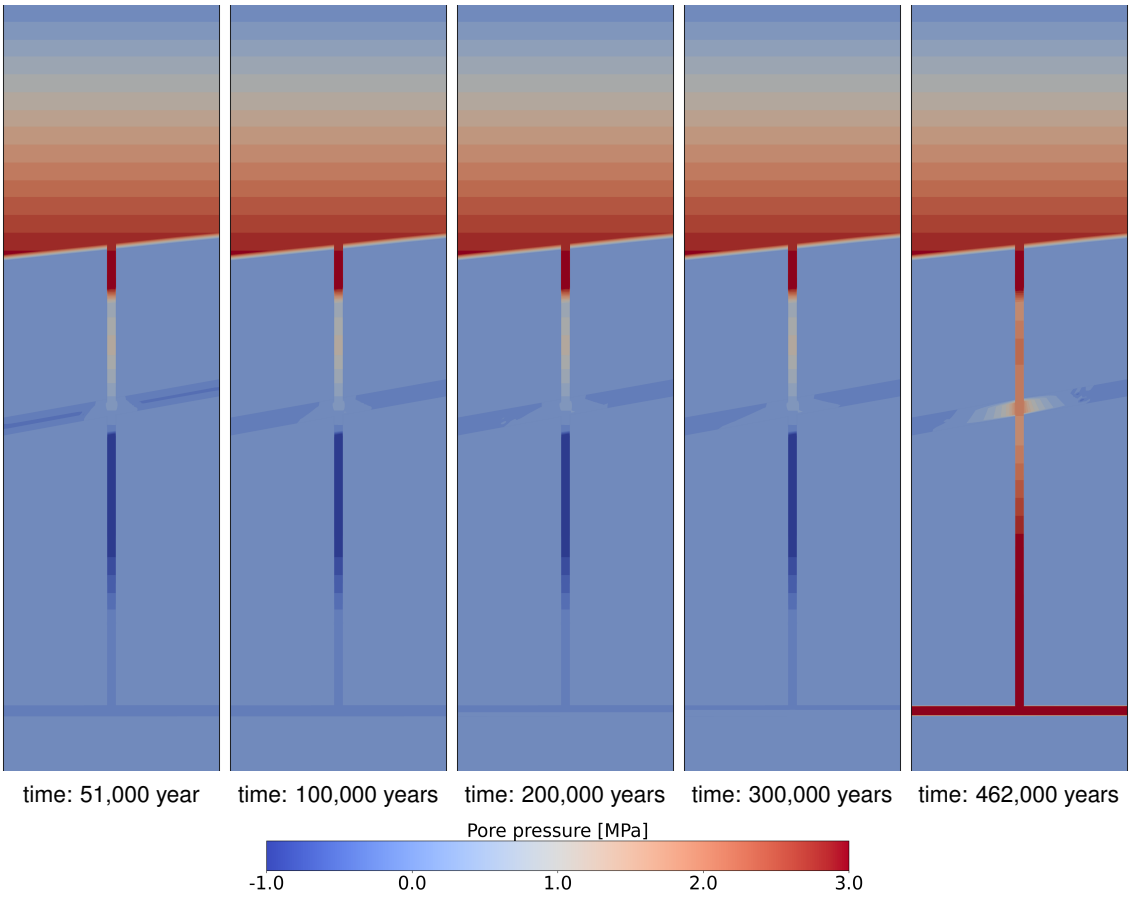

Figure 9.-6: Pore pressure distribution in the shaft and near field over time.

The corresponding pore pressure evolution in the shaft and near field is shown in Figure 9.-6. Up to 300,000 years, the pore pressure distribution appears to be in a near-equilibrium state. This state is characterized by a hydrostatic pressure in the bitumen-filled gravel, followed by an elevated pore pressure in the salt clay and bentonite seal. However, the pore pressure in these seals has not yet reached hydrostatic pressure at their respective depths. The only noticeable changes during this period occur in the infrastructure area and the anhydrite layer, where a gradual increase in pore pressure can be observed, indicating ongoing fluid migration into these regions.

At the end of the simulation (462,000 years), the system behavior changes abruptly due to the gravel column becoming fully saturated. This saturation results in a significant increase in pore pressure in the lower part of the shaft and the infrastructure area. Consequently, the pore pressure in the middle part of the shaft, particularly above the lower gravel column where the seals are located, also rises. This marks a critical transition in the hydraulic conditions, reflecting the interconnected effects of saturation and pore pressure evolution within the shaft and its surrounding environment.

Pressure and saturation evolution in the shaft

A quantitative evaluation of the pressure and saturation evolution within the shaft is presented in Figure 9.-7. the figure shows the profile of saturation and pore pressure over time along the

shaft.

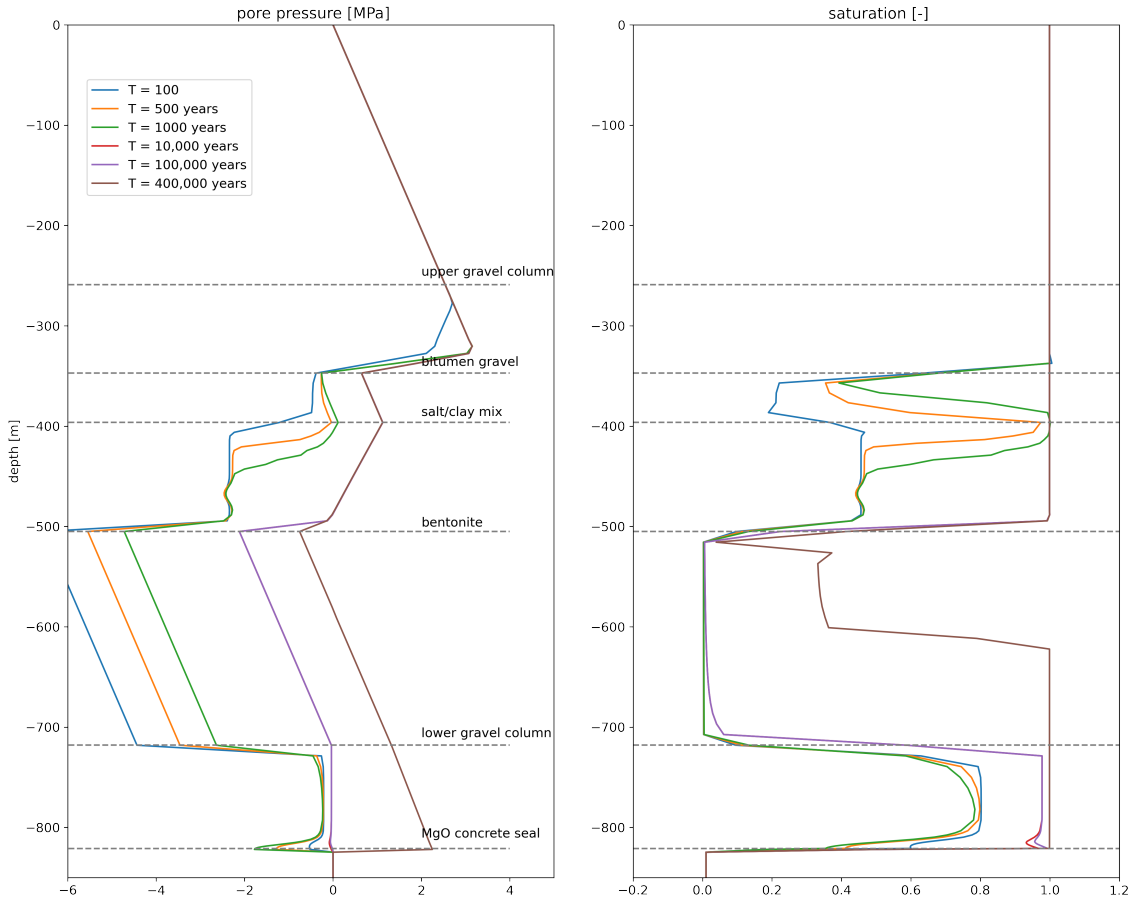

Figure 9.-7: Pore pressure and saturation profiles with depth over various time periods.

The saturation of the first sealing element, composed of bitumen gravel, occurs relatively quickly, with full saturation achieved before 100 years. By 500 years, hydrostatic pressure is already established within this element, highlighting its rapid response to inflowing water. In contrast, the salt/clay mixture seal exhibits a much slower saturation process due to its particular water retention properties. This element remains unsaturated for an extended period, achieving saturation only after 1,000 years. Despite this, the pore pressure within the salt/clay mixture remains low throughout the simulation, underscoring its limited hydraulic connectivity.

Water flowing through the salt/clay mixture infiltrates the bentonite seal, initiating its saturation. Due to the high suction capacity of bentonite, its saturation progresses slowly, with full saturation of the upper portion occurring only after 1,000 years. By 10,000 years, the bentonite seal is fully saturated across its depth.

The lower gravel column experiences suction effects over the first 100,000 years of the simulation, delaying its saturation. Positive pore pressure values, indicating saturation, are observed only in the bottom portion of the gravel column at 400,000 years, while the upper section remains dry, reflecting the limited upward water flow.

The MgO concrete seal exhibits an initial drying phase, with decreasing saturation observed up to 1,000 years. Following this period, a gradual saturation process begins. By 100,000 years,

saturation in the MgO seal reaches high levels near full saturation, with complete saturation achieved at 400,000 years.

The results demonstrate that full saturation of the infrastructure area occurs before the MgO seal is fully saturated. Once the infrastructure area is saturated, the lower gravel column begins its saturation process. This sequential behavior highlights the interconnected hydraulic evolution of the system and the critical role of the water retention and permeability properties of the individual sealing elements in controlling long-term water flow and pressure development within the shaft.

Water accumulation in the infrastructure area

Figure 9.-8 shows the volume of water that is being accumulated in the porous space of the infrastructure area that is backfilled with non-compacting basalt gravel. At the beginning of the simulation a volume of about 100 m³ is computed in the infrastructure area. This value is mainly due to the non linearity of the water retention curve. Very high capillary values are necessary to assign a saturation of near zero. Such values lead to computational issues so that the simulation was carried out with compressible parametrization of the van Genuchten function.

Over time, the volume of water accumulated grows first steadily in a double logarithmic representation. Then at around 5,000 years an inflection point is reached where the volume increase is more important. This inflection point marks the time when the capillary forces are vanishing in the basalt gravel and therefore, there is less resistance for the saturation of the porous space.

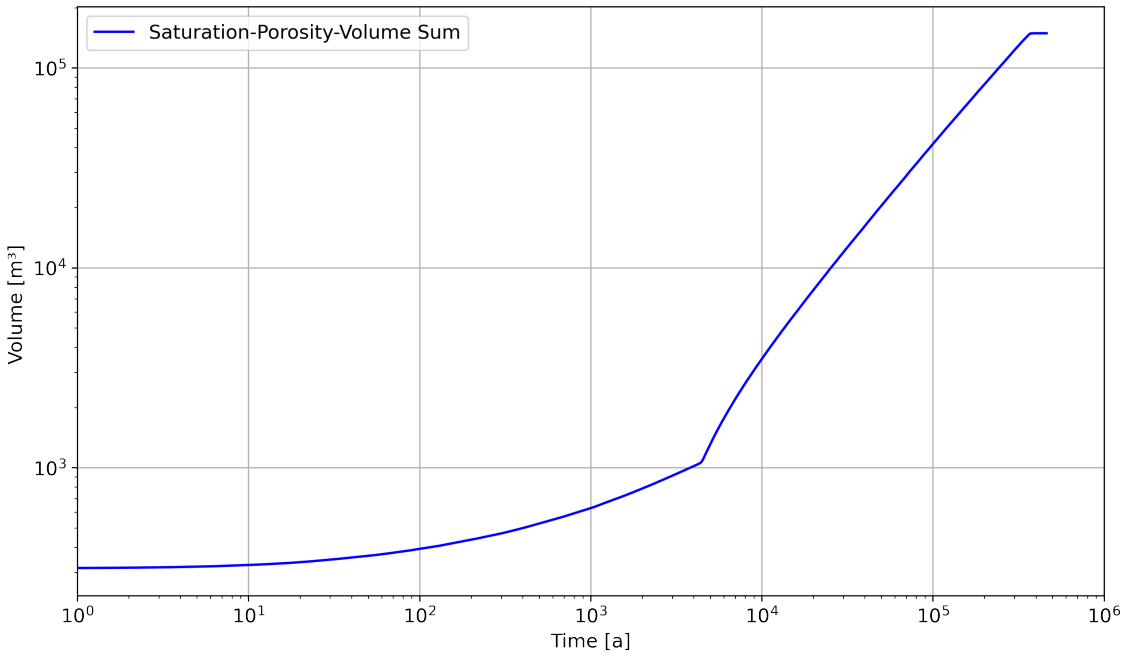

Figure 9.-8: Volume of water accumulating in infrastructure area through time for modeling case 1.

After nearly four hundreds thousand years, a plateau is reached marking the full saturation of the infrastructure area. At this time, Over less than 150,000 m³ of water has been accumulated

in the infrastructure area. At the end of the verification period of the EBS, at 50,000 years, less than 20,000 m³ of water have reached the infrastructure area. Although the present modeling case is synthetic, this value is realistic for the EBS considered in RANGERS which hydraulic specifications should remain unchanged up to 50,000 years. An alteration of the EBS is expected only afterwards.

Conclusions on System Behavior

The numerical results of modeling case 1 offer significant insights into the hydraulic flow evolution, pressure and saturation dynamics, and water accumulation behavior expected within the shaft system over time. Modeling case 1 is a synthetic model situation that allows us to investigate the system behavior under idealized conditions.

The simulation highlights that the system undergoes progressive saturation, with key elements such as the bentonite seal and MgO seal reaching full saturation only after extended periods. The gradual development of hydrostatic pressure equilibrium throughout the shaft is achieved only after half a million of years. This long-term evolution aligns with the expectations for the safe containment of radioactive waste, where the EBS and shaft sealing system maintain functionality well beyond the 50,000-year regulatory requirement.

The accumulation of water in the infrastructure area is gradual and follows a logarithmic progression. Initially, about 100 m³ of water is computed due to the nonlinear water retention curve. At around 5,000 years, an inflection point is observed where the volume of water increases more significantly, signaling the vanishing capillary forces in the basalt gravel, allowing easier saturation. By the end of the simulation, the infrastructure area reaches full saturation, with over 150,000 m³ of water accumulated. At the critical verification period of 50,000 years, less than 20,000 m³ of water has reached the infrastructure area, which is consistent with the hydraulic specifications of the EBS in the RANGERS project.

The following conclusions can be drawn for the case where water flows down the shaft from penetrated overlying aquifers, based on the simulation:

- the lower gravel column and the crushed salt/clay mixture will be the last components in the shaft to be saturated.
- Water accumulation in the lower gravel column will only begin after the infrastructure area has been fully saturated.
- The MgO seal will experience an initial desaturation phase lasting up to 5,000 years or more before becoming saturated much later.
- It is only after the full saturation of the shaft (i.e., the connection of hydraulic processes in the lower and upper part of the shaft) that a hydrostatic pressure from the surface to the disposal depth will be achieved.
- By the end of the 50,000-year verification period, no significant hydrostatic pressure is expected in the infrastructure area, indicating that hydrostatic load does not need to be considered in the design and integrity assessment of the drift seals.

Two important implications arise from these conclusions:

- Monitoring the water level in the lower gravel column can effectively demonstrate that the repository system is performing as expected, providing a clear indication of its integrity over time.
- The volume of the infrastructure area reservoir can be designed to prevent any fluid migration from the overburden into the repository mine beyond the infrastructure area. This ensures that long-term confinement can rely primarily on the shaft sealing system and the reservoir, extending for a significant portion of the one-million-year verification period. A detailed quantification of this implication will be addressed in modeling case 2.

In conclusion, the hydraulic evolution, pressure dynamics, and saturation processes of the shaft system show that the sealing components work as intended, progressively stabilizing over time. The hydraulic specifications of the EBS appear robust, and the design is expected to perform reliably up to the required time frame of 50,000 years, with only minor alterations expected afterward.

9.1.4 Numerical results for modeling case 2

The numerical model setup and parametrization are identical to those in modeling case 1 for the first 50,000 years. Refer to Table 9.-1 for detailed information about the model parameters. To simulate the system behavior under the shaft seal failure scenario after 50,000 years, the permeability values of several sealing components were increased.

For the bentonite sealing element, an average permeability of 5×10^{-16} m^2 was adopted, representing a marl clay material used here as a substitute for an insufficiently compacted binary bentonite mixture, as described in Müller-Hoeppe et al. (2012a). For the Sorel concrete sealing element, Müller-Hoeppe et al. (2012a) proposed an integral permeability of 1×10^{-15} m^2. This permeability value was achieved even under challenging location conditions in an initial experimental structure (PSB A2, a pilot flow barrier made of Sorel concrete) at the Asse site **???**. The same permeability value was applied to the Sorel concrete abutment. To increase the numerical stability and reduce the computational time, we performed the simulation by increasing the permeability of the seals by one order of magnitude instead of two.

For the crushed salt clay mixture, due to the limited data available for this novel material, we assumed the same permeability as in modeling case 1, where a conservative permeability of 1×10^{-14} m^2 was already assumed for the state pre-failure.

Hydraulic flow evolution

The system evolution is identical for modeling cases 1 and 2 during the first 50,000 years. Here, we focus on the hydraulic behavior after 50,000 years when the permeability of the shaft sealing structure is increased to simulate its failure. The effects of this failure are illustrated in Figure 9.-9, which shows the saturation distribution during the post-failure phase.

After the sealing failure, the infrastructure area becomes progressively saturated. By 73,500 years, the entire porous volume of the infrastructure area is almost fully saturated. This behavior contrasts with the previous modeling case, where no degradation of the sealing material was assumed, and the saturation of the infrastructure area occurred only after 300,000 to 450,000 years.

The figure further demonstrates that the lower gravel column becomes saturated only after the infrastructure area is fully saturated. Following this, the saturation of the surrounding anhydrite layer begins to increase over time. By 180,000 years, the the anhydrite layer in the domain of investigation becomes fully saturated. However, to estimate the extent of saturation in the anhydrite layer over a million years, a larger model domain would be required. This highlights the impact of seal degradation on the hydraulic evolution and emphasizes the need for extended modeling to capture the long-term behavior of the system.

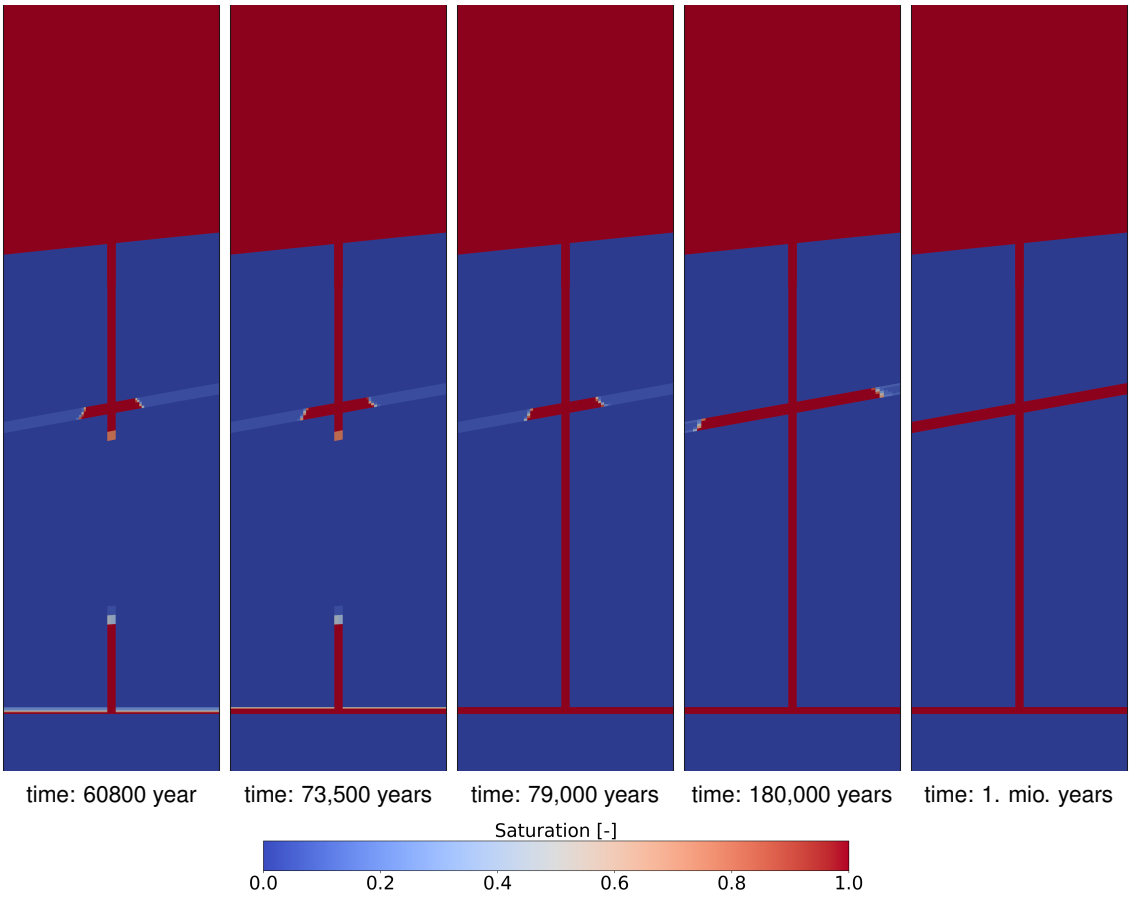

Figure 9.-9: Saturation distribution in the shaft and near field up to 1 million years.

With the saturation of the shaft, there is a corresponding buildup of hydraulic pressure. The pore pressure distribution in the shaft is shown in Figure 9.-10. Although the shaft becomes fully saturated by 79,000 years, the hydrostatic pressure regime remains divided between the upper and lower sections. In the upper part of the shaft, hydrostatic pressure occupies the porous voids up to the bentonite seal, creating a relatively uniform pressure profile. In the lower section, pressure values of at least 3 MPa develop from the infrastructure area to the bottom of the gravel column. Within the lower gravel column, a distinct pressure gradient is observed, with pressures exceeding 3 MPa at the bottom and dropping to less than 1 MPa just below the bentonite seal. This gradient reflects the influence of the water retention properties of the materials in the lower shaft section.

The water retention properties contribute to a retardation effect that limits the pressure buildup within the shaft to moderate levels up to 100,000 years, despite the loss of the shaft's sealing function at 50,000 years. This delay in pressure equalization highlights the role of material properties in slowing hydraulic responses even in the absence of an intact seal.

Over time, however, pressure in the shaft continues to rise. By 180,000 years, the pressure within the infrastructure area reaches approximately 8 MPa, not shown in the figure. This marks the eventual establishment of a near-hydrostatic pressure regime, driven by the progressive saturation and hydraulic connectivity throughout the shaft and its surrounding regions.

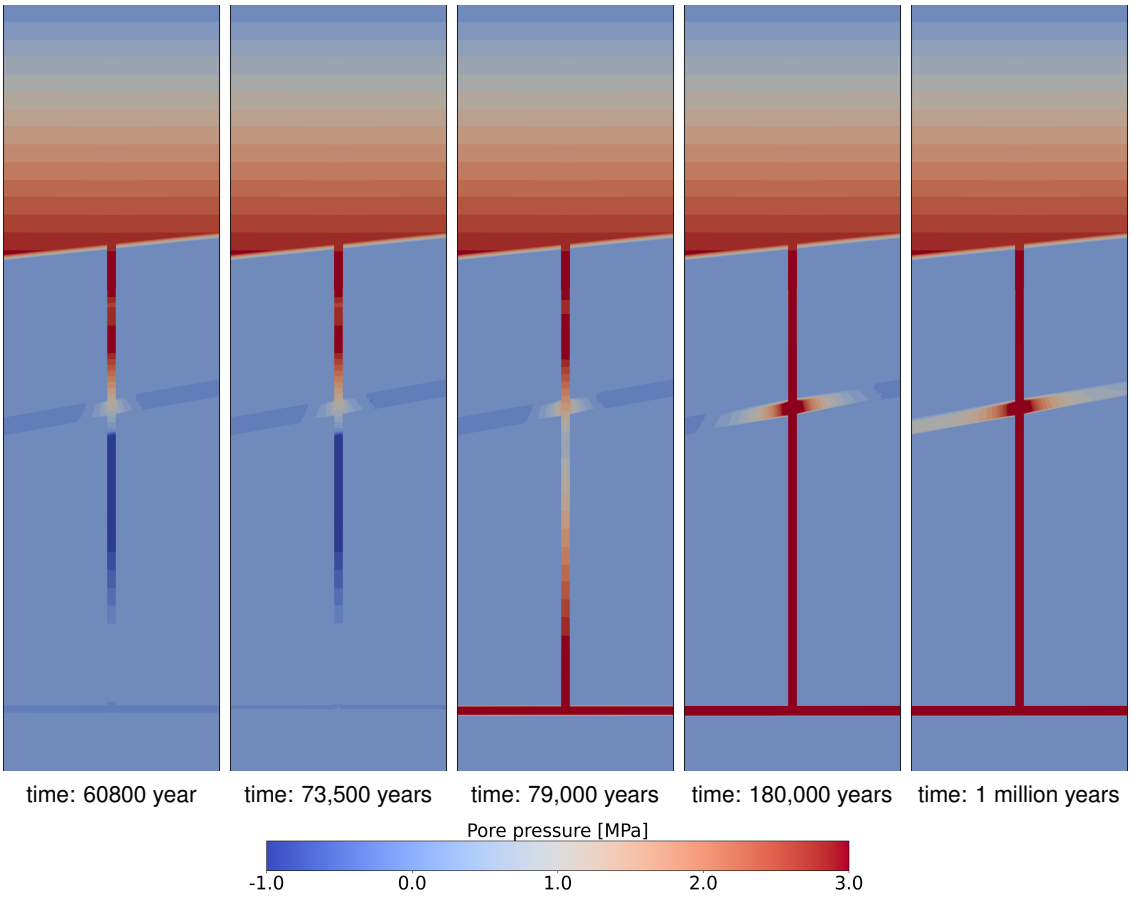

Figure 9.-10: Pore pressure distribution in the shaft and near field up to 1 million years.

Water accumulation in the infrastructure area

Figure 9.-11 shows the volume of water accumulating in the porous space of the infrastructure area, which is backfilled with non-compacting basalt gravel. During the first 50,000 years, the water accumulation curve is identical to that of modeling case 1 (see Figure 9.-8). After this period, however, there is a drastic increase in the volume of water within the infrastructure area, eventually reaching the maximum capacity of the pore space in the gravel backfill. A closer look in the figure shows that the reservoir is full at 56,000 years.

The figure indicates that the rate of water inflow is so high that it would be impractical to design a reservoir large enough to contain the total volume of water entering the infrastructure area up to the end of the verification period of 1 million years. Therefore, the reservoir should be designed to accommodate the expected water volume up to the end of the shaft sealing system's functional life at 50,000 years. Referring back to the initial results from modeling case 1, at the end of the EBS verification period, less than 20,000 m³ of water is expected to have reached the infrastructure area though one shaft. As the repository is made of two shafts, one should plan reservoir volume of 40,000 m³ in the infrastructure area.

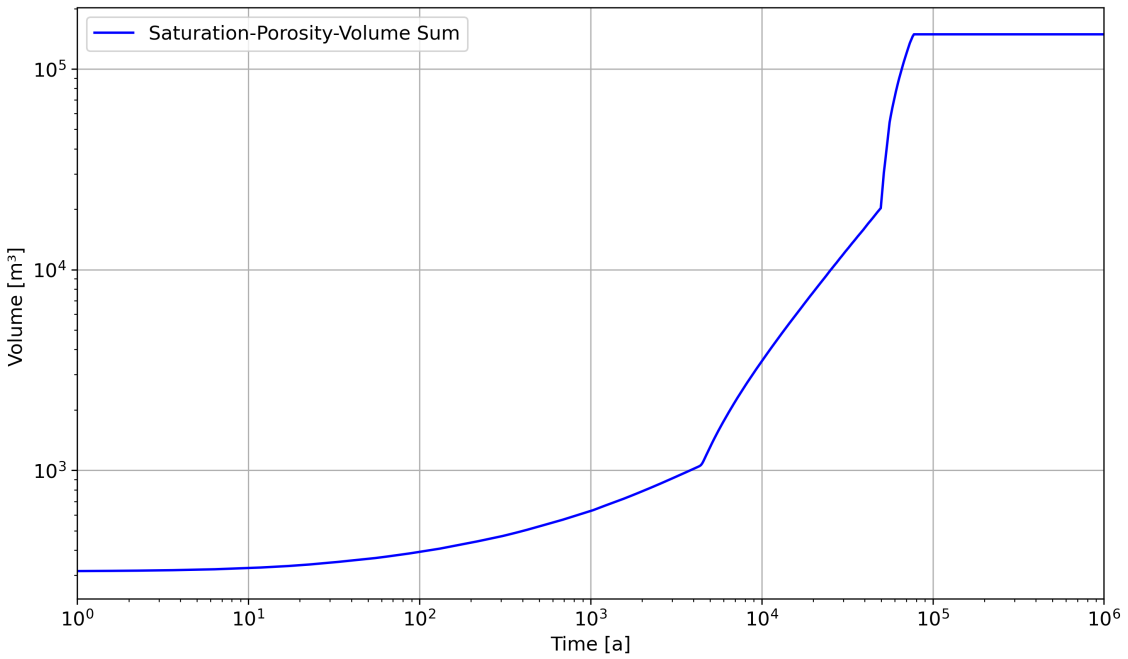

Figure 9.-11: Volume of water accumulating in infrastructure area through time for modeling case 2.

Conclusions on System Behavior

The numerical results from modeling case 2 provide critical insights into system behavior under a shaft seal failure scenario after 50,000 years. Initially, the hydraulic evolution in case 2 closely mirrors that of case 1, exhibiting similar patterns of water accumulation and saturation within the shaft and infrastructure area. However, following the assumed failure at 50,000 years, significant changes in system behavior are observed.

After failure, the infrastructure area undergoes progressive saturation, reaching full capacity within approximately 25,000 years. While the seals may be damaged, it still takes a substantial amount of time for the infrastructure area to fully accommodate inflowing water. The current results indicate that up to 75,000 years, all water entering through the shafts remains confined within the repository system. However, these findings may be optimistic, as the simulation assumes only a one-order-of-magnitude increase in seal permeability after failure, rather than the potentially higher degradation that could occur. Repeating the simulation with a two-order-of-magnitude increase in permeability is necessary to confirm this hypothesis. The retardation potential of the shaft seals is highly sensitive to their permeability post-damage, and the current results suggest that water retardation into the repository could remain effective for up to 100,000 years. Consequently, accurate characterization of the sealing materials' permeability is crucial for optimizing the performance of the EBS.

The saturation of the infrastructure also indicates that, following seal failure, water inflow is substantial, and the infrastructure area cannot accommodate the total inflow over the 1-million-year verification period. As a result, it is recommended that the infrastructure reservoir be designed to contain only the expected water volume by the end of the shaft seal's functional life at 50,000 years, estimated at 40,000 m³ for two shafts. Alternatively, the reservoir can be tailored for a specific retardation time frame. Based on the current results, assuming precise

characterization of the altered sealing materials, a retardation time of 100,000 years appears achievable.

The pore pressure distribution reveals that, despite the shaft being fully saturated by around 75,000 years, pressure buildup remains constrained due to the water retention properties of the sealing materials, particularly the MgO seal. This retention capability limits hydraulic pressure within the shaft, even after the sealing function is compromised. Over time, however, pressure continues to rise, eventually approaching hydrostatic conditions, with a pressure of approximately 8 MPa in the infrastructure area, which is reached around 180,000 years.

In summary, the shaft seal system effectively controls water ingress during its functional lifespan. However, after failure, the system faces challenges from significant water inflow and rising pressures. These findings highlight the importance of robust design strategies, focusing on seal permeability, water retention, and reservoir capacity, to ensure long-term functionality and containment within the repository infrastructure.

9.1.5 Projected system behavior and implications for modeling case 3

Based on the results from modeling case 2, we can predict the system behavior anticipated for modeling case 3, as well as for any scenario where the shaft sealing system loses its sealing function earlier than planned. As observed in case 2, once the shaft's sealing function fails, permeability increases immediately, leading to a rapid influx of water into the infrastructure area. Since the only difference between cases 2 and 3 is the timing of this assumed sealing failure, it is reasonable to expect a similar pattern at 5,000 years. Consequently, after 5,000 years, the infrastructure area would likely fill with water from the overburden within a few decades.

In this scenario, the hydrostatic pressure would increase rapidly, presenting a critical design consideration for the drift sealing system. For robustness, the Sorel concrete seals installed in the drifts should be capable of withstanding the hydrostatic pressure exerted by the water column within the shaft.

10. Performance Assessment of the EBS

The driving forces for radionuclide transport away from a heat-generating waste repository in salt include pressurization of the gas and brine phases due to:

- thermal expansion (expansion of gas and brine volumes);
- drift closure (reduction of available pore space for gas and brine);
- addition of brine from inflow down the shafts or directly to the repository level (increase of mass of brine); and
- addition of gas from corrosion (increase of mass of gas).

The thermal-hydrological-chemical numerical models in this section are posed to investigate these potential driving processes in ways not previously possible. New capabilities have been added to PFLOTRAN that allow the consideration of fully coupled chemical changes to the salt/brine system. Coupling with the mechanical response of the system is known to be important, but is still under development. Mechanical response can either be added to PFLOTRAN or coupled with PFLOTRAN. There is an existing effort to implement a simplistic geomechanical capability in PFLOTRAN, but this capability will not allow large strains, include complex salt constitutive models, or include creep closure. Coupling PFLOTRAN with existing models that handle creep and large strains with complex constitutive models, like FLAC3D, is one possible approach.

Solute transport simulations were started but were not successfully completed. Placing a solid-phase tracer source term in the drifts resulted in essentially no transport during the longest simulations (only minor amounts of diffusion–Figure 10.-30), because the drifts were essentially air filled. Solute transport was attempted with the PFLOTRAN liquid-phase solute transport mode that allows for complete dry-out (i.e., NUCLEAR_WASTE_TRANSPORT mode). Most of the drifts were single-phase gas, even as late as 2,000 years (see Section 10.3.8). During the re-saturation process, flow of water is from the far field towards the drifts. This does not promote solute advection away from the waste. Any solute transport would happen after the waste re-saturates, and would require an assumption of rapid failure of waste packages, and rapid dissolution of the waste form. Practically, solute transport requires very long-term simulations (approaching 1,000,000 years) and adds additional degrees of freedom to the simulation, which makes them require more memory and take longer to perform.

Several thermal-hydrological-chemical numerical models of the disposal area EBS were developed in PFLOTRAN to illustrate different aspects of the relevant processes–including newly implemented features–across scales and resolutions. These model implementations have different levels of detail or realism in their representation of the waste and disposal drifts.

The models presented here include:

1. Closure of drift filled around a heated waste package with crushed salt, with the waste package explicitly represented using an unstructured mesh;

2. Closure of a drift filled with a crushed salt, using a distributed heat source on a structured mesh; and
3. Closure of heated drifts filled with crushed salt and closure of drift seals while considering the entire repository system and surrounding salt pillow host rock using an unstructured mesh.

The following sub-sections will present these different analyses, which used a recently developed version of PFLOTRAN that was modified with the following abilities:

- A thermal conductivity model that varies thermal conductivity with changes in both temperature and porosity (Section 3.1.3);
- A non-Darcy flow model that implements a threshold gradient for flow that is proportional to the permeability (Section 3.1.4);
- Reduction in porosity (i.e., drift closure) through injection of solid mass fraction;
- Implementation of equations of state for halite-saturated brine in PFLOTRAN (Section 3.1.1);
- Specification of a solid material as “soluble halite” and the the fluid phase as “saturated brine” (Section 3.1.2), allowing:
  - dissolution of solid-phase halite into brine (i.e., **porosity increase**) when:
    - fresh water is added (i.e., through condensation of vapor or injection of fresh water) or
    - brine is heated so it becomes under-saturated with halite (due to temperature-dependent solubility limits); and
  - precipitation of solid-phase halite from brine (i.e., **porosity decrease**) when:
    - water from the brine is boiled or evaporated away (i.e., through addition of heat or dry air) or
    - hot saturated brine is cooled so it becomes super-saturated with halite (due to temperature-dependent solubility limits).

For several of these new features, the RANGERS project was both the motivation for their development, and the first major use of the capability for a large-scale performance assessment type model in PFLOTRAN.

10.1 Explicit waste package in a single drift

This model includes a representation of one-quarter of a waste package through two planes of symmetry with an unstructured grid. This problem includes the effects of drift closure through injection of solid phase into the crushed salt, and shows the effect of a strong thermal gradient across the crushed salt (i.e., from the hot waste package to the EDZ).

The injection of a solid phase into a source/sink in PFLOTRAN general flow mode results in the increase of pressure (and a slight increase in temperature) in the liquid phases that occupy the pores, through conservation of mass of the liquid species and the fixed volume of the element.

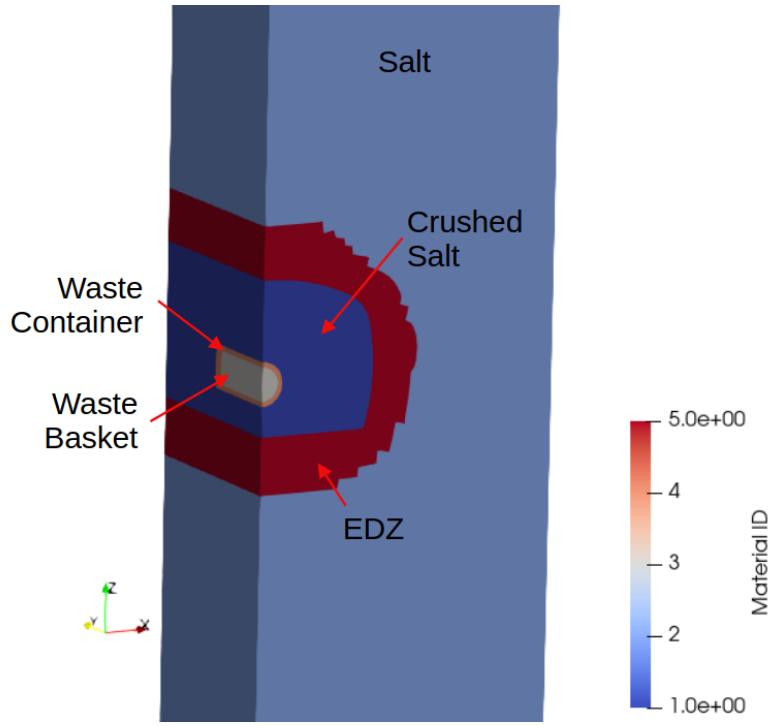

Figure 10.-1: Distribution of regions in small mesh near waste package.

In hydrological-mechanical simulators (e.g., FLAC3D), an analogous process is achieved by reducing the volume of the element through mechanical compaction. The compaction process is accompanied by an increase in liquid saturation, due to the much higher compressibility of gas compared to liquid at typical pressures. In a mechanical simulator, the volume of the elements gets smaller during compaction, while in PFLOTRAN the elements only get filled with solid. This leads to an approximation, because the drift becomes smaller in reality (i.e., distances from the center of the drift to the EDZ become shorter), while in PFLOTRAN the drift is the same dimensions, even at late time.

The domain cuts a cylindrical waste package at the x = 0 and y = 0 faces (Figure 10.-1 shows the quarter symmetry), with the model domain extents of $0 \leq x \leq 7.5$ m, $0 \leq y \leq 4.81$m, and $0 \leq z \leq -900$ m. The large vertical extent of the domain came from its initial use for mechanical simulations in FLAC3D, where it is important to move the upper and lower boundary conditions far from the waste package.

The domain consists of five materials (Figure 10.-1), summarized in Table 10.-1. The linear resistivity thermal conductivity model is used for intact salt thermal conductivity [$W/(m \cdot K)$] with the parameters

$$\lambda_{\text{lin res}}(T) = 5.2/(1 + 0.0045T) \tag{19}$$

illustrated in Figure 10.-2, while the “crushed salt” model is introduced in Section 3.1.3, here using the parameters

$$\lambda_{\text{cr salt}}(T, n) = 6.1\,(1 + 0.0045T) \cdot \left(1 - \frac{n}{0.35}\right)^{1.14} + \frac{n}{0.35} \cdot (0.42 + 0.0027T)\,, \tag{20}$$

and is illustrated in Figure 10.-3.

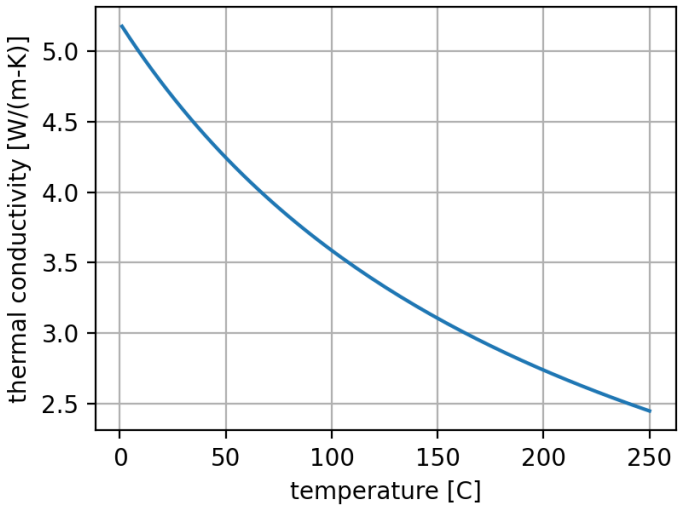

Figure 10.-2: Linear resistivity thermal conductivity model (Eq. 19) used for intact salt.

Material	Permeability (k) [m^2]	Init. Porosity (n) [$-$]	Thermal Cond. (λ) [$W/(m \cdot K)$]	Heat Cap. (ρc_p) [$MJ/(m^3 \cdot K)$]
Salt	$1.0 \cdot 10^{-20}$	0.0002	linear resistivity	3.48
Crushed Salt	$8.79 \cdot 10^{-15}$	0.35	crushed salt	1.02
Waste Basket	$1.0 \cdot 10^{-18}$	0.05	20.0	7.80
Waste Container	$1.0 \cdot 10^{-18}$	0.05	15.0	7.21
EDZ	$3.16 \cdot 10^{-16}$	0.05	crushed salt	1.79

Table 10.-1: Material properties used in quarter-symmetry model of waste package and drift.

The heat capacity (ρc_p) values listed in Table 10.-1 are for the solid phase. PFLOTRAN computes the overall heat capacity for an element as the porosity- and saturation-weighted mixture averages for all the phases present, with the density and heat capacity of brine and air coming from tabulated equations of state.

The hydrologic properties (i.e., porosity and permeability) of the Waste Basket and Waste Container materials are set to values to allow air or water to leave them during the simulation, so the waste packages do not pressurize (a process that can lead to very small time steps in the simulation); the material properties are not intended to be representative of dense, impermeable steel. The salt, crushed salt, and the EDZ materials use the same van Genuchten (vG) capillary pressure curve functions ("salt" row in Table 10.-2), while the Waste Basket and Waste Package materials use the other set of capillary pressure curve parameters ("man-made" row in same table). The waste package remains dry for the entire simulation because of three factors: 1) the waste package starts dry, 2) the man-made materials have essentially no capillarity to draw in water (maximum p_c = 1 Pa), and 3) the waste packages are hot.

The heat source starts after 2 years to allow time for the hydrologic parameters to stabilize before adding heat (from -2 to 0 years). The power source, which decays exponentially with time, is shown in Figure 10.-4. The porosity closure source term is applied across the crushed salt material. The rate is computed to reduce the initial porosity (35%) to a low value (2%) uniformly over 100 years (from 1 to 100 years).

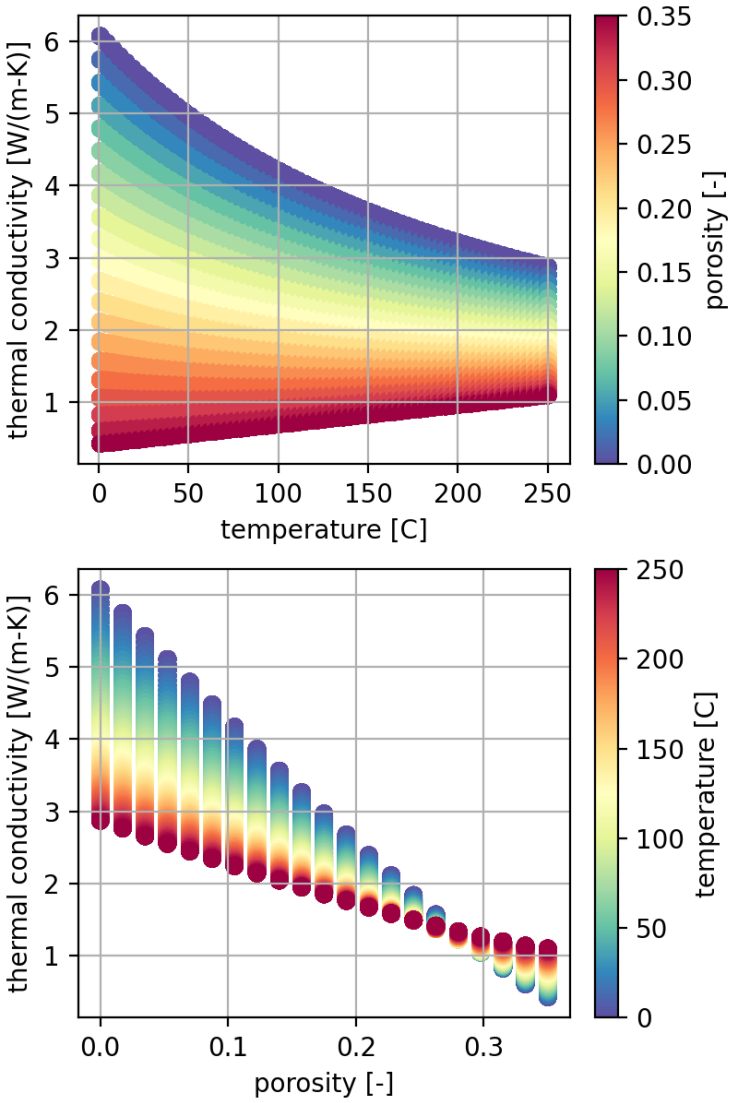

Figure 10.-3: Crushed salt thermal conductivity model (Eq. 20) used for crushed salt backfill and drift seals.

The domain is made up of 182,940 hexahedral elements; Figure 10.-5 shows the mesh near the waste package. Moving far above and below the disposal horizon (located at approximately 650 m depth), the elements become regular “brick” elements (i.e., a structured mesh).

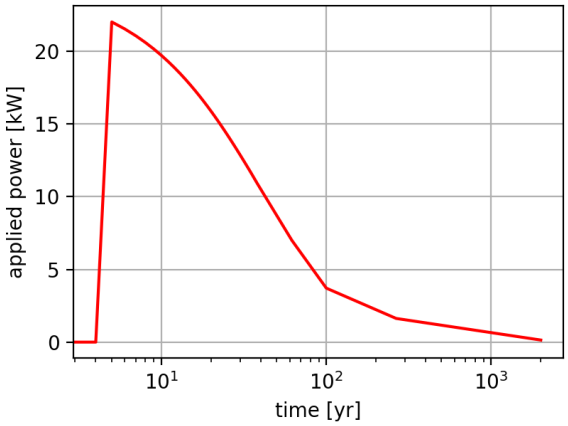

Figure 10.-4: Thermal input applied to 1/4 of waste package through time.

Material	vG alpha [1/Pa]	vG m [−]	Liq. Res. [−]	Gas Res. [−]	Max p_c [Pa]
Salt	10^{-6}	0.6	0.02	0.01	10^9
Man-made	10^{-4}	0.5	0.001	0.001	1.0

Table 10.-2: Capillary pressure curve function (van Genuchten) parameters used in quarter-symmetry waste package model.

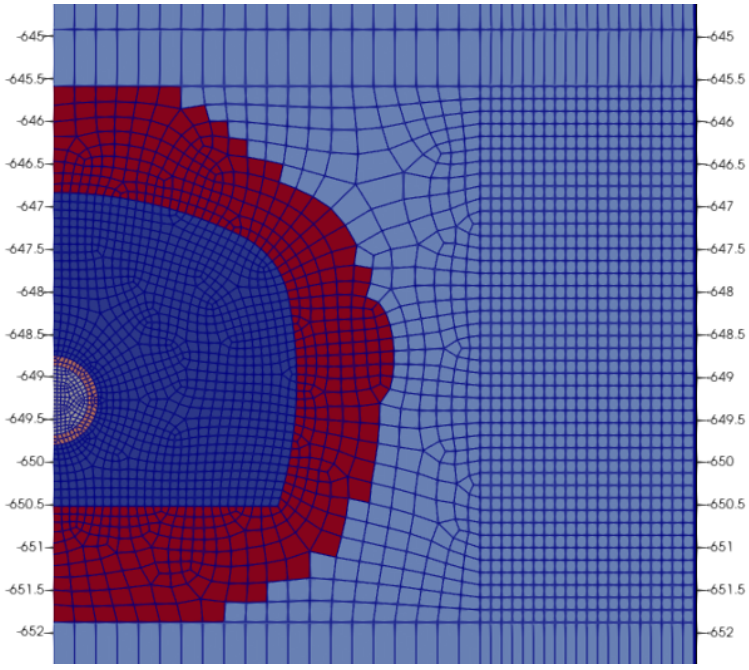

Figure 10.-5: XZ view of a section of the quarter-symmetry model at waste package with mesh shown and elements colored by material ID.

Figures 10.-6 through 10.-9 show results from the near waste-package region through time for four key variables. Temperature and porosity are changed, due to the input of thermal energy into the waste basket material and the input of solid phase in the crushed salt material. Thermal conductivity and liquid saturation then change in response to imposed changes in temperature and porosity. Between the system startup and the beginning of heating (-2 yr $\leq$ t $\leq$ 0), the liquid brine re-distributes a bit at the transition from crushed salt to EDZ and at the transition from EDZ to intact salt, due to capillarity.

Figures 10.-6 and 10.-7 show the results in the earlier part of the simulation. By 5 years, much of the crushed salt has dried out (98% air-filled initially), the porosity has reduced slightly, and the thermal conductivity has increased. By 25 years, the porosity has increased at the boundary between the crushed salt and the EDZ, where condensation is happening (dissolving salt, see red region in porosity sub-figure).

Figures 10.-8 and 10.-9 show model results for later parts of the simulation. By 50 years, the porosity that had increased due to dissolution has now reduced, and most of the crushed salt has reduced to 20% porosity or less. At 100 years, the porosity near the edge of the initial crushed salt region has reduced to nearly zero, and the liquid saturation in this area increased. This increase in saturation is because the small amount of water in these elements is now enough to saturate them with water, since the porosity has reduced. At later time (t = 200 and 400), the porosity in the crushed salt has reached its assigned lower value ($\approx$ 2%), and the saturation at the edge of the crushed salt has reduced, that was previously fully saturated. The temperature has reduced by this point (because the heat source is reduced), so the thermal conductivity is increasing, but it is nearly constant across the domain (besides the higher thermal conductivity of the metal waste package and waste basket). A small part of the dissolution (and porosity increase) and precipitation (and porosity decrease) is due to the change in halite solubility with temperature. When temperatures are rising, the brine is undersaturated, so there will be dissolution and an increase in porosity. When temperatures are decreasing, the brine is super-saturated and there will be a precipitation and a reduction in porosity.

The crushed salt near the waste package heats up rapidly beyond the boiling point, so it dries out (precipitating halite). Further away from the waste package the salt is cooler, so the steam from drying out the crushed salt condenses and dissolves salt. Also, a smaller change is associated with the brine that heats up and is now unsaturated with respect to halite, so porosity increases. In reality, natural salt deposits are heterogeneous (i.e., mostly halite, but some other minor evaporite components–some more soluble than halite, others less soluble than halite), but the current implementation in PFLOTRAN assumes the salt is uniformly pure halite.

In summary, this model illustrates how the crushed salt around the waste package dries out and can reduce porosity quickly. Complex thermal-hydrological-chemical dissolution, precipitation, and solubility-related processes happen at the edges of the boiling region during heating and cooling. Once porosity is reduced, the brine in the surrounding EDZ and intact salt can re-saturate the edge of the crushed salt, but the waste package stays dry during the first 400 years of heating. The permeability (not plotted here), varies as porosity changes through an exponent (here k = n^4); porosity reduced one order of magnitude, so permeability reduced four orders of magnitude–this significantly slows down water moving back towards the waste packages.

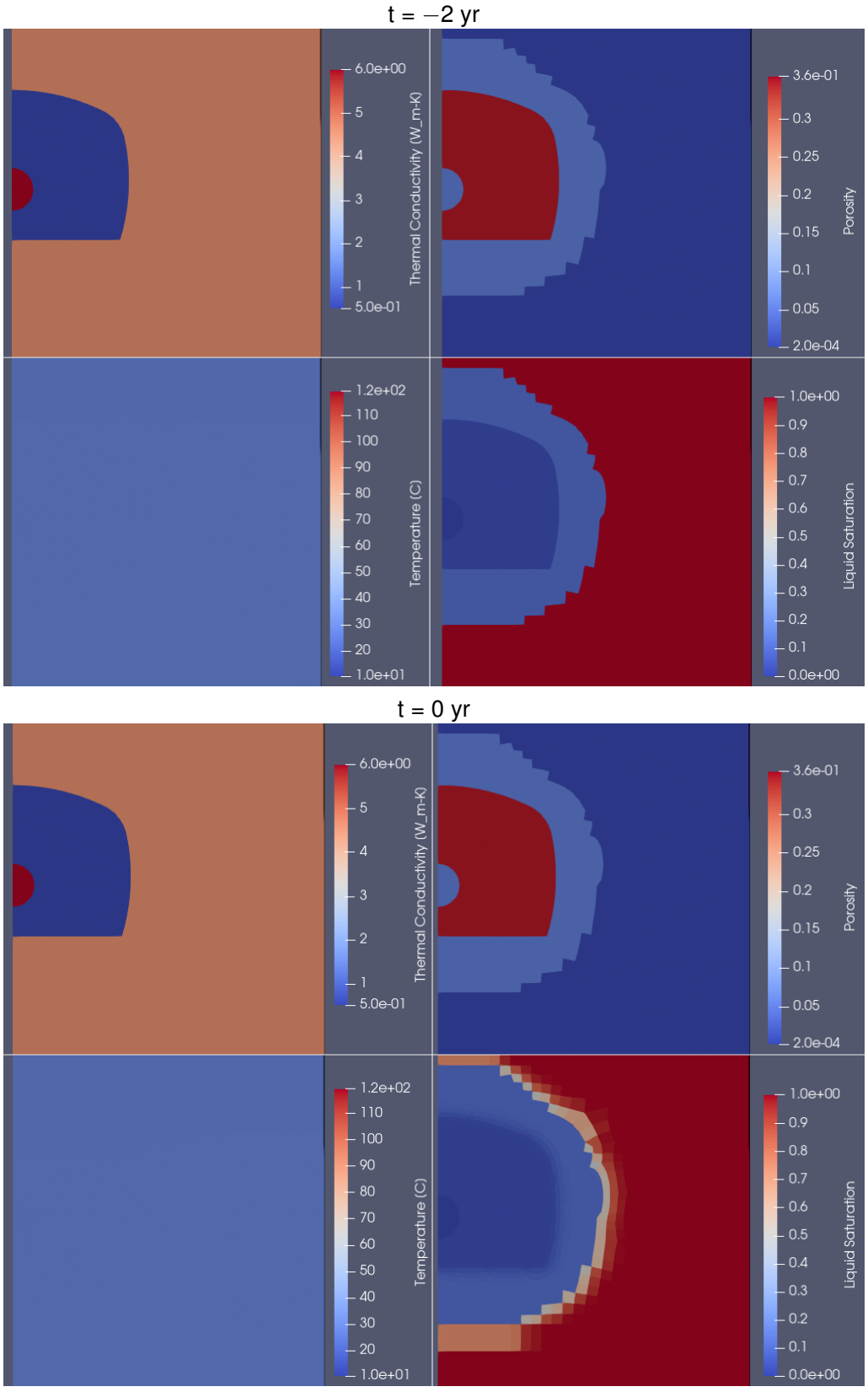

Figure 10.-6: XZ view of quarter-symmetry model showing thermal conductivity (upper-left panel), porosity (upper-right panel), temperature (lower-left panel), and liquid saturation (lower-right panel) at four times (t = $\{-2, 0\}$ yrs after heating began).

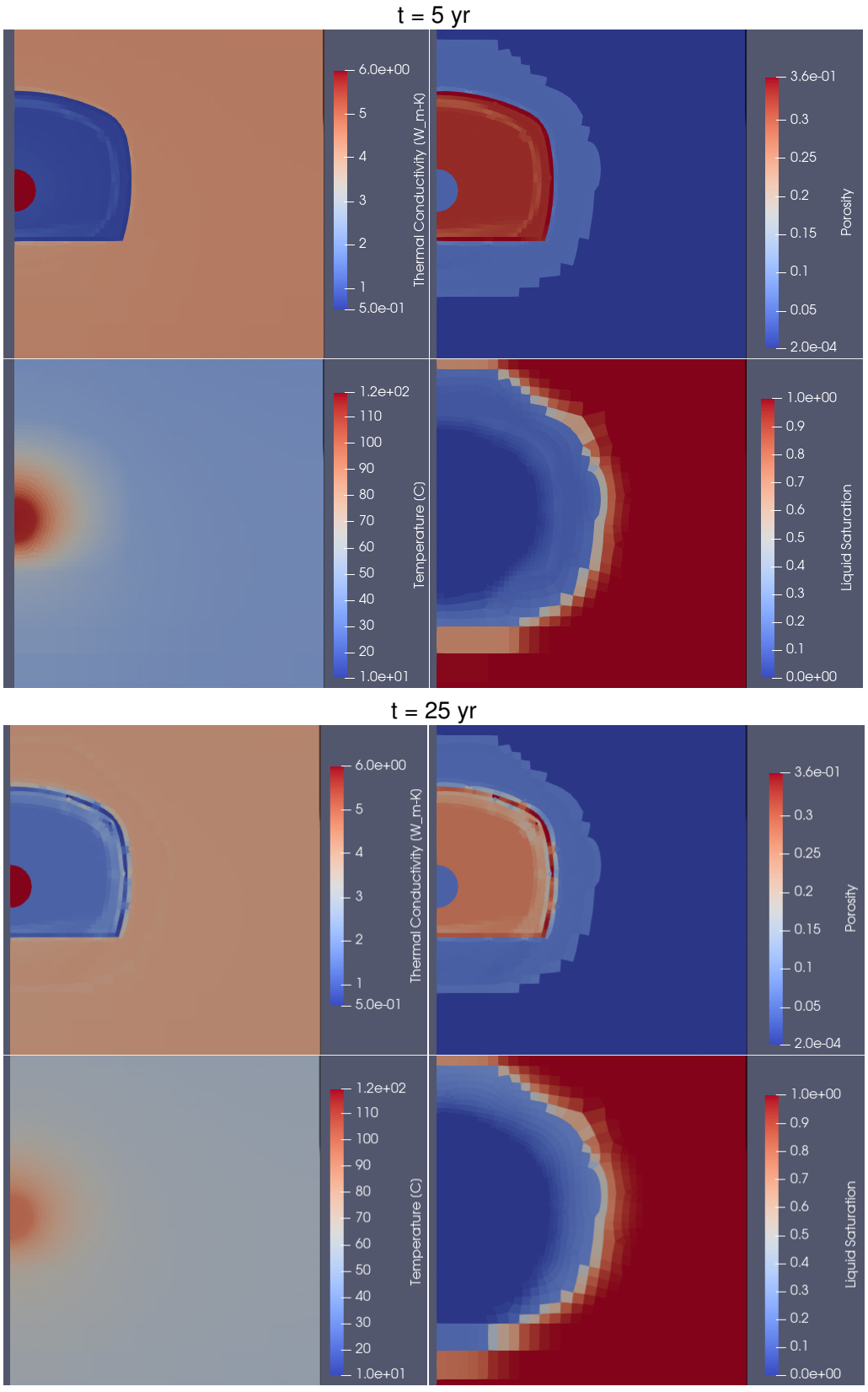

Figure 10.-7: XZ view of quarter-symmetry model showing thermal conductivity (upper-left panel), porosity (upper-right panel), temperature (lower-left panel), and liquid saturation (lower-right panel) at four times (t = $\{5, 25\}$ yrs after heating began).

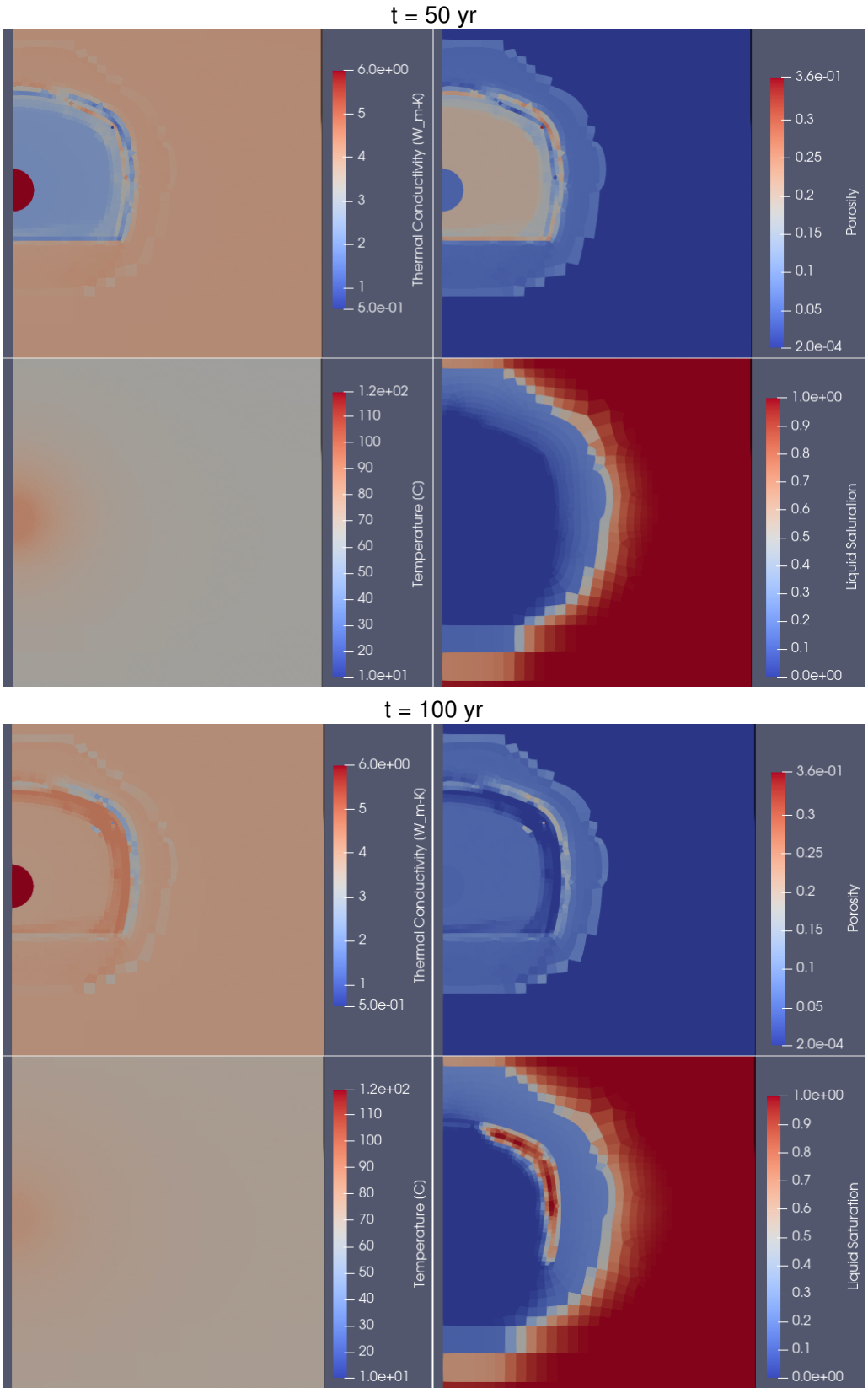

Figure 10.-8: XZ view of quarter-symmetry model showing thermal conductivity (upper-left panel), porosity (upper-right panel), temperature (lower-left panel), and liquid saturation (lower-right panel) at two times (t = $\{50, 100\}$ yrs after heating began).

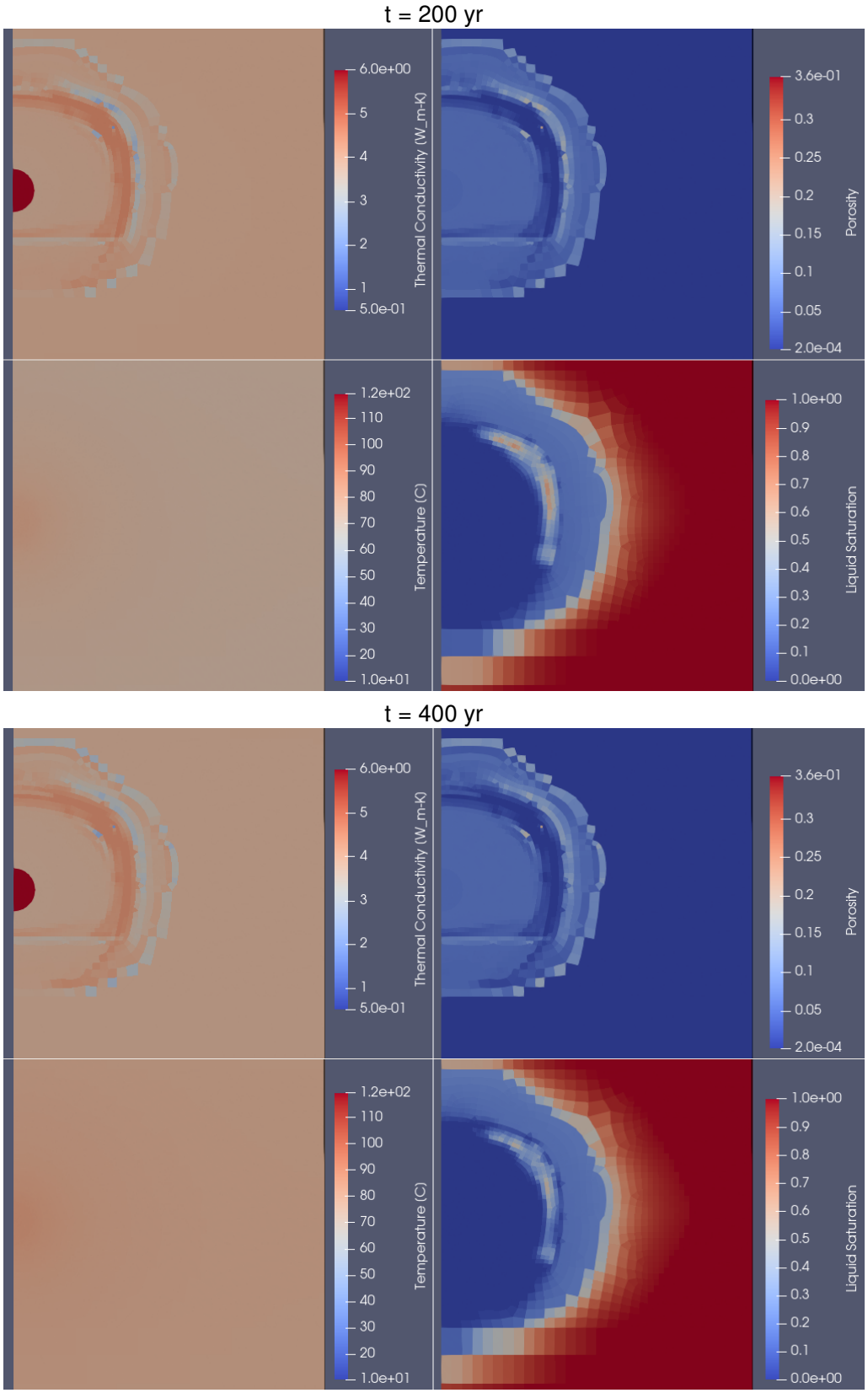

Figure 10.-9: XZ view of quarter-symmetry model showing thermal conductivity (upper-left panel), porosity (upper-right panel), temperature (lower-left panel), and liquid saturation (lower-right panel) at two times (t = $\{200, 400\}$ yrs after heating began).

10.2 Distributed heat source in a single drift

This PFLOTRAN model was created to validate/illustrate the porosity change process for a smaller structured grid 2D simulation (fewer elements) that includes the disposal drift, EDZ surrounding the drift, and intact salt, but does not include the waste package explicitly (the heat source is spread out across the disposal drift). This arrangement is similar to how the disposal drifts and waste are simulated in the large-scale model of the entire domain (Section 10.3), but the simpler structured mesh allows closer examination of the processes going on in the drift at different resolutions, and is orders of magnitude faster to run than the large models (allowing the problem to run on a single workstation) for debugging and understanding the implementation.

Figure 10.-10 shows the structured mesh used to illustrate the thermal-hydrological-chemical processes going on inside a single drift with heating and drift closure. The mesh includes 1/8 of the drift, by cutting the disposal drift in half in all three Cartesian directions. The grid extends two elements in the y-direction, with one element representing a disposal drift (187 m extent in y-direction), and an adjacent layer (0.5 m extent in y-direction) of elements representing connection to a neighboring drift (e.g., an infrastructure drift - Figure 10.-12). The neighboring drift has a single element fixed at the initial pressure and temperature, to facilitate allowing gas to escape elsewhere in the repository. The disposal drift was dimensioned to be analogous to the larger model that includes all the repository components explicitly.

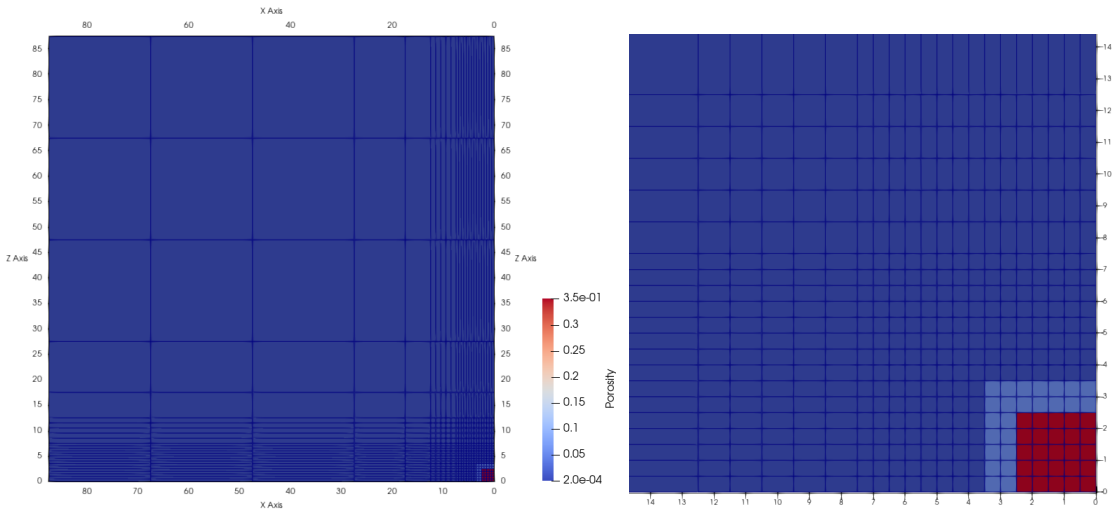

Figure 10.-10: End view (XZ) of entire domain (left) and zoom into drift portion (right) of structured mesh used to represent a 1/8 symmetry disposal drift. High initial porosity (0.35) is crushed salt; moderate initial porosity (0.05) is DRZ; low porosity (0.0002) is intact salt.

The structured 1/8-symmetry model used the salt, EDZ, and crushed salt materials from the unstructured 1/4-symmetry model of the previous section (Section 10.1). The power source applied across the crushed salt material is shown in Figure 10.-11.

Figure 10.-13 shows the evolution of several variables and parameters in the system due to the specified reduction in porosity and addition of thermal energy. The porosity of the crushed salt in the drift is reduced from 35% to $\approx$ 2% over the course of 100 years, through the constant-rate addition of solid phase across the crushed salt material, and a related reduction (from

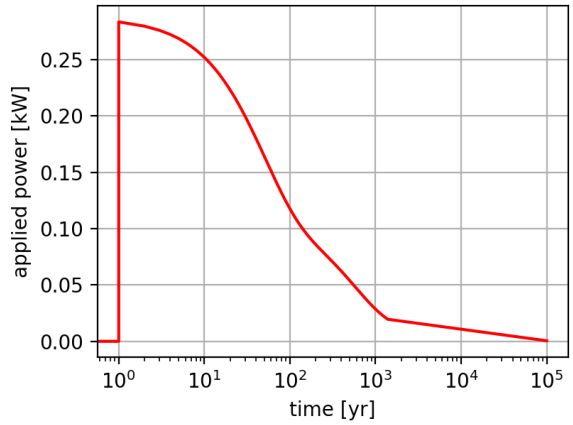

Figure 10.-11: Power applied to 1/8 of waste disposal drift through time.

5% to 2% porosity) in the EDZ. At the beginning of heating, there is a small jump in porosity within the crushed salt and EDZ (red and green shaded areas) associated with the change in the solubility of halite with temperature and the condensation of vapor. The permeability of the crushed salt reduces 4 orders of magnitude due to this change in porosity due to a power-law relationship between porosity and permeability (with exponent 4). The thermal conductivity increases from 0.5 to about 5.0 $W/(m \cdot K)$ due to the constitutive law for thermal conductivity (§3.1.3 and Figure 10.-3). Gas pressure and gas density increase significantly during the compaction (with some elements in the crushed salt approaching 10 MPa), especially near the end of the specified compaction (at 102 years). The gas pressure then quickly leaks off, by escaping into the neighboring access drift. In a coupled hydrological-mechanical simulation, the rise of gas pressure would reduce the rate of closure.

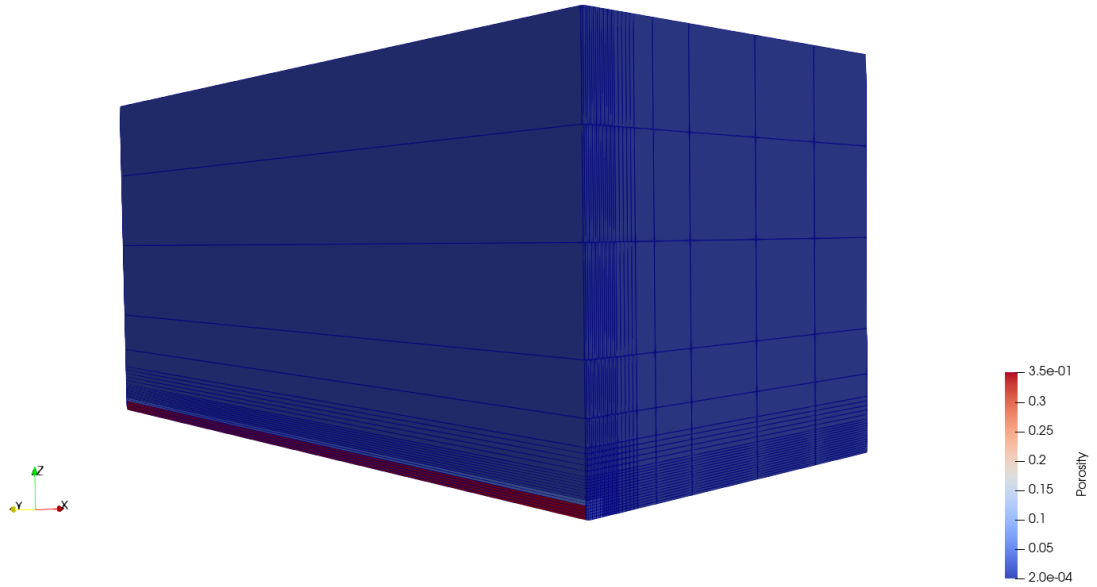

Figure 10.-12: Side view of structured mesh used to represent the near-drift region and connection to adjacent drift in 1/8 symmetry.

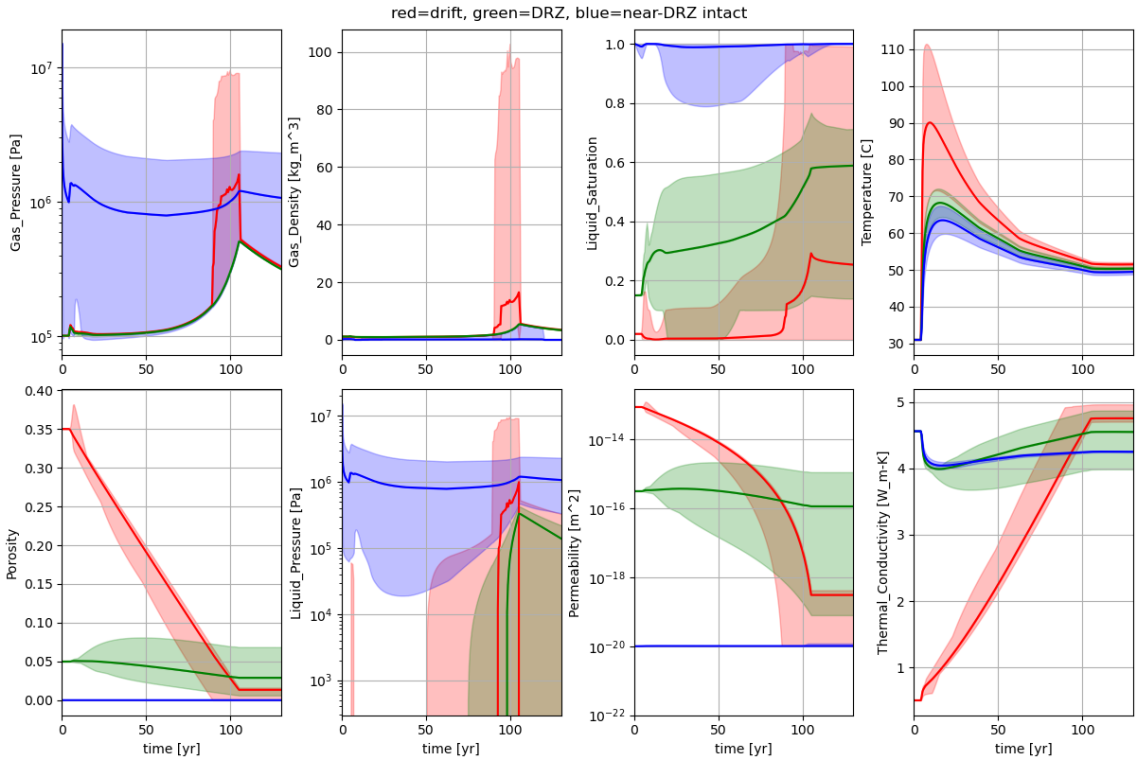

Figure 10.-13: Average (line) and bounding (min/max shading) predictions for single-drift distributed-source problem. Gas pressure, gas density, liquid saturation, temperature, porosity, liquid pressure, intrinsic permeability, and thermal conductivity are shown. Red represents the elements in the heated drift (i.e., crushed salt), green represents the EDZ, and blue represents the two elements of adjacent intact salt.

Figures 10.-14 and 10.-15 show the spatial distribution of porosity, liquid saturation, temperature, and thermal conductivity at four times. At the beginning of heating (t = 0, after 4 years of equilibration), the liquid saturation in the intact salt adjacent to the EDZ has decreased slightly. After 50 years of heating, the crushed salt (with the distributed heat source and the distributed injection of solid mass) is essentially dry, and its porosity has reduced by 1/2 (resulting in higher thermal conductivity). In these figures it is clear the corner of the drift is wetter, since it is adjacent to or nearly surrounded by the wetter EDZ. After 100 years of heating, the porosity has reached its specified low value, and the corner of the crushed salt is also at high liquid saturation (since a small amount of liquid can saturate the now nearly closed-off pore space). Like seen in the previous section with the explicit waste package (§ 10.1), by approximately 200 years the higher saturation in this region has reduced. The migration of the water back towards the heat source has slowed down significantly, due to the reduced permeability in the crushed salt (Figure 10.-13).

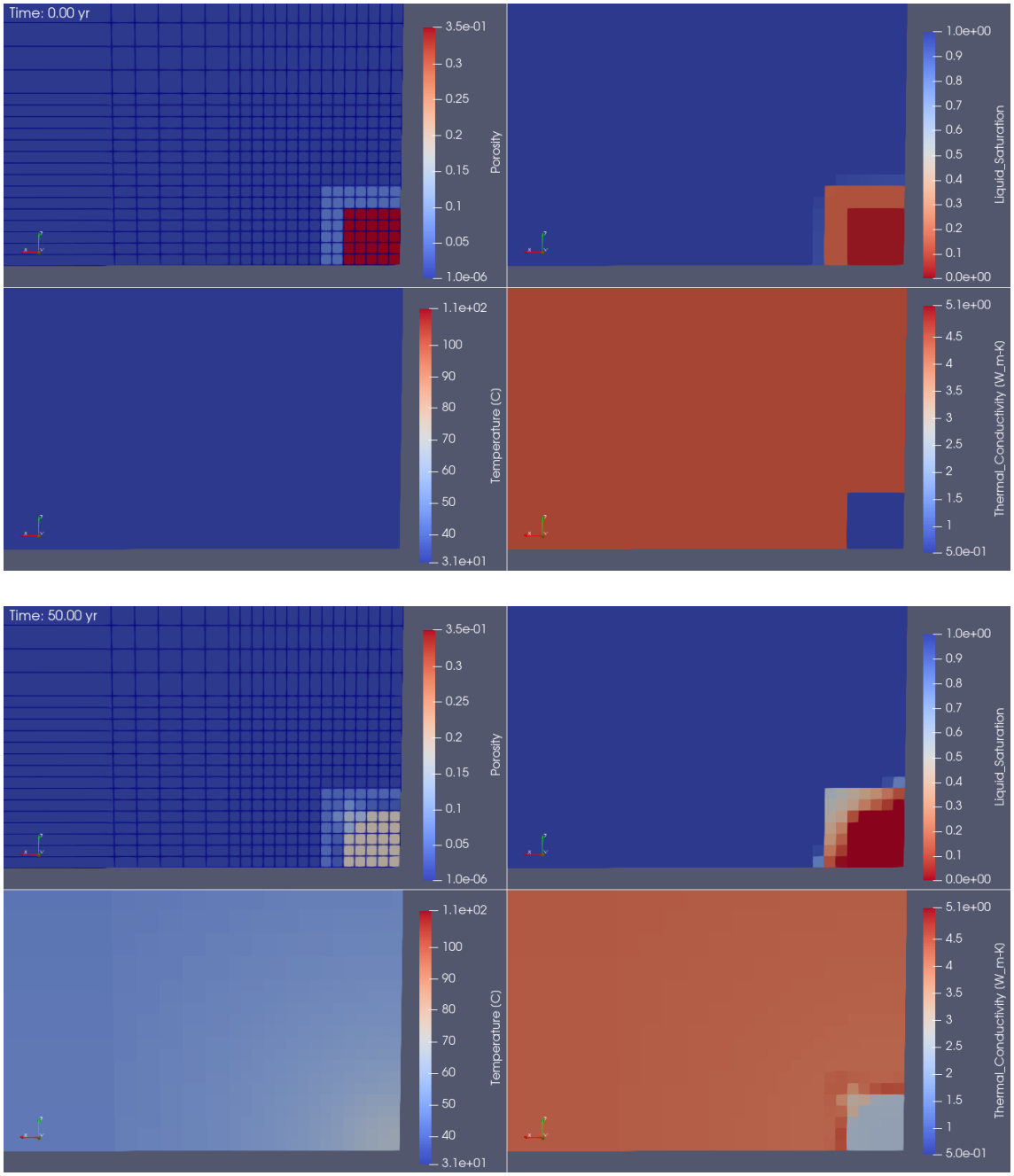

Figure 10.-14: Distribution of porosity (upper left), liquid saturation (upper right), temperature (lower left), and thermal conductivity (lower right) at two early times during heating (t = 0, 50 years).

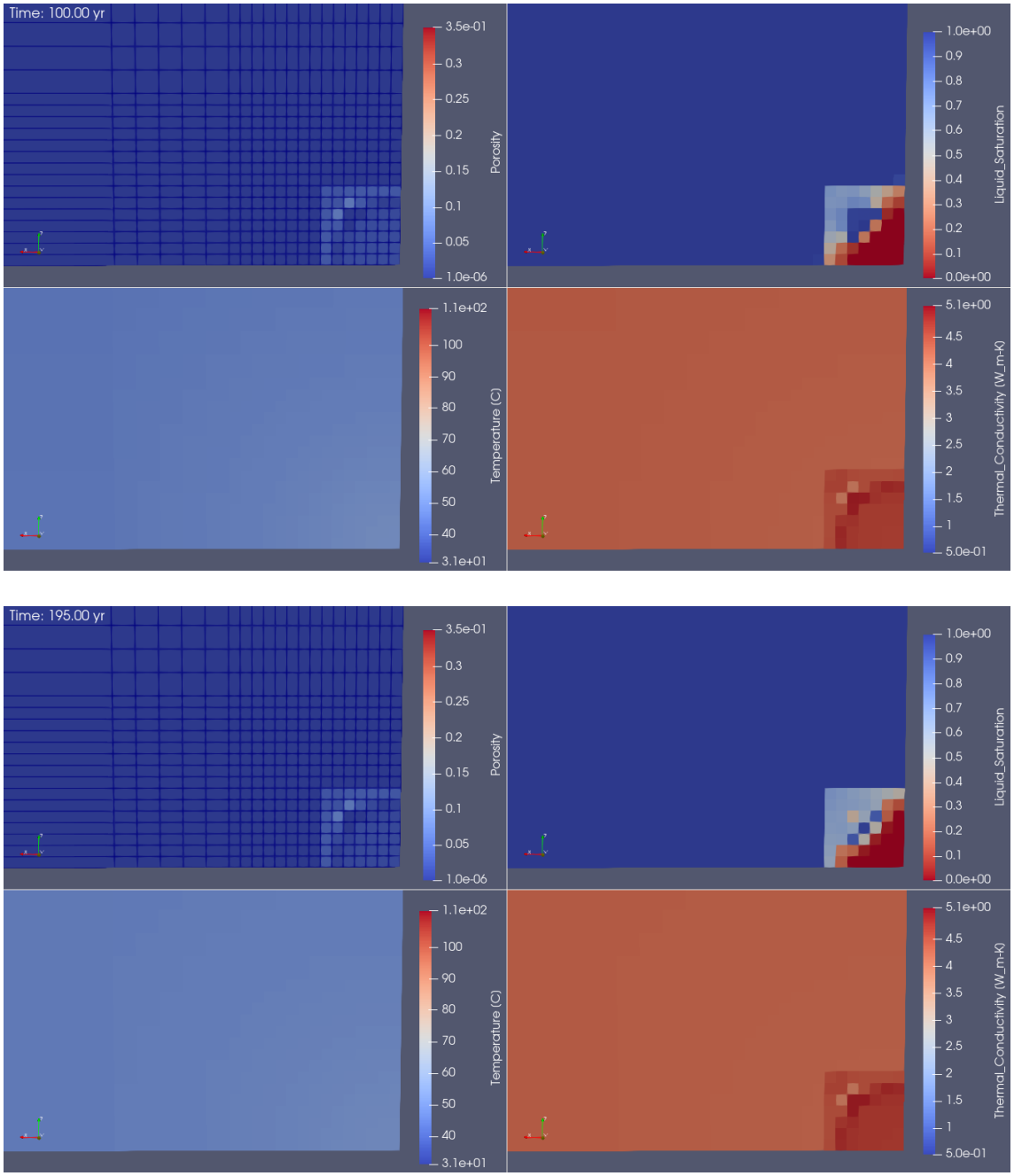

Figure 10.-15: Distribution of porosity (upper left), liquid saturation (upper right), temperature (lower left), and thermal conductivity (lower right) at two later times during heating (t = 100, 195 years).

10.2.1 Grid refinement study

One benefit of a quicker-to execute model is the ability to perform a grid refinement study. To compare to the results presented in the previous section (1,250 elements), the mesh was both coarsened (288 elements) and refined (5,000 or 20,000 elements). This section compares results, including the effects of the non-linear thermal-hydrological-chemical processes related to precipitation and dissolution of salt. The time evolution of the properties in similar regions are presented in Figures 10.-16 and 10.-17. All the meshes are only 2 elements in extent in the y direction, with the refinement occurring only in the x and z directions.

These results show similar averages (lines), but more extreme minimums and maximums (e.g., the finest mesh results in porosity of 100% at some elements in the crushed salt when heating begins). The crushed salt and EDZ have large increases in porosity at the beginning of heating, due primarily to the condensation of vapor, but also secondarily due to the increase in solubility with temperature. The temperature responses for all except the coarsest mesh are nearly identical. In the more refined meshes, the dissolution and precipitation processes can dissolve or precipitate entire elements, compared to smaller impacts on larger elements. Large changes in porosity then also have impact on the thermal conductivity and permeability, which are both coupled to the porosity value. Porosity values of 100% are not physically realistic, but are a consequence of the thermal-hydrological-chemical PFLOTRAN model with mechanical closure effects added through solid mass injection, rather than explicit inclusion of mechanical response.

The predicted peak of gas pressure at the end of the closure process is highest in the base resolution (Figure 10.-13), with the peak gas pressure predicted to be lowest in the most refined mesh. The predicted average liquid saturation is also lower in the crushed salt in the more refined models, while the liquid saturation is higher in the coarser model.

This grid resolution study shows that even a coarse representation of the drift (as used in the larger models presented in the next section), similar physical processes occur to more refined meshes–for the case where the waste package is not explicitly represented. These complex thermal-hydrological-chemical processes are effectively similar, but the simulation is much faster, allowing large-scale simulations more readily.

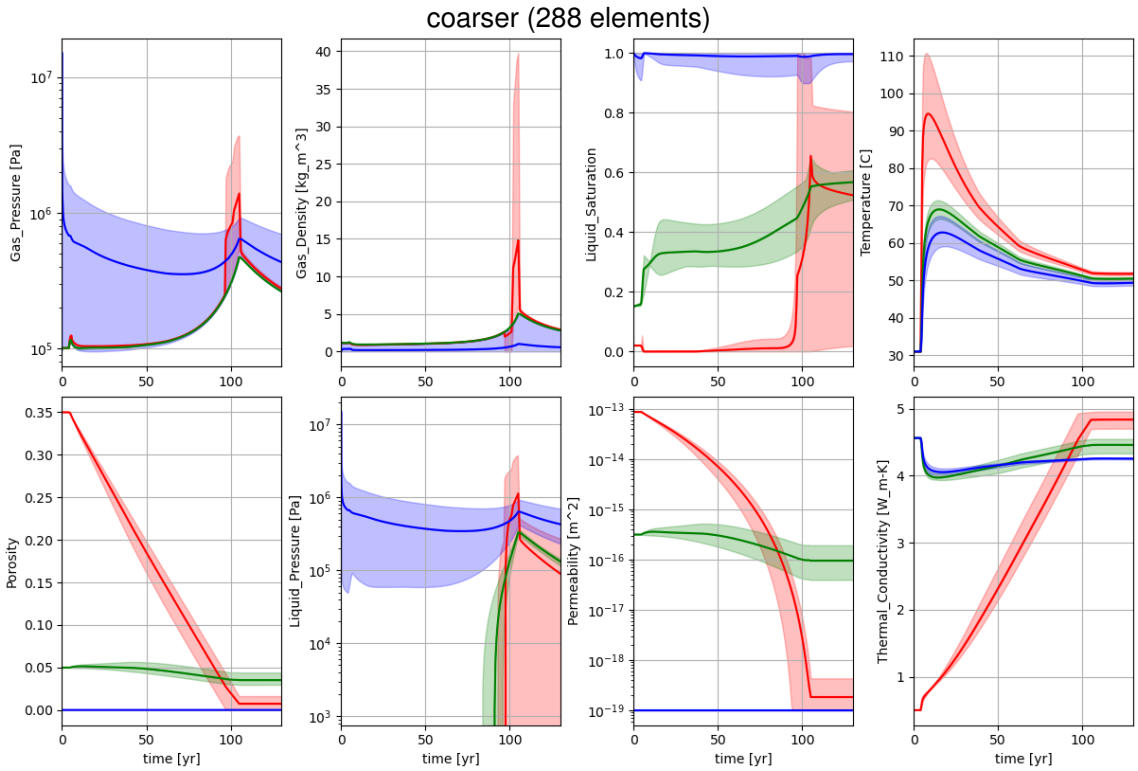

Figure 10.-16: Average (line) and bounding (min/max shading) predictions for single-drift problem with coarser mesh. Red represents the heated drift, green represents the EDZ, and blue represents adjacent intact salt.

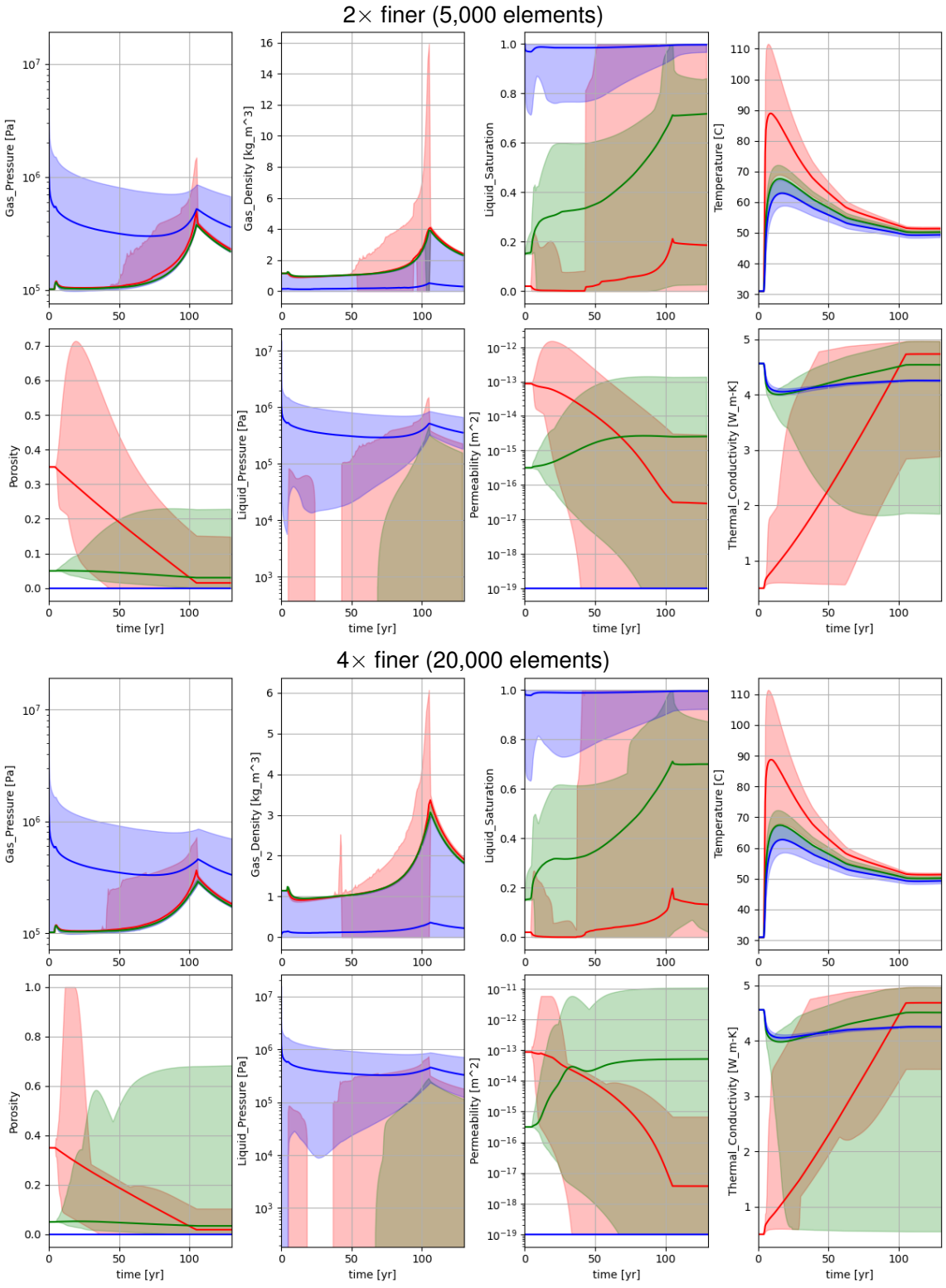

Figure 10.-17: Average (line) and bounding (min/max shading) predictions for single-drift problem with 2× finer (top) and 4× finer (bottom) mesh. Red represents the heated drift, green represents the EDZ, and blue represents adjacent intact salt.

10.3 Full repository domain with EDZ surrounding drifts

This model includes the specified variability in the regional salt pillow geology, the entire layout of the repository and shafts, and sequential emplacement of waste in disposal drifts over 30 years of operation. The heat sources are distributed across the crushed salt filled drifts (no explicit waste packages), like the previous section (§ 10.2).

10.3.1 Computational mesh

A mesh comprised of both hexahedral and wedge elements was created using meshing tools for FLAC3D. The mesh was then converted to an implicit unstructured mesh usable by PFLOTRAN via conversion tools developed for the RANGERS project. In PFLOTRAN, an implicit unstructured mesh is specified completely by mesh coordinates and the listing of mesh points associated with each volume or area elements. PFLOTRAN then computes element volumes, face areas, and element connectivity relationships from the mesh. To improve start-up times, the implicit unstructured mesh and region definitions were converted from ASCII text files ($>$ 1.6 GB in size) to the HDF5 binary file format (305 MB). This process brought in the mesh coordinates, element definitions, and regions specifications from FLAC3D, and defined the same elements and regions in PFLOTRAN, allowing direct comparison between modeling results, with the intention of transferring information between the simulations.

A series of several meshes were created and used to test this conversion, from as few as 3.5 M elements to as many as 24 M elements. Coarser meshes often ran faster, but sometimes had convergence issues related to representing steep pressure and saturation gradients around the disposal drifts. Coarser meshes also allowed simulations to be tested and debugged on a workstation, while the larger simulations required more memory than is available on a single workstation (e.g., more than 500 GB, depending on the number of variables per element), and could only be run on an institutional cluster.

A computational mesh was settled on with 13.8 M elements that included a refined EDZ region surrounding the drifts and shafts that was not prohibitively large to simulate with PFLOTRAN using available institutional computer resources at Sandia National Laboratories. Larger meshes are possible, but they require the use of a large number of cluster nodes, leading to long waits in the cluster management queue, and they can be difficult to load and visualize results (i.e., output files are several hundreds of GB in size). The final mesh included 13,786,080 hexahedra (i.e., 8 corners per element – a 2D quadrilateral extruded perpendicularly in the third dimension) and 336 wedge (i.e., 6 corners per element – a 2D triangle extruded perpendicularly in the third dimension) elements. Using 100 computational nodes (each node has 18 processors, resulting in 1,800 processors total), the simulations presented here required at least one week of time each (simulated in 36-hour chunks, as this is the maximum wall-clock for individual jobs on the cluster). The 197 defined regions were used to specify geologic layers, repository components, shaft components, the EDZ surrounding drifts and shafts, and specify the individual disposal drifts

The domain spans $0 \leq x \leq 3918$ m, $0 \leq y \leq 5922$ m, and -3090 m $\leq z \leq 0$; the domain is a 71 km^3-rectangular prism with the repository located at a depth of approximately 816 to 820 m (with the EDZ extending above and below these depths). The mesh follows the stratigraphy of the salt pillow, but is finest vertically near the repository depth, and is coarser going away from the repository, especially below the repository (Figure 10.-18).

In map view, the mesh is much more refined around the repository elements (i.e., disposal drifts, access drifts, sealing drifts, and shafts – Figure 10.-19), representing each drift and its surrounding EDZ with several elements (Figure 10.-20). The refined area associated with the repository exists at each vertical "layer" of the model, even the top and bottom of the domain, far away vertically from the repository level. This type of mesh was the most straightforward to create, but is not the most economical in terms of the number of elements. It was decided this was a good compromise for the current application.

This "flexed hexahedral" mesh was used because it allowed direct comparison between the FLAC3D (finite difference) and PFLOTRAN (finite volume) results, but other mesh types may result in more accurate thermal-hydrological-chemical flow simulations in PFLOTRAN. The most accurate PFLOTRAN meshes require the faces between elements be perpendicular to a line connecting the centers of the elements (i.e., a Voronoi partition). This ideal convention is violated in some areas, most notably at the transitions from fine to coarse mesh (e.g., see bottom subplot of Figure 10.-20). The choice to keep the same xy-discretization at each level helped to reduce errors that would otherwise have been associated with coarsening and deforming the mesh vertically as well as horizontally. This potential loss of accuracy was seen as not too significant a source of error at this point in the development, where the illustration of new capabilities is the main goal. Future efforts may use unstructured Voronoi computational meshes (e.g., those made by VoroCrust) or uniform structured meshes (a very specific type of Voronoi mesh) to improve this (LaForce et al., 2023a,b), but would require either converting between the PFLOTRAN and FLAC3D meshes, or require creating a mesh that FLAC3D could use (i.e., a conversion from PFLOTRAN to FLAC3D).

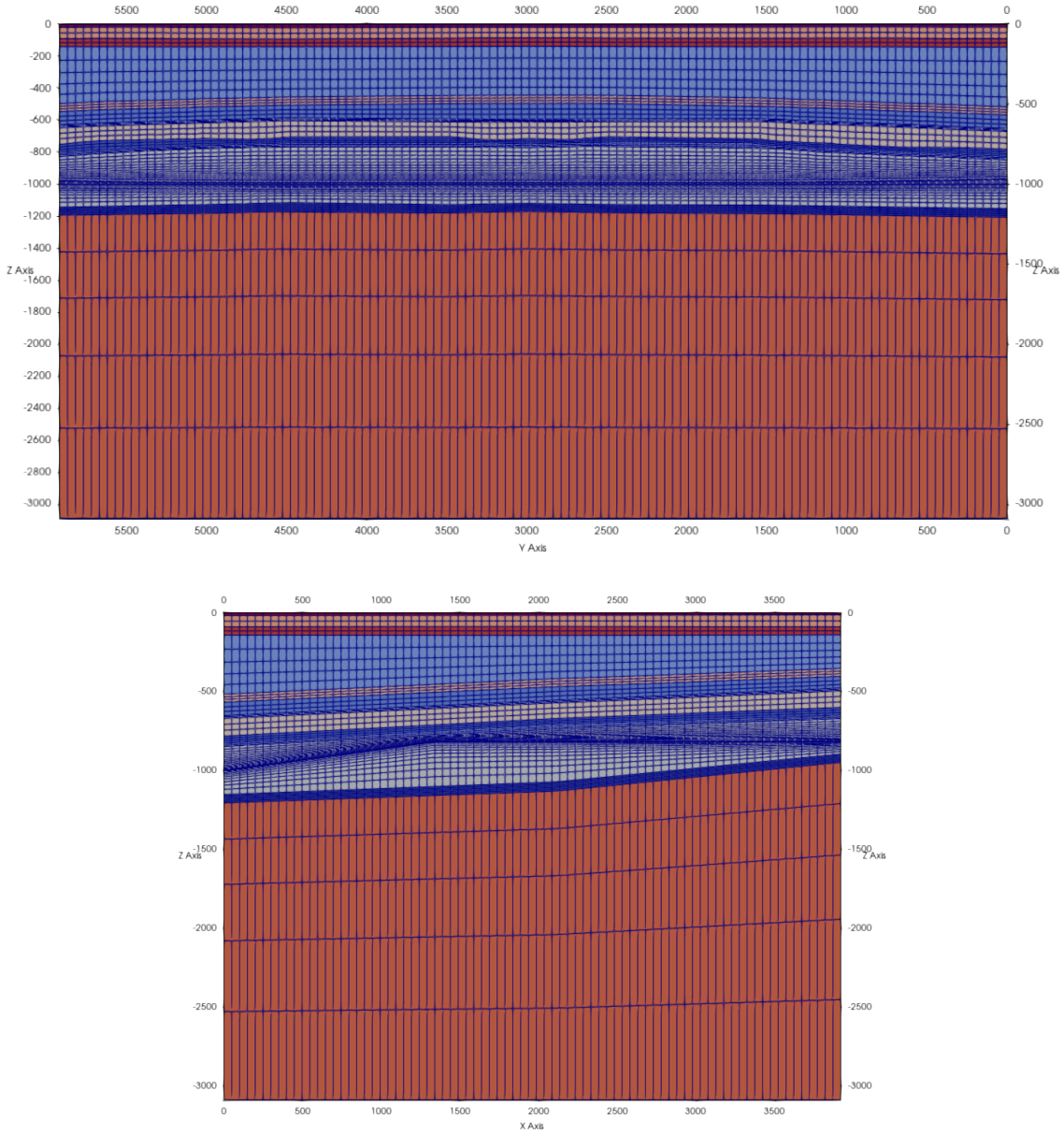

Figure 10.-18: Side views (YZ–top and XZ–bottom) of domain colored by material ID.

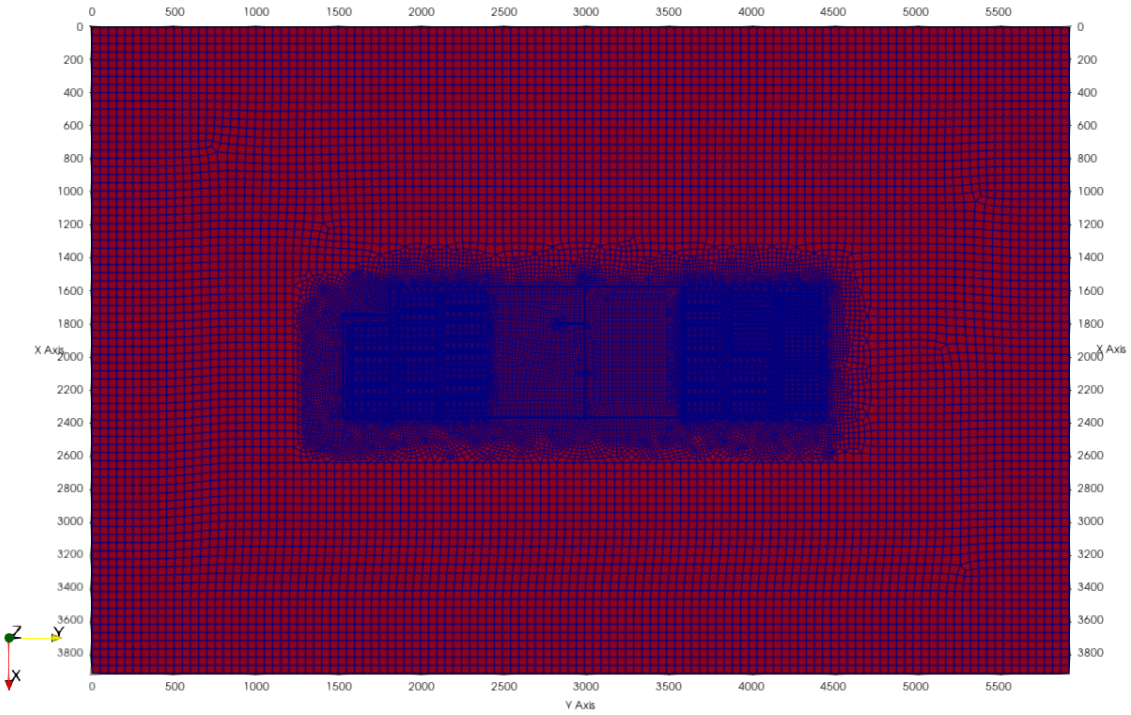

Figure 10.-19: Top view (XY) of domain colored by material ID.

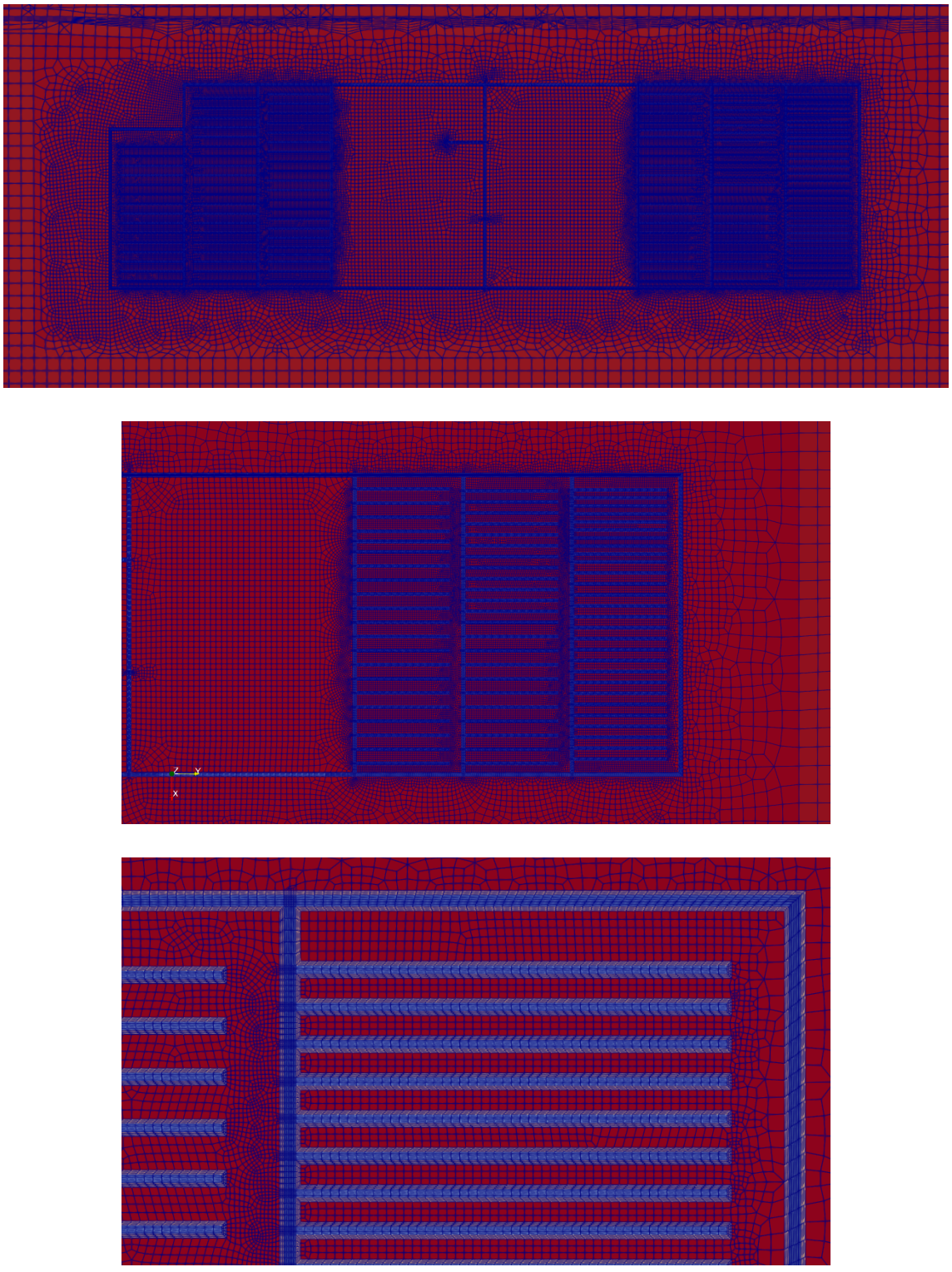

Figure 10.-20: Map views (XY) slicing through the repository elevation (z = −817 m) colored by material ID. Top view shows entire repository footprint, middle view shows half repository footprint, bottom view shows mesh refinement around disposal drifts and their EDZ.

10.3.2 Material properties

The region IDs from FLAC were modified when importing into PFLOTRAN. IDs had offsets added to them, based on the material's group identity. Geologic layers were incremented by 300 (Figure 10.-21 (top)), EDZ regions were incremented by 200, shaft materials were incremented by 100, while disposal drifts and access drifts at the repository level were left with their imported ID.

Portions of the shaft do not include an EDZ surrounding them, as is evident in the bottom two sub-panels of Figure 10.-21. The extent of the EDZ is clearer in both map (XY) and cross-section (XZ) extent in Figure 10.-22.

The main thermal and hydrologic properties were assigned to geologic units and repository-related units. Rows in the bottom section of Table 10.-3 map onto more than one material region. The disposal drifts and the seals were filled with the crushed salt material (even before the heating and drift closure were turned on during staged emplacement).

The equations of state for the halite-saturated brine liquid phase were used, as presented in § 3.1.1. This made the salinity a function of temperature, assuming the water is a saturated brine. The salinity, pressure, and temperature controls the liquid-phase density, viscosity, vapor pressure (i.e., boiling point), and enthalpy. These were implemented for a pure sodium-chloride brine system that is equilibrium with halite. In reality, there are also other accessory evaporite minerals in the system, but halite is clearly the dominant one. The brine was also assumed to be in equilibrium with halite, essentially setting the kinetic rate of halite dissolution and precipitation to be infinitely large (the dissolution rate of halite is many orders of magnitude higher than the dissolution rate for silicate rocks – Alkattan et al. (1997)). This is not a bad simplifying assumption over long time-scale simulations, but may not be accurate over very short time scales with very large, rapid changes.

Material	Therm. Cond. (λ) [W/(m · K)]	Heat Cap. (ρc_p) [MJ/(m^3 · K)]	Porosity (n) [−]	Perm. (k) [m^2]
A2C2	4.2	2.32	0.01	$1.0 \cdot 10^{-20}$
A3	4.2	2.32	0.01	$4.24 \cdot 10^{-19}$
AM3	5.0	1.96	0.01	$1.0 \cdot 10^{-20}$
BunterSS	2.6	1.90	0.15	$1.0 \cdot 10^{-18}$
K2	1.5	2.57	0.0002	$1.0 \cdot 10^{-19}$
K3	1.5	1.67	0.0002	$1.0 \cdot 10^{-22}$
NA2	(Eq. 19)	1.90	0.0002	$1.0 \cdot 10^{-20}$
NA3	5.2	1.86	0.0002	$1.0 \cdot 10^{-20}$
NA4	5.2	1.92	0.0002	$1.0 \cdot 10^{-25}$
Quat	2.3	1.90	0.25	$1.0 \cdot 10^{-15}$
Red	2.7	1.90	0.01	$1.0 \cdot 10^{-21}$
Tert	2.1	1.90	0.25	$3.2 \cdot 10^{-15}$
EDZ	(Eq. 19)	2.1	0.05	$3.2 \cdot 10^{-16}$
Gravels	3.0	2.30	0.25	$1.0 \cdot 10^{-18}$
Drifts	3.0	2.30	0.05	$1.0 \cdot 10^{-16}$
Drift Seals	3.0	2.30	0.01	$3.0 \cdot 10^{-19}$
Shafts	3.0	2.30	0.01	$1.0 \cdot 10^{-20}$
Crushed Salt	(Eq. 20)	1.02	0.35*	$8.8 \cdot 10^{-15}$

Table 10.-3: Thermal hydrological material properties assigned to geologic layers (top) and material groups (bottom). Thermal conductivity of NA2, EDZ, and crushed salt materials were assigned temperature-dependent functions (see equation numbers). Asterisk indicates initial porosity; this was changed, altering the thermal conductivity and permeability (k = n^4).

Material	vG alpha [1/Pa]	vG m [−]	Liq. Res. [−]	Gas Res. [−]	Max p_c [Pa]
All other materials	10^{-5}	0.6	0.1	0.001	10^9
Crushed salt	10^{-4}	0.6	0.1	0.001	10^6

Table 10.-4: Capillary pressure curve functions assigned to materials.

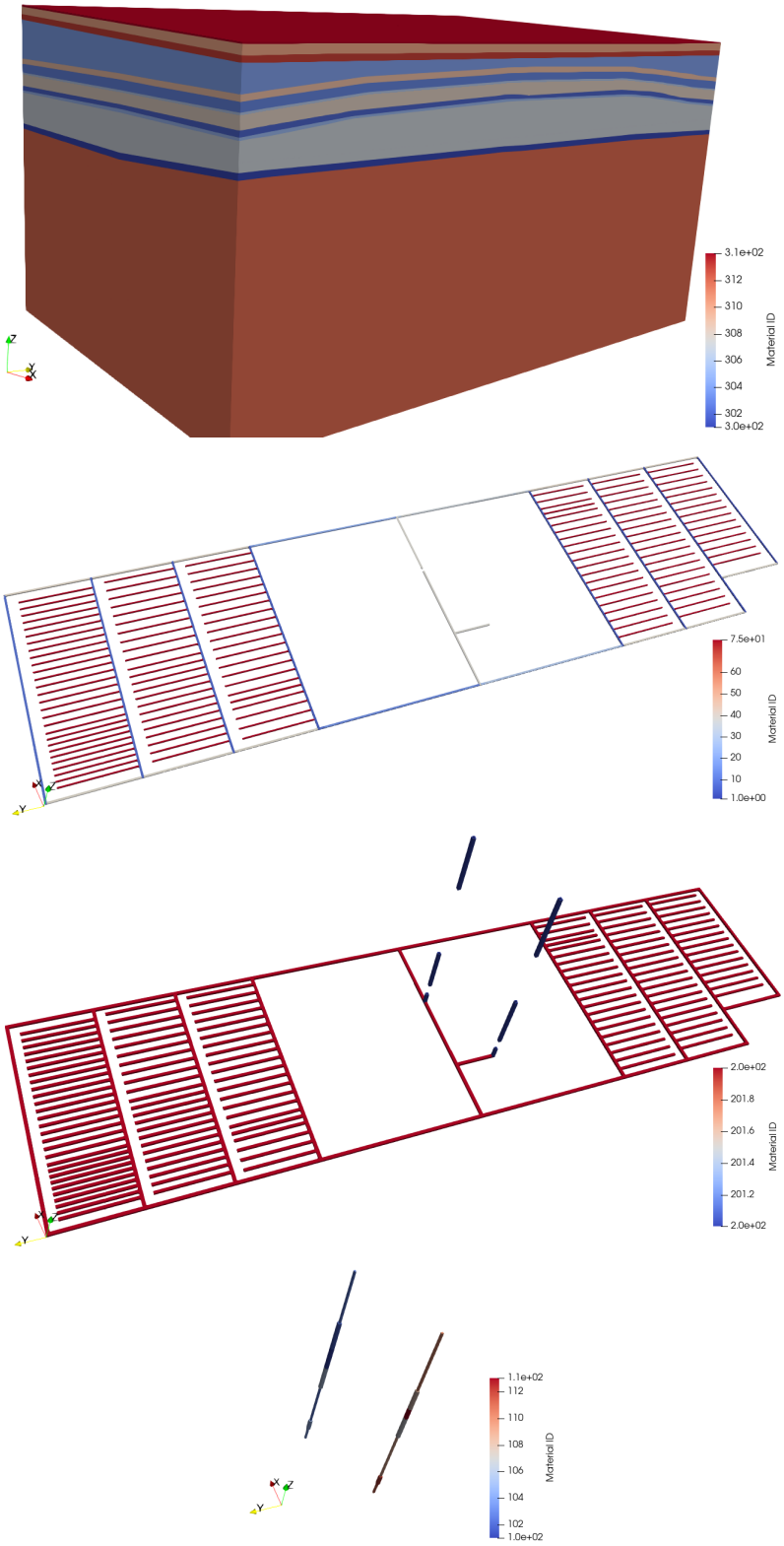

Figure 10.-21: Domain view colored by material ids for geological units on domain outer surface (top – materials 300–314). Material ids shown in oblique view (with geologic materials removed) for drifts (top middle – materials 1–75), EDZ (bottom middle – materials 201 & 202), and shafts (bottom – materials 101–113).

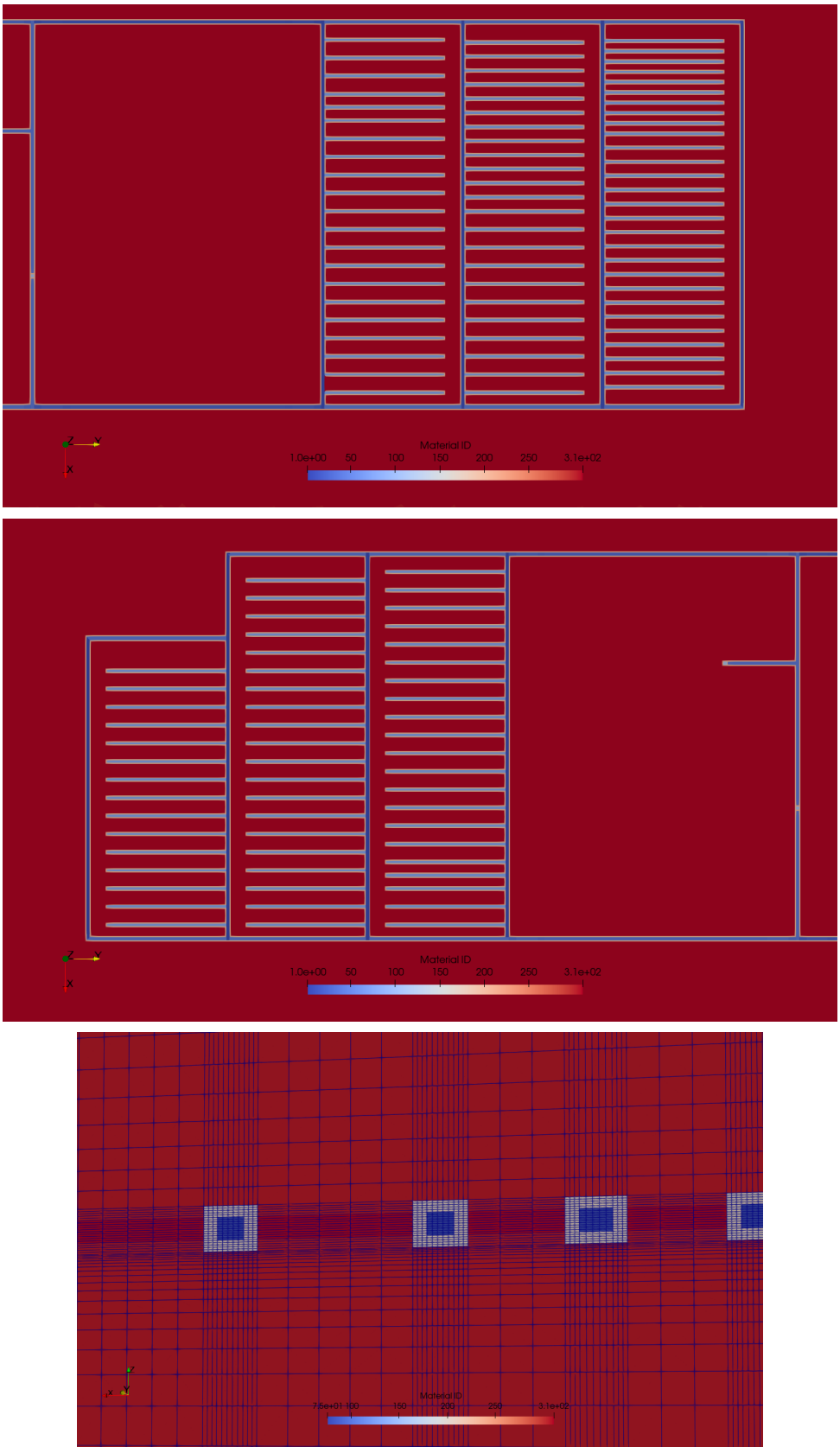

Figure 10.-22: Map view (XY) of material ids associated repository halves (top panels) and vertical cross-section (XZ) of mesh through disposal drift showing surrounding EDZ (bottom).

10.3.3 Initial and boundary conditions

The geologic layers away from the repository were given a fully liquid-saturated initial condition. Drift and shaft materials were assigned an initial liquid saturation of 2%. The EDZ was assigned an initial liquid saturation of 15%.

The liquid pressure and temperature were specified with linearly variable vertical profiles across the domain. The hydrostatic gradient liquid pressure profile had a slope of 10 MPa/km, starting from 0.102 MPa at z = 0, resulting in a liquid pressure of 31.02 MPa at z = −3091 m. The geothermal gradient had a slope of 30 K/km, starting from 9℃ at z = 0, resulting in a temperature of 101.8℃ at z = −3091 m. These were computed externally and specified as gridded datasets in PFLOTRAN.

10.3.4 Energy, solid, and gas sources

The energy sources were converted directly from the input files used in FLAC3D input, and were specified previously (§ 4.). Heat sources were specified by a power level for all the waste packages associated with a drift through time, the timing of when the heat source started, and the physical extent of the source (specified in the region definitions). Not all disposal drifts had heat sources associated with them (e.g., some low-level waste disposal drifts had no heat-generating waste). The heat source magnitude decayed as a sum of several exponentials, which were specified out beyond the end of the simulation (Figure 10.-23).

Solid salt was injected into the crushed salt that filled the heated drifts and drift seals. The rate of injection was computed to reduce the porosity from a high initial value (35%) to a low value (2%) 100 years after emplacement (the beginning of which was staged over 30 years).

Gas sources were injected into unheated disposal drifts at rates proportional to the surface area of the waste and an expected corrosion rate, depending on the type of waste packages emplaced. Assuming a minimum corrosion rate of 4.0×10^{-8} m/yr and a maximum corrosion rate of 1.5×10^{-5} m/yr for waste packages associated with non-zero water content, the hydrogen gas generation rate are given in Table 10.-5 are computed from the following assumed reaction for iron corrosion

$$3Fe_{(s)} + 4H_2O \leftrightarrow \left(Fe_2^{3+}\ Fe^{2+}\right) O_4 + 4H_{2(g)}. \tag{21}$$

If the water used in this chemical reaction was solely in the vapor phase, there would be no change in pressure, since 4 moles of gas would exist on both sides of the equation. Converting liquid H_2O to H_2 gas would result in an increase in pressure associated with the much larger molar volume of hydrogen, compared to liquid water.

Container Type	Surface Area [m^2]	Min Gas Gen. Rate [kg H_2/yr]	Max Gas Gen. Rate [kg H_2/yr]
POLLUX	30.9	4.66×10^{-4}	1.75×10^{-1}
CASTOR	44.0	6.65×10^{-4}	2.49×10^{-1}
MOSAIK	16.0	2.41×10^{-4}	9.06×10^{-2}

Table 10.-5: Per waste package corrosion-related inputs used to compute gas generation rate.

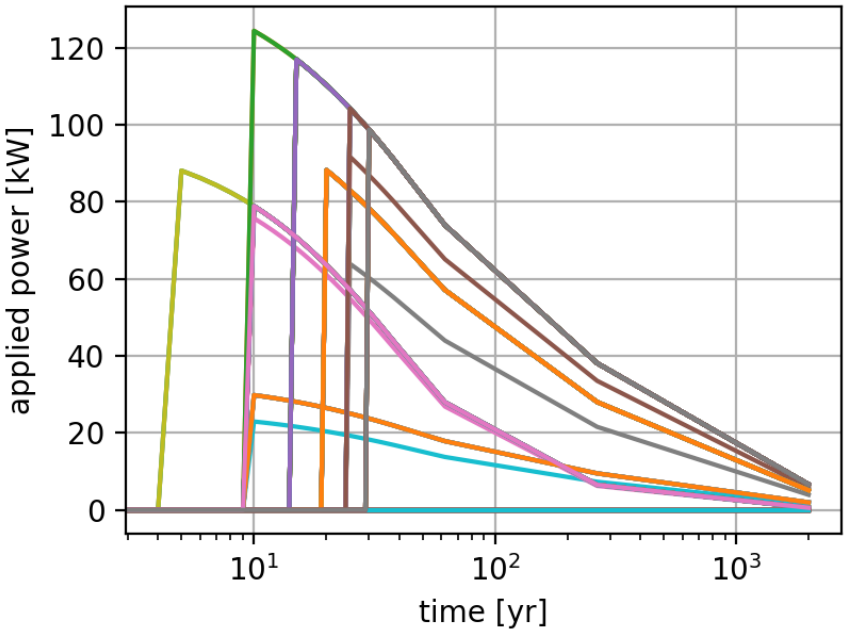

Figure 10.-23: Total power applied to individual waste disposal drifts through time, showing the staggered emplacement of waste at six different times, with several different heat load profiles (including some with no applied power).

A set of several cases were investigated with this large mesh:

1. Base case
2. Darcy flow case
3. Higher-permeability seals case
4. Base case with porosity closure case
5. Base case with porosity closure and gas generation case

10.3.5 Case 1: Base

The base case used the material properties as presented in Tables 10.-3 and 10.-4, with non-Darcy flow (i.e., no flow until a threshold gradient is exceeded). No change in porosity was specified for this base case to represent drift closure, therefore the changes in thermal conductivity were only a function of temperature in the crushed salt, EDZ, and NA2 materials. Absolute permeability did not change, but relative permeability was still a function of phase saturation according to the capillary pressure and relative permeability model of van Genuchten (1980) and Mualem (1976), as extended by Parker et al. (1987) to two-phase.

Figure 10.-24 shows the temperature distribution in the repository at the beginning of each emplacement sequence (every 5 years until all waste is emplaced), and the peak of temperatures in the repository between 100 and 1,000 years. By 2,000 years, the repository has begun to cool down significantly.

Figure 10.-25 shows the evolution of the liquid phase flow velocity with time. These velocities are averaged over the entire rock, and do not represent actual pore velocity, which would require dividing by the porosity. After the initial 5 years of hydrologic initialization ($-5 \leq$ yrt $\leq$ 0), there is a narrow halo of non-zero flux around the repository. This only grows a bit during the heating. By 1,000 years the halo has grown significantly, partially due to the decrease in viscosity of the brine with temperature, which depressurizes a larger portion of the salt formation.

Figure 10.-26 shows the evolution of liquid saturation in the repository. The host rock is saturated or almost saturated, while the drifts remain mostly air-filled. By 1,000 years, the EDZ surrounding the drifts have desaturated, and the portion of the host rock adjacent to the EDZ (especially between heated drifts) has reduced from full saturation, but only by a small amount.

Figure 10.-28 illustrates that the biggest change in saturation is at late time, when there is a continuous gas phase through much of the disposal area, including the pillars between rooms (this area has a connected gas phase, but is still mostly brine saturated). The dark blue areas (p_{gas} = 0) in these plots are areas where there is only single-phase liquid (i.e., there is no defined gas pressure). PFLOTRAN general mode includes three different states:

1. Single-phase gas (no liquid water, only humidity in air);
2. Single-phase liquid (no air, only dissolved gas in liquid water); and
3. Two-phase flow (air with humidity and dissolved gas in liquid water).

The far-field begins in single-phase liquid state, and only once gas infiltrates these elements do they become two-phase flow elements. The drifts and EDZ begin in two-phase flow mode. The hotter drifts become single-phase gas once the liquid water boils off (Figure 10.-27).

The gas pressure in the drifts is hightest in the hottest disposal drifts, and experiences a maximum of 3.1 bar. This gas pressure is only due to the heating and expanding of the trapped gas in the repository, along with some minor increases of gas pressure due to the flow of the water phase towards the drifts, as there is no closure or gas generation to increase gas pressure.

Figure 10.-29 summarizes the evolution of gas pressure across the 6 disposal fields through time. The line is the average, while the shaded region illustrates the range of pressure observed. The maximum gas pressure is observed just before 200 years in Field 2, while the lowest gas pressure is observed in Field 6 (the first one to be emplaced). A sharp rise in gas pressure is experienced right at emplacement (except in Field 6), and by 1000 years, all the gas pressures are decreasing.

As an indicative proxy for solute transport at early time, the diffusion of dissolved gas in the brine-saturated salt is shown in Figure 10.-30. Gas dissolves into the liquid phase at EDZ and drift–starting even before waste emplacement–and diffuses into the single-phase liquid region under a dissolved gas concentration gradient. Roughly a distance of two drift diameters into the intact salt is still at the initial condition for dissolved gas after 2,000 years. A tortuosity of 1.0 is used in geologic materials, so this represents an upper-bound conservative estimate of diffusive transport of an ideal tracer.

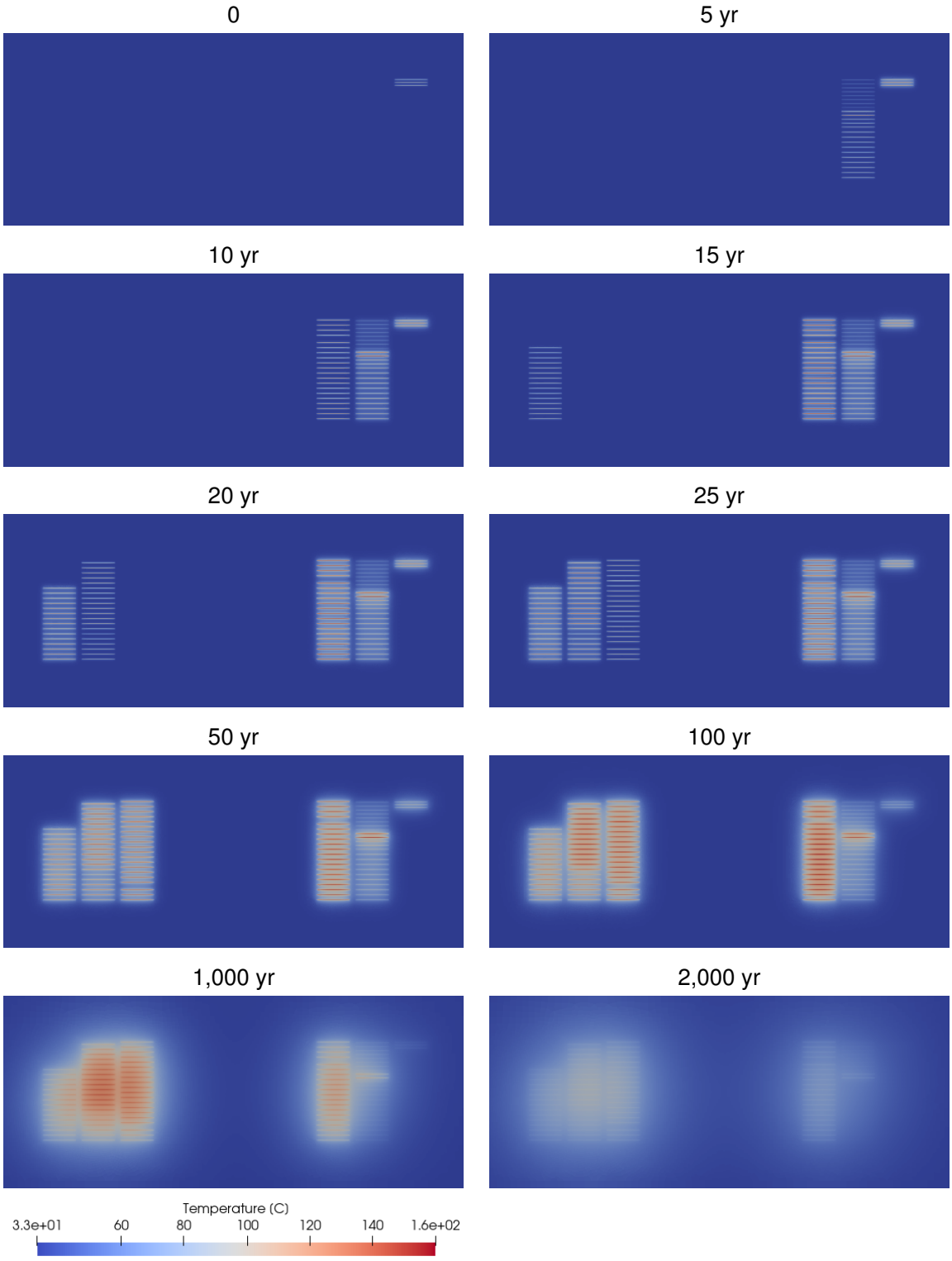

Figure 10.-24: Temperature response in and around repository (horizontal XY slice through repository at z = −817 m), showing staged emplacement of waste.

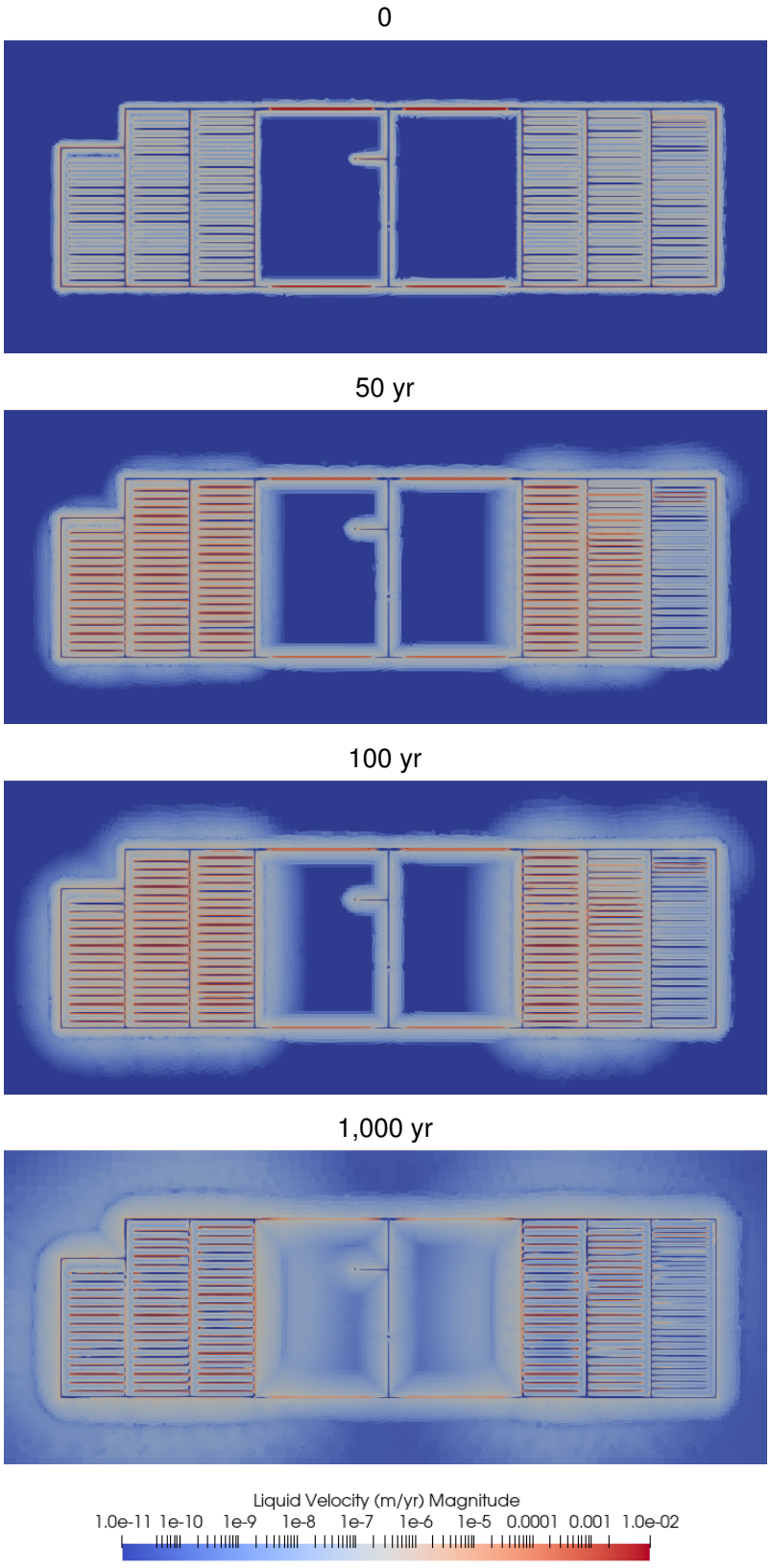

Figure 10.-25: Liquid velocity in and around repository (horizontal XY slice through repository at z = −817 m).

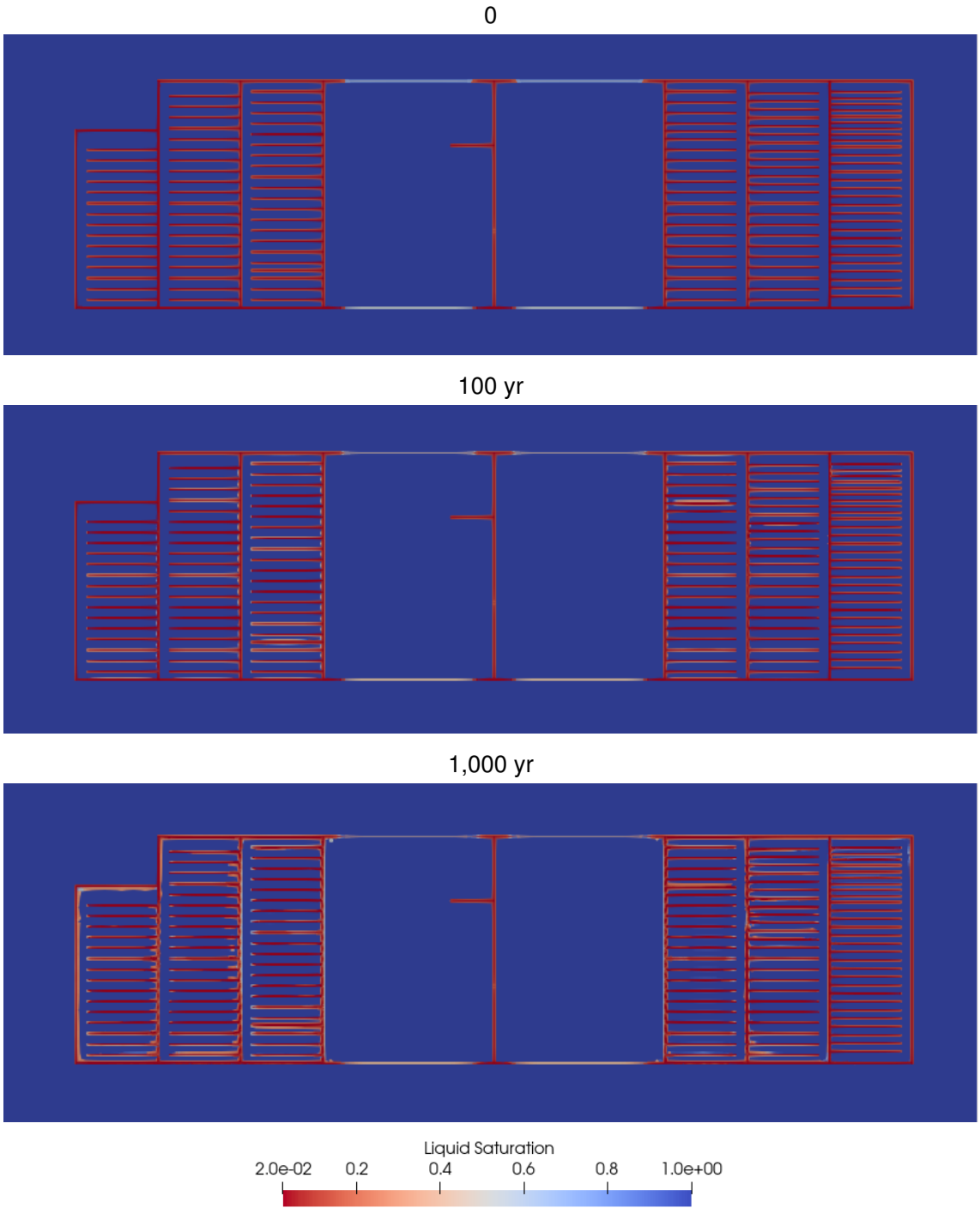

Figure 10.-26: Liquid saturation in and around repository (horizontal XY slice through repository at z = −817 m).

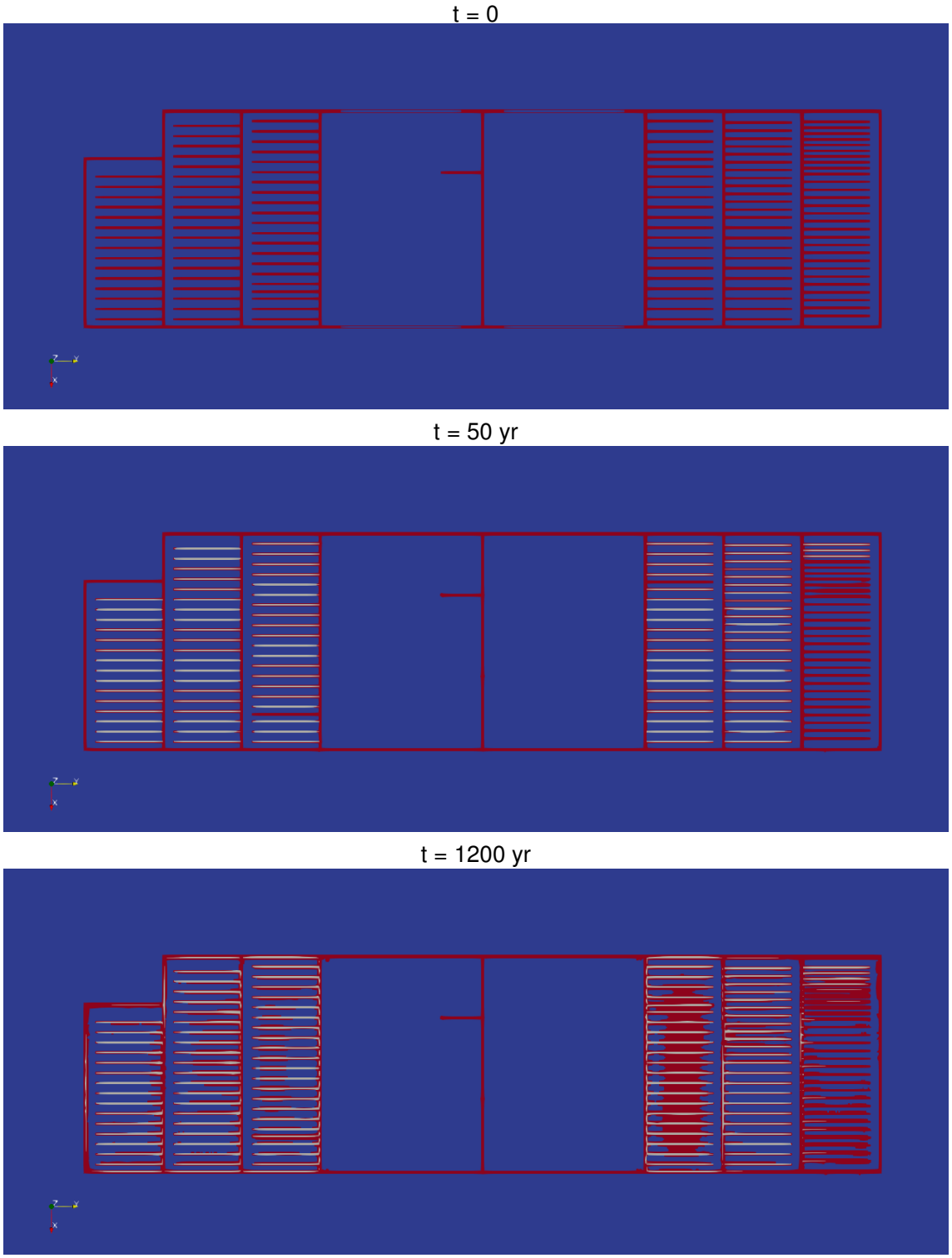

Figure 10.-27: Flow state in and around repository (horizontal XY slice through repository at z = −817 m) at three times t = $\{0, 50, 1200\}$ years; blue is single-phase liquid, white is single-phase gas, and red is two-phase.

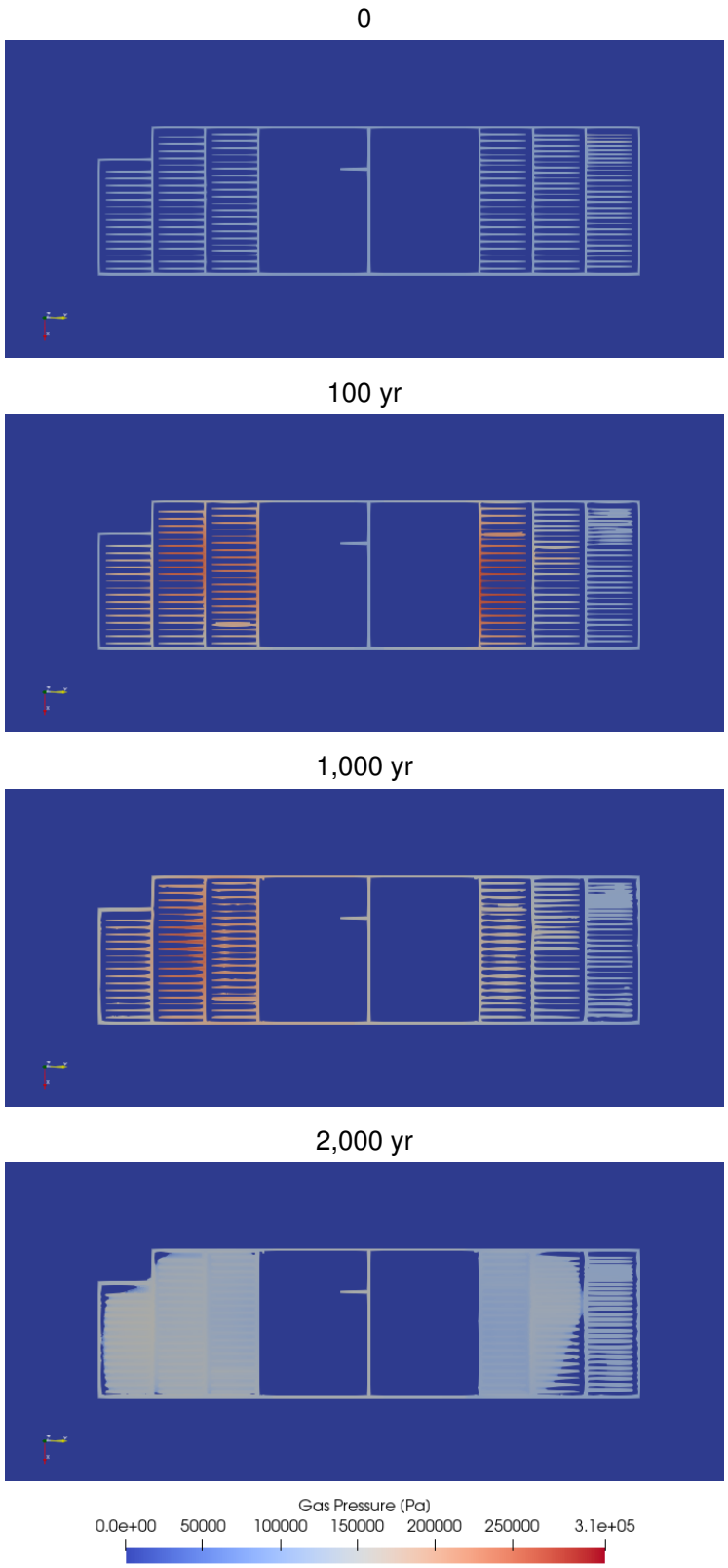

Figure 10.-28: Gas pressure in and around repository (horizontal XY slice through repository at z = −817 m).

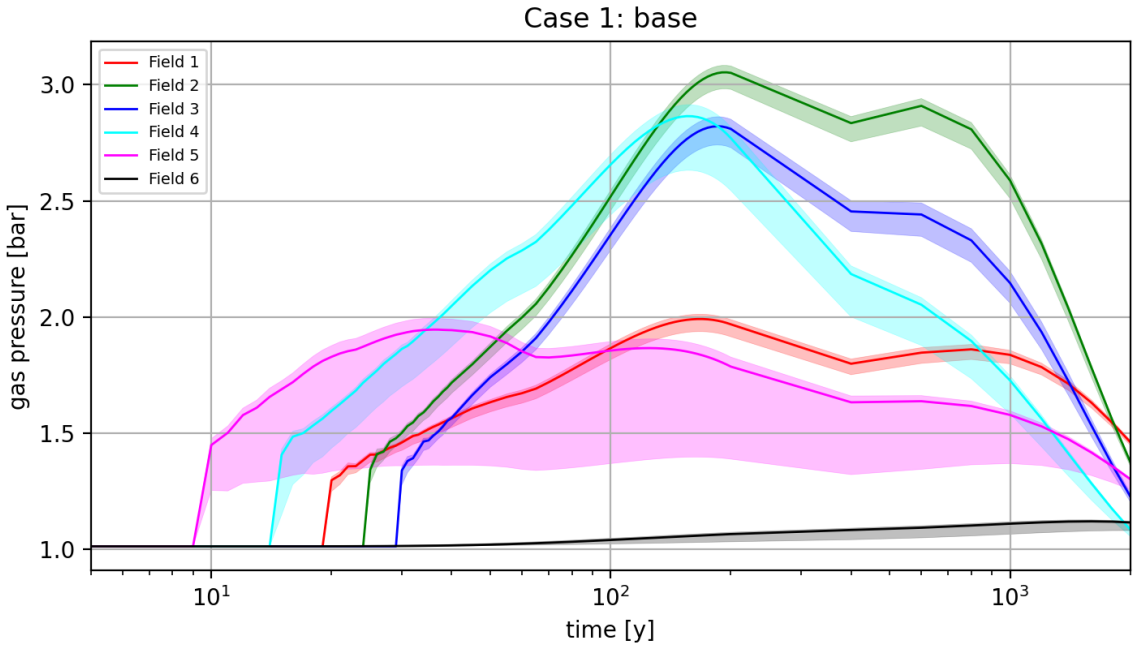

Figure 10.-29: Gas pressure in disposal drifts through time. Lines are mean gas pressure, while shaded regions denote the range observed.

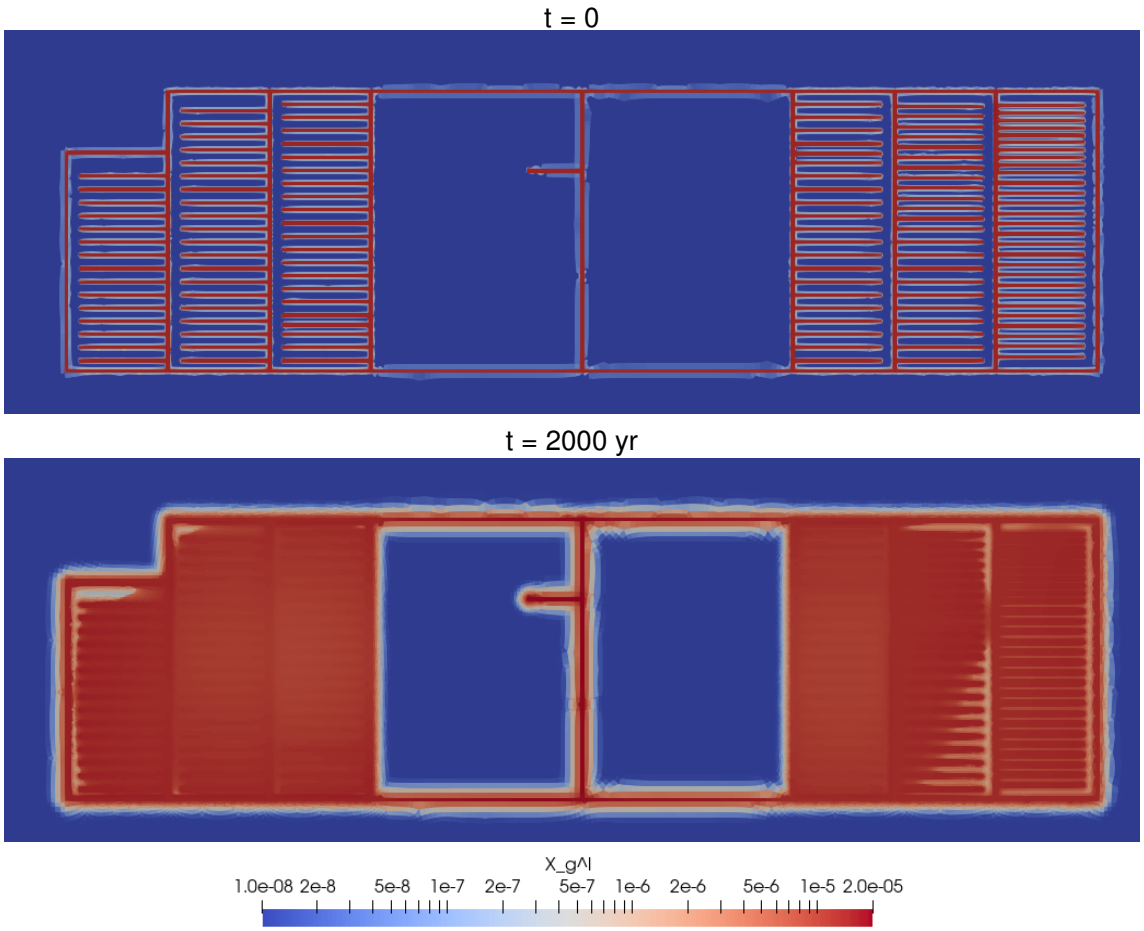

Figure 10.-30: Migration of dissolved gas away from the excavations during the extent of the simulations, showing extent of gas initially (10^{-8} is the initial condition) and after 2,000 years of diffusion (logarithmic concentration scale).

10.3.6 Case 2: Darcy flow

In this case, non-Darcy (i.e., threshold gradient – § 3.1.4) flow was disabled. The predictions in this case are what is considered “default” behavior.

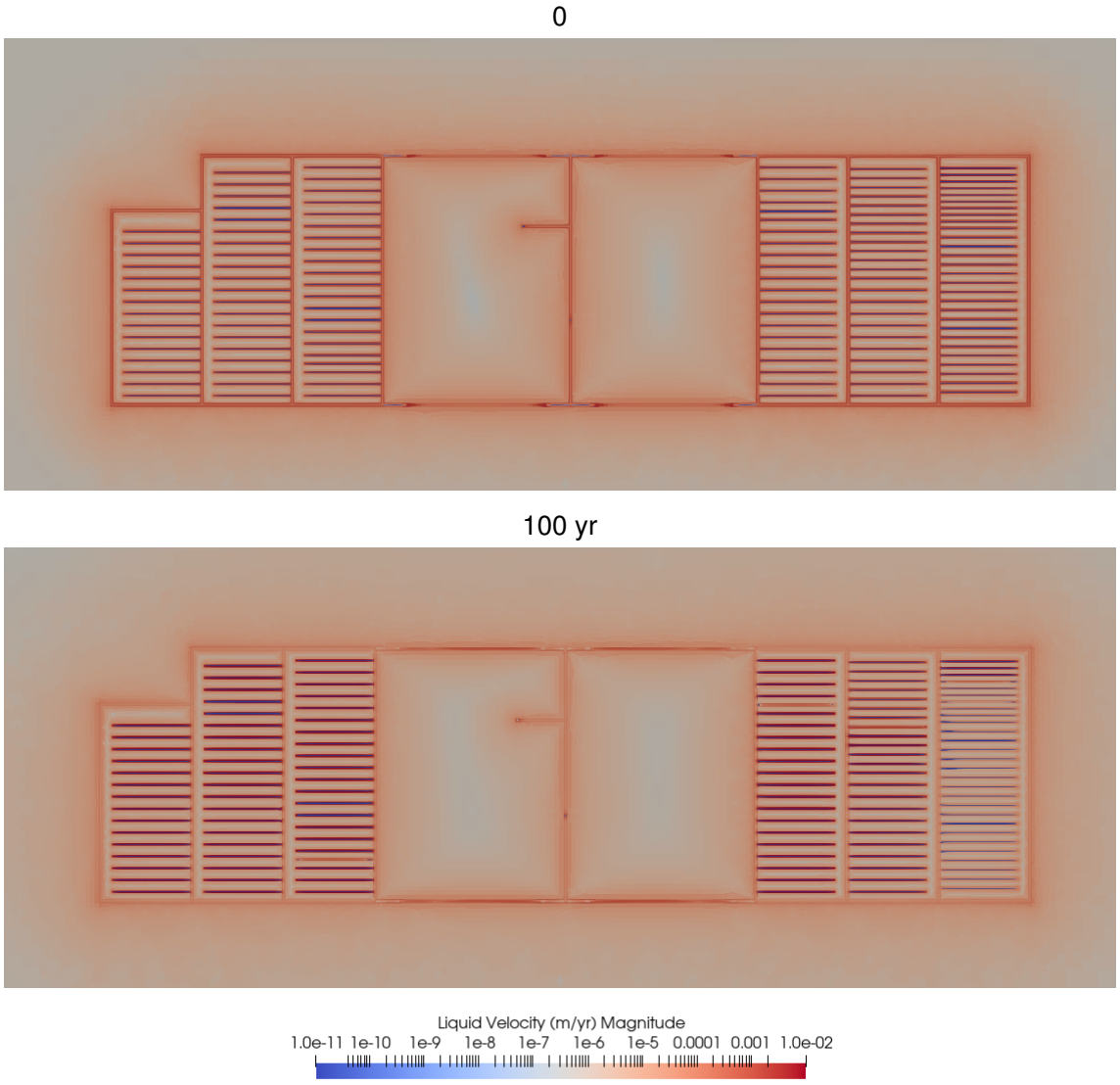

Figure 10.-31: Liquid velocity around repository (horizontal XY slice through repository at z = -817 m) for Darcy flow case.

Even at the end of the initialization period (-5 yr $\leq$ t $\leq$ 0), the flow velocity is non-zero throughout the entire domain. The permeability is very low in the formation, but the pressure gradient is also very high, so the flow is small, but non-zero. At the edge of the domain, the flux is $\approx$ 1 μm/yr for the case with Darcy flow (Figure 10.-31), while when non-Darcy flow is activated (Figure 10.-25), the flow velocity is close to zero ($< 10^{-11}$ m/yr) tens of meters outside the domain soon after excavation, and only at much later time does the increased temperature lead to higher flow velocities associated with surpassing the threshold gradient.

Through a regression Liu et al. (2012) found the threshold gradient could be expressed in terms of the intrinsic permeability, given in Eqn 18, that results in a threshold gradient of

1.6×10^4 (m head)/(m distance).

The non-Darcy flow behavior is well-documented for low-permeability rocks (Liu, 2014), where it is supported by the observation that the effect of the repository should not propagate several km through impermeable rock over short time periods. This implementation of the non-Darcy conceptual model brings together the US approach of modeling all the geologic barrier with a hydrologic model with the German approach, where flow is not calculated in the salt, because it is known to be impermeable to flow.

10.3.7 Case 3: Higher-permeability seals

This case is the base case (i.e., non-Darcy flow), but the MgO seals on the ends of the crushed salt drift seals are 100$\times$ more permeable.

The difference in gas pressure between the two scenarios is small (only visible at late time). This may be due to two factors: 1) the permeability of the EDZ surrounding the seals remained its base case value, and 2) the gas pressures were not high, so the excess gas pressure from heating was able to bleed off easily.

10.3.8 Case 4: Base case with porosity closure

This case is the base case (i.e., non-Darcy flow), with the injection of solid phase to reduce the permeability of the heated emplacement drifts and the drift seals over 100 years. Porosity is specified to change linearly from the initial value (35%) at emplacement to a low value (2%) after 100 years.

As in the simpler meshes (§ 10.2), there is a period at the beginning of heating where the water is driven off from the crushed salt. This water moves away from the heat source as vapor and condenses once the temperature drops below the boiling point, leading to local dissolution. Figure 10.-35 shows how the decrease in porosity associated with the disposal drifts is surrounded above and below by increases in porosity in the EDZ (up to 11% porosity increase). The unheated crushed salt drift seals (seen in the rear of the image) do not have this rind of increased porosity, because they are not heated and do not drive off the initial moisture in the crushed salt.

Changes in porosity and temperature drive the thermal conductivity to change (Figure 10.-36). The intact salt uses the “linear resistivity” model, that is only a function of temperature (hot salt has lower resistivity than cold salt – Figure 10.-2). The crushed salt has a more complex behavior (Figure 10.-3); decreasing porosity has the largest impact on the thermal conductivity, while increased temperature reduces the thermal conductivity at low porosity (near intact), and increased temperature increases the thermal conductivity at high porosity (near starting). The behavior at high porosity accounts for some convection and even radiation that may effectively increase the thermal conductivity, due to the large amount of air-filled space.

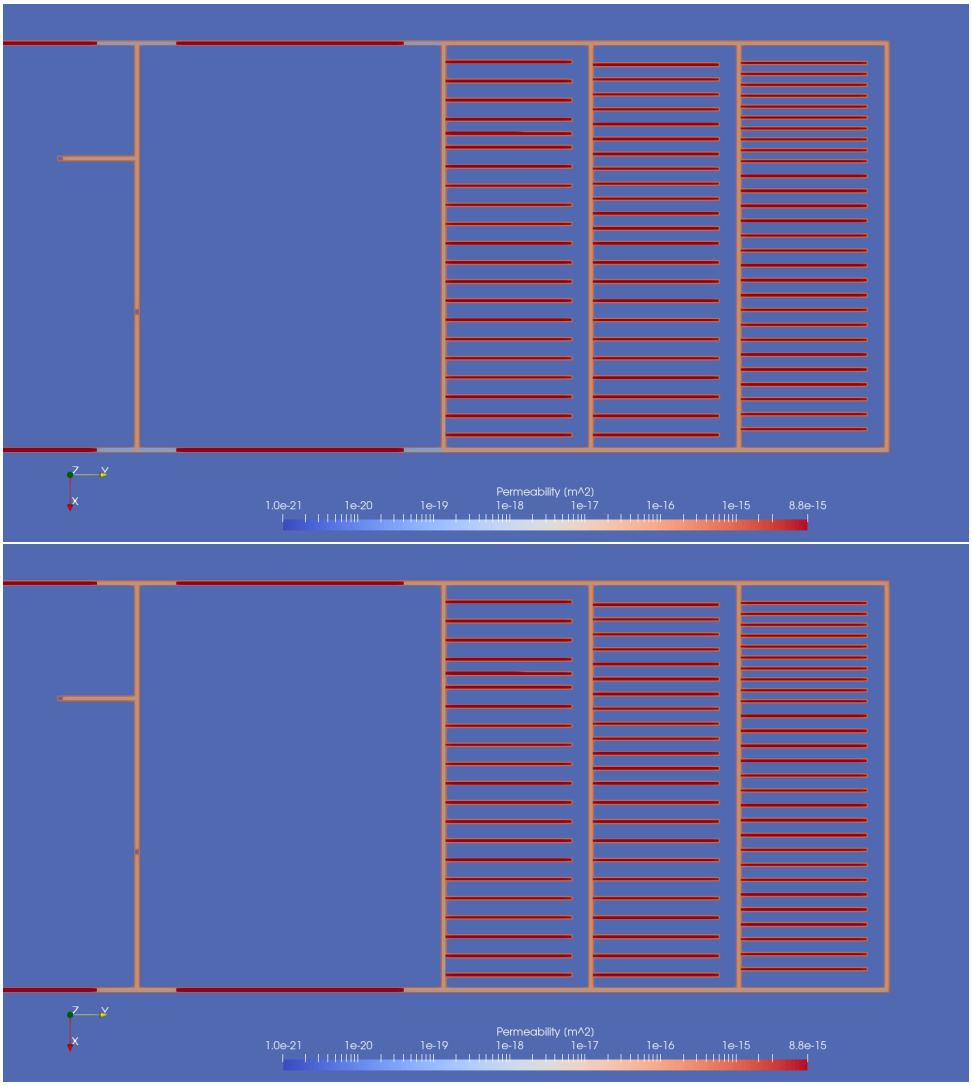

Figure 10.-32: Intrinsic permeability at repository elevation (XY plot at z = −817 m) in case 1 (top) and case 3 (bottom). Note lower permeability for MgO seals at the ends of the crushed salt seals in base case (top).

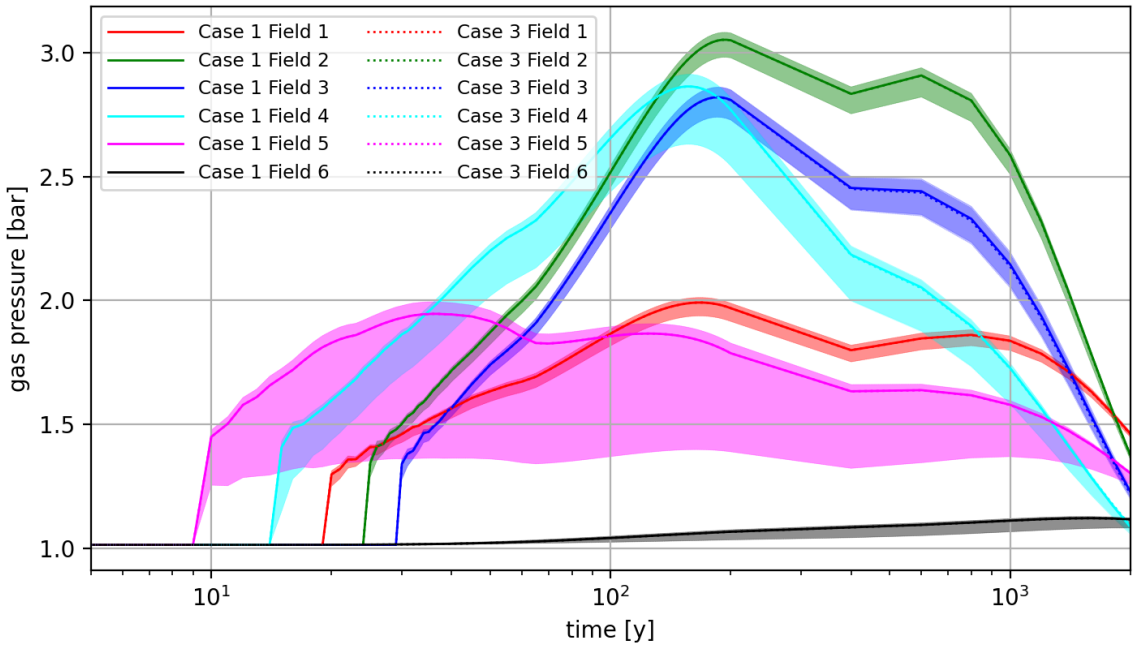

Figure 10.-33: Gas pressure in disposal drifts through time. Lines are mean gas pressure, while shaded regions denote the range observed.

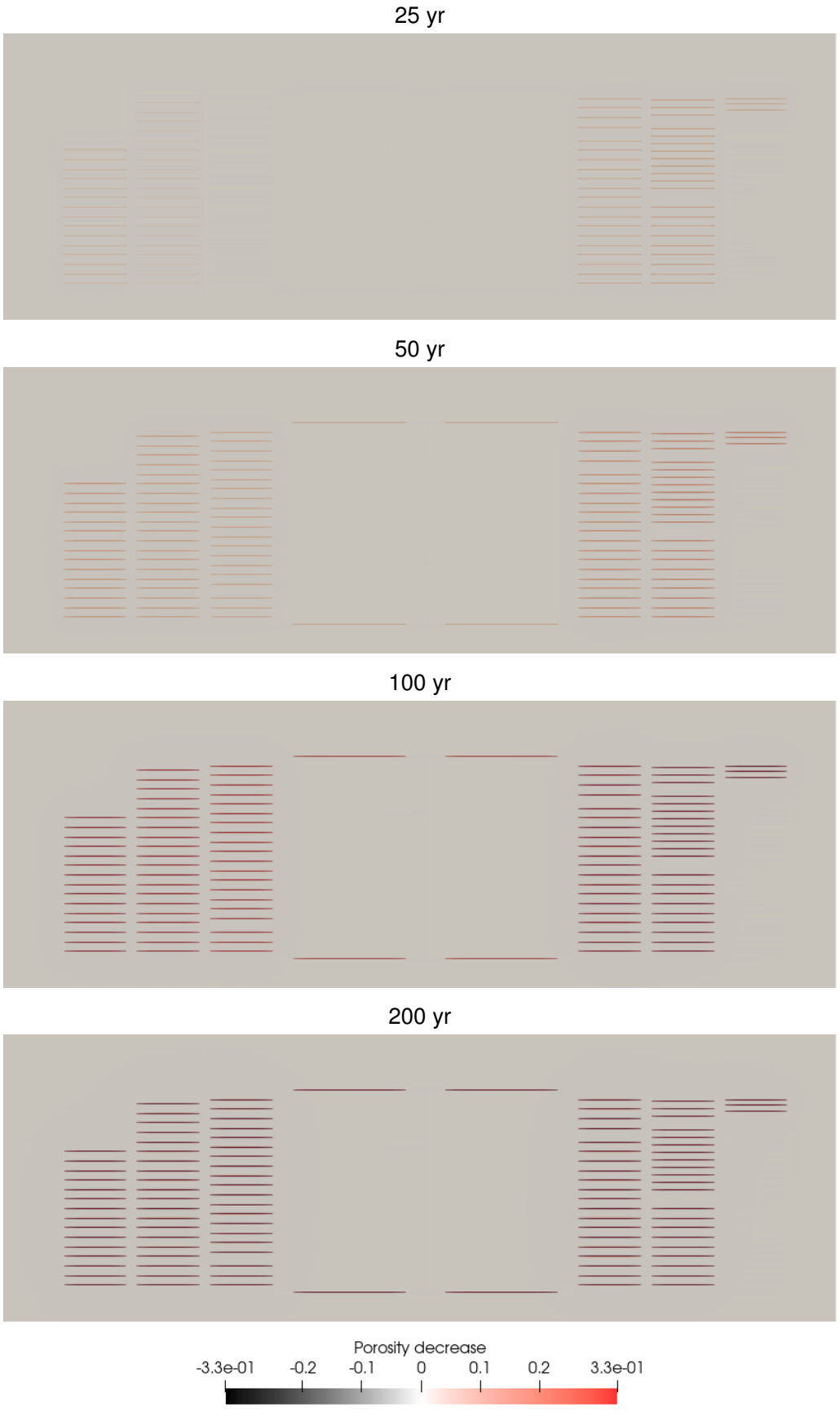

Figure 10.-34: Change in porosity (from initial value) in and around repository (horizontal XY slice through repository at z = −817 m).

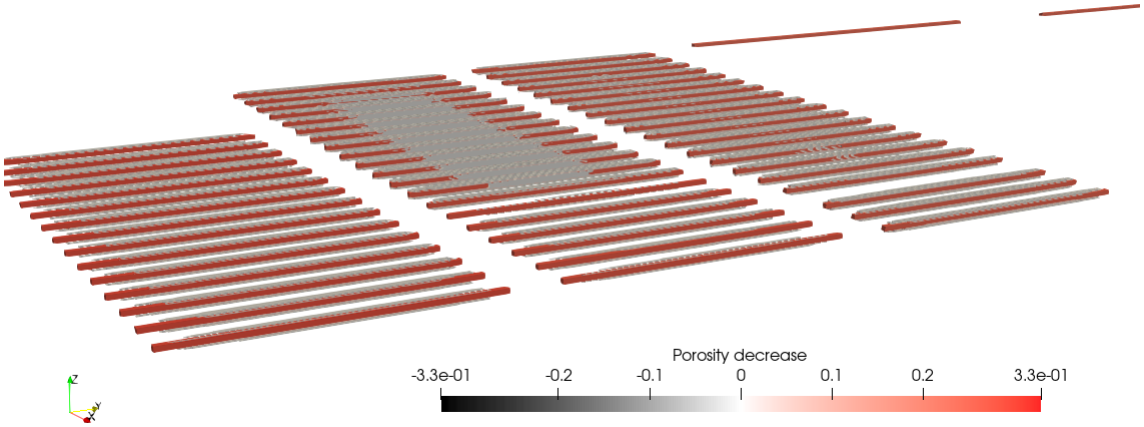

Figure 10.-35: Change in porosity from initial value shown in oblique view near disposal drifts (crushed salt seals seen in background) at 100 years. Small changes ($-0.02 \leq \delta \leq +0.02$) are set to transparent.

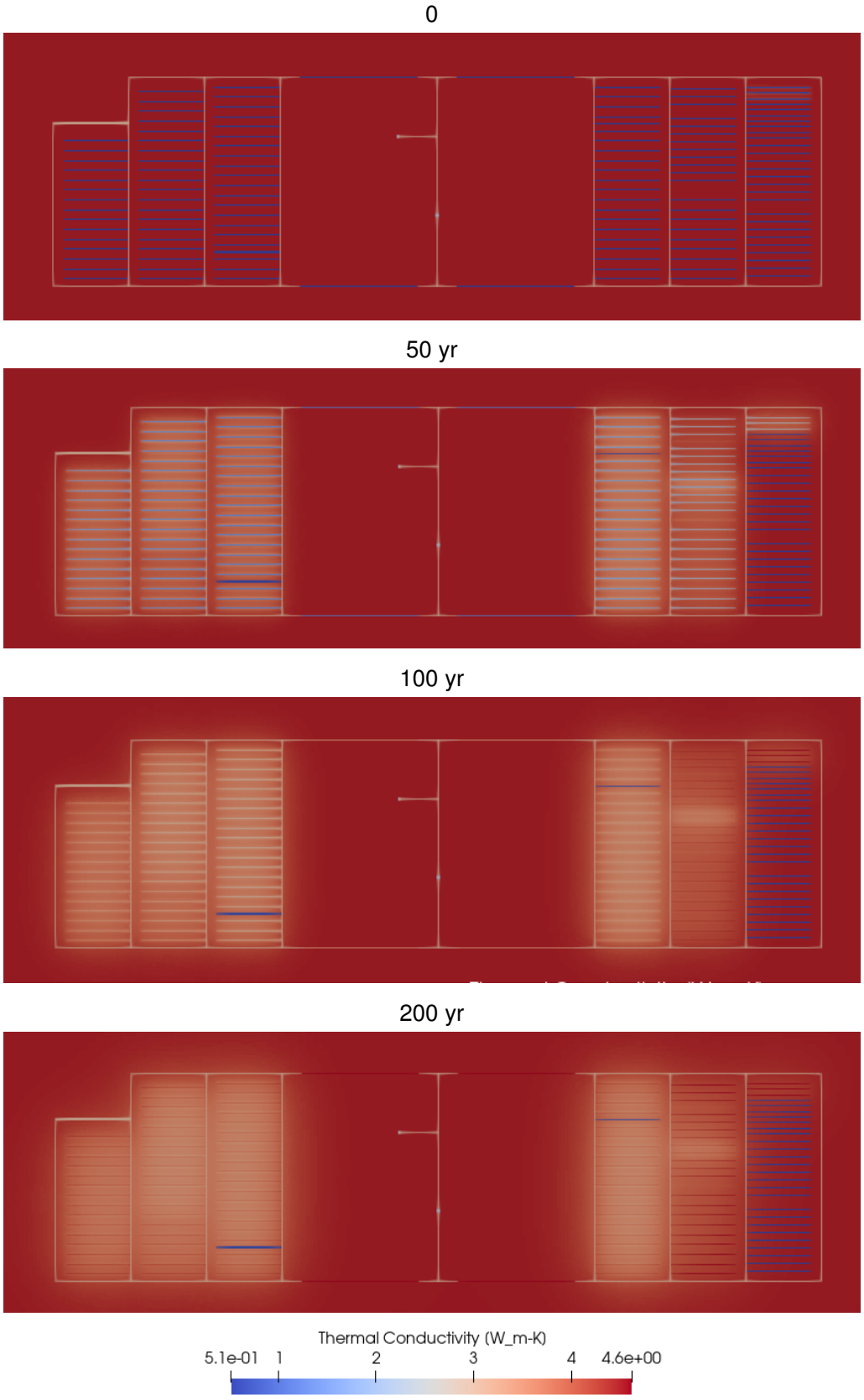

Figure 10.-36: Thermal conductivity in and around repository (horizontal XY slice through repository at z = −817 m) at several times (t = {0, 50, 100, 200} yr).

Figure 10.-38 shows the sharp increase in gas pressure associated with the final part of porosity closure (i.e., when porosity is near its minimum), but gas pressure decays quickly after that, and then decays more after 1,000 years. The uncoupled closure of porosity, without consideration of gas pressure is not realistic – porosity closure should slow down as the gas pressure increases, pushing back somewhat on the lithostatic pressure that is driving closure.

Figure 10.-37 shows the distribution of single-phase gas, single-phase liquid, and two-phase states in the model domain is quite similar between the case with closing porosity and the base case (Figure 10.-27). One notable difference is the presence of more two-phase (red) cells near the MgO abutments at the disposal ends of the drift seals. This indicates relatively gas was flowing around the MgO abutments in response to the increase in pressure at the end of compaction, and this switched the intact salt from single-phase liquid (blue) to two-phase (red).

In this simulation, only the heated drifts and the crushed salt seals were closed by injecting solid mass of halite into the pores at the same rate. In reality, the access drifts and the EDZ should close too (albeit at a slower rate than the heated drifts). The definition of the regions (all EDZ elements were a single zone) and the current implementation in PFLOTRAN made it difficult to close the porosity of the EDZ in a physically realistic manner. The current porosity closure mechanism is specified in the input file (i.e., before the simulation begins). In future efforts, the injection of solid mass would incorporate feedback from the simulation. Closure could be a function of the temperature (faster closure under hotter conditions) and liquid pressure (high back pressure of gas or brine would reduce the closure rate). Both of these approaches would be more physically realistic and should improve some of the model convergence issues that happened during some porosity closure simulations (the model would resort to very small time steps when pressures would increase rapidly).

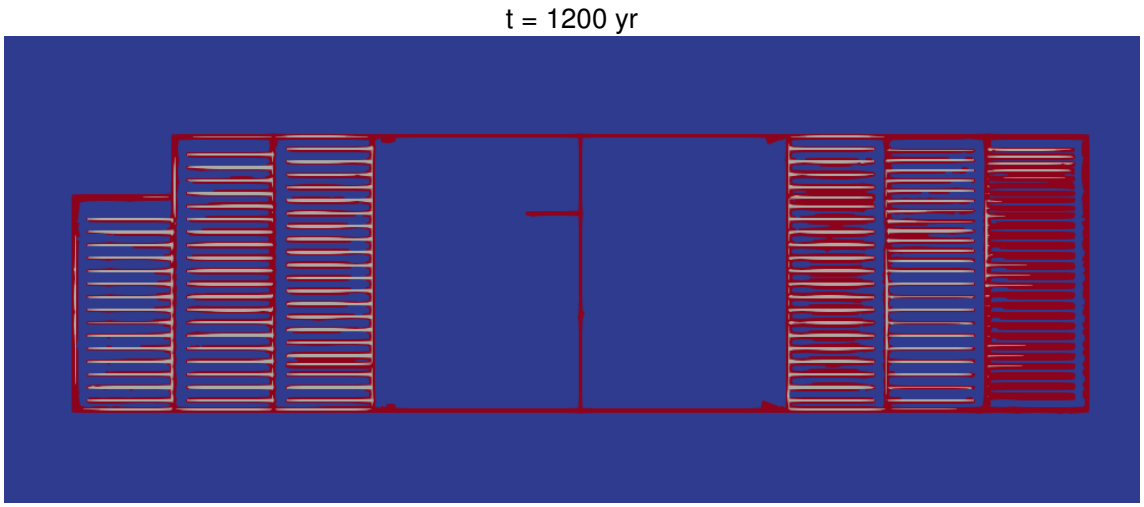

Figure 10.-37: Flow state in and around repository (horizontal XY slice through repository at z = −817 m) at t = 1200 years for porosity change case; blue is single-phase liquid, white is single-phase gas, and red is two-phase.

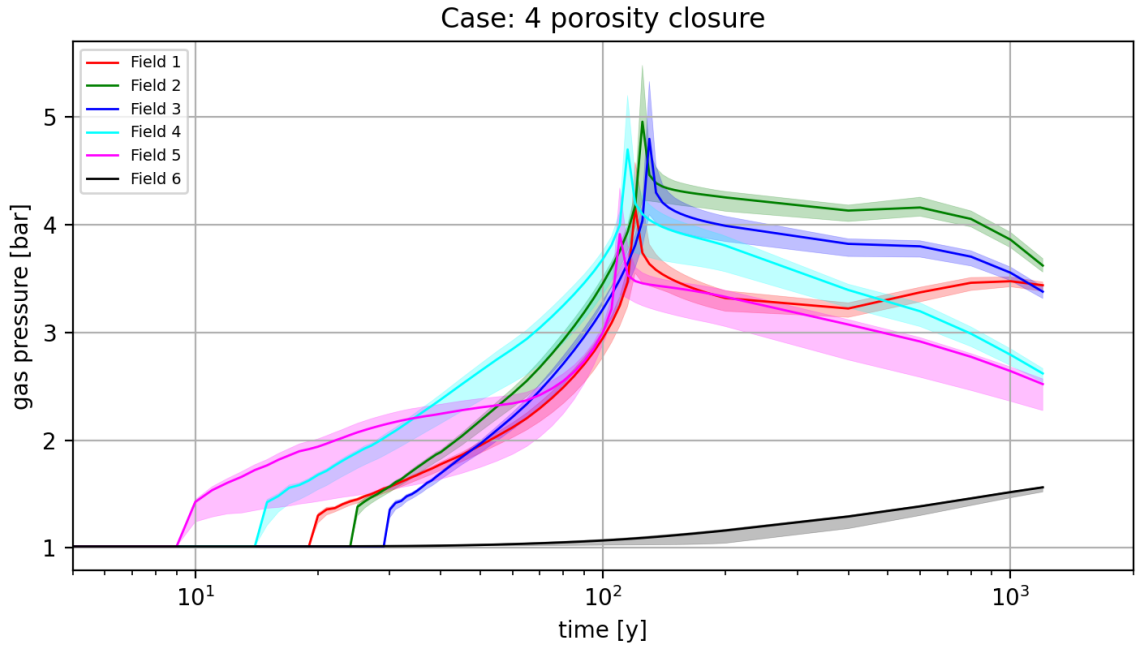

Figure 10.-38: Gas pressure in disposal drifts through time for closing porosity case. Lines are mean gas pressure, while shaded regions denote the range observed.

10.3.9 Case 5: Porosity closure case with gas generation

Gas generation is added to the unheated disposal drifts because the heated drifts are essentially dry and would not produce significant gas generation (which requires free liquid water). The effects of gas generation are minimal (the lines in Figure 10.-39 are indistinguishable), since the gas generation is assigned to single drifts in Fields 3 and 4, and most of Field 6 (clearly visible as blue in thermal conductivity plots in Figure 10.-36).

It is clear that the effects of gas generation, as specified, were insignificant compared to the effects of drift closure, which agrees with intuition. More extreme gas generation rates can be tested in future simulations, or the effects of the EDZ could be reduced, to decrease the redistribution of gas during the simulations.

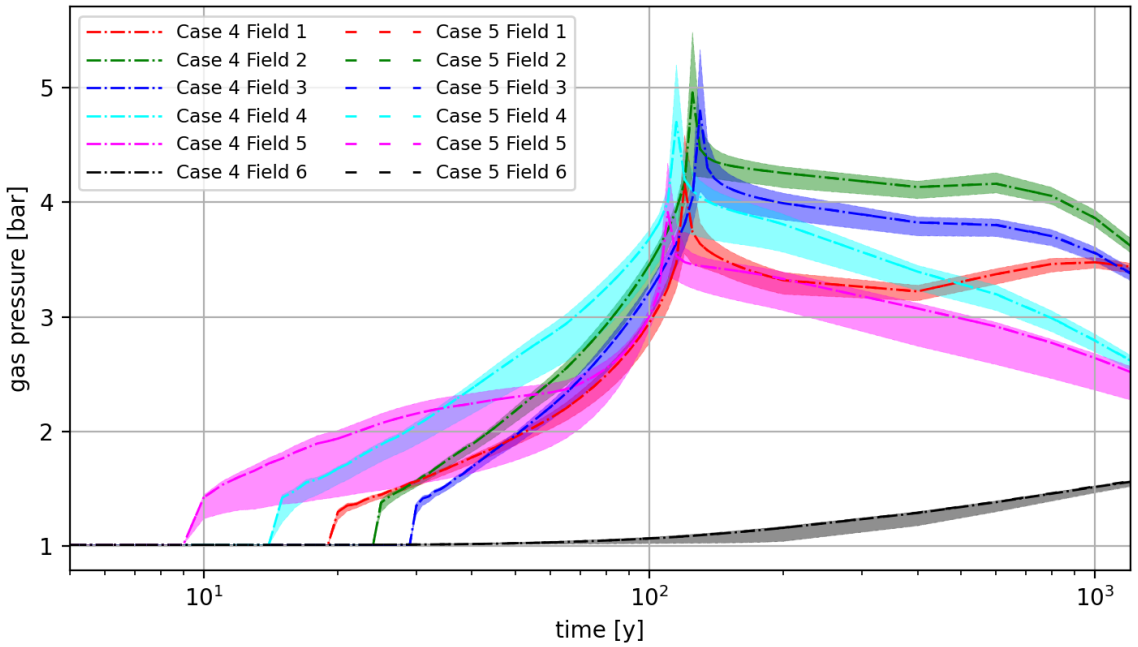

Figure 10.-39: Gas pressure in disposal drifts through time for closing porosity case and gas generation in unheated drifts. Lines are mean gas pressure, while shaded regions denote the range observed.

11. Effect of gas pressure build up on the EBS performance

The compaction of crushed salt used as backfill and long term seal in salt repositories depends primarily on the creep behavior of the salt host rock and the heat input in the repository. Due to heat, the creep behavior of the rock is accelerated as well as the compaction behaviour. However, the hydrologic and geochemical processes taking in place in the repository may affect the repository closure and thus the compaction of crushed salt. This is because the equilibrium state is a result of the concurrent processes of salt creep and fluid flow and the interaction between then (Quelle INTERA, 1996).

First analysis regarding the effect of fluid pressure in a salt repository was carried out in the scope of the WIPP Performance Assessment for disposal room closure, they were not backfilled with crushed salt (Quelle: 1 & 2). Due to the complexity of coupling the mechanical creep process of salt and its interaction with multiphase fluid flow, an approximate approach was followed. This approach consists of repository porosity functions that were computed in room closure simulations as function of gas generation. In these FE-simulations, the resistance to closure was provided by pressure produced by waste generated gas computed from the ideal gas law. The repository closure was driven by salt creep and waste and backfilled consolidation taken into account through different constitutive models. Stone (1995) used this approach to analyze the closure of a single perfectly sealed disposal room filled with waste and backfill under five different gas-generation rate histories. The five rate histories were generated by multiplying a defined gas generation curve by a factor f ranged from 0.0 to 1.0. At f = 0.0 no gas is generated. At f = 1.0 a total of 1600 moles per drum are generated over 2,000 years. The results of this analysis by Stone (1995) are presented in Figure . These results suggest factors such as room porosity and gas pressure play a significant role. The simulations show that with a higher rate of gas generation (f $\geq$ 0.4), pressurization of the room occurs rapidly, yet the impact on the room's closure is modest due to the minimal compression of waste, as most of the resistance is attributed to the gas pressure itself. In situations where gas pressure is high, the room may even expand, increasing the void volume and moderating room pressurization. Conversely, when the gas generation rate is lower (f $\geq$ 0.2), there is a more substantial closure of the room and more pronounced compression of waste. In scenarios without gas generation (f = 0.0), the room stabilizes at a porosity of 0.22 after two millennia of closure. The porosity remained high due to the presence of the waste in the disposal room.

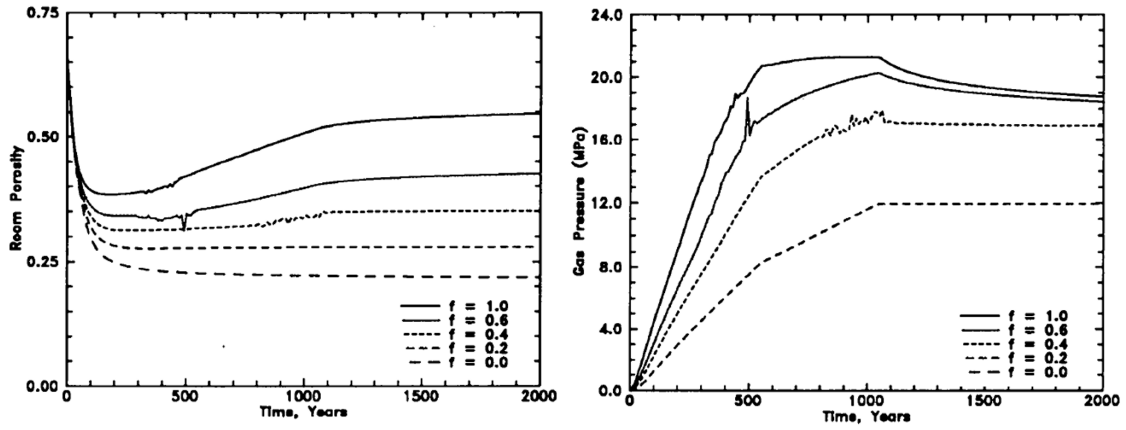

(a) Room Porosity

(b) Room Pressure

Figure 11.-1: Simulation results for the closure of a perfectly sealed disposal room under five gas-generation rate histories, differentiated by a rate multiplier f (after Stone, 1995).

The porosity-time-pressure functions were eventually included in PA calculations. Simulation results with TOUGH2 using this approach have shown the validity of this approach as long as the room pressurization in the PA simulation was similar to the obtained pressurization from mechanical analyses. It was noted that even if there is a notable deviation in the pressurization history, the approximation remains reasonable as long as the pressures in the repository are sufficiently low to prevent any substantial room expansion.

In the scope of RANGERS, the effect of gas was in the considered repository system was analyzed similarly in a simplified manner. Although different assumptions have to be made to take into account the specificity of the German repository concept underlying the repository system and the scarcity of data regarding the gas production of POLLUX casks. In difference to the study by Stone (1998), no compaction can occur in the cask so that only the compaction of crushed salt is of interest and the porosity can decrease to zero. in the absence of gas generation curve, the compaction of the crushed salt was analyzed for fixed gas pressure in the drift. The main focus of this analysis was to estimate how much the gas can affect the closure of disposal drifts backfilled with crushed salt.

The model used for this analysis is similar to the one already described in section 6.1 to analyze the compaction behavior in a single drift located in the middle of a emplacement field where the thermal output is maximum. This model consist of a single drift embedded in the geological model in which a POLLUX cask is disposed and the drift is backfilled with crushed salt. The cask in the model comprises two components: an outer casing for shielding against radioactive radiation and a container basket holding the high-level radioactive wastes, acting as a heat source in the model. The numerical model takes account the thermal superposition and the resulting temperature increases coming from the neighboring drifts by considering thermal symmetry boundary conditions as a quarter model of a cask embedded in a partial model of the rock formation, allowing the simulation of a large disposal field. In this model, the distance from the drift axis to the model boundary in the transverse direction of the drift equals half the drift distance, and the distance from the cask's end face to the model boundary in the drift direction equals half the cask distance. In this model, we assume a different cask spacing of 20 m as the one optimized in the design of the repository (3 m). This helps us to better estimate the compaction of part of the drift that are fully backfilled with crushed salt next to drift

section where the cask is disposed. The model is depicted if Figure 11.-2. The computations was carried out thermal-mechanically with FLAC3D in the version 7 (Itasca Consulting Group, Inc., 2021). All material parameters and models used in this study can be found in Chapter 8.

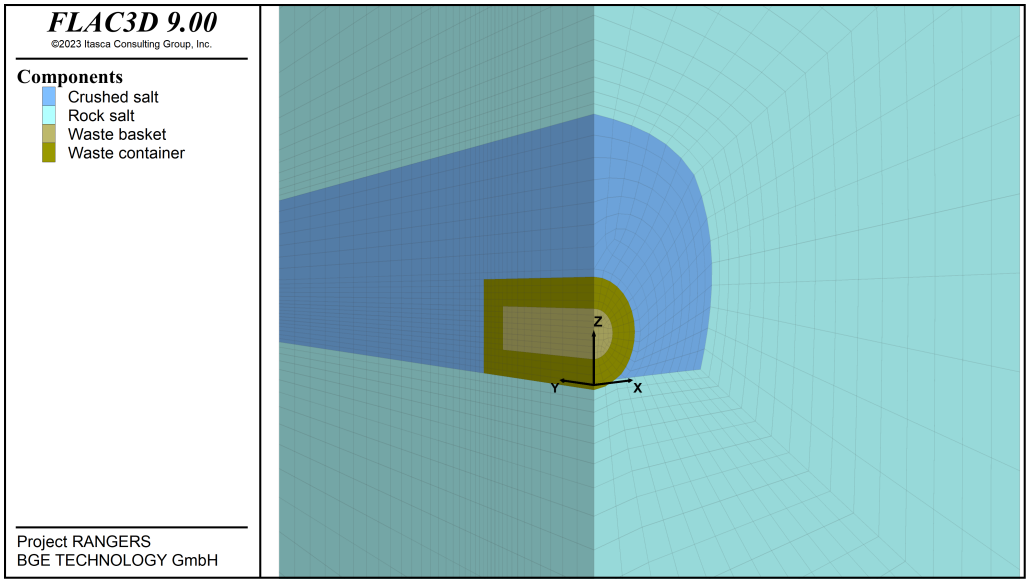

Figure 11.-2: Numerical model for the investigation the effect of gas on crushed salt compaction.

As previously noted, this study does not account for gas generation per se. Instead, it incorporates the impact of gas generation by initializing a corresponding gas pressure within the disposal drift. This approach facilitates an investigation into the compaction behavior under varying constant gas pressures, thereby enhancing our understanding of compaction dynamics across both low and high gas pressure conditions.

Initially, we juxtapose the outcomes of the thermal-hydrological-mechanical (THM) simulation, which assumes an absence of gas pressure, with those of the thermal-mechanical (TM) simulation as delineated in chapter 8. The benchmark results, as depicted in Table 11.-1, focus on a key mechanical variable: displacement. Specifically, the table illustrates the displacement magnitude distribution, calculated as the square root of the sum of the squares of the displacement components, observed at a decade post disposal and backfill operations.

A comparative analysis reveals a near-identical match between the results from both simulation types, which aligns with expectations. Such a correlation serves to affirm the accuracy of the THM simulation, lending credibility to the simulation results and methodologies employed.

Table 11.-1: Comparison of compaction analysis with THM and TM numerical framework of FLAC3D.

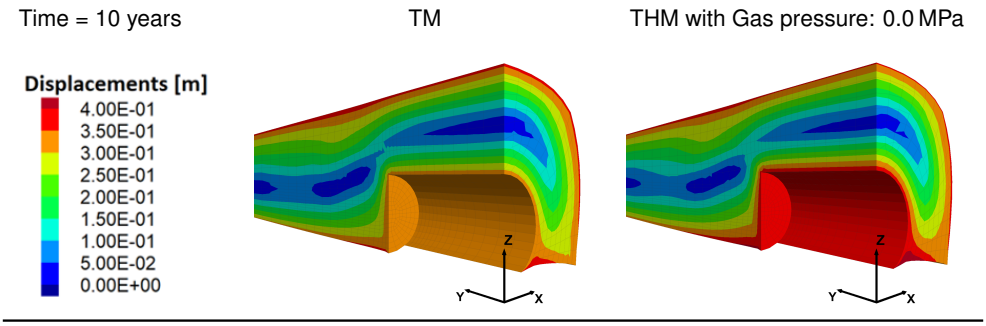

In order to analyze the compaction behaviour at low gas pressure regime, three simulations with fixed gas pressure of 0.25 MPa, 0.5 MPa and 1 MPa were performed. The results of this simulation are reported in Table 11.-2. The table showcases the porosity distribution at different times (1 year, 5 years, 10 years, 30 years, and 40 years) and at varying low gas pressures (0.25 MPa, 0.5 MPa, and 1 MPa) and illustrates how porosity and compaction evolve over time under the influence of different levels of gas pressure. As time progresses from 1 year to 40 years, the porosity in the disposal drift decreases, indicative of increasing compaction of the crushed salt backfill. Here the effect of gas pressure is clearly noticeable as higher gas pressure hinders the compaction process in this simulated environment. Nevertheless, the effect of gas pressure remains limited. By the 40-year mark, the material under all three gas pressure conditions is fully compacted and by a time of 30 years, the difference in the porosity distribution becomes negligible.

Table 11.-3 shows the analogous investigation at high gas pressure regime. In this case, three simulations were carried under gas pressure of 5 MPa, 10 MPa, and 20 MPa. The porosity distribution at different times (1 year, 20 years, 40 years, 70 years, and 100 years) for the three gas pressures is shown in the table. Here, the previous observation from the simulation at low gas pressure conditions remains true with the difference that at high pressure, the compaction is this time severely hindered. For example, the porosity distribution under 5 MPa of gas pressure at 20-year mark is roughly similar to the one under 10 MPa at a time of 100 years. This means that increasing the gas pressure from 1 to 10 MPa delays the compaction process to nearly 80 years. Interestingly, no compaction is observed at gas pressure of 20 MPa. These observations are clearly evidence in Figure 11.-3 where the average porosity over time is displayed for the three gas pressure conditions here. The figure shows that the compaction is clearly retarded at 10 MPa compared to 5 MPa but the porosity remains nearly at the initial value after 100 years. This means that at high gas pressure can completely stop stop the compaction process or even lead to a dilation as it has been shown by Stone, 1995.

Table 11.-3 extends the compaction behavior analysis to scenarios of high gas pressure. This segment of the study subjected the model to elevated gas pressures of 5 MPa, 10 MPa, and 20 MPa, with the resulting porosity distributions captured at intervals of 1, 20, 40, 70, and 100 years post-disposal. As with the low-pressure simulations, the high-pressure conditions also impact compaction, albeit more drastically.

Table 11.-2: Porosity evolution under different low gas pressures acting in the disposal drift.

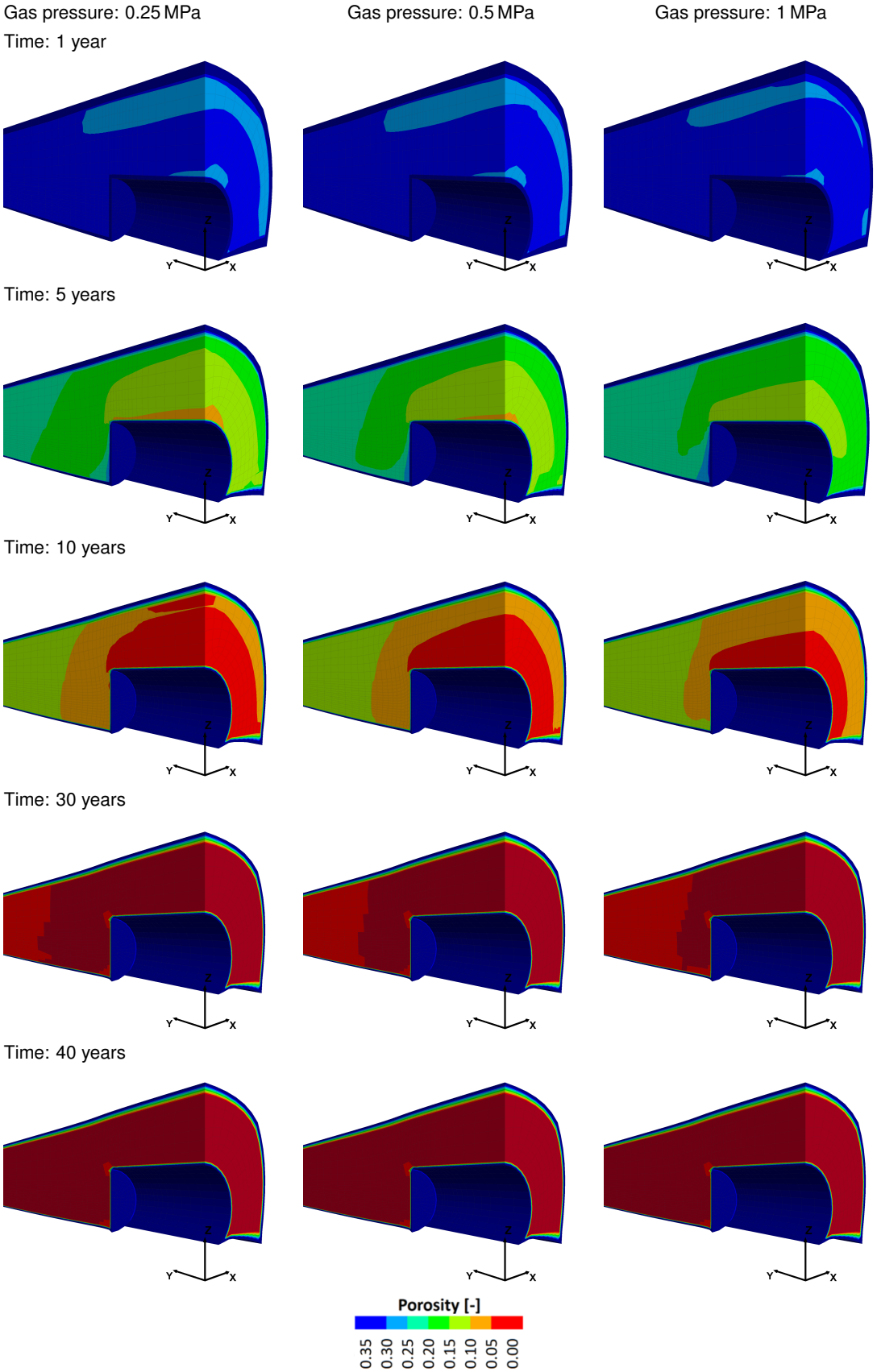

Table 11.-3: Porosity evolution under different high gas pressures acting in the disposal drift.

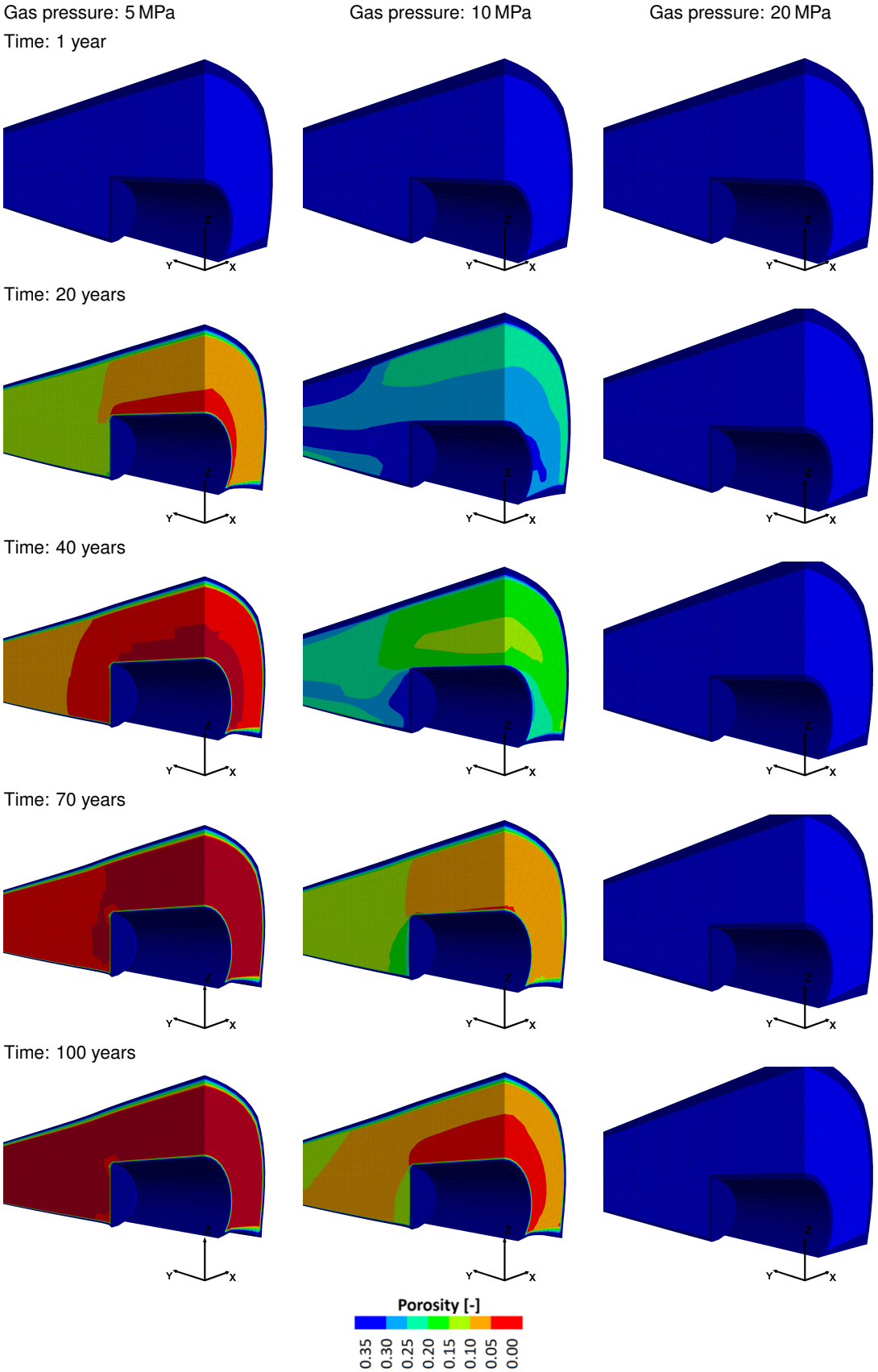

For instance, at 20 years, the porosity under a 5 MPa pressure is comparable to that observed at a century under 10 MPa. Such findings suggest a pronounced delay in compaction progression, with an increase in pressure from 1 to 10 MPa postponing the process by approximately 80 years. Notably, at the extreme pressure of 20 MPa, the compaction appears to be entirely inhibited.

These outcomes are visualized in Figure 11.-3, which presents a comparative overview of average porosity changes over time for the different high-pressure environments. This visualization corroborates that a 10 MPa pressure significantly retards compaction relative to 5 MPa. Even after 100 years, porosity levels under high pressure of 20 MPa remain close to their initial values, implying that such pressure levels can halt compaction entirely or may reverse the compaction process by dilating the backfill similar to the findings presented by Stone (1995).

From the analysis conducted within this study, several key insights have been ascertained:

- Under low gas pressure conditions, the influence of gas pressure on the compaction of crushed salt is relatively modest.
- Conversely, at elevated gas pressures, the impact on compaction is marked, with the potential to significantly postpone the compaction process by several decades, and in some cases, even centuries.
- In instances of extremely high gas pressures, there is a possibility for gas pressure to not only halt the compaction process entirely but also to induce a reversal, resulting in the dilation of the backfill.

These conclusions underscore the significance of gas pressure as a decisive factor affecting the long-term evolution and integrity of salt repositories. Incorporating the effect of gas pressure into performance assessment is therefore necessary to ensure the long term safety and effectiveness of those repositories.

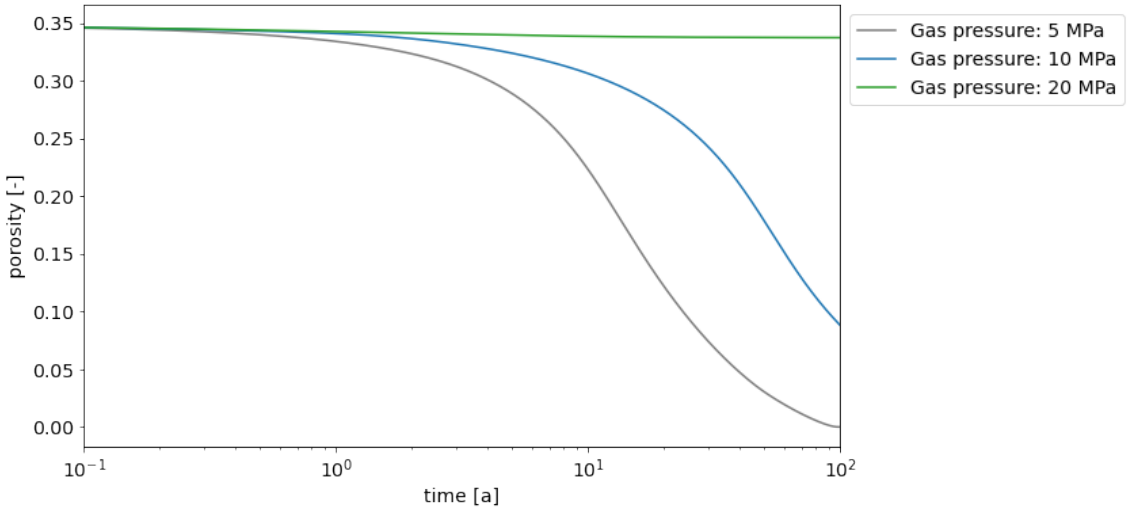

Figure 11.-3: Porosity evolution at different gas pressures in the drift.

12. Safety Evaluation of the Engineer Barrier System in Salt

In this chapter, we evaluate the results of the integrity and performance assessment of the Engineered Barrier System for a generic salt formation as designed in the project RANGERS. The developed EBS consists of two shaft sealing systems installed in the shafts of the repository complemented with four drift sealing systems installed in the two main drifts of the repository mine closing the access to the emplacement wings. These sealing system maintain the confinement of the repository until the long term seal made of crushed salt has taken its function. Therefore the analyses regarding the gain of function of the crushed salt backfill were complementary performed.

The methodology developed in this project recommends the independent analysis of the reference scenario evolutions as well as of the alternative scenarios. For each of this analysis different performance measures are established. Whereas for the reference scenario a quantitative integrity and performance assessment is required, the study of the alternatives scenarios lies in the understanding of the system behavior in severe conditions and thus helps to better assess the robustness and optimization potential of the EBS.

For both kind of analyses, the methodology allows us to derive in a stringent manner the loads acting on the EBS based on the evaluation of the available FEPs and scenarios development known for salt repositories. From these FEPs and scenarios a modeling concept were developed from which the modeling case to be analyzed derived. The main idea coming from this modeling concept is to consider as much FEPs as possible in a single modeling case in order to account for their interaction. For those FEPs that cannot be included in the main modeling case, additional modeling case was defined.

For the reference scenario evolution, the mechanical integrity assessment of the shaft and drift sealing structures were carried out in this report. This was complemented with the hydraulic assessment of the shaft sealing structure. A similar assessment for the drift sealing structure derives from the application of the methodology but is still pending.

Five modeling cases could be identified as a result of the FEP analysis. The first one comprises the main processes that have a direct effect on the mechanical integrity such as the FEPs heat flow, thermal expansion/contraction, mechanical stress changes, convergence. This permanent loading conditions are further enhanced by considering the time dependency of the sealing materials from which a degradation can be expected over time. The third modeling case consists of hydraulic loading situations that will come over time. The fourth modeling case considers the effect of seismicity and gas explosion on the EBS. The last case studies the EBS behavior in the scope of the alternative scenario evolutions.

The main results deriving from the drift sealing structure integrity assessment is that the drift seals in the repository will subjected to horizontal stresses coming from the thermal expansion of the salt. This horizontal stresses will lead to the extension or elongation of the seals. Thus, tensile stresses will developed in the seals eventually leading to vertical cracks in the seal. Fortunately, the results of the assessment for the designed seal shows that the seals will remain intact. The heat load in the emplacement fields are not high enough to induce cracks. Even for thermal impacts, simple mitigation measures can be taken to ensure that the seals remain crack free.

The analyses for the drift sealing structure indicate the formation of a loosening zone, or Excavation Damaged Zone (EDZ), in areas close to the drift contour. This means that the dilatancy criterion is exceeded in these areas, causing the rock to begin losing stability and displaying increased porosity. The dilatancy criterion is a critical factor in assessing the integrity of salt as it shows where potential microcracking and increased permeability could allow minimal but notable fluid migration.

However, the EDZ and the zone with high dilatancy remains spatially limited. Over time, the regions with high dilatancy vanish as the EDZ compacts. Almost no loosening zone is observed at the contour of the drift seals in the simulation. This is due the high stiffness of the MgO concrete helping to rapidly compact the EDZ when convergence of the rock occurs. Taking into account the self-sealing potential of the salt, it can be expected that the EDZ will quickly recover over time.

It has been also showed in the compaction analyses that the long-term seal between the drift seals will quickly gain its function. This sealing components will reach full compaction in a period of time of less than 1,000 years according to the constitutive model used for this analysis. As this model is a very simple one, a better prediction will be attend by considering the use of more advanced and calibrated models.

Also from the compaction analyses, it has been shown that the crushed salt in all of the drifts in the emplacement fields as well as in the main and cross drifts will be quickly compacted in few decades after disposal due the accelerated effect of temperature. The simulation showed that the part of the repository behind the drift sealing system will be closed at less than 100 years. This means that the confinement of the repository is achieved right after the closure of the repository.

The integrity assessment of the shaft sealing structure has shown that the sealing elements installed in the shafts will not experience any damage over time. This is for crucial importance for the MgO concrete element were cracks undermine their sealing effectiveness. The bentonite elements modeled with Cam Clay constitutive model shows some plastic strains which is inherent to high plastic materials such as bentonite and cannot be interpreted as failure. Other sealing element where modeled with Mohr-Coulomb and there no damage was observed.

At the contact zone along the shaft, a zone surrounding the shaft with high dilatancy was observed. This zone gradually decreases over time and eventually completely vanishes due to the convergence of the rock acting towards the sealing elements.

The hydraulic integrity analyses showed for the reference scenario that only 20,000 m^3 of inflowing fluids will reach the infrastructure area through one of the shaft by the end of the lifetime of the shaft sealing system after 50,000 years. Twice this amount can be assumed for both shafts. Only after full saturation of the infrastructure area, do the shafts start to fill up with water. Only at this moment, does an increase of hydrostatic pressure happen in the shaft. This pressure subsequently acts on the surface of the drift seals. This only takes place after >50,000 years for the reference scenario.

The evaluation of the EBS in the scope of the integrated performance assessment has shown that no significant gas pressure increase is to be expected in the repository. The phenomenon

behind this low gas pressure is the high temperature transforming water to steam, which migrates away from the cask through the backfill into the EDZ. Therefore the EDZ will be enriched with water, while the backfill will be dried out. In the absence of water, no corrosion is to be expected. The few atmosphere of gas pressure that was computed in the simulation was due to the corrosion of the waste packages with negligible heat-generation.

The low gas pressure in the repository also means that no further hydraulic load is to be expected for the drift seals within the repository. This also implies that the gas diffusion over time within the repository and through the seals is limited. The low gas pressure in the repository is also beneficial to the crushed salt compaction in the repository. As it as been shown in the additional analyses of compaction under gas pressure in the repository, the compaction under low gas pressure is slightly retarded but it is severely hindered at high gas pressure. This important finding of low gas pressure in the repository needs however further investigations and experimental evidence to be conclusive.

Due to the high computation effort required for the integrity assessment, analysis in regard to the integrity evaluation could not be carried out in the fullest extent. Nevertheless a strategy to carry out the required simulation can be derived from the modeling concept established in this report.

For the mechanical integrity of the EBS, the integrity evaluation is mostly relevant for the drift sealing system. The alternative scenario of a shaft sealing failure results in an hydraulic load acting on the drift seal near the shaft. At the end of the simulation time of the analysis of the drift sealing system, the seals are still subjected to tensile stresses meaning that they cannot sustain additional hydraulic loads. Longer simulation time is required to see at which period of time the seal will be able to sustain such loads. Mitigation measures may be necessary to increase the robustness of the systems at early in the repository.

For the alternative scenario of drift seal failure, no additional load is to be expected from gas pressure build up on the lower components of the shaft sealing systems as it has been demonstrated in the scope of the performance assessment that the gas generation due to corrosion in the repository is minimal. A similar assumption was assumed in integrity assessment of the shaft seals in VSG (Müller-Hoeppe et al., 2012a).

Compared to the assessment methodology from previous projects which relied on component models such as in the VSG, the proposed approach of using repository scale models has the advantages of considering as much FEPs as possible in a single model. It is also more precise regarding the loads acting on the EBS as these loads results from the global response of the repository system upon THMC evolution.

Thankfully, the loads deriving from the application of the FEPs analysis was similar to those considered in the VSG. In Müller-Hoeppe et al. (2012b), five design situations were identified based on the scenario development. These include the design situations of the reference scenario without earthquake, reference scenario with earthquake, failure of the shaft seal, failure of the drift seal, as well as the modified impact one creep class below/above the probable range, which should be addressed within the scope of an extraordinary design situation (Müller-Hoeppe et al., 2012b).

As suggested by Müller-Hoeppe et al. (2012a), the scenario involving variations in creep

classes can be excluded, as these classes can be accurately characterized during the geological site assessment. Accordingly, (Müller-Hoeppe et al., 2012a) conducted a calibration based on available convergence measurements from the Gorleben site. For the generic site considered in the RANGERS project, no such data is available, and thus this design scenario is not considered.

In this regard, the primary failure mechanism of the drift seals, which results from the horizontal thermal expansion of the salt in the emplacement fields, was not identified in the VSG drift seal assessment. In the VSG assessment, the lithostatic stress was assumed to be present at the location of the drift seals in the component model used for this analysis. In contrast, in this project, the stresses at the drift location result from the thermal-mechanical evolution of the repository. Consequently, in the VSG drift seal assessment, the seals were able to withstand the hydraulic loads much earlier in the repository evolution compared to the analysis presented in the current report.

As reported in Müller-Hoeppe et al. (2012a), in the design scenario “failure of the shaft seal”, the EDZ is subject to high compressive stresses at the drift seal location after 1,300 years, resulting in a sufficiently high pressure that the fluid pressure criterion for the hypothetical pore pressure is met.

The modeling approach for assessing the integrity of the shaft sealing structure in this project is similar to the methodology used in the VSG analyses, particularly in terms of handling the effects of pore water pressure within the shaft. The pore pressure is applied as an internal boundary condition. This approach captures the stress changes resulting from solution pressure buildup without directly simulating the flow process, thus keeping computational times manageable (Müller-Hoeppe et al., 2012a).

Similar to the VSG assessment of the shaft, the thermal-mechanical evolution of the repository system facilitates the build up compressive stresses towards the excavation-damaged zone and the contact zone. Müller-Hoeppe et al. (2012a) further explain, by comparing two simulation cases–with and without thermal impact–that thermal-mechanical effects do not fundamentally result in different critical stress states for design. Instead, these stress states occur at an earlier time, indicating that the thermal-mechanical influence from the repository essentially accelerates the process.

In the VSG assessment, the integrity criteria were evaluated by comparing the stresses acting on the sealing elements with the material strengths. A similar approach was applied to evaluate the state of the contact zone, where compressive stresses are present in the normal direction, and shear stresses remain well below the design limit. In this project, the evaluation was enhanced by using suitable constitutive models for each material, allowing damage assessment based on material-specific behavior. For the contact zone, we apply the dilatancy criterion along the shaft, which indicates rock loosening and provides a more conservative assessment compared to the strength criterion.

The seismic impacts on the Engineered Barrier System (EBS) were not analyzed in the VSG study, nor were they evaluated in this report. According to Müller-Hoeppe et al. (2012a), seismic loading conditions do not typically govern the design in cases of low additional accelerations, such as those expected during a safety-level earthquake. This is because dynamic material strengths (resistances) usually increase more than the applied stresses un-

der seismic conditions. However, an exception exists if the failure mode is associated with shear failure and is not geometrically restricted. In such cases, shear strengths may decrease due to earthquake-induced reductions in normal stress, which could potentially affect the contact zone, as shear failure in this zone is a possible failure mode. Nonetheless, since shear strength utilization in the contact zone is minimal, potential failure of the contact zone is deemed unlikely. This assessment, however, requires further verification.

The use of large models for assessment poses a drawback due to the high computational costs required. Consequently, with the computational tools available, it was not feasible to perform fully coupled THM (thermal-hydrological-mechanical) simulations to accurately represent the hydraulic evolution of the repository system. Further advancements in numerical modeling for salt structures under THM conditions are therefore essential.

Uncertainties remain regarding the contact zone, as it was not explicitly represented in the numerical models, and appropriate modeling approaches for it are yet to be defined. Additionally, the constitutive models for salt used in this report do not account for rock damage, a feature that is critical in the contact zone analysis. Depending on the modeling conditions, damage may occur in the sealing material, the contact zone, or the surrounding rock. This aspect should be addressed in future analyses and calibrated against experimental data.

13. Concluding Remarks

The RANGERS project has successfully developed and demonstrated the application of a methodology for the integrity and performance assessment of an Engineered Barrier System (EBS) for high-level waste (HLW) and spent nuclear fuel (SNF) repositories in salt formations. As part of a multi-barrier containment system, the EBS and the natural salt barriers maintain confinement, ensuring safety over a defined functional period until long-term backfill compaction is achieved.

This methodology provides a workflow to evaluate EBS integrity in generic salt-based repositories, incorporating integrated performance assessments. It builds upon extensive experience and knowledge from research conducted in Germany and the United States on the design, construction, and evaluation of seals.

In this report, the RANGERS methodology was applied to evaluate the integrity and performance of a generic salt repository for HLW and SNF. Starting from a Features, Events, and Processes (FEP) analysis, a structured modeling concept was developed to guide the integrity assessments through rigorous numerical simulations. This approach enabled a robust analysis of the thermal, mechanical, and hydrological evolution within the EBS and surrounding salt rock.

For the integrity assessment of the reference scenario, the analyses carried out in this report highlights that the EBS as designed in the project RANGERS is able to sustain the thermal-mechanical loads resulting from the heat generated by the waste in the formation. Dilatancy zones, which form locally around the drift and shaft walls, display spatial limitations and are predicted to recover over time due to salt's natural creep and convergence properties.

The crushed salt backfill, forming the long-term seal in the drifts, is projected to reach full compaction within approximately 1,000 years, ensuring containment for extended timescales. This finding is supported by rapid compaction observations in elevated temperature zones, suggesting effective sealing of backfilled drifts within decades. Hydraulic assessment of the shaft seal reveals minimal fluid migration, with a calculated inflow volume into the infrastructure area remaining below significant levels for up to 50,000 years.

A key outcome from the performance assessment is the expectation of low gas pressures within the repository, owing to initial high temperatures driving the migration of evaporated water into the surrounding rock, reducing corrosion potential. This, in turn, minimizes gas generation and reduces the associated hydraulic load within the repository, ultimately supporting the EBS's long-term containment function.

The RANGERS findings underscore the reliability of salt formations as containment solutions for radioactive waste disposal. The methodology provides a rigorous, adaptable framework for future performance assessments. Based on this methodology, the analyses of the integrity assessment can be extended for the integrity evaluation, optimization and robustness assessment. The results obtained so far for the integrity assessment already validate the EBS's capacity to maintain its integrity and functionality under regulatory timescales, thus establishing a basis for sustainable, long-term radioactive waste management in salt repositories.

Acknowledgments

The Sandia co-authors of this report were funded by the US Department of Energy Office of Nuclear Energy's (DOE-NE) Spent Fuel and Waste Science and Technology (SFWST) program.

This article has been co-authored by employees of National Technology & Engineering Solutions of Sandia, LLC under Contract No. DE-NA0003525 with the U.S. Department of Energy. The employees own all right, title and interest in and to the article and is solely responsible for its contents. The United States Government retains and the publisher, by accepting the article for publication, acknowledges that the United States Government retains a non-exclusive, paid-up, irrevocable, world-wide license to publish or reproduce the published form of this article or allow others to do so, for United States Government purposes. The DOE will provide public access to these results of federally sponsored research in accordance with the DOE Public Access Plan `https://www.energy.gov/downloads/doe-public-access-plan`.

References

Alkattan, M., Oelkers, E. H., Dandurand, J.-L., and Schott, J. (1997). Experimental studies of halite dissolution kinetics, 1 the effect of saturation state and the presence of trace metals. *Chemical Geology*, 137(3-4):201–219.

Amelung, P., Jobmann, M., Lerch, C., Polster, M., and Schonebeck, M. (2005). Berechnungen zur endlagerauslegung im steinsalz und tongestein - eine vergleichende gegenüberstellung. Präsentation auf dem Workshop "Gegenüberstellung von Endlagerkonzepten im Salz und Tonstein" - GEIST: Peine, 2005.

Batzle, M. and Wang, Z. (1992). Seismic properties of pore fluids. *Geophysics*, 57(11):1396–1408.

Bertrams, N., Bollingerfehr, W., Eickemeier, R., Fahland, S., Flügge, J., Frenzel, B., Hammer, J., Kindlein, J., Liu, W., Maßmann, J., Mayer, K.-M., Mönig, J., Mrugalla, G., Müller-Hoeppe, N., Reinhold, K., Rübel, A., Schubarth-Engelschall, N., Simo, E., Thiedau, J., Thiemeyer, T., Weber, J. R., and Wolf, J. (2020). Resus - grundlagen zur bewertung eines endlagersystems in flach lagernden salzformationen.

Beuth, T., Bracke, G., Buhmann, D., Dresbach, C., Keller, S., Krone, J., Lommerzheim, A., Mönig, J., Mrugalla, G., Rübel, A., and Wolf, J. (2012). Szenarienentwicklung - methodik und anwendung: Bericht zum arbeitspaket 8 ; vorläufige sicherheitsanalyse für den standort gorleben.

Bollingerfehr, W., Buhmann, D., Filbert, W., Keller, S., Krone, J., Lommerzheim, A., Mönig, J., Mrugalla, S., Müller-Hoeppe, N., Weber, J. R., and Wolf, J. (2013). Status of the safety concept and safety demonstration for an hlw repository in salt.- summary report isibel project, fkz 02e107 and 02e10729.

Bollingerfehr, W., Filbert, W., Dorr, S., Herold, P., Lerch, C., Burgwinkel, P., Charlier, F., Thomasuske, B., Bracke, G., and Kilger, R. (2012). Endlangerauslegung und optimierung. Technical Report GRS-281, Gesellschaft für Anlagen- und Reaktorsicherheit (GRS) gGmbH.

Bräuer, V., Jobmann, M., Langer, M., Schlüter, R., and Schatz, T. (2016). Entwicklung und bewertung eines generischen endlagerkonzepts für hochradioaktive abfälle in tongestein. *Entsorgungsbericht*, 45:345–367.

Czaikowski, O. and Friedenberg, L. (2020). Benchmarking for validation and verification of thm simulators with special regard to fluid dynamic processes in repository systems project benvasim. Technical Report GRS - 588, GRS, Braunschweig.

Czaikowski, O., Friedenberg, L., Wieczorek, K., Müller-Hoeppe, N., Lerch, C., Eickemeier, R., Laurich, B., Liu, W., Stührenberg, D., Svensson, K., Zemke, K., Lüdeling, C., Popp, T., Bean, J., Mills, M., Reedlunn, B., Düsterloh, U., Lerche, S., and Zhao, J. (2023). Kompass: Compaction of crushed salt for the safe containment. Technical Report GRS-608, Gesellschaft für Anlagen- und Reaktorsicherheit (GRS).

DOE (2019). Title 40 CFR Part 191 Subparts B and C Compliance Recertification Applicaiton 2019 for the Waste Isolation Pilot Plant. Technical Report DOE/WIPP-19-3609, US Department of Energy Carlsbad Field Office.

Endlagerkommission, D. B. (2016). *Bericht der Kommission Lagerung hoch radioaktiver Abfallstoffe*. Deutscher Bundestag, Berlin.

EndlSiAnfV (2020). Verordnung über sicherheitsanforderungen an die endlagerung hochradioaktiver abfälle (endlagersicherheitsanforderungsverordnung - endlsianfv).

Haas Jr., J. L. (1976). Physical properties of the coexisting phases and thermochemical properties of the h_2o component in boiling nacl solutions. Technical Report Bulletin 1421-A, US Geological Survey.

Herold, P., Prignitz, S., Bertrams, N., Simo, E., Filbert, W., Friedrich, C., and Becker, A. (2018). Technische konzepte für die rückholung der einlagerungsvariante horizontale streckenlagerung in salzformationen. In *Entwicklung technischer Konzepte zur Rückholung von Endlagerbehältern mit wärmeentwickelnden radioaktiven Abfällen und ausgedienten Brennelementen aus Endlagern in Salz- und Tongesteinsformationen (ERNESTA)*. BGE TECHNOLOGY GmbH, Peine.

Itasca Consulting Group, Inc. (2021). *FLAC3D Manual*. Minneapolis, MN. Version 9.0.

Keller, A., Mills, M., Hagdu, T., Herold, P., Jayne, R., Kuhlman, K., Lommerzheim, A., Matteo, E., and Simo, E. (2021). State of the art and sciences on engineered barrier systems in salt formations. Technical Report BGE TEC 2021-13 / SAND2022-0204 R, BGE TECHNOLOGY GmbH, SANDIA, Peine, Albuquerque.

Kock, I., Eickemeier, R., Friedling, G., Heusermann, S., Knauth, M., Minkley, W., Navarro, M., Nipp, H.-K., and Vogel, P. (2012). Integrität der geologischen barriere: Bericht zum arbeitspaket 9.1 vorläufige sicherheitsanalyse für den standort gorleben grs-286.

Kuhlman, K., Mills, M., Jayne, R., Matteo, E., Herrick, C., Nemer, M., Heath, J., Xiong, Y., Choens, C., Stauffer, P., Boukhalfa, H., Guiltinan, E., Rahn, T., Weaver, D., Dozier, B., Otto, S., Rutqvist, J., Wu, Y., Hu, M., Uhlemann, S., and Wang, J. (2020). FY20 update on brine availability test in salt. Technical Report SAND2020-9034R, Sandia National Laboratories.

Kuhlman, K. L., Lopez, C. M., Mills, M. M., Rimsza, J., and Sassani, D. (2018). Evaluation of spent nuclear fuel disposition in salt (FY18). Technical Report SAND2018-11355R, Sandia National Laboratories.

LaForce, T., Basurto, E., Bigler, L., Chang, K. W., Ebeida, M., Jayne, R., Leone, R., Mariner, P., and Sharpe, J. (2023a). GDSA repository systems analysis investigations for FY 2023. Technical Report SAND2023-09454R, Sandia National Laboratories.

LaForce, T., Ebeida, M., Jordan, S., Miller, T. A., Stauffer, P. H., Park, H., Leone, R., and Hammond, G. (2023b). Voronoi meshing to accurately capture geological structure in subsurface simulations. *Mathematical Geosciences*, 55(2):129–161.

Liu, H.-H. (2014). Non-Darcian flow in low-permeability media: key issues related to geological disposal of high-level nuclear waste in shale formations. *Hydrogeology Journal*, 22(7):1525.

Liu, H.-H. (2017). *Fluid flow in the subsurface*. Springer.

Liu, H.-H., Li, L., and Birkholzer, J. (2012). Unsaturated properties for non-Darcian water flow in clay. *Journal of Hydrology*, 430:173–178.

Liu, W., Völkner, E., Popp, T., and Minkley, W. (2017). Zusammenstellung der materialparameter für thm-modellberechnungen - ergebnisse aus dem vorhaben kosina. In BGR, editor, *Konzeptentwicklung für ein generisches Endlager für wärmeentwickelnde Abfälle in flach lagernden Salzschichten in Deutschland sowie Entwicklung und Überprüfung eines*

Sicherheits- und Nachweiskonzeptes (KOSINA). Bundesanstalt für Geowissenschaften und Rohstoffe, Hannover.

Mariner, P. E., Nole, M. A., Basurto, E., Berg, T. M., Chang, K. W., Debusschere, B. J., Eckert, A. C., Ebeida, M. S., Gross, M., Hammond, G. E., Harvey, J., Jordan, S. H., Kuhlman, K. L., LaForce, T. C., Leone, R. C., McLendon III, W. C., Mills, M. M., Park, H. D., Perry, F. V., Salazar III, A., Seidl, D. T., Sevougian, S. D., Stein, E. R., and Swiler, L. P. (2020). Advances in GDSA framework development and process model integration. Technical Report SAND2020-10787R, Sandia National Laboratories.

Mualem, Y. (1976). A new model for predicting the hydraulic conductivity of unsaturated porous media. *Water Resources Research*, 12(3):513–522.

Müller-Hoeppe, N., Breustedt, M., Wolf, J., Czaikowski, O., and Wieczorek, K. (2012a). Integrität geotechnischer barrieren teil 2: Vertiefte nachweisführung: Bericht zum arbeitspaket 9.2; vorläufige sicherheitsanalyse für den standort gorleben.

Müller-Hoeppe, N., Buhmann, D., Czaikowski, O., Engelhardt, H.-J., Herbert, H.-J., Lerch, C., Linkamp, M., Wieczorek, K., and Xie, M. (2012b). Integrität geotechnischer barrieren teil 1: Vorbemessung: Bericht zum arbeitspaket 9.2; vorläufige sicherheitsanalyse für den standort gorleben.

Naumov, D., Bilke, L., Lehmann, C., Fischer, T., Wang, W., Shao, H., Buchwald, J., Rink, K., Chen, C., Mollaali, M., Kessler, K., and Max, J. (2024). Opengeosys.

Nole, M., Beskardes, G. D., Fukuyama, D., Leone, R. C., Mariner, P., Park, H. D., Paul, M., Salazar, A., Hammond, G. E., and Lictner, P. C. (2022). PFLOTRAN development FY2022. Technical Report SAND2022-10526R, Sandia National Laboratories.

Nole, M., Beskardes, G. D., Fukuyama, D., Leone, R. C., Park, H. H., Paul, M., Salazar, A., Hammond, G. E., and Lichtner, P. C. (2023). Recent advancements in PFLOTRAN development for the GDSA framework. Technical Report SAND2023-07655, Sandia National Laboratories.

Parker, J., Lenhard, R., and Kuppusamy, T. (1987). A parametric model for constitutive properties governing multiphase flow in porous media. *Water Resources Research*, 23(4):618–624.

Parkhurst, D. L. and Appelo, C. A. J. (2013). Description of input and examples for PHREEQC version 3—A computer program for speciation, batch-reaction, one-dimensional transport, and inverse geochemical calculations. Technical Report USGS Survey Techniques and Methods, Book 6, Chapter A43, US Geological Survey.

Simo, E., Herold, P., Hagdu, T., Jayne, R., Keller, A., Kuhlman, K., Lommerzheim, A., Matteo, E., and Mills, M. (2024). Methodology report on design and performance assessment of engineered barrier systems in a salt repository for hlw/snf. Technical Report BGE TEC 2024-XX / SAND2024-XXXX R, BGE TECHNOLOGY GmbH, SANDIA, Peine, Albuquerque.

Somerton, W. H., Keese, J. A., and Chu, S. L. (1974). Thermal behavior of unconsolidated oil sands. *Society of Petroleum Engineers Journal*, 14(5):513–521.

Sparrow, B. S. (2003). Empirical equations for the thermodynamic properties of aqueous sodium chloride. *Desalination*, 159(2):161–170.

van Genuchten, M. Th. (1980). A closed-form equation for predicting the hydraulic conductivity of unsaturated soils. *Soil Science Society of America Journal*, 44(5):892–898.

Villar, M., Besuelle, P., Cernochova, K., Collin, F., Cuevas, J., Cuss, R., de Lesquen, C., Dizier, A., El Tabbal, G., Gens, A., Gimeno, N., Graham, C., Grgic, D., Harrington, J., Imbert, C., Kašpar, V., Kaufhold, S., Leupin, O., Levasseur, S., Mašín, D., Najser, J., Narkŭnienè, A., Ollin, M., Reijonen, H., Šachlová, v., Sayenko, S., Simo, E., Svensson, D., Svoboda, J., Tatomir, A., Vettese, G., Yliharju, J., and Zoblenko, B. (2023). D7.2 hitec. updated state-of-the-art on thm behaviour of buffer clay materials and host clay formations. Technical Report Deliverable n° 7.2, EURAD Project, Horizon 2020. 129 pp.

Wolery, T. J. (2010). EQ3/6 a software package for geochemical modeling. Technical Report LLNL-CODE-638958, Lawrence Livermore National Laboratory.

BGE TECHNOLOGY GmbH
Eschenstraße 55
31224 Peine – Germany
T + 49 5171 43-1520
F + 49 5171 43-1506
info@bge-technology.de
www.bge-technology.de